THESE DE DOCTORAT DE

NANTES UNIVERSITE

ECOLE DOCTORALE N° 596
Matière, Molécules, Matériaux et Géosciences
Spécialité : « *(Sciences des Matériaux)* »

Par
Abbas KHAN

Tailored oxides and carbides as active materials for high power energy storage devices

Thèse présentée et soutenue à Nantes, le 16 Octobre 2024
Unité de recherche : Institut des Matériaux Jean Rouxel (IMN), UMR 6502

Rapporteurs avant soutenance :

Isabelle MONOT-LAFFEZ	Professeur, GREMAN, CNRS – UMR 7347 Université de Tours
Valérie PRALONG	Directeur de recherche, CNRS – CRISMAT Caen, UMR 6508

Composition du Jury :

Président :	Thierry DJENIZIAN	Professeur de l'Ecole des Mines – IMT St Etienne
Examinateurs :	Andrea BALDUCCI	Full professor, Friedrich Schiller Universität Jena
Dir. de thèse :	Thierry BROUSSE	Professeur, IMN, UMR 5026 Université de Nantes
Co-encadrant de thèse :	Olivier Crosnier	Maître de conférences, IMN, UMR 5026 Université de Nantes

Invité(s)
Prénom Nom Fonction et établissement d’exercice

Acknowledgements

My Ph.D. journey has come to an end, a milestone I am immensely proud of. Before discussing the scientific aspects, I want to take a moment to sincerely thank everyone who supported me throughout this journey.

I would like to express my heartfelt gratitude to my Ph.D. advisor, Thierry Brousse, for the opportunity to work under his guidance. My research journey began during my master's studies in Pakistan, when I was introduced to his renowned paper, *"To be or not to be pseudocapacitive?"*. It was the first ever research paper I read on electrochemical energy storage materials, and it left a lasting impression on me. From that moment, I aspired to one day work with him – a dream that has since become a reality. I remember our first meeting when he drove me to the campus and said, *"You bring sun to Nantes..."*. Though he was referring to the weather, those words brought me great joy and marked the beginning of my Ph.D. journey. As a researcher, he constantly encouraged me to push the boundaries of my work and contribute meaningfully to the field of electrochemical energy storage. As a teacher, he instilled in me the importance of effectively presenting and communicating my results, a skill I will always strive to improve. As a mentor and an exceptional human being, he was kind, approachable, and willing to discuss challenges even beyond science. Overall, the guidance and support I have received from him is the reason I am able to complete this dissertation and to become a more versatile researcher. Being able to call him my advisor has been an immense honor.

I extend my heartfelt gratitude to Olivier Crosnier, my thesis co-supervisor, for his unwavering support and kindness throughout this journey. I remember my arrival in a new country and a new city – an experience that could have been overwhelming – transformed into a warm welcome as he greeted me at the train station and personally drove me to the accommodation. He guided me about the Nantes city and helped me in initial adjustment. His ability to encourage open discussions allowed me to navigate even the most fundamental questions about my experiments with confidence. He was always there to support me, especially with diffraction experiments, and remained approachable, despite his busy schedule. Beyond academics, I thoroughly enjoyed our conversations about cooking and his curiosity for Pakistani spices – I believe they even found a special place in his kitchen :-)

I am deeply thankful to the reviewers and all the members of my jury for their invaluable contributions. Prof. Isabelle Monot-Laffez and Prof. Valerie Pralong for their thorough review of my manuscript with encouraging comments on the quality of research and writing. The engaging discussions during my defense were both enriching and inspiring. I also extend my heartfelt thanks to Prof. Thierry Djenizian and Prof. Andrea Balducci for their feedback and constructive suggestions during the defense. Furthermore, I extend my sincere appreciation to Prof. Laurent Cario and Prof. Liliane Guerlou-Demourgues, members of my CSI (Individual Ph.D. Committee), for their consistent guidance and constructive feedbacks during our yearly progress meetings.

I would like to sincerely thank Prof. Andrea Balducci from Friedrich Schiller University Jena, my secondment supervisor under the DESTINY project, for his invaluable support and for providing me with the opportunity to undertake a research stay in his group. I greatly appreciate the time he devoted to our meetings and the insightful feedbacks, both during my stay and throughout my Ph.D. journey. My deepest thanks to my DESTINY colleague from Jena, Metin Orbay, with whom I closely collaborated on this project. It was a truly enriching experience to work together and discuss such an interesting topic. I am also grateful to the amazing and kind-hearted members of the group – Juan Luis GU, Indrajit MP, Khai Shin T, Sandesh DM, Michel K, Siqi L, Christian L, Fabian AK, Lukas K, and all the other team members, including Massimo M and Silvia, the exchange PhD students from Italy. I thoroughly enjoyed every moment, from working together in the group to the fun activities we shared, including our enjoyable evenings playing volleyball and weekend hiking adventures. The farewell moments, remains one of the most cherished memories of my time with them.

I would also like to thank everyone whose expertise contributed to the success of my experiments. My gratitude goes to Eric Quarez for always being there to help with structural refinements – I admire him for his detailed analysis and impressive discussions. I am equally grateful to Nicolas Dupre for the insightful NMR experiments conducted during this thesis, which were both instructive and enriching. Sincere thanks to Eric Gautron for his collaboration on TEM experiments – I truly appreciate the effort he invested, especially during the final stages of my work. I also extend my gratitude to Stephane Grolleau for the BET measurements – Marion Allart and Thomas Fournier for their helpful tips with the microscope (SEM–EDX).

I sincerely appreciate the funding sources that supported this work. As one of the projects of the DESTINY PhD programme, this thesis was partly funded by the European Union's Horizon2020 Research and Innovation Programme under the Marie Skłodowska-Curie Action PhD COFUND (Grant Agreement #945357). In addition, this thesis was also financially supported by Région des Pays de la Loire.

I cannot forget to thank the amazing Ph.D. students and postdocs of our supercaps team at Chantrerie, whom I had the privilege of meeting during this journey. I would especially thank Etienne LC, Nicolas GB, and David B, for their unwavering support during my initial adjustments and experiments in the lab. A heartfelt thanks to Camille Douard, who was always there to assist me countless times – from working in the chemistry lab to handling instruments, accompanying me to synchrotron experiments, and even helping with the translation of French administrative documents that always worried me.

A special mention goes to my office mates: Julio, for his helpful advice during the early days of my Ph.D.; Allan L, a long-term office mate, for our countless discussions about Ph.D. progress – I will always remember his kindness and support throughout these years; and Hugo M and Oumar T, who joined towards the end of my Ph.D. – thank you for the good times, the laughter, and the jokes we shared in the office. A special mention for two wonderful and supportive team members Marcelo A and Patrick G, whose encouragement and approachable nature made them a pleasure to be around, and I truly enjoyed their company. With Charlotte B, Thibaud G, Camille P, Nicolas D, Jeremy B, Laurence A, I was fortunate to share memorable times in the lab. Playing badminton with you, the supercap crew, during lunch breaks remains one of my fondest memories.

I warmly thank all my colleagues at Chantrerie for the enjoyable coffee breaks and birthday events – Louise B, Hugues M, Juliette T, Vincent K, Laurent C, Fanch G, Paul D, David B, and Cedric M. I also cherish the lunch moments at Crous with Anas R, Martin C, Ilana, and Pauline. From Lombarderie, I am grateful to the Ph.D. students with whom I built strong bonds and shared great times, especially Boluwatife Igbaroola (a.k.a. Matt) and Mohammad. Meeting them on my first day led to many beautiful memories of exploring Nantes and playing games.

Finally, yet importantly, I faced some of the most challenging moments of my life during my Ph.D. Early on, I lost my beloved mother to lung cancer just two months after starting this journey. It was a devastating blow. I will always be grateful for the unwavering support of research team, especially Thierry, whose kindness and trust despite barely knowing me then, remain close to my heart. I dedicate this achievement to my mother, wishing she could have seen me reach this milestone – an accomplishment never before achieved in our family. Other family members were my pillars of strength. My father, Muhammad Ilyas, though unfamiliar with science, had unwavering belief in me. At the start of my final year, he underwent a failed prostate surgery, followed by five additional procedures, including a complex urethroplasticity. It was a tough time for our family, and I am deeply grateful to my younger brother, Waqas

Ahmed, who sacrificed his job and returned to Pakistan from the UAE to take care for our father, enabling me to continue my Ph.D. A million thanks to my beloved wife, Sana Khan, for always being by my side, for her support and tireless encouragement throughout this journey – I cannot wait to see you earn your Dr. title too! To my kind sisters, and all the pretty nieces and handsome nephews, your unflagging love, sacrifices, and prayers meant the world to me.

Table of contents

Résumé de Thèse 1

General Introduction 7

Chapter 1: Literature review 10

1.1 Overview of lithium ion batteries (LIBs) 10

1.1.1 History and applications 10

1.1.2 Working principle 11

1.2 Materials for Li-ion batteries: 12

1.2.1 Positive electrode materials 13

1.2.2 State-of-the-art negative electrode materials 14

1.3 ABO_3-type perovskite structures 16

1.4 Defect engineering in ABO_3 perovskites 19

1.5 Recent developments in ABO_3 perovskite as a negative electrode materials for LIBs 19

1.5.1 BO_3-type pseudo-perovskite structures 19

1.5.2 ABO_3-type titanates as negative electrodes for LIBs 21

1.5.3 ABO_3-type vanadates as negative electrodes for LIBs 23

1.5.4 ABO_3-type niobates as negative electrodes for LIBs 25

1.6 Transition metal based carbides: MAX phases 30

1.6.1 MAX phases 30

1.6.2 Synthesis of Ti_3AlC_2 phases: State-of-the-art and novel routes 31

References related to chapter 1 34

Chapter 2: Synthesis and Li^+ storage in $AgNbO_3$, $Ag_{1-3x}La_x\square_{2x}NbO_3$ and $Ag_{1-x}\square_xNbO_{3-\delta}$ perovskites model system 44

2.1 Polyacrylamide synthesis of $Ag_{1-3x}La_x\square_{2x}NbO_3$ perovskites 44

2.2 Crystal structure and morphology 46

2.3 Li^+ storage in $Ag_{1-3x}La_x\square_{2x}NbO_3$ perovskites under 1.2 – 3.0V potential window .. 49

2.4 Li^+ storage in $Ag_{1-3x}La_x\square_{2x}NbO_3$ perovskites under extended potential windows ... 50

2.5 Published paper 52

Lithium storage behaviour of $AgNbO_3$ perovskite: Understanding electrochemical activation and charge storage mechanisms 53

Graphical Abstract 53

Abstract 53

Introduction 54

Experimental section 56

Material synthesis 56
Physical characterizations 56
Electrochemical measurements 57
Results and Discussions 58
Crystal structure and characterizations of $AgNbO_3$ 58
Ag reduction and exsolution process in $AgNbO_3$ crystal lattice 60
Electrochemical performance characterization 68
Conclusion 70
Acknowledgments 70
References related to paper 71
2.6 Supplementary information associated to research paper 75
References related to SI of paper 82
2.7 Intrinsic A-site deficient $Ag_{1-x}\square_xNbO_{3-\delta}$: Synthesis and Li^+ storage performance ... 83
2.7.1 Synthesis and powder XRD characterizations 83
2.7.2 Li^+ storage performance of $Ag_{1-x}\square_xNbO_{3-\delta}$ perovskite system 84
2.8 Conclusion 89
References related to chapter 2 91
Chapter 3: Study of Li^+ storage in tailored perovskite $K_{1-3x}La_x\square_{2x}NbO_3$ ($0 \leq x \leq 0.15$) negative electrode materials 93
3.1 Introduction 93
3.2 Submitted paper 94
Effect of A-site deficiency on Li^+ storage in tailored perovskite $K_{1-3x}La_x\square_{2x}NbO_3$ ($0 \leq x \leq 0.15$) negative electrode 94
Graphical Abstract 95
Abstract 95
Introduction 96
Experimental 98
Material synthesis 98
Physical characterizations 98
Electrochemical measurements 99
Results and Discussion 99
Crystal structure and physical characterizations 99
Li^+ storage behaviour of $K_{1-3x}La_x\square_{2x}NbO_3$ materials 103
Crystal structure evolution during charge/discharge 105
Li^+ storage performance under extended potential window 110

Conclusion 112
Acknowledgments 113
References related to Paper 113
3.3 Conclusion 123
References related to chapter 3 124
Chapter 4: Wet chemical synthesis approach for Ti_3AlC_2 MAX phases and their Li^+ storage performance 126
4.1 Introduction 126
4.2 Polyacrylamide synthesis approach for Ti_3AlC_2 MAX phases 127
4.3 Crystallization approaches for achieving Ti_3AlC_2 MAX phase 128
4.3.1 Strategy 1: Pre-oxidation and subsequent annealing of xreogel in Ar/H_2 130
4.3.2 Strategy 2: Direct annealing of xreogel in Ar/H_2 atmosphere 132
4.4 Electrochemical characterizations of synthesized carbide materials 138
4.5 Conclusion 140
References related to chapter 4 141
General Conclusion 145
Perspectives and Critical Reflections on this Thesis Work 147
Annex 150

Résumé de Thèse

Depuis leur introduction commerciale dans les années 1990, les batteries lithium-ion (LIBs) sont devenues essentielles pour réduire les émissions de carbone et intégrer les énergies renouvelables. Offrant flexibilité, évolutivité et haute densité énergétique, les LIBs ont révolutionné le stockage d'énergie en alimentant de nombreux équipements, des appareils électroniques portables aux véhicules électriques (VE). Avec le développement des VE, des défis récents sont apparus, tels que la limitation des matières premières, les problèmes de sécurité comme les emballements thermiques, et l'impact environnemental de l'élimination des batteries. L'un des défis les plus critiques réside dans l'amélioration des matériaux d'électrodes, notamment en trouvant des alternatives aux anodes en graphite et aux cathodes à base de cobalt, afin d'améliorer les performances, de réduire les coûts et d'assurer leur durabilité. Ces avancées sont également essentielles pour permettre une charge plus rapide, car les matériaux actuels des électrodes peuvent se dégrader dans des conditions de forte puissance, limitant ainsi la possibilité de charge rapide des VE.

Cette thèse s'inscrit dans le cadre du projet européen COFUND DESTINY (Doctorate Programme on Emerging Battery Storage Technology INspiring Young Scientists), coordonné par le Prof. Christian Masquelier à l'Université de Picardie Jules Verne à Amiens. Soutenu par le programme Horizon 2020 Marie Skłodowska-Curie COFUND de la Commission européenne (Accord de subvention #945357), DESTINY vise à former 50 doctorants dans diverses institutions, en se concentrant sur la réinvention des matériaux pour batteries, le développement de fonctionnalités intelligentes et l'intégration de nouvelles technologies dans l'industrie. L'objectif général de cette thèse s'aligne sur les objectifs du projet, en mettant l'accent sur la synthèse et l'application de nouveaux matériaux d'électrodes adaptés pour des LIBs à haute puissance. Ces matériaux doivent trouver un équilibre entre densité énergétique, puissance, rentabilité et durabilité environnementale, avec des méthodes de synthèse innovantes jouant un rôle clé dans leur développement. Dans le cadre du projet, le travail inclut également une mobilité dans le laboratoire du Prof. Andrea Balducci à l'Université Friedrich-Schiller de Jena, en Allemagne, pour tester les matériaux oxydes dans des électrolytes innovants élaborés par le groupe de Jena.

L'objectif de cette thèse était d'explorer et de développer de nouveaux matériaux d'électrodes pour les LIBs en mettant l'accent sur l'amélioration des performances de stockage d'énergie, en particulier la capacité à haut régime et la stabilité en cyclage. Au cours de ce travail, diverses

stratégies ont été développées pour synthétiser et optimiser les matériaux, en s'appuyant sur les recherches de base établies dans le chapitre bibliographique. Les recherches concernent le développement et l'optimisation de la méthode de synthèse par méthode polyacrylamide (une méthode sol-gel couplée à une polymérisation) pour des matériaux de type oxydes multicationiques. Des pérovskites modèles $Ag_{1-3x}La_x\square_{2x}NbO_3$ (avec $0 \leq x \leq 0{,}20$; $\square$ désignant une lacune sur le site A) ont été précédemment synthétisées par l'équipe *via* des méthodes céramiques haute température et sol-gel. Ces matériaux ont été étudiés comme électrodes négatives et le rôle des lacunes dans l'amélioration du stockage du Li^+ a ainsi été démontré. La méthode de synthèse sol-gel présente plusieurs avantages par rapport à la synthèse céramique: basse température de traitement thermique, production de particules à l'échelle nanométrique, meilleure homogénéité du produit final grâce à un mélange à l'échelle moléculaire, et morphologie uniforme. Cependant, obtenir une stœchiométrie uniforme et une répartition homogène des cations avec une faible agglomération reste un défi clé pour la méthode sol-gel dans la synthèse des oxydes multicationiques. La technique du gel polyacrylamide est une méthode de synthèse adaptée qui peut relever efficacement ces défis. Elle est rapide, économique, reproductible et capable de produire des matériaux fins de haute qualité à température relativement basse.

Cette méthode a été utilisée pour synthétiser les pérovskites modèles $Ag_{1-3x}La_x\square_{2x}NbO_3$ ($0 \leq x \leq 0{,}20$). Comparée à la méthode sol-gel, la synthèse par polyacrylamide produit des matériaux avec une morphologie uniforme et bien définie sans agglomération des particules, ainsi qu'une composition uniforme. Il a été démontré que la formation de lacunes dans une pérovskite *via* la substitution de La permet l'insertion de Li^+ dans une fenêtre de potentiel stable (0,2 – 3,0 V *vs* Li^+/Li).

D'un point de vue électrochimique, l'accent est mis sur une étude détaillée du stockage de Li^+ dans les pérovskites $Ag_{1-3x}La_x\square_{2x}NbO_3$ dans des fenêtres de potentiel élargies (0,6 – 3,0 V et 0,01 – 3,0 V vs Li^+/Li). Une instabilité électrochimique des pérovskites $Ag_{1-3x}La_x\square_{2x}NbO_3$ a été observée à des bas potentiels de coupure, où le matériau de l'électrode subit des modifications structurales irréversibles au cours du premier cycle, entraînant un stockage de Li^+ accru lors des cycles suivants. Ce processus unique d'activation a été observé à la fois dans les matériaux de base et dans les matériaux substitués au La. Cependant, les échantillons substitués au La possèdent une grande quantité de lacunes sur le site A et une concentration insuffisante de cations Ag sur le site A pour maintenir la stabilité de la structure pérovskite, ce qui conduit finalement à un effondrement structural. Celui-ci entraîne une diminution significative de la capacité dans les échantillons substitués après 100 cycles. Par conséquent, le matériau $AgNbO_3$ non modifié a été sélectionné pour une enquête approfondie du processus d’activation *via* des caractérisations avancées.

Lors de la première lithiation, $AgNbO_3$ subit une exsolution de Ag du site A de la structure, entraînant une non-stœchiométrie A/B, ce qui entraîne une compensation partielle de Ag^+ par l’intercalation de Li^+. Une transition structurale oxyde cristallin / amorphe est observée en dessous de 0,3 V vs Li^+/Li. L'insertion de lithium s'accompagne d'une réduction irréversible de Nb^{5+} jusqu'à une valeur estimée de Nb^{3+} lors de la première lithiation, et d'un processus redox réversible Nb^{4+}/Nb^{3+} lors des cycles suivants. De plus, des mécanismes de stockage basés sur la formation réversible d’alliages Li-Ag interviennent à la fin du processus de réduction (en dessous de ~0,3 V). Globalement, $AgNbO_3$ a affiché une capacité spécifique stable de 226 mAh.g^{-1} dans une fenêtre de potentiel élargie (0,01 – 3,0 V vs Li^+/Li), soit treize fois la capacité obtenue dans la fenêtre de potentiel électrochimiquement stable (1,2 – 3,0 V vs Li^+/Li). En outre, l’électrode a démontré d’excellentes performances en conditions de forte puissance avec une rétention de capacité de 72 mAh.g^{-1} à 2 A.g^{-1} (2,2 minutes de charge) et une très bonne stabilité cyclique à 1 A.g^{-1} (8 minutes de charge) après 2500 cycles. Ce travail a contribué à comprendre comment les transformations structurales dynamiques pendant les processus électrochimiques peuvent améliorer les performances des électrodes à base de pérovskite. Grâce au développement de matériaux *via* plusieurs stratégies de modification, telles que les pérovskites lacunaires en site A substituées au La ($Ag_{1-3x}La_x\square_{2x}NbO_3$, $0 \leq x \leq 0{,}20$) et les pérovskites non dopées lacunaires en site A ($Ag_{1-x}\square_xNbO_{3-\delta}$, $0 < x < 0{,}55$), il a été démontré que les matériaux pérovskites ABO_3 sont des structures hôtes polyvalentes et prometteuses pour construire des électrodes de stockage cationique avec des propriétés optimales.

Fait intéressant, il existe plusieurs autres pérovskites cubiques à base de Nb thermodynamiquement stables, avec des cations monovalents sur le site A, sous la forme $A^{1+}Nb^{5+}O_3$. Cela inclut principalement les pérovskites basées sur les métaux alcalins, comme $LiNbO_3$, $KNbO_3$, $NaNbO_3$, et $RbNbO_3$. Tous ces matériaux forment une structure pérovskite avec Nb^{5+} comme cation sur le site B, similaire à $AgNbO_3$, bien que des structures cristallographiques alternatives puissent être obtenues. Cette similarité structurale contribue à leurs propriétés chimiques et électroniques étroitement liées. La présence de Nb^{5+} dans tous ces composés devrait produire un environnement de liaison et une structure électronique comparables. Cependant, en raison des différences dans les cations du site A, la stabilité thermodynamique et les effets de substitution peuvent varier de manière significative. De plus, leur comportement de stockage de Li^+ et leurs performances pourraient également différer, car les variations des cations du site A peuvent influencer des facteurs tels que la mobilité ionique, la formation de défauts et la stabilité électrochimique globale.

Les niobates basés sur les métaux alcalins représentent des alternatives économiques et durables à $AgNbO_3$. En termes d'abondance, Na et K sont les plus disponibles, suivis de Li, qui est modérément abondant comparé à Ag. Par exemple, selon le rapport *Mineral Commodity Summaries 2024*, l'abondance du lithium est d'environ 20 parties par million (ppm), celle du sodium est de 23 000 ppm et celle du potassium est de 15 000 ppm, tandis que celle de l'argent est seulement de 0,075 ppm. Cette abondance impacte directement le coût : alors que le prix des métaux purs est d'environ 100 à 150 \$ par kilogramme (kg) pour Li, de 2 à 3 \$/kg pour Na et de 35 à 40 \$/kg pour K, le coût de l'argent est bien plus élevé, atteignant environ 752 \$/kg. Cette différence de coût affecte directement la faisabilité d'utiliser $AgNbO_3$ par rapport aux niobates alcalins tels que $LiNbO_3$, $NaNbO_3$ et $KNbO_3$ dans des applications à grande échelle. Bien que $AgNbO_3$ offre des propriétés intéressantes, telles qu'une bonne conductivité électrique, facilitant un stockage rapide de Li^+, son coût élevé le rend moins attractif pour les applications commerciales. Adapter les niobates métalliques alcalins moins chers à ces applications pourrait fournir des alternatives économiquement viables avec une fonctionnalité similaire.

Sur la base de cette analyse, la structure pérovskite hôte $KNbO_3$ a été choisie pour étendre la stratégie développée à un système plus économique. La conception du système pérovskite $K_{1-3x}La_x\square_{2x}NbO_3$ (avec $0 \leq x \leq 0,15$; $\square$ représentant une lacune sur le site A) offre de multiples avantages pour créer un matériau polyvalent. Ce système devrait améliorer les performances de stockage de Li^+ grâce à la présence de lacunes dans sa structure. En outre, la taille appropriée des lacunes dans le site du potassium pourrait permettre une compatibilité avec l'insertion de K^+, une caractéristique non atteinte avec $Ag_{1-3x}La_x\square_{2x}NbO_3$ pour le stockage de Na^+. Par conséquent, le système pérovskite $K_{1-3x}La_x\square_{2x}NbO_3$ ($0 \leq x \leq 0,15$) a été conçu, synthétisé et sa relation structure-propriété en tant qu'électrode négative pour le stockage de Li^+ a été étudiée en détail.

Une augmentation de la symétrie du réseau a été obtenue avec les substitutions de La sur le site A occupé par K^+ dans la structure pérovskite, entraînant une transformation du groupe d'espace de Amm2 pour $KNbO_3$ non modifié à R3m pour $K_{0.55}La_{0.15}\square_{0.30}NbO_3$. Les mesures électrochimiques ont confirmé une amélioration des performances des matériaux substitués pour le stockage de Li^+, avec une capacité spécifique multipliée par trois et une meilleure capacité à haut régime comparée à la structure de base. La structure hautement substituée $K_{0.55}La_{0.15}\square_{0.30}NbO_3$ (30 % de lacunes atomiques sur le site A) a montré une capacité spécifique de 164 $mAh.g^{-1}$ à 0,02 $A.g^{-1}$ dans une fenêtre de potentiel de 0,05 – 3,0 V vs Li^+/Li. Les lacunes dans la structure ont servi de sites d'insertion pour Li^+, facilitant l'accessibilité au réseau pérovskite et, par conséquent, à l'environnement proche des octaèdres $[NbO_6]$. Les structures ont montré une stabilité électrochimique accrue, comme en témoigne une coupure de potentiel à 50 mV vs Li^+/Li, une caractéristique rare dans les oxydes à base de Nb. L'analyse par diffraction des rayons X *in situ* a révélé un mécanisme de stockage de type solution solide avec un changement de volume maximal de seulement 1,3 % lors de l'insertion de Li^+. Cela explique la remarquable stabilité de la capacité obtenue après 900 cycles à 0,1 $A.g^{-1}$.

En lien avec les études sur le système modèle $Ag_{1-3x}La_x\square_{2x}NbO_3$ ($0 \leq x \leq 0,20$), cette étude valide davantage le rôle significatif que peuvent jouer les modifications structurales contrôlées dans l'optimisation des performances des matériaux pour les électrodes LIB, en particulier dans le cadre de l'ingénierie des lacunes.

S'appuyant sur ces découvertes, le dernier chapitre de cette thèse se concentre sur une autre famille de matériaux ayant un fort potentiel pour le stockage de l'énergie : les carbures ternaires connus sous le nom de phases MAX. Nous avons présenté une utilisation innovante de la voie chimique humide à base de polyacrylamide pour synthétiser des phases MAX Ti_3AlC_2, une méthode qui n'a pas été rapportée auparavant dans la littérature. Cette transition est motivée par les applications prometteuses des phases MAX dans le stockage d'énergie, notamment leur capacité à former des MXènes, une classe de matériaux offrant d'excellentes performances en tant qu'électrodes dans les systèmes de stockage d'énergie électrochimique à haute puissance. La synthèse réussie de structures lamellaires similaires au Ti_3AlC_2 a été réalisée, et ces matériaux ont été étudiés comme matériaux d'électrode négative pour les LIBs. Les résultats ont montré que Ti_3AlC_2@C présentait des capacités spécifiques plus élevées et une meilleure stabilité en cyclage par rapport au Ti_3AlC_2 commercial, en grande partie grâce au rôle bénéfique du carbone excédentaire dans l'amélioration de la conductivité et la contribution au stockage de Li^+. Cependant, des défis liés à la pureté de la phase obtenue et au carbone excédentaire ont également été observés, soulignant la nécessité d'une optimisation supplémentaire du processus de synthèse.

Dans l’ensemble de ces études, un thème commun a été l’importance de la synthèse contrôlée des oxydes et des carbures, par des voies différentes et le contrôle structural, pour améliorer les performances des électrodes de LIB. Les recherches présentées dans cette thèse démontrent qu’en employant différentes stratégies, telles que l’activation *in situ*, la substitution cationique et les techniques de synthèse adaptées, il est possible d’améliorer de manière significative la capacité de stockage de Li^+, la stabilité en cyclage et les performances globales. Bien que chaque système de matériaux ait posé des défis particuliers, l’ensemble des résultats offrent des perspectives précieuses sur les principes de fabrication qui peuvent guider le développement de futurs matériaux d'électrode à haute performance.

Dans l’ensemble, cette thèse a apporté une contribution significative au domaine du stockage de l'énergie en explorant de nouveaux systèmes de matériaux et en fournissant une compréhension plus approfondie des propriétés structurelles et électrochimiques qui régissent leurs performances dans les LIB. Les perspectives obtenues à partir des études sur les oxydes pérovskites ($AgNbO_3$, $Ag_{1-3x}La_x\square_{2x}NbO_3$, $Ag_{1-x}\square_xNbO_{3-\delta}$, et $K_{1-3x}La_x\square_{2x}NbO_3$) et les carbures ternaires (phases MAX Ti_3AlC_2) non seulement améliorent les connaissances actuelles sur ces matériaux, mais fournissent également une base pour les recherches futures visant à optimiser les matériaux d'électrode pour les technologies de stockage d'énergie de nouvelle génération à haute puissance.

General Introduction

In 2021, global CO_2 emissions surged to 36.3 billion tons, nearly matching the set pre-pandemic levels despite the economic slowdown caused by COVID-19. With global energy demand projected to rise 4% by 2030, the challenge of balancing energy needs with environmental sustainability has intensified (IEA's World Energy Outlook, 2022 and 2023). Renewable energy capacity is growing rapidly, with a 50% increase in 2023 compared to 2022 driven mainly by solar PV installations (IRENA World Energy Transitions Outlook 2023).

Despite the growth in renewable energy, fossil fuels continue to dominate global consumption, accounting for 80% of energy use in recent decades. Projections indicate this share may fall to 73% by 2030, as clean energy technologies, become more widespread. This transition is vital for reducing CO_2 emissions, as coal and oil produce over 800 g and 700 g of CO_2 per kWh, respectively (IPCC AR6 Climate Change 2021, and IRENA World Energy Transitions Outlook 2023). By accelerating this transition, the global energy landscape can mitigate some of the worst impacts of climate change.

Except nuclear power, plants that benefit from controllable electricity production over time, renewable energies have intermittent energy production that depends on the presence of wind, or sunlight, for example. Energy storage is an effective means of overcoming this drawback. This partly justifies the recent development of numerous energy storage devices. In this context, researchers and industry professionals continue to make progress in various fields (electrochemical energy storage, thermal salt, hydroelectricity, etc.). Traditionally, energy storage devices are classified based on their energy density, which corresponds to the amount of energy they can provide per unit of mass or volume (Wh/g or Wh/L), and their power density, which corresponds to the rate at which energy is released per unit of mass or volume (W/g or W/L). The Ragone plot is useful for representing all energy storage devices. While supercapacitors and flywheels are very powerful, batteries and fuel cells have high energy densities. Indeed, due to their diversity and flexibility, electrochemical devices are one of the most promising pathways for the future storage of renewable energies.

Since their commercial introduction in the 1990s, Lithium-ion batteries (LIBs) emerged as critical in reducing carbon emissions and integrating renewable energy. Offering flexibility, scalability, and high energy density, LIBs have revolutionized energy storage by powering everything from portable electronics to electric vehicles (EVs). As EVs adoption accelerates, recent challenges have emerged, such as limited raw material supply, safety concerns like thermal runaway, and the environmental impact of battery disposal. One of the most critical challenges lies in improving electrode materials, particularly finding alternatives to traditional graphite anodes and cobalt-based cathodes, to enhance performance, reduce costs, and ensure sustainability. These material advancements are also crucial for enabling faster charging, as current electrode materials can degrade under high-power conditions, limiting the potential for rapid charging in EVs.

This thesis is part of the DESTINY project (Doctorate Programme on Emerging Battery Storage Technology INspiring Young Scientists), coordinated by Prof. Christian Masquelier at Université de Picardie Jules Verne, Amiens. Supported by the European Commission’s Horizon 2020 Marie Skłodowska-Curie COFUND PhD Programme (Grant Agreement #945357), DESTINY seeks to train 50 PhD students across various institutions, focusing on reinventing battery materials, developing smart functionalities, and integrating new technologies into industry. The general aim of this thesis aligns with the project’s objectives, concentrating on the synthesis and application of tailored electrode materials for high-power LIBs. These materials must strike a balance between energy density, power capacity, cost-effectiveness, and environmental sustainability, with innovative synthesis methods playing a key role in their development. As part of the project, the work also involves mobility in Prof. Andrea Balducci laboratory, Friedrich-Schiller-University Jena, Germany with the focus on testing the already developed oxide materials in innovative electrolytes developed by the group in Jena.

In Chapter 1, a review of the current state of LIBs is presented, focusing on materials that can serve as negative electrodes while offering high specific capacities at high currents. Special attention is given to niobium-based tailored perovskite oxides and titanium-based carbides, which are explored for their synthesis, crystallographic structures and electrochemical properties.

In Chapter 2, a model materials tailored for high power electrode is introduced. More precisely, $AgNbO_3$ perovskites, La-substituted A-site deficient ($Ag_{1-3x}La_x\square_{2x}NbO_3$, $x \leq 0.20$) perovskites, and undoped A-site deficient ($Ag_{1-x}\square_xNbO_{3-\delta}$, $0 < x < 0.55$) compositions were designed, synthesized, and systematically studied as model negative electrode materials for Li^+ storage applications. A novel polyacrylamide gel synthesis method was developed to enhance the morphology and compositional uniformity of the materials. Comprehensive characterization techniques were employed to investigate the *in situ* electrochemical activation mechanisms in pristine $AgNbO_3$, the effects of La substitution on Li^+ storage performance, and the unique behavior observed in the A-site deficient $Ag_{1-x}\square_xNbO_{3-\delta}$ system. Furthermore, the chapter examines the influence of various material optimization strategies on specific capacity, cycling stability, and rate capability, offering significant insights into the development of perovskite-based LIB electrodes.

Capitalizing on the findings from Chapter 2, Chapter 3 shifts focus to alkali metal-based niobates, specifically $KNbO_3$, as a cost-effective and sustainable alternative to $AgNbO_3$. A new perovskite system, $K_{1-3x}La_x\square_{2x}NbO_3$ ($0 \leq x \leq 0.15$), was designed and synthesized to investigate the effects of A-site deficiencies and La-doping on Li^+ storage performance. The chapter explores the structural, electrochemical, and material properties of this system, aiming to optimize its Li^+ storage capabilities while maintaining stability and enhancing overall performance.

Finally, Chapter 4 presents an innovative use of the polyacrylamide-based wet chemical route used in the previous chapters. Indeed, this synthesis method was used to prepare carbides, and more precisely Ti_3AlC_2 MAX phases. It must be pointed out that only one paper reports the synthesis of carbide through this technique. Consequently, this chapter explores the role of carbon nonstoichiometry in phase formation and assesses the electrochemical performance of the resulting materials, even where the desired phases were not satisfactorily prepared.

The overarching goal of this thesis is to contribute to the advancement of high-power LIBs batteries through the development of innovative electrode materials. A general conclusion summarizes the main findings and offers insights into future research directions, building on the results obtained throughout this work.

Chapter 1: Literature review

The main objective of this chapter is to explain the basic operating principles and key concepts concerning the physico-chemical properties of electrochemical energy storage devices with a particular focus on fast charging lithium ion batteries (LIBs). In the following stage, the chapter will focus on the negative electrode materials in high power batteries with an aim to elucidate the current state of knowledge on the subject, emphasizing the chemistry of targeted transition metal oxides and carbides materials.

1.1 Overview of lithium ion batteries (LIBs)

1.1.1 History and applications

The history of electrochemical energy storage devices dates back to the time of first battery referred as "Voltaic Pile" invented in 1800 by Alejandro Volta [1]. However, after the first commercialization of Li-ion batteries in 1991 by Sony Corporation, this technology has garnered great interest because of superior energy storage characteristics [2]. Since then, achieving efficient and sustainable LIBs become a hot topic among research community and industrial sector, with a focus on developing innovative materials, designs and manufacturing process. Now a day, LIBs has a noticeable impact on powering portable electronics and Internet of Things (IoT) devices. They become crucial in development of electric vehicles on one hand, and storing the energy produced by renewable sources on the other hand. The applications of LIBs continue to expand, driving the advancement in technology and sustainability.

In battery research, LIBs system has gained considerable interest due to unique characteristics of lithium, a metal element discovered in 1800 by Johann August Arfvedson. The word "lithium" originates from the Greek *"lithos"* which mean stone. It exists mainly as minerals in earth crust, which are mined in the form of lithium carbonate (Li_2CO_3) and extracted from seawater for LIBs. As of 2023, lithium production is mainly distributed among few key regions of the world with Australia being on top contributing about 52% of world's supply, while Chile and Argentina follows with a collective 45% of global lithium production [3]. Driven by an increasing needs of energy storage solutions for transportation sector and intermittent renewable sources, the demand of lithium is significantly grown over the years and a 500 % increase is projected by 2030 [4].

By battery point of view, Li is the lightest (d = 0.53 $g.cm^{-3}$) and most electropositive (reduction potential of -3.04 vs. SHE) element, thus a best candidate to deliver a high volumetric energy density (300 $Wh.l^{-1}$) and a high gravimetric energy density (150-200 $Wh.kg^{-1}$) [5]. The development of LIBs began when Whittingham and his team in 1977 invented a battery with intercalation type positive electrode (TiS_2) with metallic Li as a negative electrode [6,7]. However, this system posed a severe safety issue due to dendrite formation on metallic Li during battery operation leading to a short-circuit. The problem was addressed when graphite was chosen as a negative electrode instead of Li metal, as graphite ensured a relatively high operating potential and mitigate the risks of dendrite formation [8,9]. In 1980, Goodenough and his team reported further advancement by providing a system based on the use of $LiCoO_2$ intercalation-type material for both electrodes [10]. The rocking chair battery, based on the reversible intercalation of Li^+, was born. In 1991, Sony Corporation brought the graphite/$LiCoO_2$ battery to the market for the first time, and it rapidly became a worldwide success. Fast forward 2019, the development in the field of LIBs was recognized by the award of Noble Prize in Chemistry to John B. Goodenough, Stanley Whittingham and Akira Yoshino for their groundbreaking contributions to the field [11]. However, still there are many rooms for improvement of batteries to enable the widespread adoption of electric vehicles and renewable energy sources. Batteries with enhanced cyclic life, improved power and energy density, safety and recycling are crucial to the development of sustainable technology.

1.1.2 Working principle

LIB is a system of two electrodes namely a positive and a negative electrode containing battery active materials, and liquid electrolyte in between electrodes which facilitate the ion flow while preventing the electron flow. During its operation, chemical energy contained in the active material is converted into electrical energy reversibly by mean of redox reactions. Figure 1.1 shows an example of LIB with first commercially used positive electrode $LiCoO_2$ and widely known graphite negative electrode [12]. During charging, lithium contained in positive electrode material released in the form of Li^+ and migrates through electrolyte into negative electrode (named as lithiation), meanwhile electrons are released from positive electrode into external circuit maintaining a charge neutrality. During discharging, a reversible process take place for both Li^+ and electron movements (named as delithiation) generating electrical current in the external circuit. Charging of battery increases the potential difference between two electrodes as energy is absorbed and stored while discharging decreases the potential difference as energy is released. The chemical reactions during charging and discharging of system are described in Equation I.1 and Equation I.2:

At positive electrode: $LiCoO_2 \leftrightarrow Li_{1-x}CoO_2 + x\ Li^+ + x\ e^-$ Equation I.1

At negative electrode: $C_6 + x\,Li^+ + x\,e^- \leftrightarrow Li_xC_6$ Equation I.2

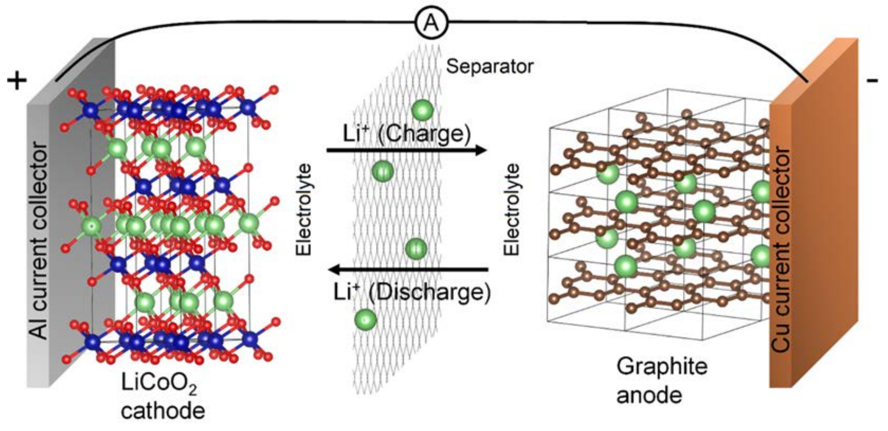

Figure 1.1. Schematics representation of working principle of LIB with graphite negative electrode, $LiCoO_2$ positive electrode and an electrolyte. [10]

1.2 Materials for Li-ion batteries:

The rapid growth of rechargeable battery technology in recent years has introduced numerous challenges in the study of electrode materials. Achieving a high energy density in LIBs require a significant voltage difference between the electrodes. Specifically, the positive electrode should operate at a high potential, typically between 2.5 and 4.5V, while the negative electrode at a low potential. Figure 1.2 illustrates typical contenders for positive and negative electrode materials in LIBs, commonly referred to as the cathode and anode, respectively [3]. It is notable that transition metal oxides of various crystal structures are a versatile class of materials. These oxides are commercially known for their high performance as positive electrodes, however, they also hold potential as negative electrode materials.

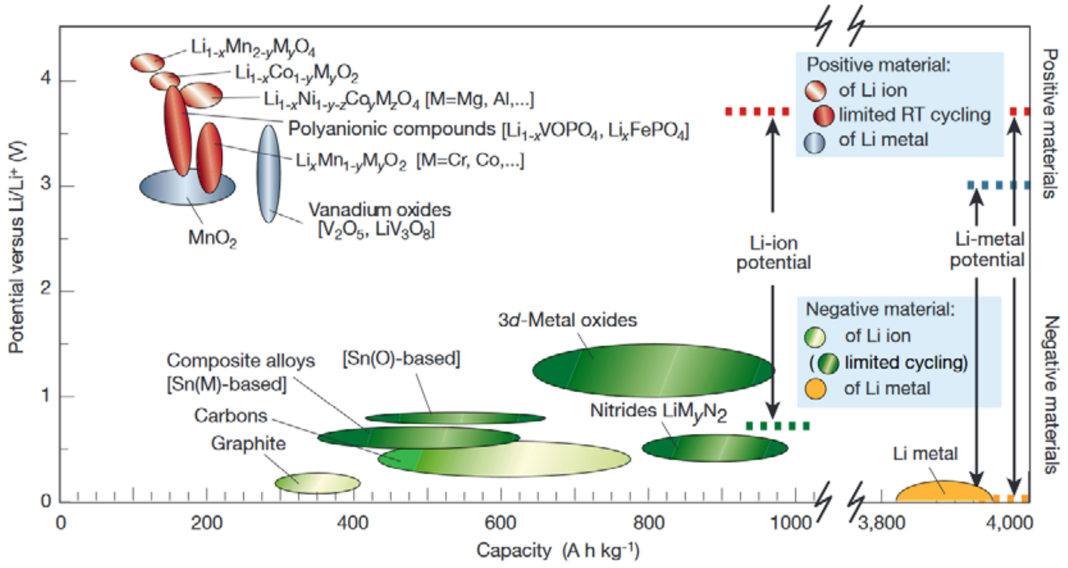

Figure 1.2. Typical candidates for positive and negative electrode materials in LIBs, with their potentials (V vs Li^+/Li) and gravimetric capacities (Ah/kg). [3]

1.2.1 Positive electrode materials

Lithium containing transition metal oxides have garnered significant attention as positive electrode materials due to their high capability for Li^+ extraction/insertion. Depending on the Li^+ insertion sites in the structure, positive electrode materials can be categorized into three main types: spinel oxides, layered oxides, and olivine oxides as shown in Figure 1.3.

1.2.1.1 Layered oxides

The layered oxide $LiCoO_2$ (LCO) was the first positive electrode material for Li-ion batteries, as suggested by the Mizushima and Goodenough groups [10]. For the first twenty years of Li-ion battery commercialization, LCO was the most extensively used material for positive electrodes. Operating within a voltage range of 3.2V to 4.5V, it gained popularity in commercial applications due to its high energy density and stability [13].

Nevertheless, due to the raised demand for energy storage, the interest in LCO has reduced due to concerns over high cost, high toxicity, and scarcity of Co. A few alternative solutions are, totally or partially replacing Co with other metals such as nickel (Ni), manganese (Mn), aluminum (Al), or iron (Fe) [14]. The main benefits of such substitutions are to considerably reduce battery cost and toxicity. Furthermore, the use of quaternary compounds aids the facile Li insertion and enhances the energy densities and power densities of batteries, while keeping safe operation [15–17]. The partial substitution of Co can lead to layered metal-oxide such as $LiNi_{1-x-y}Al_xCo_yO_2$ (NCA) and $LiNi_{1-x-y}Co_xMn_yO_2$ (NMC), which can accomplish an excellent cycling performance. Nowadays, these compounds are used very commonly for commercial systems [18,19].

1.2.1.2 Spinel Oxides

Spinel-type materials have been extensively investigated for positive electrodes as alternatives to lithium cobalt oxide (LCO), with $LiMn_2O_4$ (LMO) being the most prominent among them. $LiMn_2O_4$ has been widely incorporated in commercial systems since 1996 because of its high stability, safety, low cost, and eco-friendly attributes, as it does not contain cobalt [20]. Nonetheless, it has a relatively low theoretical capacity of 120 $mAh.g^{-1}$ and low stability due to the dissolution of Mn^{2+} into the electrolyte at high temperature [16,21]. The performance of such materials could be enhanced either by partially substituting Mn to reduce its dissolution or by applying surface coatings. $LiMn_{0.5}Ni_{0.5}O_2$ has emerged as a promising compound due to its relatively high theoretical capacity of 146 $mAhg^{-1}$, which is comparable to that of LCO. However, the insertion of lithium into $LiMn_{0.5}Ni_{0.5}O_2$ requires a high voltage (around 4.5V), which accelerates the degradation of the electrolyte, resulting in poor cycle life [22]. Therefore, ongoing research is necessary to optimize and identify alternative positive electrode candidates that offer good stability, high energy density, cost-effectiveness, and safety for the environment.

1.2.1.3 Olivine

In 1997, among the olivine family ($LiMPO_4$ (with M = Fe, Mn, Co, Ni)), $LiFePO_4$ (LFP) was first utilized as a positive electrode for Li-ion batteries [23,24]. This material is notable for its exceptional stability, high safety, environmental non-toxicity, and abundance of iron in the earth's crust. Additionally, LFP possesses a competitive theoretical capacity of approximately 170 $mAh.g^{-1}$.

Regardless of several advantages, the low ionic and electronic conductivity of LFP limits its electrochemical performance [25,26]. This challenge can be overcome by adding conductive additives such as carbon particles into composite electrodes and reducing particle sizes [27,28]. Although LFP initially captured a significant portion of the Li-ion battery market, its prominence has started to decline due to the improved performance offered by layered oxide materials such as NMC and NCA.

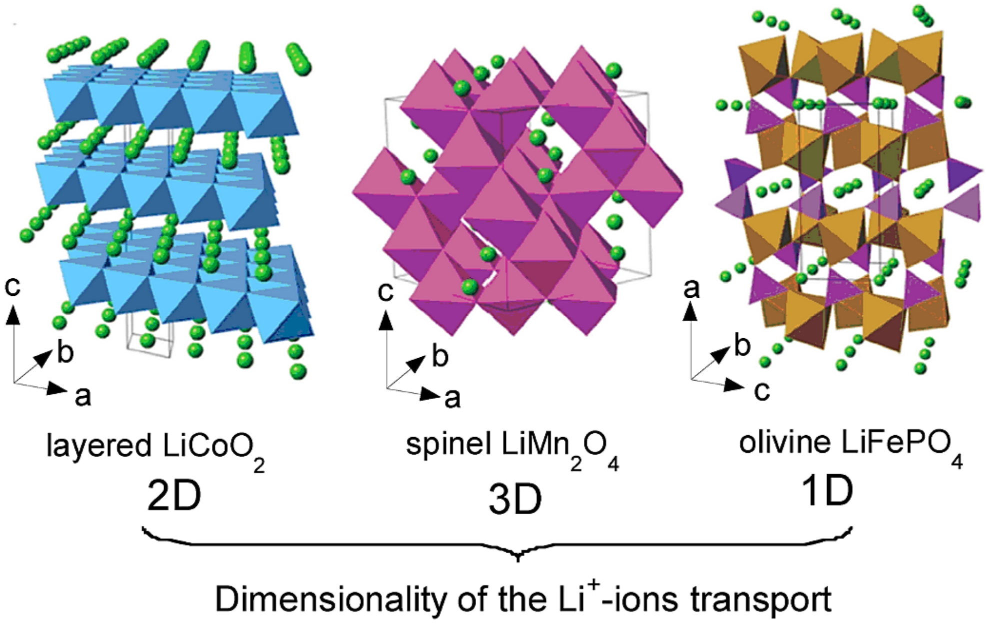

Figure 1.3. Well-known Li containing transition metal oxides positive electrode materials for LIBs.

1.2.2 State-of-the-art negative electrode materials

Despite the development of a variety of positive electrode materials with significantly improved performance over past 30 years, graphite has continued to be preferred negative electrode material since the advent of LIBs in 1991 [29,20,30]. Graphite have been promising choice due to its Li^+ storage theoretical capacity (372 $mAh.g^{-1}$), cost effectiveness and outstanding lithium reversible intercalation [31]. However, Li plating on graphite anodes occurs when charging rate surpasses the rate of Li intercalation into the graphite structure. This issue arises from polarization effects including charge-transfer overpotential that cause the anode potential to drop below the Li^+/Li equilibrium potential, leading to metallic Li deposition on the surface rather than proper intercalation. This leads to electrolyte decomposition, loss of lithium inventory, and the formation of internal micro-shorts [32].

Given the low potential proximity of graphite vs Li^+/Li couple, alternatives with safer working potential are being explored as fast charging anodes. One excellent candidate, spinel $Li_4Ti_5O_{12}$ (LTO), which has been well-studied, offers reliable performance at high charging rates (> 10 C) [33]. Companies such as Toshiba took this material to commercial level successfully, where 90% charge in just 10 minutes has been achieved. However, it mainly suffer from a low capacity (175 $mAh.g^{-1}$) and higher operating potential (1.55 V *vs* Li^+/Li), which limit its suitability for electric vehicles requiring extended range.

Toshiba progressed further in adopting other transition metal oxides as an alternative to LTO. Their advancements include development of carbon-coated $TiNb_2O_7$ (TNO), which has a theoretical capacity of 388 $mAh.g^{-1}$, close to that of graphite [34]. TNO store Li^+ involving both Ti^{4+}/Ti^{3+} and Nb^{5+}/Nb^{3+} redox couples. In TNO/NMC622 full cell operation, it demonstrates the ability to charge from 0% to 90% state-of-charge in under 6 minutes, and retaining 86% capacity after 7,000 cycles at 1C [32].

Specific capacity is another crucial parameter in addition to operating potential, as high-capacity anodes can reduce electrode thickness, meaning a lower charge carrier transport distance that support fast charging. Silicon (Si) has been extensively explored as an anode material due to its high theoretical capacity of 4,200 $mAh.g^{-1}$ and slightly higher operating potential compared to graphite. Although Si technology has matured, its fast charging at commercial mass loadings is rarely claimed in full cells [35,36]. Nonetheless, Si-dominant anodes have been disclosed as fast charging anodes. On the other hand, Li metal anodes has been under immense research interest due to highest theoretical capacity. Despite notable progress, Li metal continues to face unresolved fundamental challenges, such as low Coulombic efficiency and uncontrolled deposition morphology. These factors become more challenging under fast charging conditions [37].

Recently, several Nb-based oxides have gained significant research interests. It mainly includes Wadsley-Roth phases with 3D open structures such as $CoNb_{11}O_{29}$, $Nb_{16}W_5O_{55}$ and, PNb_9O_{25}

have gained great interest as high power negative electrode owing to their fast kinetics, robust ion diffusion, and good structural stability [38–40]. In addition to these materials, another class of oxides namely ABO_3-type perovskites with vacancies (acting as Li^+ transport channels) in their intrinsic or doped structures have garnered research interests. The next sections will be dedicated to the structural details of such perovskites and their recent advancements as negative electrode materials for LIBs.

1.3 ABO_3-type perovskite structures

The typical ABO_3 perovskite oxide structure consists of a large sized A-site cation coordinated by 12 oxygen anions and a relatively small sized B-site cation coordinated by 6 oxygen anions forming (BO_6) octahedra. In three-dimensional framework of ABO_3, A-site cation is positioned at the body center, surrounded by corner-sharing (BO_6) octahedra (Figure 1.4(a)). This class of oxides material has a huge diversity in choice of A and B-site cations in addition to possibility of partial substitution at each site. As shown in Figure 1.4(b), over half of elements in periodic table have been reported for formation of such structures, with infinitely many new combinations to be discovered in future [41].

The stability of a perovskite structure depends mainly on A and B-site cations and is estimated by their ionic radii. The Goldschmidt tolerance factor (t) is a widely known predictor for determining the stability and distortion of the perovskite crystal structure [42]. It can be calculated using Equation 1.3:

$$t = \frac{r_A + r_O}{\sqrt{2}\,(r_B + r_O)} \qquad \text{Equation 1.3}$$

Where, r_A, r_B, and r_O indicate the ionic radii of the A and B-site cation, and O-site anion, respectively. Tolerance factor value close to 1 indicates an ideal and stable perovskite structure, while a significant deviation from 1 suggest potential distortions or alternative structural arrangements. The typical perovskite range for "t" is 0.8 – 1.1. Such a simple concept serves quite well in predicting ABO_3-type perovskites. However, its quantitative accuracy is approximately 70% [43]. Therefore, a modified relation with better accuracy was introduced for the prediction of both perovskite and non-perovskite structures, as presented in Equation 1.4 [44]:

$$\tau = \frac{r_O}{r_B} - n_A\left(n_A - \frac{r_A/r_B}{ln(r_A/r_B)}\right) \qquad \text{Equation 1.4}$$

Where n_A is oxidation state of A-site cation considered for calculations in addition to ionic radii. For a perovskite-type compounds, the new tolerance factor "τ" typically ranges from 1.0 – 4.0 with an accuracy of 92%.

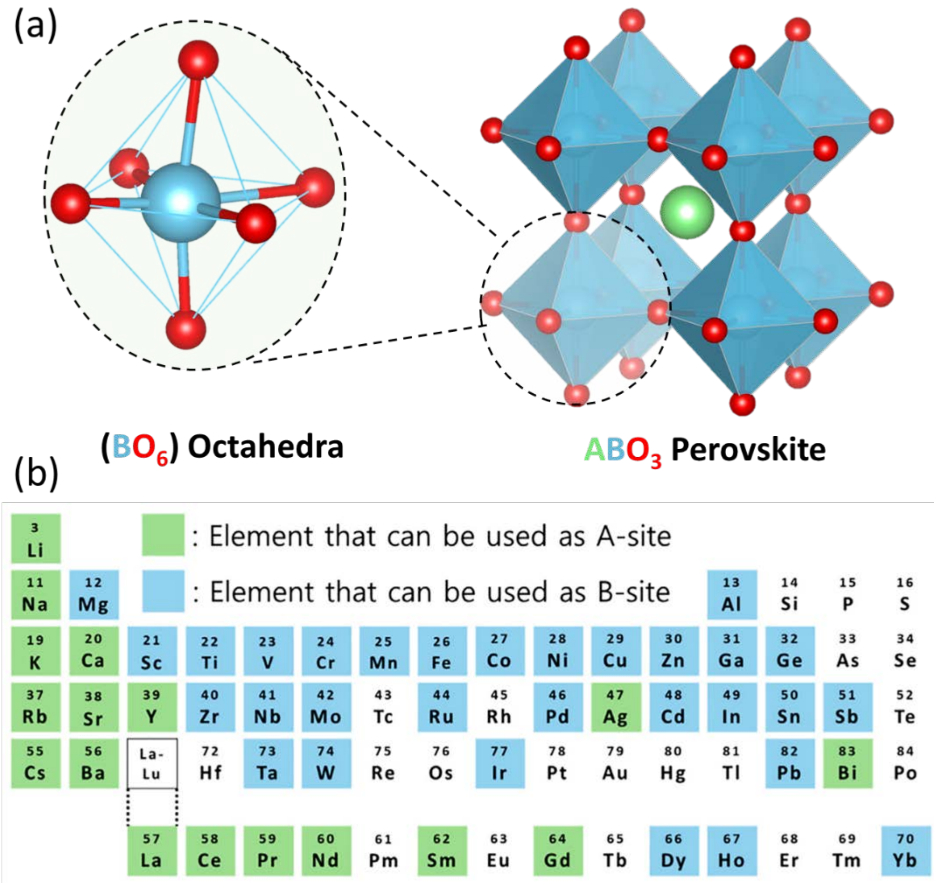

Figure 1.4. (a) Schematic illustration of ideal cubic perovskite in ABX_3 configuration, where the A is center cation surrounded by a network of corner shared (BX_6) octahedra. (b) Perovskite periodic table with elemental map showing possibility of A, B, and/or X sites occupancy for 576 experimentally characterized perovskite/non-perovskite structures at ambient conditions. [39]

Despite low accuracy of Goldsmith estimation, it facilitated the understanding of phase transitions and perovskite/non-perovskite nature of structures by developing an interesting correlation based on t values and experimental observations (Figure 1.5) [45]. $SrTiO_3$ being considered as an ideal cubic perovskite, defines the tolerance factor range of 0.9 – 1.0 for such structures [46]. Positive deviation ($t > 1.0$) induce distortions by stretching the B-O bonds, which results in displacive distortions in (BO_6) octahedra. These conditions favored the formation of reduced symmetry phases like tetragonal/hexagonal, as reported for $BaTiO_3$ [46,47]. Contrary, a negative shift ($t < 0.9$), shortened the B-O bonds and cause a lattice strain. To compensate this, (BO_6) octahedra undergoes a rotation or tilting followed by A-O bond stretching. This typically results in orthorhombic or rhombohedral lattices, such as $CaTiO_3$ [46,48]. However, if the tolerance factor falls outside the limits ($0.71 < t > 1.1$), corner-sharing of (BO_6) octahedra (perovskite structure) transformed to a face-sharing octahedral polytypes (non-perovskite structures), such as ambient-pressure $BaIrO_3$ [47,48]. Nonetheless, such correlation involves the ionic radius consideration while ignoring other factors such as bond strengths, electronegativity differences, and the effect of different spin states [49].

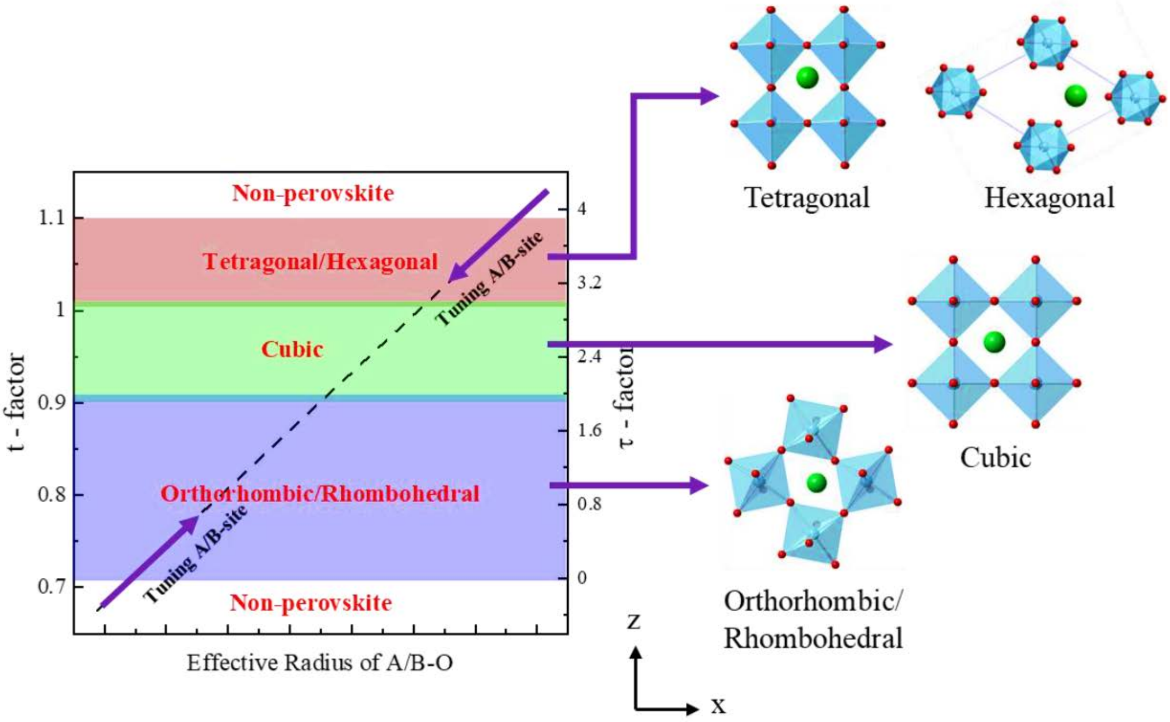

Figure 1.5. Correlation of Goldsmith tolerance factor (t) with structural distortions in perovskite and transformation limit to non-perovskite structures. Corresponding structural representation is presented on the right panel. The diagonal dashed line is an eye-guide.

Additionally, lattice distortions have an influence on electronic structure and properties of perovskites in addition to crystal structure. Symmetry-breaking modes, such as octahedral rotations and Jahn-Teller distortions based transformation of metallic compounds into insulators has been reported [50]. Depending on band structure, ABO_3 perovskites exhibit insulating, semiconducting, or metallic nature. Semiconducting and insulating perovskites have a band gap between the conduction and valence bands, typically exhibiting resistivities (ρ) greater than $10^{-2}\ \Omega.cm^{-1}$ [51,52]. General families of semiconducting or insulating perovskites include stoichiometric alkali or alkaline earth A-site cations with (BO_6) octahedra (B = Ti, Sn, Co). While, conductive perovskites with stoichiometric alkaline earth A-site metals with (BO_6) octahedra (B = V, Nb, Mo) have exhibited electrical resistivities ranging from approximately 10^{-2} to $10^{-5}\ \Omega.cm^{-1}$ and primarily crystallize in cubic (Pm-3m), hexagonal (P6-3m), and orthorhombic (Pnma) space groups [53,54]. However, due to the diversity within this class of materials and A-site nonstoichiometry, many perovskites may fall outside these general classifications.

1.4 Defect engineering in ABO_3 perovskites

ABO_3 type perovskites have the ability to undergo lattice modifications through several ways such as substitutional/interstitial doping, oxygen vacancies, and cation vacancies. Defect engineering is an effective and versatile way for tuning the A/B-O interactions and obtaining desired properties through structure-property relationship discussed in previous section [55]. For example, substituting Na with Sr atoms into the A-site of semiconducting $NaNbO_3$ perovskites ($Sr_xNa_{1-x}NbO_3$), caused an orthorhombic to cubic phase transition and imparts metallic-like properties [54,56]. This strategy allows modifying structural and electronic features that would otherwise be unachievable with A/B-site single atom stoichiometry. In another example, a mixed ionic/electronic conductivity have been attained for Sr-doped perovskites ($Sr_xLa_{1-x}CoO_3$ and $Sr_xSm_{1-x}CoO_3$), making them potential candidates for solid oxide fuel cells. It is important to mention that cation doping is effective strategy to tune the properties but oxidation state of dopant also has a significant role in designing the stable structures at required doping level. For example, monovalent Li^+ or Na^+, divalent Ca^{2+}, and trivalent Sm^{3+} substitutions at A-site of $KNbO_3$ (a monovalent alkali metal based niobate perovskite) have been studied in literature [57–60]. While monovalent dopants induce strains in the structure due to size mismatch and favored a phase stabilization, di- or trivalent dopants require an additional charge compensation. Notably, in most of the cases, the charge compensation has been reported by due of oxygen vacancies. Dudhe *et al.*, studied the cubic-orthorhombic phase transition in $KNbO_3$ by varying oxygen vacancies through La-doping at A-site [61]. However, charge compensation at the cost of cation vacancies in ABO_3 lattice has rarely been investigated. Such substitution dependent vacancy engineering can enable ion storage capabilities in perovskite. It allows the use of not so common class of ABO_3-type perovskites as battery electrode materials.

1.5 Recent developments in ABO_3 perovskite as a negative electrode materials for LIBs

1.5.1 BO_3-type pseudo-perovskite structures

BO_3-type structures can be classified as ABO_3 pseudo-perovskites, with the A-cation site vacant, and B-site typically a cation bridged with O anion to form (BO_6) octahedra. Rhenium trioxide (ReO_3) and tungsten trioxide (WO_3) are the only thermodynamically stable binary oxides crystallizing in BO_3-type pseudo-perovskite structure [62]. ReO_3, a deep red colored oxide, was first reported in the early 1930’s, with its synthesis and structure determination [63].

However, significant research attention arose in 1965 when Goodenough and colleagues reported its metallic conductivity, comparable to that of copper (Cu) [64]. Being an oxide conductor, this property of ReO_3 compound was particularly noteworthy. Due to missing A-site cations and octahedral arrangements, these materials have wide-open channels where Li^+ insertions is possible. Both structures are presented in Figure 1.6a and b.

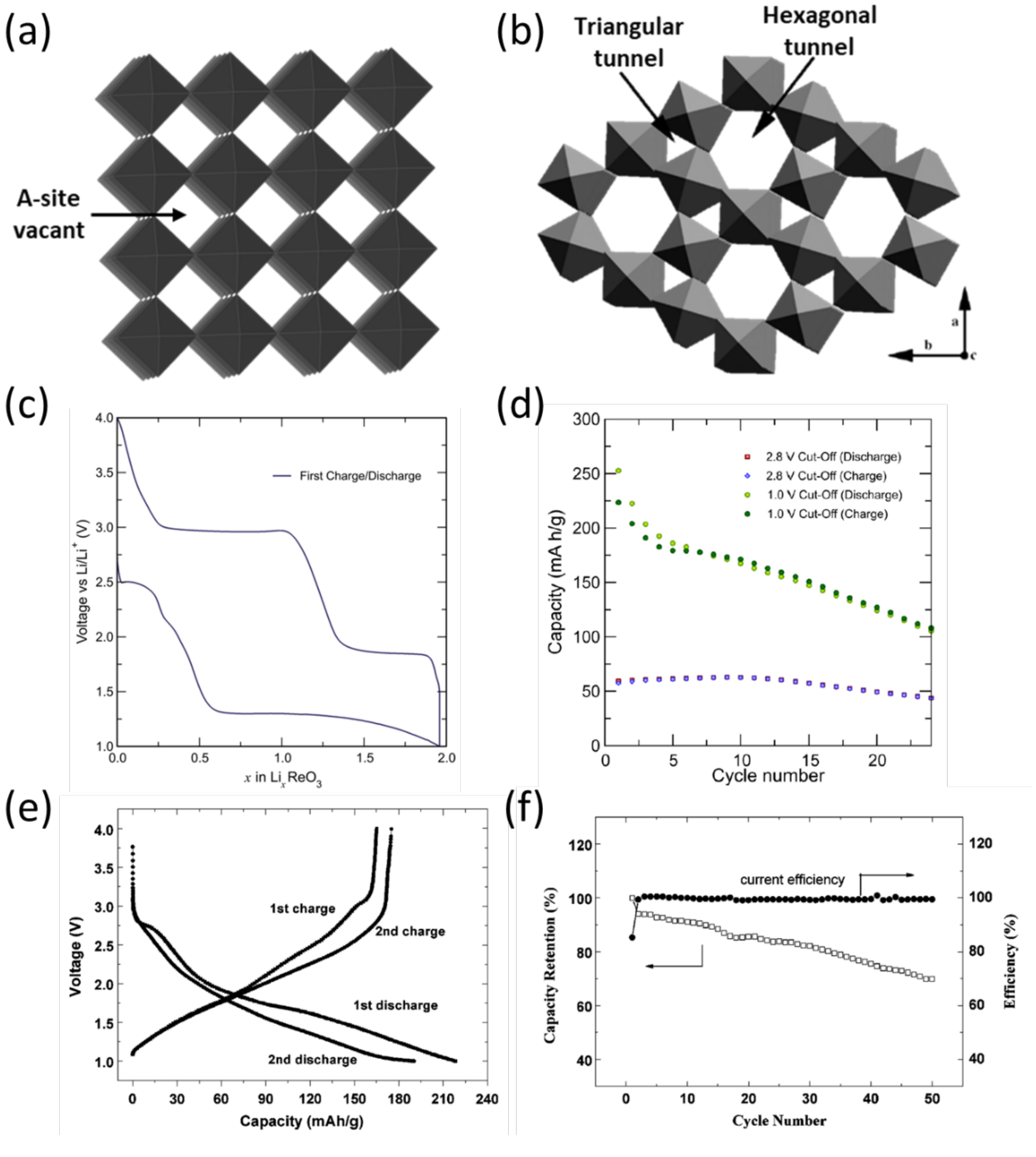

Figure 1.6. Schematic representation of pseudo-perovskite structures (a) c-ReO_3 (b) h-WO_3. Li^+ storage performance of c-ReO_3 (c) Potential vs Li^+ insertion in Li_xReO_3 during first cycle. (d) Specific capacity decay over 25 cycles at different cutoff potentials. Li^+ storage performance of c-WO_3 (e) Potential vs specific capacity curves for first two cycles. (f) Capacity decay over the period of cycles. [64, 66]

Reversible lithiation in ReO_3 was first examined in 1980 by Cava *et al.*, and explained in details by Melot and co-workers later on [65,66]. Up to 2 Li^+ insertion per formula unit with a high capacity of 228 $mAh.g^{-1}$ was achieved. It was found that ReO_3 undergoes phase changes involving correlated twisting of corner-sharing $(ReO)_6$ octahedral subunits during lithiation, causing significant lattice strains and capacity fade, with only 40% of the initial capacity retained after 25 cycles at a cutoff potential of 1.0 V vs Li^+/Li. However, stabilizing the capacity was achieved by setting the cutoff potential to 2.8 V vs Li^+/Li, which avoids major structural distortions but capacity was compromised (Figure 1.6c and d). It was found that the phase transformations and structural collapse were driven by local lattice strains rather than polaron migration and metallic character was maintained up to Li_2ReO_3.

WO_3 has a similar structure but significantly different in properties. At room temperature, ReO_3 is a primitive cubic and conductive material, whereas WO_3 is monoclinic and insulating. This distinction is attributed to their contrasting M-O-M bond angles. ReO_3 has bond angles of 180°, while WO_3 exhibits angles between 165° and 179° [67]. The distortion in hexagonal tungsten trioxide (h-WO_3) is due to the tendency of tungsten atoms to deviate from the ideal cubic positions within the $(WO)_6$ octahedral environments, a behavior supported by DFT calculations [62]. However, the unique tunnel structures also facilitate Li^+ intercalation in h-WO_3. The specific capacity of different types of nanostructured h-WO_3 has typically been obtained in the range of 200-300 $mAh.g^{-1}$ [68–70]. Some studies reported conductive cubic WO_3 (c-WO_3) phase in special morphologies with relatively high specific capacity of around 526 $mAh.g^{-1}$ following a mechanism similar to ReO_3 [70,71]. However, the common drawback is a significant capacity decay per cycle that typically falls within the range of 0.5-0.82% per cycle due to structural collapse (Figure 1.6e and f). Under this category of materials, metastable phase of cubic MoO_3 have also gained interest as lithium storage material, but its stable phase exist in the form of orthorhombic-layered type structural arrangements, which is beyond the interest of current topic [72].

1.5.2 ABO_3-type titanates as negative electrodes for LIBs

Recent studies have demonstrated vacancy-engineered A-site deficient titinates as high-rate negative electrodes for LIBs [73–75]. Among cubic perovskite titanates, Li-doped $LaTiO_3$ has been well known as solid state Li-ion conductor due to their impressive ionic conductivity values (2×10^{-5} $S.cm^{-1}$ by D.C. method) [76,77]. Its robust perovskite structure consists of corner shared TiO_6 octahedra framework with La atoms at the center along with large number of vacant sites at the unoccupied 18d and 6a positions [78]. These compounds typically has intrinsic low electronic conductivities. However, an interesting insulator to conductor transformation have been observed upon their reaction with Li below 1.50 V, as obtained for spinel $Li_4Ti_5O_{12}$ [79–82]. For this reason, interest has grown over the time in exploring Li^+ storage properties of titanate cubic perovskites. Initially, Li^+ insertion properties of $La_{2/3}TiO_3$ as an intrinsic A-site deficient structure have been investigated [82]. Upon Li^+ insertion, La^{3+}

stayed unchanged and Ti^{4+} to Ti^{3+} was obtained, however La^{3+} does not contribute to the reduction reaction. Besides, the perovskite framework remains undisturbed indicating a good electrochemical stability during lithium insertion, with minimal changes in the crystal lattice. However, in most of the cases Li doped $La_{2/3}TiO_3$ used instead of pristine $La_{2/3}TiO_3$ as it helped in stabilizing the structure under lower potentials and enhance the electronic conductivity, as discussed below by few specific examples.

First example is Li-doped $NdTiO_3$ perovskite, as A-site deficient $Li_{0.35}Nd_{0.55}TiO_3$ (LNTO) reported by Chen and co-workers [74]. The structure crystallized in tetragonal phase with Nd-rich and Nd-poor sites forming a superlattice along the c-axis, which provides three-dimensional Li^+ migration channels (Figure 1.7 a). With an average potential of 0.73 V vs. Li^+/Li, LNTO achieved a specific capacity of 202 $mAh.g^{-1}$ at 0.1 C, and showed an excellent rate performance, retaining 58% capacity at 40 C (117 $mAh.g^{-1}$) as shown in Figure 1.7 b and c. After 1600 cycles, a capacity retention of 93.5% at 10 C was reported. A solid-solution type mechanism with low volume changes (5.51%) and minimal morphological changes was obtained, indicating high structural stability. The superior Li^+ storage performance was supported by 87.8% capacitive contribution and high apparent lithium diffusion coefficients of 2.07×10^{-11} $cm^2.s^{-1}$ and 2.78×10^{-11} $cm^2.s^{-1}$ during lithiation and delithiation, respectively. Such structures were further optimized by replacing neodymium (Nd) with praseodymium (Pr) in the host structure in the form of $Li_{0.38}Pr_{0.54}TiO_3$ (LPTO) [83]. The new structure exhibited a low band gap (2.57 eV) and enhanced lithium ion diffusion (energy barrier = 0.11 eV). An improved overall specific capacity and rate performance was achieved while keeping the high cyclic stability due to solid-solution process accompanied by a phase transition from tetragonal to pseudo-cubic symmetry.

The second example is Li-doped $LaTiO_3$ termed as $La_{0.5}Li_{0.5}TiO_3$ (LLTO) [75] having tetragonal perovskite structure with an arrangement of La-rich and La-poor layers as shown in Figure 1.7 d. Operating at an average potential of 1.0 V vs. Li^+/Li, LLTO exhibited an initial discharge capacity of 449 $mAh.g^{-1}$ at 0.1 C, stabilizing at 229 $mAh.g^{-1}$ on subsequent cycles. Due to a reversible phase transition from tetragonal to pseudo-cubic structure, it maintained a specific capacity of 225 $mAh.g^{-1}$ with a minimal volume expansion of ~0.068% for over 3000 cycles. LLTO delivered nearly 100 $mAh.g^{-1}$ at 10 C (Figure 1.7 e and f). A pseudocapacitive mechanism was reported as a dominating lithium storage process, with a capacitive contribution of ~76% at 6 $mV.s^{-1}$. The pseudocapacitive mechanism refers to the fast, reversible faradaic charge-transfer processes, such as surface or near-surface redox reactions that occur in electrode materials. These results were supported by DFT calculations, which revealed lower lithium diffusion barriers, a narrower band gap, and enhanced conductivity.

These studies highlight the potential of substitution induced vacancy engineering in titanate perovskites as a negative electrode for LIBs.

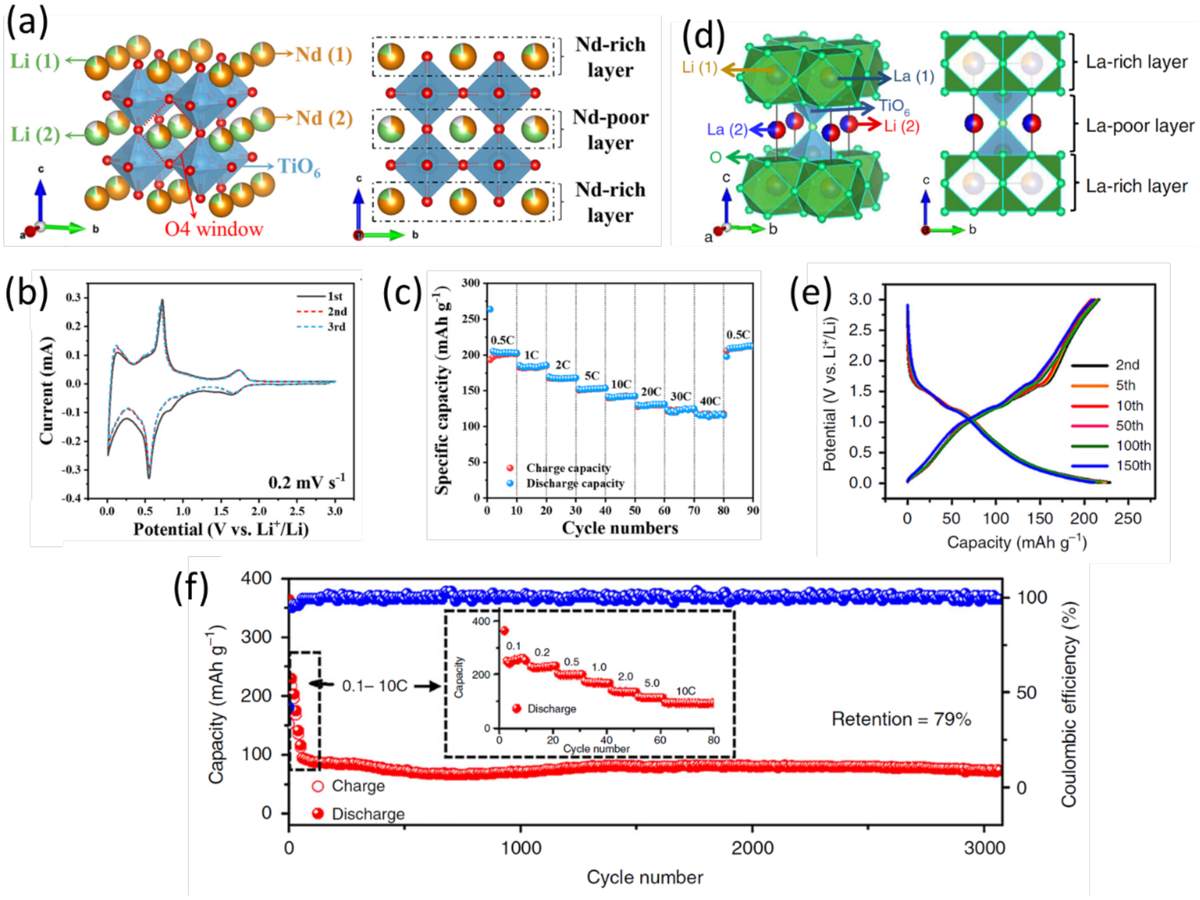

Figure 1.7. A-site deficient $Li_{0.35}Nd_{0.55}TiO_3$ perovskite (a) Crystal structure representation. (b) Cyclic voltamograms at 0.2 mV.s^{-1}. (c) Specific capacity at different C-rates. $La_{0.5}Li_{0.5}TiO_3$ perovskite (d) Crystal structure representation. (e) Galvanostatic charge-discharge curves. (f) Cyclic stability with inset of specific capacity at different C-rates. [74. 75]

1.5.3 ABO$_3$-type vanadates as negative electrodes for LIBs

Among vanadate-based perovskites, metallic $SrVO_3$ is the only promising material recently investigated as negative electrode for LIBs. Historically, $SrVO_3$ studied as cathode material, specific capacity of under 100 mAh.g^{-1} was achieved [84,85]. Considering its high electronic and ionic conductivity (3.5×10^4 and 10^{-8} S.cm^{-1}, respectively) of $SrVO_3$ together with low working potential make it a potential negative electrode material [86,84,87]. Liu and co-workers have progressively investigated $SrVO_3$ perovskites as an anode material for LIBs from fundamental understandings of its intrinsic behavior to a series of structural modifications for achieving an enhanced Li$^+$ storage performance. The initial study laid the groundwork by demonstrating that $SrVO_3$ structure delivered a specific capacity of 324 mAh g^{-1} and excellent cycling stability with only 2.3% volume expansion upon full lithiation [88]. A solid-solution type storage mechanism involving the reversible Li^+ intercalation into the 3c Wyckoff site of perovskite structure (V cation acted as the redox center) was demonstrated. Afterwards, the $SrVO_3$ was tailored by Sr cation and O anion deficiency engineering in as non-stoichiometric $Sr_xVO_{3-\delta}$ materials, and its effect on Li^+ storage was studied [89]. Sr and O vacancies provided additional Li^+ storage sites and preferential transport channels, which improved the rate performance in addition to specific capacity (Figure 1.8 a-c). With optimized $Sr_{0.63}VO_{3-\delta}$ structure, a maximum capacity of 444 $mAh.g^{-1}$ was obtained indicating a 37% increase over stoichiometric $SrVO_3$. The modified structure inserted Li^+ ions in both the 3c interstitial sites and the newly created Sr vacancies (Figure 1.8 d and e). Despite the enhanced performance, the structure maintained excellent stability with a volume change of less than 3.7% upon lithiation, ensuring high capacity retention over 6000 cycles. Afterwards, the structure was further modified to create defective $Sr_xVO_{3-\delta}$ with an amorphous-crystalline dual-phase material [90]. This modification significantly impacted the lithium storage mechanism. Due to high defects concentration in the amorphous phase, Li^+ storage capacity was enhanced. Whereas, the crystalline phase helped to maintain high conductivity. This dual-phase structure resulted in a specific capacity of 508 $mAh.g^{-1}$, representing a 40% improvement over pure $SrVO_3$, while maintaining low volume expansion. The new structure allowed better lithium storage performance. The above discussion established a conclusion that the structural evaluation and defect engineering in $SrVO_3$ perovskites have led to substantial improvements in specific capacity, rate performance keeping overall structure stability.

However, it is important to note that $SrVO_3$ is one of few exceptions among perovskites, exhibiting metallic properties primarily due to controlled oxidation state of vanadium (V). Synthesis of $SrVO_3$ poses several significant challenges. It involves a complex two-step process: (1) rapid solution combustion synthesis of $Sr_2V_2O_7$ in air, and (2) followed by thermal reduction in an H_2 atmosphere [88]. Hence, it require precise control of conditions to form the desired phase. Handling intermediate impurity phases like $Sr_3V_2O_8$, which form due to Sr cation segregation and V^{5+} stability, adds complexity to obtaining pure $SrVO_3$. The presence of V^{5+} species on the surface indicates difficulties in maintaining V^{4+} throughout the material. Furthermore, the thermal reduction step at 800 °C in a flowing H_2 atmosphere requires specialized equipment for safe handling. Given the processing costs and synthesis complexities, this material may not be feasible for practical applications despite their fascinating properties and performance. Nonetheless, this underscores the Li^+ storage capabilities of ABO_3-type perovskites and provokes further research interests.

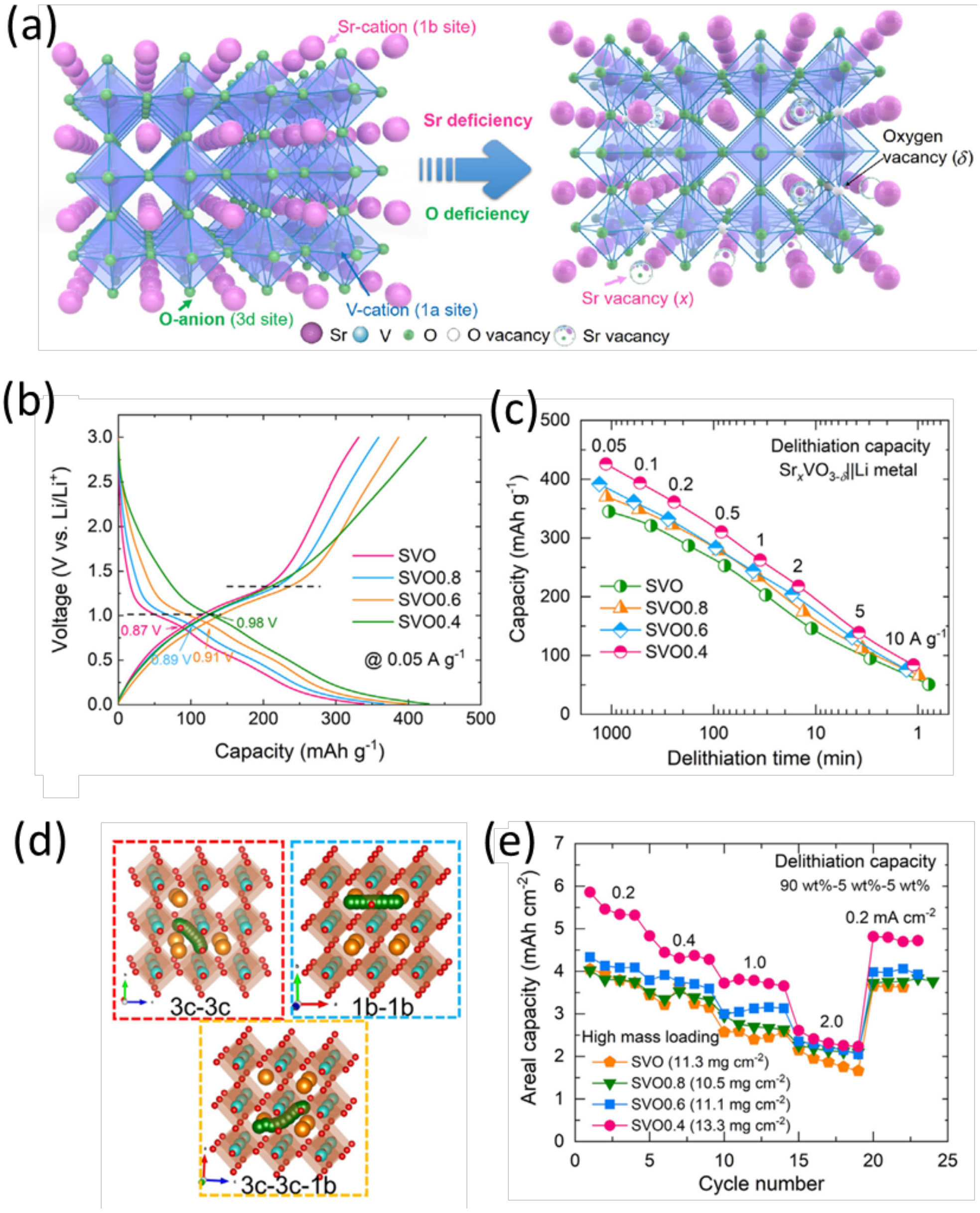

Figure 1.8. (a) Structural representation of $SrVO_3$ and $Sr_xVO_{3-\delta}$. (b) Potential vs capacity graph of and $Sr_xVO_{3-\delta}$ at x = 1.0, 0.8, 0.6, and 0.4. (c) Rate capability comparison of $Sr_xVO_{3-\square}$ at various specific currents ranges. (d) DFT calculations showing three routes in Sr cation-deficient $Sr_{0.75}VO_3$ unit cell. (e) Comparison of Specific capacity of $Sr_xVO_{3-\square}$ electrodes. [88. 89]

1.5.4 ABO_3-type niobates as negative electrodes for LIBs

Niobates are versatile in terms of their structural flexibility as compared to titanates and vanadates. In addition, the work done in this thesis mainly focused on niobate perovskites. Therefore, this section discuss in detail the recent progresses by classifying the materials in the following order: 1) fully occupied A and B-site cations, 2) Intrinsic A-site deficient structures and 3) Doped A-site deficient structures.

1.5.4.1 Fully occupied A and B-sites

ABO_3-type perovskites with fully occupied A and B sites lack an open channel for Li^+ insertion into the bulk due to the high packing factor of the structure. There are few examples, first we will discuss about vanadium based and then Nb based perovskites reported in literature. $SrVO_3$, a rare example of this class with metallic conductivity, has recently been reported to insert Li^+ into the 3c site of the structure, which is the distance between Sr – Sr site, as discussed in the previous section. This section will begin with a discussion of a few Nb-based examples from the literature.

In this regards, there are only two examples: $NaNbO_3$ and $LiNbO_3$ studied as anode materials for LIBs [91,92]. $NaNbO_3$ delivered a specific capacity of 130 and 55 $mAh.g^{-1}$ at current densities of 0.1 and 3.2 $A.g^{-1}$, with an exceptional cycling stability, increasing 85% of its initial capacity after 1000 cycles at 2 $A.g^{-1}$. During the initial discharge, Li^+ ions intercalate into the crystal lattice, reducing Nb^{5+} to Nb^{4+} and then to Nb^{3+}. This process is partially reversible during the charging cycle, where Nb revert its oxidation states. Supported by *ex situ* XRD and XPS analysis, authors proposed a pseudocapacitive mechanism, where the majority of the capacity is attributed to surface-controlled kinetics rather than diffusion-controlled processes. In case of $LiNbO_3$, a chemical activation with perchloric acid was performed prior to to its investigation as negative electrode material. This process introduces oxygen vacancies and lithium deficiencies in the lattice. As a result an increases cell volume by 4.9%, while a decrease in crystallite size from 90.3 nm to 34.8 nm was obtained. Such an activation process enhanced the Li^+ diffusion and electronic conductivity, as evidenced by a significant reduction in activation energy from 0.89 eV (pristine) to 0.35 eV (activated) and a slight decrease in band gap from 4.00 eV (pristine) to 3.95 eV (activated). Due to this, an initial specific discharge capacity of 440 $mAh.g^{-1}$ and 107 $mAh.g^{-1}$ retention after 100 cycles was achieved.

However, a critical limitation shared by both studies is the lack of clear mechanistic evidence regarding how lithium ions are inserted into these perovskite structures. They focused more on empirical performance metrics, such as improved capacity and cycling stability, rather than elucidating the fundamental lithium storage mechanisms.

1.5.4.2 Intrinsic A-site deficient structures

There are some examples in literature demonstrating the stability of perovskite niobates with A-site deficiency without substitution, similar to $La_{2/3}TiO_3$ perovskite discussed in previous section. It mainly includes $La_{1/3}NbO_3$, $Pr_{1/3}NbO_3$, and $Ce_{1/3}NbO_3$ as reported in literature [93–96]. The studies on $La_{1/3}NbO_3$ and $Pr_{1/3}NbO_3$ revealed significant insights into lithium storage behavior of these materials. Both materials leverage the redox activity of niobium, with $La_{1/3}NbO_3$ focusing on the Nb^{5+}/Nb^{4+} redox couple, while $Pr_{1/3}NbO_3$ uniquely identifies both Nb^{5+}/Nb^{4+} and Nb^{4+}/Nb^{3+} couples, which is rarely reported. This rare claim is substantiated through *ex-situ* XPS and supported by earlier studies [97], providing a strong foundation for the reported electrochemical behavior. Both materials demonstrate a robust pseudocapacitive mechanism, characterized by fast lithium-ion diffusion and minimal structural changes during cycling. $La_{1/3}NbO_3$ maintains structural integrity with a modest increase in Nb-O bond length and a slight reduction in tetragonal distortion upon lithium insertion (Figure 1.9 a – c) [98,99]. $Pr_{1/3}NbO_3$ exhibits a low-strain lithium storage behavior with a maximum unit cell volume change of 2.21%, and a low mechanical degradation over long-term cycling.

In terms of electrochemical performance, $Pr_{1/3}NbO_3$ stands out with a higher specific capacity of 221.4 mAh.g^{-1} at 0.1C, and 161.9 mAh.g^{-1} at 10C, with cyclic stability of 97.4% after 3000 cycles at 10C (Figure 1.9 e – h) [95]. $Li_xLa_{1/3}NbO_3$, while demonstrating good capacity and stability, faces challenges at high lithium content as structural changes strongly correlated with depth of discharge process. The insertion/desertion of Li^+ in A-site vacancies is compensated by tilting of NbO_6 octahedra, which prevents large volume change [99]. However, insertion of Li^+ in 3c-sites of structure (at lower potentials of 0.8V vs Li^+/Li) caused a significant decay of capacity over the cycles due to irreversible structural transformation around Nb – O bond (Figure 1.9 d) [100]. This motivates to study A-site doped perovskite structures, where doped cation may additional support to maintain structural stability upon deep Li^+ insertion.

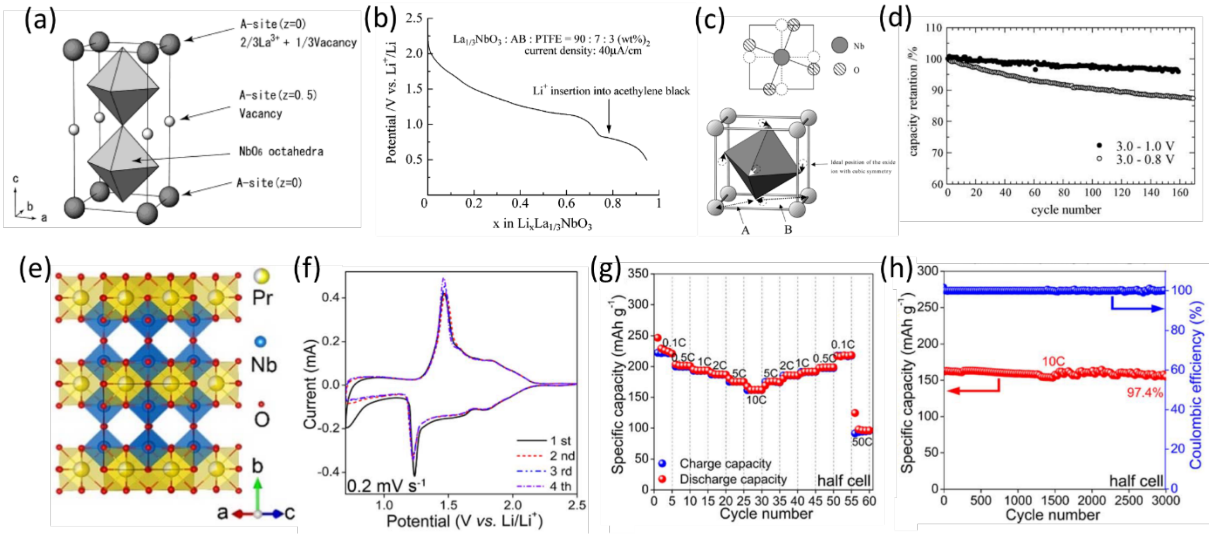

Figure 1.9. Li^+ storage in intrinsic A-site deficient niobate perovskites $La_{1/3}NbO_3$ (a) crystal structure showing A-site vacancies. (b) Li^+ insertion into $Li_xLa_{1/3}NbO_3$ structure under galvanostatic charging. (c) 2D and 3D schematics of model used to describe NbO_6 octahedral tilting and La – O bond change after Li^+ insertion in line with EXAFS analysis. (d) cyclic stability at two different cut-off potentials vs Li^+/Li. $Pr_{1/3}NbO_3$ (e) Crystal structure representation. (f) Cyclic voltammogram at 0.2 mV.s^{-1} under 0.8 – 3.0V vs Li^+/Li. (g) Rate performance. (h) Cyclic stability at 10C. [95, 98, 99]

1.5.4.3 Doped A-site deficient structures

The exploration of doped A-site deficient niobate peroskites has been systematically advanced over several years. Motivated by $La_{1/3}NbO_3$ structure, $Li_xLa_{1/3}NbO_3$ materials have been studied as anodes to deepen the understanding about this material. It is known that this structure features intrinsic vacancies that play a crucial role in lithium storage. Structural changes upon Li^+ insertion are compensated by NbO_6 octahedra tilting, a property that directly correlates with its long-term stability and performance. The earliest study published by Nakayama and co-workers in 2005, provided the foundational understanding of the cyclability and structural response in the material upon Li^+ insertion [100]. The main findings from this study was a correlation between amount of Li^+ insertion and structural degradation. While deeper lithium insertion into 3c-sites increase the specific capacity to approximately 150 mAh.g^{-1}, but led to reduced cyclic stability (~80% retention over 20 cycles). These findings were further investigated and validated by DFT analysis [101]. The most recent study by Che and co-workers, took these insights and thoroughly evaluated the electrochemical performance at optimised composition (Figure 1.10 a and b) [102]. The investigation into $Li_{0.1}La_{0.3}NbO_3$ revealed a significant improvement in Li^+ storage performance. An initial discharge capacity of 288 mAh.g^{-1} and a reversible capacity of 220 mAh.g^{-1} at 0.1 C was achieved under 0.8 – 3.0V vs Li^+/Li.

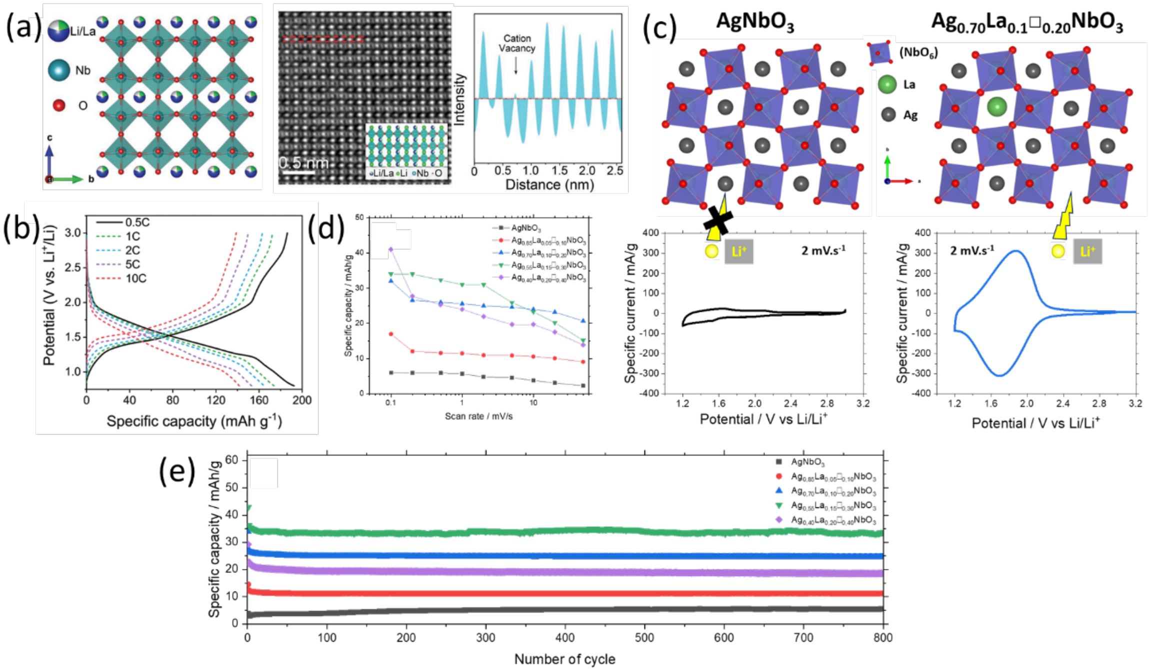

Figure 1.10. A-site doped niobate perovskites as negative electrodes for LIBs. $Li_{0.1}La_{1/3}NbO_3$ (a) Structure and visualization of vacancies at atomic scale using STEM analysis. (b) Charge discharge curves at different C-rates. $Ag_{1-3x}La_x\square_{2x}NbO_3$ (with $x \leq 0.20$ and where $\square$ is a A-site vacancy) (c) Structural representation of substitution induced vacancies and corresponding increase in activity of material shown by cyclic voltammograms. (d) Capacity at different scan rates for series of substituted samples. (e) Cyclic stability. [102, 103]

This study also demonstrated outstanding rate performance, where material retained 64.5% of its capacity even at a high rate of 10 C, and its exceptional cyclic stability, with 99.8% capacity retention after 2000 cycles at 10 C. These improvements were attributed to the low strain characteristic of the material (1.17% volume change) during cycling, withstanding deep Li^+ insertion conditions.

Another study performed by our group recently, has a direct relevance to the work presented in later chapters of this thesis. $AgNbO_3$ perovskite structure has been modified through the strategic substitution of silver (Ag) atoms with lanthanum (La) in order to activate the material for Li^+ insertion [103]. The idea behind this substitution was to introduce controlled changes in the in the lattice by replacing Ag with La, which carries a higher charge (3^+ compared to 1^+ for Ag) and has a larger ionic radius. Such a substitution leads to creation of artificial vacancies in the structure providing pathways for Li^+ insertion, thereby facilitating efficient charging and discharging. It was found that, the introduction of La into perovskite caused a lattice expansion to compensate the size mismatch and reduced the $[NbO_6]$ octahedra distortions, leading to a more symmetrical and stable structure (Figure 1.10 c). The highly substituted material ($x = 0.15$, which corresponds 30% A-site vacancies) exhibited 35 mAh g^{-1} at 0.1 mVs^{-1}, with 95% capacity retention after 800 cycles within a potential window of 1.2 – 3.0 V vs. Li^+/Li. Moreover, when cycled at high scan rate of 50 $mV.s^{-1}$, a 64% capacity retention was achieved. While *ex-situ* ^7Li MAS NMR confirmed the Li^+ insertion in the structure, *in situ* XRD combined with kinetic analysis revealed the ability to store charge without solid-state ion-diffusion limitations. However, these structures have quite narrow stability potential windows. This is primarily due to silver cation (Ag^+) sensitivity towards external stimuli, which results in its reduction followed by exsolution from the structure of metallic silver when exposed to extended potential windows.

General overview of ABO_3-type perovskites and their basic characteristics from a negative electrode's perspective is presented in Figure 1.11.

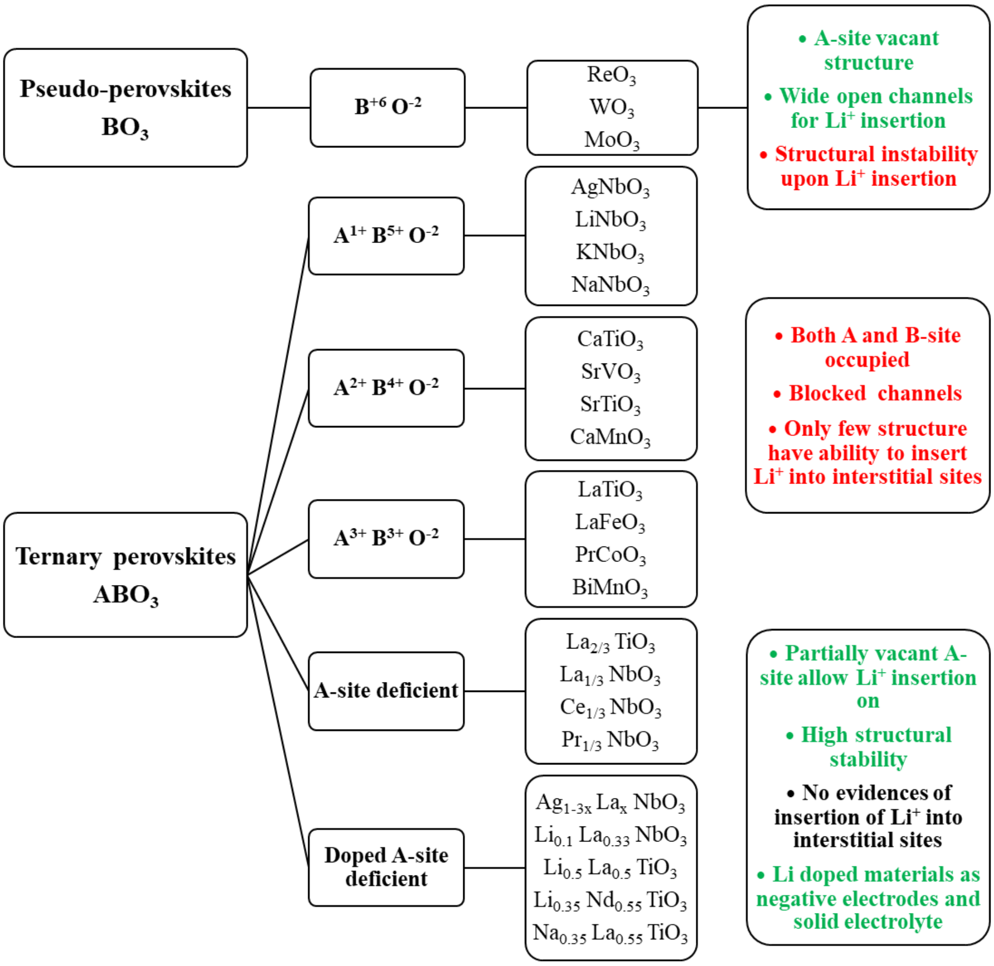

Figure 1.11. Overview of ABO$_3$-type perovskites from a LIB's negative electrode perspective.

As research into transition metal oxides continued to uncover their potential in energy storage applications, attention expanded to other transition metal compounds with similar properties. Transition metal-based carbides, such as MAX phases, offer unique structural and functional properties, making them attractive for applications where both ceramic-like and metallic behavior are desirable. The subsequent section will discuss the properties of such materials and a particular focus of synthesis of Ti_3AlC_2 MAX phases.

1.6 Transition metal based carbides: MAX phases

1.6.1 MAX phases

MAX phases, a family of over 70 ternary carbides and nitrides crystalizes in a hexagonal P63/mmc structure [104,105]. These phases are represented by general formula $M_{n+1}AX_n$, where M is an early transition metal, A is typically from groups 13 to 15, and X is carbon, nitrogen, or both (in case of solid solutions). The value of n is usually 1, 2, or 3, or in some cases greater than 3 has been reported [106,107]. MAX phase structure comprised of layers of edge-sharing M_6X octahedra separated by layers of A-element. Starting with n value 1 (known as 211 phases), number of M_6X octaherdra layers are directly proportional to “n” (Figure 1.12 a and b).

The discovery of MAX phases dates back to 1960 when Kudielka and Rohde first reported carbosulfides of Zr and Ti [108]. In coming years, Nowotny and colleagues did notable research efforts and classified these materials as H-phases [109,110]. However, the revival of these phases begin with synthesis and characterizations of Ti_3SiC_2 by Barsoum and co-workers in 1996 [111]. They revealed the interesting properties of this class of materials. MAX phases possess a combination of mechanical, electrical, and thermal properties that are uncommon in traditional ceramics and metals. They are both stiff and soft, have electrical and thermal conductivity, and show remarkable chemical resistance. In addition, certain MAX phases exhibit exceptional oxidation and fatigue resistance, enduring pressures up to 1GPa at room temperature without fatigue, which positions them between ceramics and metals. These phases gained enormous research interest after discovery of novel class of material named as “MXenes” in 2011, where MAX phases function as precursors [112].

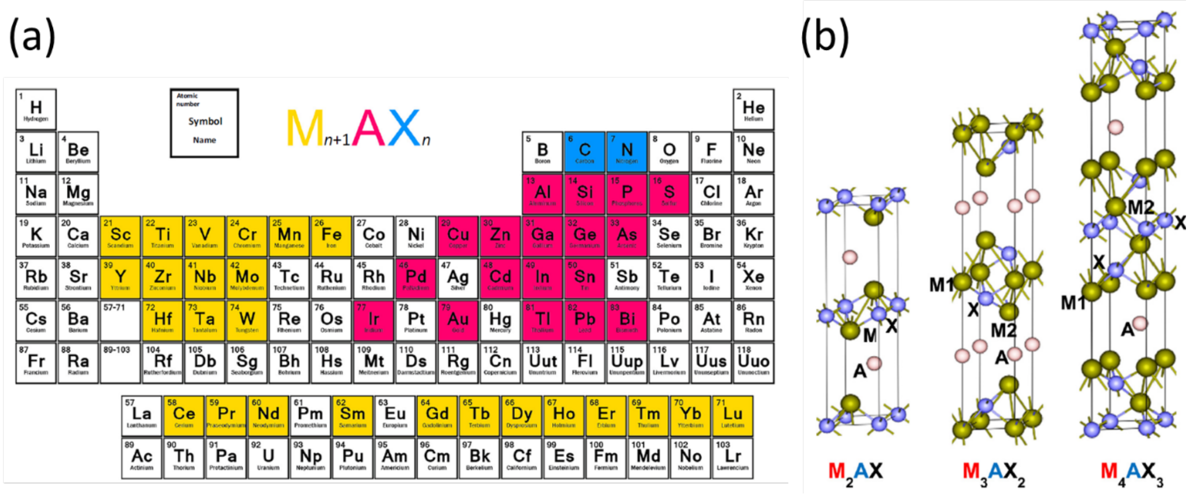

Figure 1.12. (a) Periodic table MAX phases based on known phases and solid solution. (b) Unit cell of a 211, 312, 413 MAX phases showing edge-sharing octahedra.

1.6.2 Synthesis of Ti_3AlC_2 phases: State-of-the-art and novel routes

The current state of the art of MAX phase synthesis is presented in this section, with focus on the one which is of particular interest to this work and most studied among MAX phases, Ti_3AlC_2. As stated in the previous section, numerous MAX phased compounds were discovered around 1960, including Ti_3AlC_2 and its derivatives.

Since the pioneering work on Ti_3AlC_2 [113], several routes have been developed for processing of this phase, either in the form of pressure induced dense discs or in the form of pressure-less sintering, yielding the powder product [114]. Synthesis routes and conditions that were mainly reported in literature for Ti_3AlC_2 are summarized in Table I.1. Methods like hot pressing (HP) and spark plasma sintering (SPS) or pulse discharge sintering (PDS) have proven effective in producing dense, high-purity Ti_3AlC_2 phases. However, the pressure required during fabrication or post-densification, introduces inefficiencies and problems of mass production. Therefore, methods based on pressureless sintering (PS) have been developed that are capable of producing Ti_3AlC_2 powders with high purity. However, almost all of these techniques requires elemental precursors of high purity as starting material.

Table I.1. Summary of different routes and conditions for Ti_3AlC_2 MAX phase processessing.

Precursors and stoichiometry	Methods	Heating conditions	Phase compositions	references
Ti/Al_4C_3/C	HP	1400◦C, 16 h, 70 MPa	~4% Al_2O_3 impurities, dense	[115]
Ti/Al/C 3 : 1 : 2	HP	1500◦C, 5 min, 25 MPa	Phase pure (100%), dense	[116]
Ti/Al/TiC	SPS	1300◦C, 15 min, 30 MPa	Phase pure (100%), dense	[117]
Ti/Al/C 3:1:1.88	PS	1500°C, 1 h	Pure phase (100%)	[118]
Ti/Al/C 3:1:2	PS	900 – 1400°C, 0 – 20h	Purity (96% at 1400°C) Impurities = Ti_2AlC and TiC	[119]
TiC/Al/C 2:1:1	PS	1200 – 1400°C, 0.25 – 1h	Purity (97% at 1300°C) Impurities = TiC	[120]

Typical synthesis requires elemental powders to be mixed, grinded, pelletized and sealed in an evacuated quartz ampoule, which subsequently sintering for a long period of time at a high temperature upto 1500 °C. In this process, samples pelletized (or not), can also be sintered (or reactive sintered) to high temperatures under controlled reducing environment (in a tube furnace), which eliminate the tube sealing step. Underlying reaction pathway may vary depending on the route adopted. However, general mechanism for formation of Ti_3AlC_2 from elemental precursors follow these steps [116,119,114,121]:

1. Powder mixed and grinded. No reaction between elemental precursors occurs below 660 °C.
2. Melting of Al powder starts at around 660 °C. It accumulate on Ti powder and form intermetallics such as TiAl from 740 °C to 900 °C.
3. Further increasing temperature causes Al from outer layer to react with inner Ti and form single phased $AlTi_3$.

4. At 1300 °C, carbon diffuse into Ti–Al intermatallics and form carbide derivatives like Ti_2AlC, Ti_3AlC and TiC.
5. Finally, these carbide derivatives and remaining C powder reacts at about 1400 °C to form Ti_3AlC_2.

These steps are schematically represented in Figure 1.13a and supported by XRD results shown in Figure 1.13b.

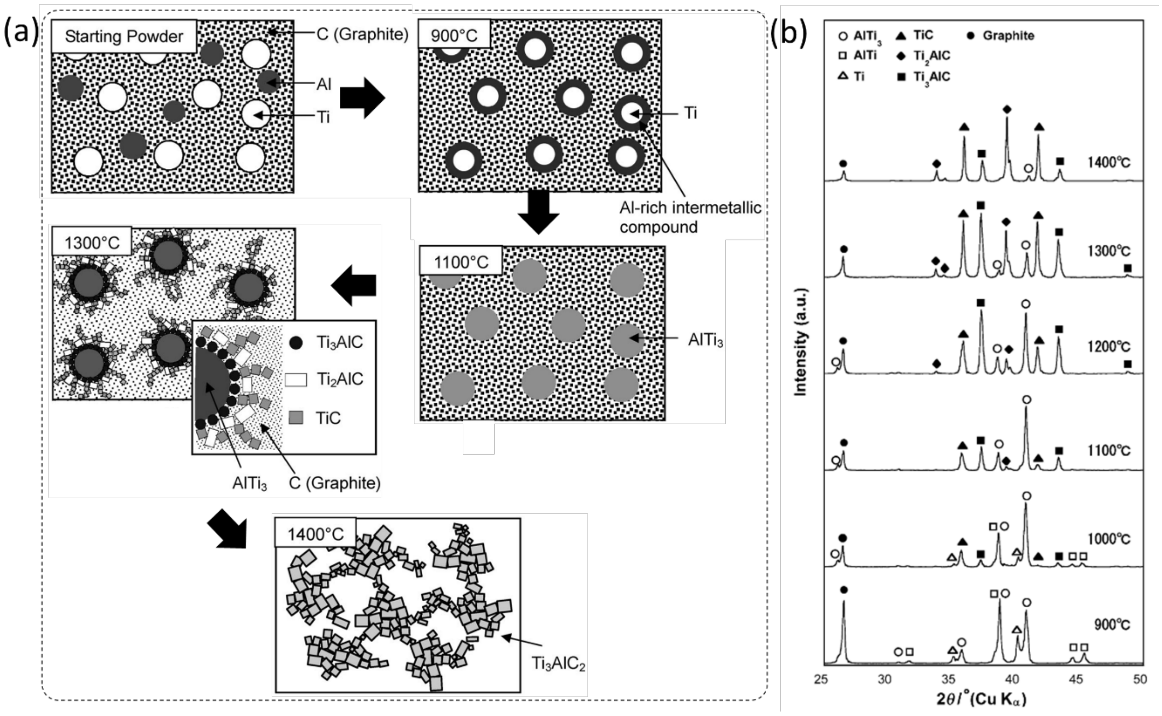

Figure 1.13. (a) Schematic illustration of Ti_3AlC_2 formation process from its elemental precursors. (b) Corresponding XRD patterns.

Beyond solid-state synthesis, sol-gel chemistry has emerged as a promising technique in the MAX phase family, first demonstrated in 2019 for synthesis of magnetic Cr_2GaC MAX phase by Birkel and co-workers [122]. In addition to low formation temperature of 900 °C, its processability was highlighted by the ability to decorate hollow carbon microspheres with Cr_2GaC. Early mechanistic studies revealed that the metal precursors initially oxidize, followed by the reduction of these oxides by carbon, and finally leading to the formation of the MAX phase. These results were supported by simultaneous thermal analysis and mass spectrometry, which confirmed the underlying carbothermal reduction mechanism. Afterwards, this process was further optimized quite recently by the same group where they mainly target the other magnetic MAX phases such as Cr_2GeC and V_2GeC [123]. However, their method is tested for specific metal based magnetic MAX phases that have formation temperature of around 1000 °C, where graphite demonstrate its maximium reductive strength. Hence, there is still major challenge of considering such synthesis route for Ti_3AlC_2 phase which has the most promising properties, especially for electrochemical energy storage applications when processed as $Ti_3C_2T_x$ MXenes.

In this work, we attempted to tackle the challenge of developing a wet chemistry synthesis method for Ti_3AlC_2 and highlighted the mechanistic difficulties encountered during the process.

References related to chapter 1

[1] W.M. Sudduth, The Voltaic Pile and Electro-Chemical Theory in 1800, Ambix 27 (1980) 26–35. https://doi.org/10.1179/amb.1980.27.1.26.

[2] A. Yoshino, The Birth of the Lithium-Ion Battery, Angew Chem Int Ed 51 (2012) 5798–5800. https://doi.org/10.1002/anie.201105006.

[3] J.-M. Tarascon, M. Armand, Issues and challenges facing rechargeable lithium batteries, Nature 414 (2001) 359–367. https://doi.org/10.1038/35104644.

[4] J.T. Frith, M.J. Lacey, U. Ulissi, A non-academic perspective on the future of lithium-based batteries, Nat Commun 14 (2023) 420. https://doi.org/10.1038/s41467-023-35933-2.

[5] M. Li, J. Lu, Z. Chen, K. Amine, 30 Years of Lithium-Ion Batteries, Advanced Materials 30 (2018) 1800561. https://doi.org/10.1002/adma.201800561.

[6] A.H. Thompson, M.S. Whittingham, Transition metal phosphorus trisulfides as battery cathodes, Materials Research Bulletin 12 (1977) 741–744. https://doi.org/10.1016/0025-5408(77)90134-9.

[7] M.S. Whittingham, Chemistry of intercalation compounds: Metal guests in chalcogenide hosts, Progress in Solid State Chemistry 12 (1978) 41–99. https://doi.org/10.1016/0079-6786(78)90003-1.

[8] R. Yazami, K. Zaghib, M. Deschamps, Carbon fibres and natural graphite as negative electrodes for lithium ion-type batteries, Journal of Power Sources 52 (1994) 55–59. https://doi.org/10.1016/0378-7753(94)01933-9.

[9] J.R. Dahn, T. Zheng, Y. Liu, J.S. Xue, Mechanisms for Lithium Insertion in Carbonaceous Materials, Science 270 (1995) 590–593. https://doi.org/10.1126/science.270.5236.590.

[10] K. Mizushima, P.C. Jones, P.J. Wiseman, J.B. Goodenough, Li_xCoO_2 (0<x<-1): A new cathode material for batteries of high energy density, Materials Research Bulletin 15 (1980) 783–789. https://doi.org/10.1016/0025-5408(80)90012-4.

[11] A. Ramanan, Nobel Prize in Chemistry 2019, (n.d.). https://www.ias.ac.in/article/fulltext/reso/024/12/1381-1395.

[12] J.B. Goodenough, K.-S. Park, The Li-Ion Rechargeable Battery: A Perspective, J. Am. Chem. Soc. 135 (2013) 1167–1176. https://doi.org/10.1021/ja3091438.

[13] Y. Lyu, X. Wu, K. Wang, Z. Feng, T. Cheng, Y. Liu, M. Wang, R. Chen, L. Xu, J. Zhou, Y. Lu, B. Guo, An Overview on the Advances of $LiCoO_2$ Cathodes for Lithium-Ion Batteries, Advanced Energy Materials 11 (2021) 2000982. https://doi.org/10.1002/aenm.202000982.

[14] M.S. Whittingham, Ultimate Limits to Intercalation Reactions for Lithium Batteries, Chem. Rev. 114 (2014) 11414–11443. https://doi.org/10.1021/cr5003003.

[15] K.K. Lee, W.S. Yoon, K.B. Kim, K.Y. Lee, S.T. Hong, Characterization of $LiNi_{0.85}Co_{0.10}M_{0.05}O_2$ (M = Al, Fe) as a cathode material for lithium secondary batteries, Journal of Power Sources 97–98 (2001) 308–312. https://doi.org/10.1016/S0378-7753(01)00516-X.

[16] C.S. Johnson, N. Li, C. Lefief, M.M. Thackeray, Anomalous capacity and cycling stability of $_{x}Li_2MnO_3\cdot_{(1-x)}LiMO_2$ electrodes (M=Mn, Ni, Co) in lithium batteries at 50°C, Electrochemistry Communications 9 (2007) 787–795. https://doi.org/10.1016/j.elecom.2006.11.006.

[17] C. Julien, A. Mauger, K. Zaghib, H. Groult, Comparative Issues of Cathode Materials for Li-Ion Batteries, Inorganics 2 (2014) 132–154. https://doi.org/10.3390/inorganics2010132.

[18] N. Nitta, F. Wu, J.T. Lee, G. Yushin, Li-ion battery materials: present and future, Materials Today 18 (2015) 252–264. https://doi.org/10.1016/j.mattod.2014.10.040.

[19] Z. Liu, A. Yu, J.Y. Lee, Synthesis and characterization of $LiNi_{1-x-y}Co_xMn_yO_2$ as the cathode materials of secondary lithium batteries, Journal of Power Sources 81–82 (1999) 416–419. https://doi.org/10.1016/S0378-7753(99)00221-9.

[20] G. Zubi, R. Dufo-López, M. Carvalho, G. Pasaoglu, The lithium-ion battery: State of the art and future perspectives, Renewable and Sustainable Energy Reviews 89 (2018) 292–308. https://doi.org/10.1016/j.rser.2018.03.002.

[21] J. Xu, S. Dou, H. Liu, L. Dai, Cathode materials for next generation lithium ion batteries, Nano Energy 2 (2013) 439–442. https://doi.org/10.1016/j.nanoen.2013.05.013.

[22] B. Scrosati, J. Garche, Lithium batteries: Status, prospects and future, Journal of Power Sources 195 (2010) 2419–2430. https://doi.org/10.1016/j.jpowsour.2009.11.048.

[23] K. Karthikeyan, S. Amaresh, G.W. Lee, V. Aravindan, H. Kim, K.S. Kang, W.S. Kim, Y.S. Lee, Electrochemical performance of cobalt free, $Li_{1.2}(Mn_{0.32}Ni_{0.32}Fe_{0.16})O_2$ cathodes for lithium batteries, Electrochimica Acta 68 (2012) 246–253. https://doi.org/10.1016/j.electacta.2012.02.076.

[24] A. Kumar, P. Bashiri, B. Mandal, K. Dhindsa, K. Bazzi, A. Dixit, M. Nazri, Z. Zhou, V. Garg, A. Oliveira, P. Vaishnava, V. Naik, G.-A. Nazri, R. Naik, Optimization of Electrochemical Performance of $LiFePO_4$/C by Indium Doping and High Temperature Annealing, Inorganics 5 (2017) 67. https://doi.org/10.3390/inorganics5040067.

[25] S.-Y. Chung, J.T. Bloking, Y.-M. Chiang, Electronically conductive phospho-olivines as lithium storage electrodes, Nature Mater 1 (2002) 123–128. https://doi.org/10.1038/nmat732.

[26] X. Huang, X. Li, H. Wang, Z. Pan, M. Qu, Z. Yu, Synthesis and electrochemical performance of Li_2FeSiO_4/C as cathode material for lithium batteries, Solid State Ionics 181 (2010) 1451–1455. https://doi.org/10.1016/j.ssi.2010.08.007.

[27] N. Ravet, Y. Chouinard, J.F. Magnan, S. Besner, M. Gauthier, M. Armand, Electroactivity of natural and synthetic triphylite, Journal of Power Sources 97–98 (2001) 503–507. https://doi.org/10.1016/S0378-7753(01)00727-3.

[28] H. Huang, S.-C. Yin, L.F. Nazar, Approaching Theoretical Capacity of $LiFePO_4$ at Room Temperature at High Rates, Electrochem. Solid-State Lett. 4 (2001) A170. https://doi.org/10.1149/1.1396695.

[29] M.S. Whittingham, Lithium Batteries and Cathode Materials, Chem. Rev. 104 (2004) 4271–4302. https://doi.org/10.1021/cr020731c.

[30] M. Winter, B. Barnett, K. Xu, Before Li Ion Batteries, Chem. Rev. 118 (2018) 11433–11456. https://doi.org/10.1021/acs.chemrev.8b00422.

[31] H. Zhang, Y. Yang, D. Ren, L. Wang, X. He, Graphite as anode materials: Fundamental mechanism, recent progress and advances, Energy Storage Materials 36 (2021) 147–170. https://doi.org/10.1016/j.ensm.2020.12.027.

[32] Y. Liu, Y. Zhu, Y. Cui, Challenges and opportunities towards fast-charging battery materials, Nat Energy 4 (2019) 540–550. https://doi.org/10.1038/s41560-019-0405-3.

[33] H.-G. Jung, M.W. Jang, J. Hassoun, Y.-K. Sun, B. Scrosati, A high-rate long-life $Li_4Ti_5O_{12}$/$Li[Ni_{0.45}Co_{0.1}Mn_{1.45}]O_4$ lithium-ion battery, Nat Commun 2 (2011) 516. https://doi.org/10.1038/ncomms1527.

[34] N. Takami, K. Ise, Y. Harada, T. Iwasaki, T. Kishi, K. Hoshina, High-energy, fast-charging, long-life lithium-ion batteries using $TiNb_2O_7$ anodes for automotive applications, Journal of Power Sources 396 (2018) 429–436. https://doi.org/10.1016/j.jpowsour.2018.06.059.

[35] I.H. Son, J. Hwan Park, S. Kwon, S. Park, M.H. Rümmeli, A. Bachmatiuk, H.J. Song, J. Ku, J.W. Choi, J. Choi, S.-G. Doo, H. Chang, Silicon carbide-free graphene growth on silicon for lithium-ion battery with high volumetric energy density, Nat Commun 6 (2015) 7393. https://doi.org/10.1038/ncomms8393.

[36] S. Ahmed, I. Bloom, A.N. Jansen, T. Tanim, E.J. Dufek, A. Pesaran, A. Burnham, R.B. Carlson, F. Dias, K. Hardy, M. Keyser, C. Kreuzer, A. Markel, A. Meintz, C. Michelbacher, M. Mohanpurkar, P.A. Nelson, D.C. Robertson, D. Scoffield, M. Shirk, T. Stephens, R. Vijayagopal, J. Zhang, Enabling fast charging – A battery technology gap assessment, Journal of Power Sources 367 (2017) 250–262. https://doi.org/10.1016/j.jpowsour.2017.06.055.

[37] D. Lin, Y. Liu, Y. Cui, Reviving the lithium metal anode for high-energy batteries, Nature Nanotech 12 (2017) 194–206. https://doi.org/10.1038/nnano.2017.16.

[38] Y. Yang, J. Zhao, Wadsley–Roth Crystallographic Shear Structure Niobium-Based Oxides: Promising Anode Materials for High-Safety Lithium-Ion Batteries, Advanced Science 8 (2021) 2004855. https://doi.org/10.1002/advs.202004855.

[39] M. Saber, M.B. Preefer, S.K. Kolli, W. Zhang, G. Laurita, B. Dunn, R. Seshadri, A. Van Der Ven, Role of Electronic Structure in Li Ordering and Chemical Strain in the Fast Charging Wadsley–Roth Phase PNb_9O_{25}, Chem. Mater. 33 (2021) 7755–7766. https://doi.org/10.1021/acs.chemmater.1c02059.

[40] H. Liu, C. Chen, Wadsley–Roth phase $CoNb_{11}O_{29}$ as a high-performance anode for lithium-ion batteries, J. Mater. Chem. A 12 (2024) 5414–5421. https://doi.org/10.1039/D3TA07865E.

[41] D. Kim, L.S. Oh, J.H. Park, H.J. Kim, S. Lee, E. Lim, Perovskite-based electrocatalysts for oxygen evolution reaction in alkaline media: A mini review, Front. Chem. 10 (2022) 1024865. https://doi.org/10.3389/fchem.2022.1024865.

[42] V.M. Goldschmidt, Die Gesetze der Krystallochemie, Naturwissenschaften 14 (1926) 477–485. https://doi.org/10.1007/BF01507527.

[43] H. Liu, J. Cheng, H. Dong, J. Feng, B. Pang, Z. Tian, S. Ma, F. Xia, C. Zhang, L. Dong, Screening stable and metastable ABO_3 perovskites using machine learning and the materials project, Computational Materials Science 177 (2020) 109614. https://doi.org/10.1016/j.commatsci.2020.109614.

[44] C.J. Bartel, C. Sutton, B.R. Goldsmith, R. Ouyang, C.B. Musgrave, L.M. Ghiringhelli, M. Scheffler, New tolerance factor to predict the stability of perovskite oxides and halides, Sci. Adv. 5 (2019) eaav0693. https://doi.org/10.1126/sciadv.aav0693.

[45] T. Ofoegbuna, Defect Engineering in Strained Low-Dimensional ABO_3 Perovskite Nanoparticles for Next-Generation Energy Storage, Louisiana State University and Agricultural & Mechanical College, 2021.

[46] N. Raengthon, C. McCue, D.P. Cann, Relationship between tolerance factor and temperature coefficient of permittivity of temperature-stable high permittivity $BaTiO_3$ – $Bi(Me)O_3$ compounds, J. Adv. Dielect. 06 (2016) 1650002. https://doi.org/10.1142/S2010135X16500028.

[47] J.-G. Cheng, J.A. Alonso, E. Suard, J.-S. Zhou, J.B. Goodenough, A New Perovskite Polytype in the High-Pressure Sequence of $BaIrO_3$, J. Am. Chem. Soc. 131 (2009) 7461–7469. https://doi.org/10.1021/ja901829e.

[48] C. Sun, J.A. Alonso, J. Bian, Recent Advances in Perovskite-Type Oxides for Energy Conversion and Storage Applications, Advanced Energy Materials 11 (2021) 2000459. https://doi.org/10.1002/aenm.202000459.

[49] J. Vieten, B. Bulfin, P. Huck, M. Horton, D. Guban, L. Zhu, Y. Lu, K.A. Persson, M. Roeb, C. Sattler, Materials design of perovskite solid solutions for thermochemical applications, Energy Environ. Sci. 12 (2019) 1369–1384. https://doi.org/10.1039/C9EE00085B.

[50] J. Varignon, M. Bibes, A. Zunger, Origin of band gaps in 3d perovskite oxides, Nat Commun 10 (2019) 1658. https://doi.org/10.1038/s41467-019-09698-6.

[51] S. Kasap, C. Koughia, H. Ruda, R. Johanson, Electrical Conduction in Metals and Semiconductors, in: S. Kasap, P. Capper (Eds.), Springer Handbook of Electronic and Photonic Materials, Springer US, Boston, MA, (2006) 19–45. https://doi.org/10.1007/978-0-387-29185-7_2.

[52] H. Kawanaka, E. Kawawa, Y. Nishihara, F. Iga, A. Kondo, K. Kindo, Y. Matsuda, Magnetic properties of perovskite $Ca_{1-x}Sr_xFeO_3$, AIP Advances 8 (2018) 101418. https://doi.org/10.1063/1.5042695.

[53] R.B. Macquart, B.J. Kennedy, M. Avdeev, Neutron diffraction study of phase transitions in perovskite-type strontium molybdate $SrMoO_3$, Journal of Solid State Chemistry 183 (2010) 250–255. https://doi.org/10.1016/j.jssc.2009.11.005.

[54] D.Y. Wan, Y.L. Zhao, Y. Cai, T.C. Asmara, Z. Huang, J.Q. Chen, J. Hong, S.M. Yin, C.T. Nelson, M.R. Motapothula, B.X. Yan, D. Xiang, X. Chi, H. Zheng, W. Chen, R. Xu, Ariando, A. Rusydi, A.M. Minor, M.B.H. Breese, M. Sherburne, M. Asta, Q.-H. Xu, T. Venkatesan, Electron transport and visible light absorption in a plasmonic photocatalyst based on strontium niobate, Nat Commun 8 (2017) 15070. https://doi.org/10.1038/ncomms15070.

[55] W. Li, J. Shi, K.H.L. Zhang, J.L. MacManus-Driscoll, Defects in complex oxide thin films for electronics and energy applications: challenges and opportunities, Mater. Horiz. 7 (2020) 2832–2859. https://doi.org/10.1039/D0MH00899K.

[56] D. Wan, B. Yan, J. Chen, S. Wu, J. Hong, D. Song, X. Zhao, X. Chi, S. Zeng, Z. Huang, C. Li, K. Han, W. Zhou, Y. Cao, A. Rusydi, S.J. Pennycook, P. Yang, Ariando, R. Xu, Q.-H. Xu, X.R. Wang, T. Venkatesan, New Family of Plasmonic Photocatalysts without Noble Metals, Chem. Mater. 31 (2019) 2320–2327. https://doi.org/10.1021/acs.chemmater.8b04185.

[57] P.D. Durugkar, A.G. Katpatal, Growth and characterization of pure, and doped crystals of potassium niobate, Journal of Crystal Growth 162 (1996) 161–166. https://doi.org/10.1016/0022-0248(95)00924-8.

[58] V.A. Trepakov, M.E. Savinov, V. Železný, P.P. Syrnikov, A. Deyneka, L. Jastrabik, Li doping effect on properties and phase transfomations of $KNbO_3$, Journal of the European Ceramic Society 27 (2007) 4071–4073. https://doi.org/10.1016/j.jeurceramsoc.2007.02.113.

[59] S.R. Burns, M.R. Dolgos, Sizing up $(K_{1-x}Na_x)NbO_3$ films: a review of synthesis routes, properties & applications, New J. Chem. 45 (2021) 7408–7436. https://doi.org/10.1039/D1NJ01092A.

[60] G. Song, Y. Song, J. Su, K. Zhang, L. Xing, H. Yang, N. Zhang, High temperature dielectric properties and magnetic behavior of $K_{1-x}Ca_xNbO_3$ ceramic, Physica B: Condensed Matter 602 (2021) 412593. https://doi.org/10.1016/j.physb.2020.412593.

[61] C.M. Dudhe, S.J. Khambadkar, Oxygen vacancy dependent structural phases in $KNbO_3$, Materials Letters 216 (2018) 97–100. https://doi.org/10.1016/j.matlet.2018.01.011.

[62] H.A. Evans, Y. Wu, R. Seshadri, A.K. Cheetham, Perovskite-related ReO_3-type structures, Nat Rev Mater 5 (2020) 196–213. https://doi.org/10.1038/s41578-019-0160-x.

[63] H. Zheng, J.Z. Ou, M.S. Strano, R.B. Kaner, A. Mitchell, K. Kalantar-zadeh, Nanostructured Tungsten Oxide – Properties, Synthesis, and Applications, Adv Funct Materials 21 (2011) 2175–2196. https://doi.org/10.1002/adfm.201002477.

[64] A. Ferretti, D.B. Rogers, J.B. Goodenough, The relation of the electrical conductivity in single crystals of rhenium trioxide to the conductivities of Sr_2MgReO_6 and Na_xWO_3, Journal of Physics and Chemistry of Solids 26 (1965) 2007–2011. https://doi.org/10.1016/0022-3697(65)90237-4.

[65] R.J. Cava, A. Santoro, D.W. Murphy, S. Zahurak, R.S. Roth, The structures of lithium-inserted metal oxides: $LiReO_3$ and Li_2ReO_3, Journal of Solid State Chemistry 42 (1982) 251–262. https://doi.org/10.1016/0022-4596(82)90004-4.

[66] N.H. Bashian, S. Zhou, M. Zuba, A.M. Ganose, J.W. Stiles, A. Ee, D.S. Ashby, D.O. Scanlon, L.F.J. Piper, B. Dunn, B.C. Melot, Correlated Polyhedral Rotations in the Absence of Polarons during Electrochemical Insertion of Lithium in ReO_3, ACS Energy Lett. 3 (2018) 2513–2519. https://doi.org/10.1021/acsenergylett.8b01179.

[67] S. Tanisaki, Crystal Structure of Monoclinic Tungsten Trioxide at Room Temperature, J. Phys. Soc. Jpn. 15 (1960) 573–581. https://doi.org/10.1143/JPSJ.15.573.

[68] Z. Gu, H. Li, T. Zhai, W. Yang, Y. Xia, Y. Ma, J. Yao, Large-scale synthesis of single-crystal hexagonal tungsten trioxide nanowires and electrochemical lithium intercalation into the nanocrystals, Journal of Solid State Chemistry 180 (2007) 98–105. https://doi.org/10.1016/j.jssc.2006.09.020.

[69] K. Huang, Q. Pan, F. Yang, S. Ni, X. Wei, D. He, Controllable synthesis of hexagonal WO_3 nanostructures and their application in lithium batteries, J. Phys. D: Appl. Phys. 41 (2008) 155417. https://doi.org/10.1088/0022-3727/41/15/155417.

[70] Y. Liu, Y. Jiao, H. Zhou, X. Yu, F. Qu, X. Wu, Rational Design of WO_3 Nanostructures as the Anode Materials for Lithium-Ion Batteries with Enhanced Electrochemical Performance, Nano-Micro Lett. 7 (2015) 12–16. https://doi.org/10.1007/s40820-014-0013-5.

[71] S. Yoon, C. Jo, S.Y. Noh, C.W. Lee, J.H. Song, J. Lee, Development of a high-performance anode for lithium ion batteries using novel ordered mesoporous tungsten oxide materials with high electrical conductivity, Phys. Chem. Chem. Phys. 13 (2011) 11060. https://doi.org/10.1039/c1cp20940j.

[72] J. Zhou, N. Lin, L. Wang, K. Zhang, Y. Zhu, Y. Qian, Synthesis of hexagonal MoO_3 nanorods and a study of their electrochemical performance as anode materials for lithium-ion batteries, J. Mater. Chem. A 3 (2015) 7463–7468. https://doi.org/10.1039/C5TA00516G.

[73] K. Dai, Q. Wang, Y. Xie, M. Shui, J. Shu, Disordered carbon coating free $Li_{0.2375}La_{0.5875}TiO_3$: a superior perovskite anode material for high power long-life lithium-ion batteries, J Mater Sci 57 (2022) 2825–2838. https://doi.org/10.1007/s10853-021-06713-4.

[74] H. Liu, J. Xiao, H. He, K. Cao, Y. Li, B. Pan, C. Chen, Cation-deficient perovskite $Li_{0.35}Nd_{0.55}TiO_3$ as a high-performance anode for lithium-ion batteries, Nano Energy 119 (2024) 109065. https://doi.org/10.1016/j.nanoen.2023.109065.

[75] L. Zhang, X. Zhang, G. Tian, Q. Zhang, M. Knapp, H. Ehrenberg, G. Chen, Z. Shen, G. Yang, L. Gu, F. Du, Lithium lanthanum titanate perovskite as an anode for lithium ion batteries, Nat Commun 11 (2020) 3490. https://doi.org/10.1038/s41467-020-17233-1.

[76] Y. Inaguma, C. Liquan, M. Itoh, T. Nakamura, T. Uchida, H. Ikuta, M. Wakihara, High ionic conductivity in lithium lanthanum titanate, Solid State Communications 86 (1993) 689–693. https://doi.org/10.1016/0038-1098(93)90841-A.

[77] T. Teranishi, Y. Ishii, H. Hayashi, A. Kishimoto, Lithium ion conductivity of oriented $Li_{0.33}La_{0.56}TiO_3$ solid electrolyte films prepared by a sol–gel process, Solid State Ionics 284 (2016) 1–6. https://doi.org/10.1016/j.ssi.2015.11.029.

[78] S. Stramare, V. Thangadurai, W. Weppner, Lithium Lanthanum Titanates: A Review, Chem. Mater. 15 (2003) 3974–3990. https://doi.org/10.1021/cm0300516.

[79] Y.J. Shan, L. Chen, Y. Inaguma, M. Itoh, T. Nakamura, Oxide cathode with perovskite structure for rechargeable lithium batteries, Journal of Power Sources 54 (1995) 397–402. https://doi.org/10.1016/0378-7753(94)02110-O.

[80] O. Bohnke, Mechanism of ionic conduction and electrochemical intercalation of lithium into the perovskite lanthanum lithium titanate, Solid State Ionics 91 (1996) 21–31. https://doi.org/10.1016/S0167-2738(96)00434-1.

[81] S. Scharner, W. Weppner, P. Schmid-Beurmann, Evidence of Two-Phase Formation upon Lithium Insertion into the $Li_{1.33}Ti_{1.67}O_4$ Spinel, J. Electrochem. Soc. 146 (1999) 857–861. https://doi.org/10.1149/1.1391692.

[82] M. Nakayama, T. Usui, Y. Uchimoto, M. Wakihara, M. Yamamoto, Changes in Electronic Structure upon Lithium Insertion into the A-Site Deficient Perovskite Type Oxides $(Li,La)TiO_3$, J. Phys. Chem. B 109 (2005) 4135–4143. https://doi.org/10.1021/jp046062j.

[83] H. Liu, J. Xiao, K. Cao, N. Ren, H. He, Y. Li, J. Si, S. Zeng, B. Pan, C. Chen, A-site deficient perovskite lithium praseodymium titanate as a high-rate anode for lithium-ion batteries, Chemical Engineering Journal 479 (2024) 147765. https://doi.org/10.1016/j.cej.2023.147765.

[84] Yuejinshan, L. Chen, Y. Inaguma, M. Shikano, M. Itoh, T. Nakamura, Lithium insertion into ceramic $SrVO_{3-\delta}$, Solid State Ionics 70–71 (1994) 429–433. https://doi.org/10.1016/0167-2738(94)90349-2.

[85] Y. Shan, The effect of electrostatic potentials on lithium insertion for perovskite oxides, Solid State Ionics 79 (1995) 245–251. https://doi.org/10.1016/0167-2738(95)00069-I.

[86] M. Onoda, H. Ohta, H. Nagasawa, Metallic properties of perovskite oxide $SrVO_3$, Solid State Communications 79 (1991) 281–285. https://doi.org/10.1016/0038-1098(91)90546-8.

[87] L. Zhang, Y. Zhou, L. Guo, W. Zhao, A. Barnes, H.-T. Zhang, C. Eaton, Y. Zheng, M. Brahlek, H.F. Haneef, N.J. Podraza, M.H.W. Chan, V. Gopalan, K.M. Rabe, R. Engel-Herbert, Correlated metals as transparent conductors, Nature Mater 15 (2016) 204–210. https://doi.org/10.1038/nmat4493.

[88] X. Li, Z. Lin, N. Jin, X. Yang, Y. Du, L. Lei, P. Rozier, P. Simon, Y. Liu, Perovskite-Type $SrVO_3$ as High-Performance Anode Materials for Lithium-Ion Batteries, Advanced Materials 34 (2022) 2107262. https://doi.org/10.1002/adma.202107262.

[89] X. Li, Z. Lin, N. Jin, X. Yang, L. Sun, Y. Wang, L. Xie, X. Chen, L. Lei, P. Rozier, P. Simon, Y. Liu, Boosting the lithium-ion storage performance of perovskite $SrVO_{3-\delta}$ via Sr cation and O anion deficient engineering, Science Bulletin 67 (2022) 2305–2315. https://doi.org/10.1016/j.scib.2022.11.006.

[90] X. Li, Z. Lin, N. Jin, L. Sun, X. Yang, Y. Liu, High-capacity anode materials for lithium-ion batteries: perovskite strontium vanadate with crystalline-amorphous dual-phase structure, Materials Today Chemistry 30 (2023) 101542. https://doi.org/10.1016/j.mtchem.2023.101542.

[91] M.M.S. Sanad, A. Toghan, Chemical activation of nanocrystalline $LiNbO_3$ anode for improved storage capacity in lithium-ion batteries, Surfaces and Interfaces 27 (2021) 101550. https://doi.org/10.1016/j.surfin.2021.101550.

[92] T. Yan, R. Ding, D. Ying, Y. Huang, Y. Huang, C. Tan, X. Sun, P. Gao, E. Liu, An intercalation pseudocapacitance-driven perovskite $NaNbO_3$ anode with superior kinetics and stability for advanced lithium-based dual-ion batteries, J. Mater. Chem. A 7 (2019) 22884–22888. https://doi.org/10.1039/C9TA09233A.

[93] B.J. Kennedy, C.J. Howard, Y. Kubota, K. Kato, Phase transition behaviour in the A-site deficient perovskite oxide $La_{1/3}NbO_3$, Journal of Solid State Chemistry 177 (2004) 4552–4556. https://doi.org/10.1016/j.jssc.2004.08.047.

[94] Z. Yang, R.E. Ward, N. Tanibata, H. Takeda, M. Nakayama, T. Asaka, Arrangement in $La_{1/3}NbO_3$ Obtained by First-Principles Density Functional Theory with Cluster Expansion and Monte Carlo Simulation, J. Phys. Chem. C 124 (2020) 9746–9754. https://doi.org/10.1021/acs.jpcc.0c01350.

[95] G. Liang, L. Yang, X. Xiong, X. Liu, X. Zhang, R. Che, High-rate electrochemical lithium-ion storage through Li^+ intercalation pseudocapacitance in the $Pr_{1/3}NbO_3$ anode, J. Mater. Chem. A 10 (2022) 23675–23682. https://doi.org/10.1039/D2TA03741F.

[96] G. Liang, L. Yang, X. Xiong, K. Pei, X. Zhao, C. Wang, W. You, X. Liu, X. Zhang, R. Che, Interfacial Space Charge Enhanced Sodium Storage in a Zero-Strain Cerium Niobite Perovskite Anode, Adv Funct Materials 32 (2022) 2206129. https://doi.org/10.1002/adfm.202206129.

[97] A.R.H.F. Ettema, C. Haas, An X-ray photoemission spectroscopy study of interlayer charge transfer in some misfit layer compounds, J. Phys.: Condens. Matter 5 (1993) 3817–3826. https://doi.org/10.1088/0953-8984/5/23/008.

[98] M. Nakayama, K. Imaki, H. Ikuta, Y. Uchimoto, M. Wakihara, Electrochemical Lithium Insertion for Perovskite Oxides of $Li_yLa_{(1-y)/3}NbO_3$ ($y = 0, 0.1, 0.25$), J. Phys. Chem. B 106 (2002) 6437–6441. https://doi.org/10.1021/jp0258659.

[99] M. Nakayama, H. Ikuta, Y. Uchimoto, M. Wakihara, Y. Terada, T. Miyanaga, I. Watanabe, Changes in Local Structure during Electrochemical Li Insertion into A-Site Deficient Perovskite Oxides, $La_{1/3}NbO_3$, J. Phys. Chem. B 107 (2003) 10715–10721. https://doi.org/10.1021/jp034262+.

[100] M. Nakayama, Y. Uchimoto, M. Wakihara, Investigation on cyclability in $Li_xLa_{1/3}NbO_3$ electrode material for rechargeable lithium ion battery, Journal of Power Sources 146 (2005) 674–677. https://doi.org/10.1016/j.jpowsour.2005.03.066.

[101] M. Nakayama, J. Shirakawa, M. Wakihara, Ab initio density functional study on changes in local structure in perovskite compound, $Li_xLa_{1/3}NbO_3$, Solid State Ionics 177 (2006) 1259–1266. https://doi.org/10.1016/j.ssi.2006.06.028.

[102] X. Xiong, L. Yang, G. Liang, C. Wang, G. Chen, Z. Yang, R. Che, A Low Strain A-Site Deficient Perovskite Lithium Lanthanum Niobate Anode for Superior Li^+ Storage, Adv Funct Materials 32 (2022) 2106911. https://doi.org/10.1002/adfm.202106911.

[103] E. Le Calvez, J.C. Espinosa-Angeles, G.J. Whang, N. Dupré, B.S. Dunn, O. Crosnier, T. Brousse, Investigating the Perovskite $Ag_{1-3x}La_xNbO_3$ as a High-Rate Negative Electrode for Li-Ion Batteries, Front. Chem. 10 (2022) 873783. https://doi.org/10.3389/fchem.2022.873783.

[104] M.W. Barsoum, The $M_{n+1}AX_n$ phases: A new class of solids, Progress in Solid State Chemistry 28 (2000) 201–281. https://doi.org/10.1016/S0079-6786(00)00006-6.

[105] M.W. Barsoum, MAX phases: properties of machinable ternary carbides and nitrides, Wiley-VCH Verlag GmbH & Co. KGaA, Weinheim, Germany, 2013.

[106] J.-P. Palmquist, S. Li, P.O.Å. Persson, J. Emmerlich, O. Wilhelmsson, H. Högberg, M.I. Katsnelson, B. Johansson, R. Ahuja, O. Eriksson, L. Hultman, U. Jansson, $M_{n+1}AX_n$ phases in the Ti−Si−C system studied by thin-film synthesis and *ab initio* calculations, Phys. Rev. B 70 (2004) 165401. https://doi.org/10.1103/PhysRevB.70.165401.

[107] M. Sokol, V. Natu, S. Kota, M.W. Barsoum, On the Chemical Diversity of the MAX Phases, Trends in Chemistry 1 (2019) 210–223. https://doi.org/10.1016/j.trechm.2019.02.016.

[108] H. Rohde, H. Kudielka, Strukturuntersuchungen an Carbosulfiden von Titan und Zirkon, Zeitschrift Für Kristallographie - Crystalline Materials 114 (1960) 447–456. https://doi.org/10.1524/zkri.1960.114.16.447.

[109] W. Jeitschko, H. Nowotny, F. Benesovsky, Die H-Phasen Ti_2TlC, Ti_2PbC, Nb_2InC, Nb_2SnC and Ta_2GaC, Monatshefte for Chemie 95 (1964) 431–435. https://doi.org/10.1007/BF00901306.

[110] W. Jeitschko, H. Nowotny, F. Benesovsky, Die H-Phasen: Ti_2CdC, Ti_2GaC, Ti_2GaN, Ti_2InN, Zr_2InN and Nb_2GaC, Monatshefte for Chemie 95 (1964) 178–179. https://doi.org/10.1007/BF00909264.

[111] M.W. Barsoum, T. El-Raghy, Synthesis and Characterization of a Remarkable Ceramic: Ti_3SiC_2, Journal of the American Ceramic Society 79 (1996) 1953–1956. https://doi.org/10.1111/j.1151-2916.1996.tb08018.x.

[112] M. Naguib, M. Kurtoglu, V. Presser, J. Lu, J. Niu, M. Heon, L. Hultman, Y. Gogotsi, M.W. Barsoum, Two-Dimensional Nanocrystals Produced by Exfoliation of Ti_3AlC_2, Advanced Materials 23 (2011) 4248–4253. https://doi.org/10.1002/adma.201102306.

[113] M.A. Pietzka, J.C. Schuster, Summary of constitutional data on the Aluminum-Carbon-Titanium system, JPE 15 (1994) 392–400. https://doi.org/10.1007/BF02647559.

[114] X.H. Wang, Y.C. Zhou, Layered Machinable and Electrically Conductive Ti_2AlC and Ti_3AlC_2 Ceramics: a Review, Journal of Materials Science & Technology 26 (2010) 385–416. https://doi.org/10.1016/S1005-0302(10)60064-3.

[115] N.V. Tzenov, M.W. Barsoum, Synthesis and Characterization of Ti_3AlC_2, Journal of the American Ceramic Society 83 (2000) 825–832. https://doi.org/10.1111/j.1151-2916.2000.tb01281.x.

[116] X. Wang, Y. Zhou, Solid–liquid reaction synthesis of layered machinable Ti_3AlC_2 ceramic, J. Mater. Chem. 12 (2002) 455–460. https://doi.org/10.1039/b108685e.

[117] Y. Zou, Z. Sun, H. Hashimoto, S. Tada, Synthesis of high-purity polycrystalline Ti_3AlC_2 through pulse discharge sintering Ti/Al/TiC powders, Journal of Alloys and Compounds 456 (2008) 456–460. https://doi.org/10.1016/j.jallcom.2007.02.105.

[118] X. Lu, Y. Zhou, Pressureless Sintering and Properties of Ti_3AlC_2, Int J Applied Ceramic Tech 7 (2010) 744–751. https://doi.org/10.1111/j.1744-7402.2009.02403.x.

[119] M. Yoshida, Y. Hoshiyama, J. Ommyoji, A. Yamaguchi, Reaction mechanism for the synthesis of Ti_3AlC_2 through an intermediate carbide of Ti_3AlC from elemental Ti, Al, and C powder mixture, J. Ceram. Soc. Japan 118 (2010) 37–42. https://doi.org/10.2109/jcersj2.118.37.

[120] C. Peng, C.-A. Wang, Y. Song, Y. Huang, A novel simple method to stably synthesize Ti_3AlC_2 powder with high purity, Materials Science and Engineering: A 428 (2006) 54–58. https://doi.org/10.1016/j.msea.2006.04.042.

[121] Z. Zhang, X. Duan, D. Jia, Y. Zhou, S. Van Der Zwaag, On the formation mechanisms and properties of MAX phases: A review, Journal of the European Ceramic Society 41 (2021) 3851–3878. https://doi.org/10.1016/j.jeurceramsoc.2021.02.002.

[122] J.P. Siebert, L. Bischoff, M. Lepple, A. Zintler, L. Molina-Luna, U. Wiedwald, C.S. Birkel, Sol–gel based synthesis and enhanced processability of MAX phase Cr_2GaC, J. Mater. Chem. C 7 (2019) 6034–6040. https://doi.org/10.1039/C9TC01416K.

[123] J.P. Siebert, K. Patarakun, C.S. Birkel, Mechanistic Insights into the Nonconventional Sol–Gel Synthesis of MAX Phase M_2GeC (M = V, Cr), Inorg. Chem. 61 (2022) 1603–1610. https://doi.org/10.1021/acs.inorgchem.1c03415.

Chapter 2: Synthesis and Li^+ storage in $AgNbO_3$, $Ag_{1-3x}La_x\square_{2x}NbO_3$ and $Ag_{1-x}\square_xNbO_{3-\delta}$ perovskites model system

2.1 Polyacrylamide synthesis of $Ag_{1-3x}La_x\square_{2x}NbO_3$ perovskites

The research work of this thesis begins with the development and optimization of polyacrylamide synthesis route (an advanced sol-gel method accompanied with polymerization) for these multicationic oxide materials. Model $Ag_{1-3x}La_x\square_{2x}NbO_3$ ($x \leq 0.20$) perovskites with artificial vacancies were previously synthesized in the group by solid state and sol-gel routes [1]. These materials were studied as negative electrodes and role of vacancies in enhanced Li^+ storage was concluded. The sol-gel synthesis method offers several key advantages over solid-state synthesis. The main advantages include low processing temperature, production of particles at nanoscale, better homogeneity in the final product through molecular-level mixing, and uniform morphology [2]. However, obtaining uniform stoichiometry and homogenous cation distribution with low agglomeration is the key challenge for sol-gel method when used for synthesis of multicationic oxides.

Polyacrylamide gel technique is a suitable synthesis method that can effectively tackle these challenges. It is quick, cost effective, reproducible, and have ability to produce high quality fine material at relatively low temperature [3]. The underlying reaction mechanism of polyacrylamide route for $Ag_{1-3x}La_x\square_{2x}NbO_3$ ($x = 0, 0.10, 0.20$) perovskites is as follows:

1. **Mixing of precursors:** At first step, metal precursors are mixed in a suitable solvent at room temperature. Choice of solvent depends on the solubility of precursors and solution is mixed until a transparent solution is obtained.
2. **Chelation reaction:** Citric acid (added to the solution in appropriate molar ratio) is used as a complexing agent. Citric acid ($C_6H_8O_7$) has carboxyl groups (-COOH) and hydroxyl group (-OH) attached to the central carbon atom, which are the primary sites for coordination with metal cations. Ag^+, with a +1 charge, typically forms simple complexes with one or two carboxylate groups. The bonding occurs through the oxygen atoms of the deprotonated carboxyl groups, which donate electron density to the Ag^+ ion. In contrast, highly charged Nb^{5+} cations form multiple bonds bridged with carboxylates and the hydroxyl groups from multiple citric acid molecules, resulting in a more extensive chelation

sphere to make stable metal-ligand complexes. In case of substitution, La^{3+} with a higher charge, forms more extensive coordination networks compared to Ag^{1+}, involving multiple carboxylate and hydroxyl groups.

3. **3D polymerization network:** Small amount of acrylamide (monomer system) is added to the solution, the monomer radicals are formed which open up the double bonds of acrylamide and provide a new activation site which leads to linking–up of second monomer unit and thus propagate the chain process by transfer of radicals. Polyacrylamide grows in a linearly chained system. However, N, N'–methylene bis-acrylamide is added in the system. It acts as cross-linker and it helps to grow and develop a complex network of interconnected loops. The solution is then heated to 90 °C while stirring and ammonium persulfate ($(NH_4)_2S_2O_8$) or hydrogen peroxide (30% w/w H_2O_2 in H_2O by Sigma Aldrich) are added to initiate the polymerization. The polymer network binds the ions in the solution and makes them evenly distributed in this space leading to a regular morphology and uniform distribution. Polymeric gel is formed after 20 min. The formation of 3D polymeric gel is presented in Figure 2.1.

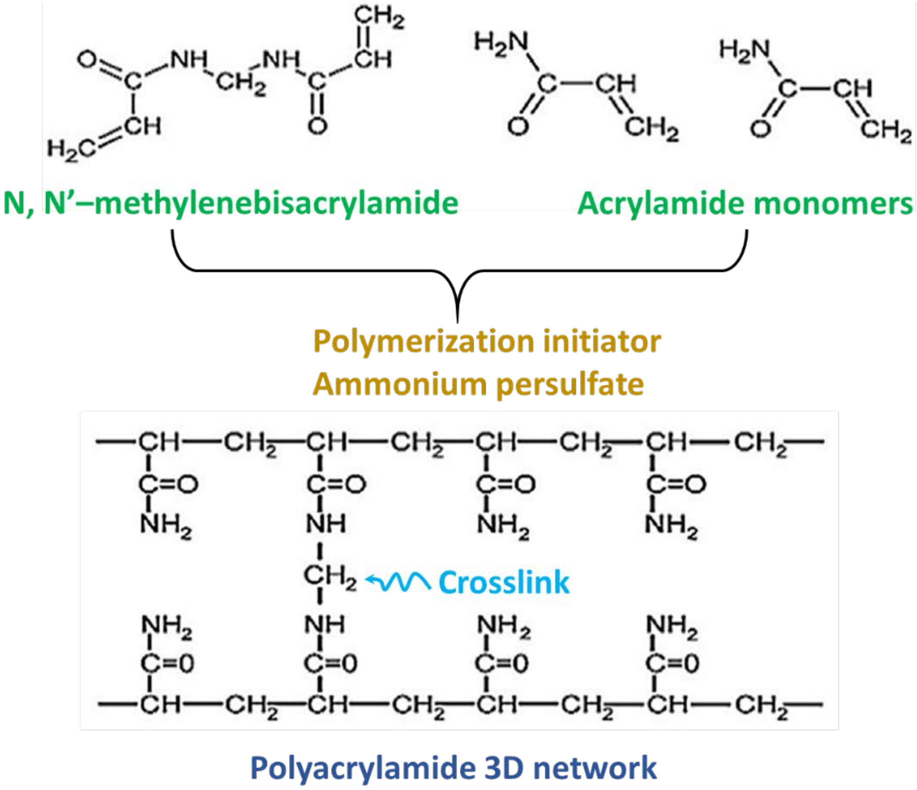

Figure 2.1. Illustration of 3D polymeric gel formation.

4. **Final product:** Wet polymeric gel is converted to xerogel when kept in oven at 200 - 300 °C. The final $Ag_{1-3x}La_x\square_{2x}NbO_3$ materials were obtained by grinding xerogel and annealing at 650 °C in air for 12 hrs.

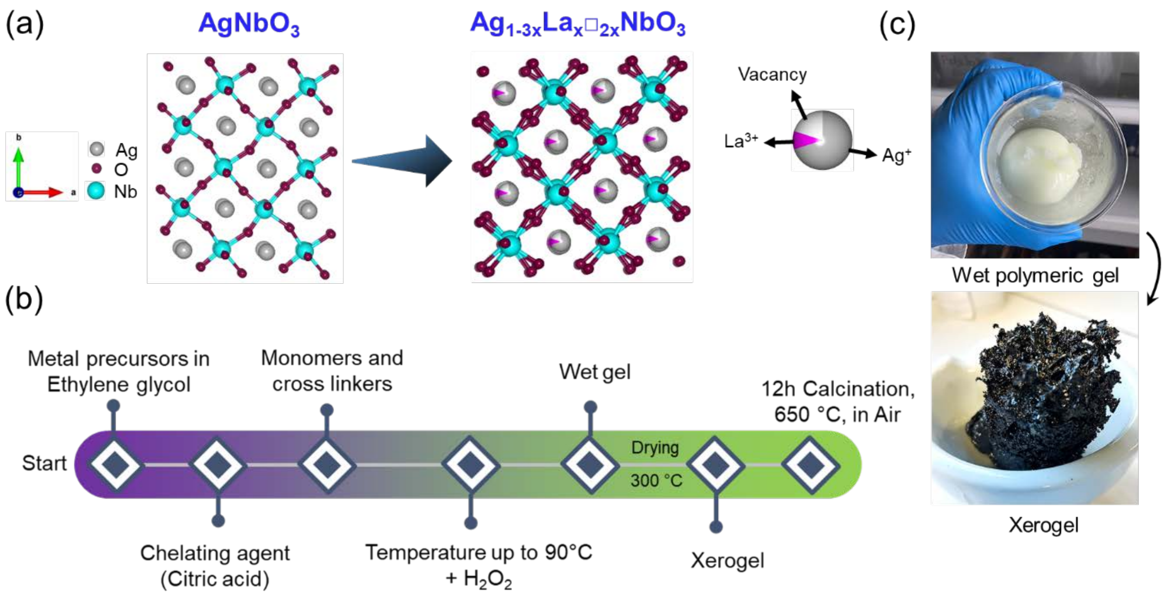

Figure 2.2. (a) Crystal structure of pristine $AgNbO_3$ and La-substituted $Ag_{1-3x}La_x\square_{2x}NbO_3$ materials showing the presence of vacancies at A-site. (b) Step by step polyacrylamide synthesis process. (c) Photographs of wet polymeric gel and dried xerogel.

The structure of $AgNbO_3$ and $Ag_{1-3x}La_x\square_{2x}NbO_3$ substituted materials are presented in Figure 2.2a, whereas synthesis process and photographs of wet polymeric gel and dried xerogel are shown in Figure 2.2b and c, respectively. Here, three samples at three different compositions were synthesized based on $Ag_{1-3x}La_x\square_{2x}NbO_3$ general formula at x = 0, 0.10, and 0.20.

2.2 Crystal structure and morphology

Rietveld refinement of the powder XRD pattern of $Ag_{1-3x}La_x\square_{2x}NbO_3$ perovskites prepared by polyacrylamide synthesis was performed to analyze the crystallographic structure. The $Ag_2Nb_4O_{11}$ phase is consistently present in all the patterns. Rietveld refinements were carried out to obtain the mass % of $Ag_{1-3x}La_x\square_{2x}NbO_3$ and $Ag_2Nb_4O_{11}$ phases (Figure 2.3a-c). Two structures of $Ag_2Nb_4O_{11}$ are reported in the literature. The first one crystallizes in Cc space group with cell parameters a = 10.764 Å, b = 6.200 Å, c = 12.858 Å, β = 106.183° and cell volume V = 824 $Å^3$ [4]. The second adopts the R3c space group with cell parameters a = 6.208 Å, c = 37.013 Å and cell volume V = 1235 $Å^3$ [5]. Preliminary Le Bail refinements considering Pbcm space group for the $Ag_{1-3x}La_x\square_{2x}NbO_3$ phase and Cc or R3c space group for the $Ag_2Nb_4O_{11}$ phase lead to a better systematic fit with Cc space group. Therefore, the Cc space group was chosen for the Rietveld refinements. Refinement of the cell parameters of the $AgNbO_3$ powder indicates a clear difference between a and b parameters, validating the use of orthorhombic space group. The obtained cell parameters and cell volume are very close to those reported in the literature [6]. The mass percentage of $Ag_2Nb_4O_{11}$ in the $AgNbO_3$ powder pattern is about 11%. The crystallite sizes of the $AgNbO_3$ and $Ag_2Nb_4O_{11}$ phases were determined to be about 76 nm and 102 nm, respectively. Further details of refinements of $AgNbO_3$ are presented in supplementary information of the related published paper in section 2.6.

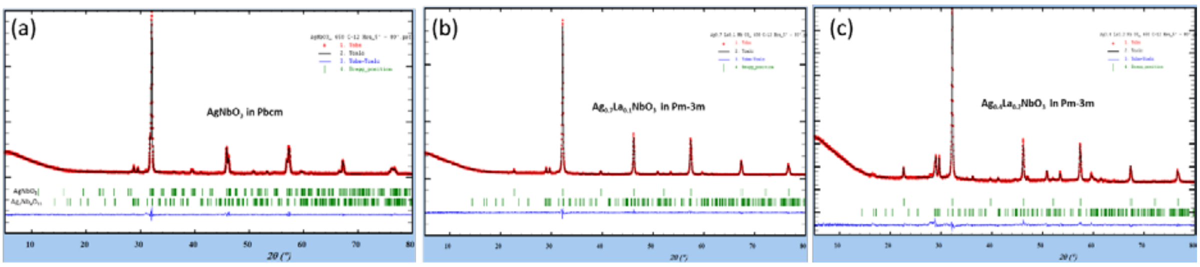

Figure 2.3. Rietveld refinements of powder XRD patterns of (a) $AgNbO_3$. (b) $Ag_{0.70}La_{0.10}\square_{0.20}NbO_3$. (c) $Ag_{0.40}La_{0.20}\square_{0.40}NbO_3$.

For substituted samples, in the Pbcm space group, it is noticed that the parameters a and b are very close to each other (a = 5.5524(2) Å and b = 5.56793(17) Å in $Ag_{0.70}La_{0.10}\square_{0.20}NbO_3$ and a = 5.5540(5) Å and b = 5.5646(5) Å in $Ag_{0.40}La_{0.20}\square_{0.40}NbO_3$). They are close enough to consider a cell with a = b. In this case, we can consider tetragonal or cubic space groups, which are more symmetric than the orthorhombic Pbcm space group. Therefore, Rietveld refinements were also performed in the P4/mbm and Pm-3m space groups. For $Ag_{0.70}La_{0.10}\square_{0.20}NbO_3$ and $Ag_{0.40}La_{0.20}\square_{0.40}NbO_3$, the cell parameters and the cell volume are very close to each other (for example, the cell volumes are 485.77(3) and 485.64(9) in Pbcm, 121.42(10) and 121.40(6) in P4/mbm, 60.7092(16) and 60.703(3) in Pm-3m). Substitution of Ag by La in these two compounds has minimal effect on the cell parameters and cell volume. However, it has some effects on the intensity of some peaks, for example (144) reflection at $2\theta = 22°$, whose intensity increases when x increases ($Ag_{0.70}La_{0.10}\square_{0.20}NbO_3$ pattern: $I_{22°}/I_{32°} = 1508/26777 = 5.6\%$, $Ag_{0.40}La_{0.20}\square_{0.40}NbO_3$ pattern: $I_{22°}/I_{32°} = 1853/15548 = 11.9\%$). It is likely due to enhanced scattering from specific lattice planes that are more sensitive to the local environment around Lanthanum cations. For the $Ag_{0.70}La_{0.10}\square_{0.20}NbO_3$ powder pattern, the mass percentage of $Ag_2Nb_4O_{11}$ is about 9%. However, a higher La substitution in $Ag_{0.40}La_{0.20}\square_{0.40}NbO_3$ further increases $Ag_2Nb_4O_{11}$ concentration with mass percentage increasing up to 38%. This analysis shows that the substitution of Ag by La stabilizes the structure in the more symmetric space group, i.e. Pm-3m. The crystallite sizes were determined for each refinement. For the

$Ag_{0.70}La_{0.10}\square_{0.20}NbO_3$ and $Ag_{0.40}La_{0.20}\square_{0.40}NbO_3$ powders, the crystallite size is quite similar between 70 and 80 nm. For the $Ag_2Nb_4O_{11}$ powder, the crystallite size is about 81-85 nm in the case of the $Ag_{0.70}La_{0.10}\square_{0.20}NbO_3$ powder pattern and smaller, about 65-68 nm, in the case of the $Ag_{0.40}La_{0.20}\square_{0.40}NbO_3$ powder pattern. The refinement details are presented in Table 2.1 and Table 2.2.

Table 2.1. Results of the Rietveld refinement of $Ag_{0.70}La_{0.10}\square_{0.20}NbO_3$ powder pattern.

	Pbcm	P4/mbm	Pm-3m
a (Å)	5.5524(2)	5.5583(19)	3.93021(6)
b (Å)	5.56793(17)	= a	= a
c (Å)	15.7130(6)	3.930(3)	= a
V (Å^3)	485.77(3)	121.42(10)	60.7084(16)
R(obs) % $Ag_{0.7}La_{0.1}NbO_3$	1.68	1.49	1.36
R(obs) % $Ag_2Nb_4O_{11}$	5.43	4.90	4.78
GOF	1.37	1.36	1.38
Rp %	2.84	2.81	2.83
wRp %	3.79	3.77	3.81
Mass% $Ag_{0.7}La_{0.1}NbO_3$ / $Ag_2Nb_4O_{11}$	90.71(11) / 9.29(11)	90.5(2) / 9.5(2)	90.5(2) / 9.5(2)
Crystallite size $Ag_{0.7}La_{0.1}NbO_3$ (nm)	80.9(8)	73.9(7)	71.7(5)
Crystallite size $Ag_2Nb_4O_{11}$ (nm)	81.9(5)	84.5(8)	85.8(8)

Table 2.2. Results of the Rietveld refinement of $Ag_{0.40}La_{0.20}\square_{0.20}NbO_3$ powder pattern.

	Pbcm	**P4/mbm**	**Pm-3m**
a (Å)	5.5540(5)	5.5586(11)	3.93011(12)
b (Å)	5.5646(5)	= a	= a
c (Å)	15.7135(19)	3.9291(16)	= a
V (Å^3)	485.64(9)	121.40(6)	60.703(3)
R(obs) % $Ag_{0.4}La_{0.2}NbO_3$	2.56	2.66	3.29
R(obs) % $Ag_2Nb_4O_{11}$	5.15	5.36	5.43
GOF	1.61	1.62	1.64
Rp %	3.17	3.20	3.25
wRp %	4.50	4.55	4.59
Mass% $Ag_{0.4}La_{0.2}NbO_3$ / $Ag_2Nb_4O_{11}$	61.9(4) / 38.1(5)	61.4(5) / 38.6(5)	61.3(4) / 38.7(4)
Crystallite size $Ag_{0.4}La_{0.2}NbO_3$ (nm)	79.8(9)	76.7(8)	70.9(7)
Crystallite size $Ag_2Nb_4O_{11}$ (nm)	65.9(7)	65.5(8)	68.2(8)

The morphology of $AgNbO_3$ by sol-gel synthesis and polyacrylamide synthesis are compared in Figure 2.4a and b. Sol-gel synthesis showed agglomerated nanomaterials with irregular shapes, while polyacrylamide synthesis resulted in well-defined shaped particles necked together with no particle agglomeration. Similarly, for highly substituted $Ag_{0.40}La_{0.20}\square_{0.40}NbO_3$ perovskites (involving more cations in desired stoichiometry), a clear difference of agglomeration-free uniform morphology is obtained as shown in Figure 2.4c and d.

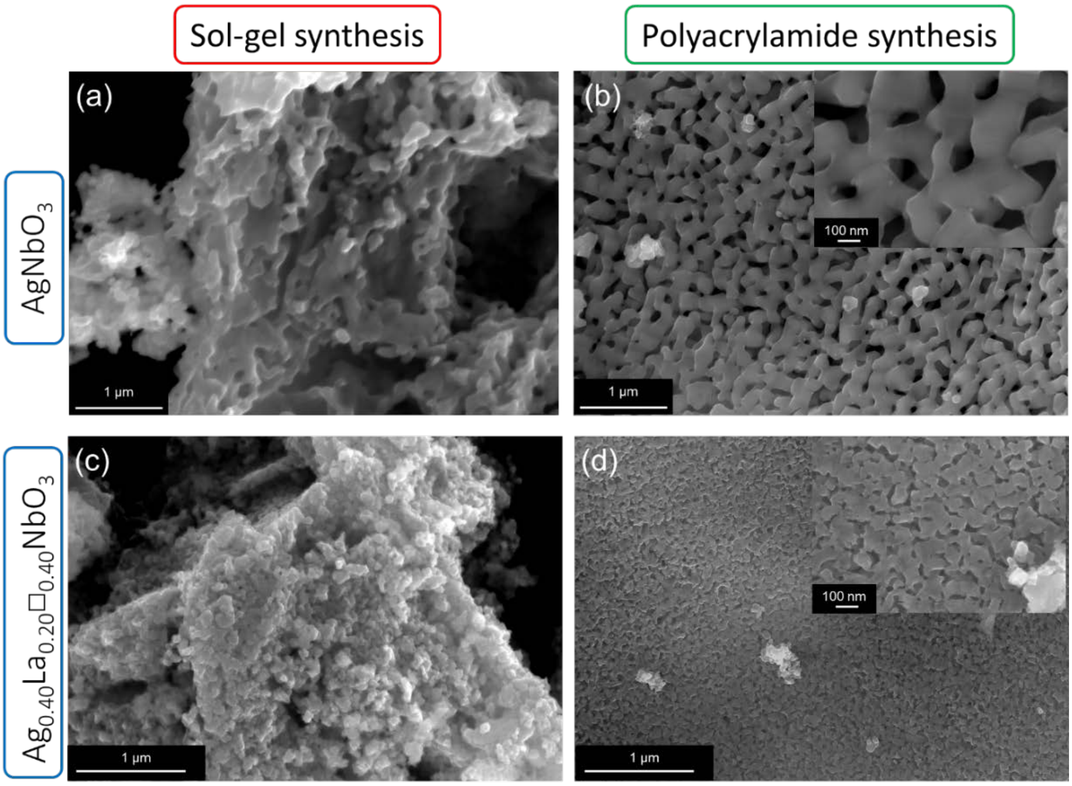

Figure 2.4. SEM images of pristine $AgNbO_3$ synthesized by (a) Sol-gel route. (b) Polyacrylamide route. SEM images of pristine $Ag_{0.40}La_{0.20}\square_{0.40}NbO_3$ synthesized by (c) Sol-gel route. (d) Polyacrylamide route.

2.3 Li^+ storage in $Ag_{1-3x}La_x\square_{2x}NbO_3$ perovskites under 1.2 – 3.0V potential window

In $Ag_{1-3x}La_x\square_{2x}NbO_3$, the substitution of each Ag^+ with La^{3+} cation results in the creation of two vacancies providing channels for Li^+ insertion in the structure at fast rates without affecting the crystal lattice. Figure 2.5a shows that by increasing the number of vacancies in the structure, the specific capacity increased and a maximum of 48 mAh.g^{-1} at 0.02 A.g^{-1} was achieved for highly substituted $Ag_{0.40}La_{0.20}\square_{0.40}NbO_3$ under a stable potential window of 1.2 – 3.0V vs Li^+/Li. The overall Li^+ storage performance of materials at current densities from 0.02 to 2.0 A.g^{-1} (corresponding to 2.5 h and 45 sec of discharge/charge, respectively) are presented in Figure 2.5b. A capacity retention of 57% and 52% at 2.0 A.g^{-1} (45 sec of charge time) was obtained for $Ag_{0.70}La_{0.10}\square_{0.20}NbO_3$ and $Ag_{0.40}La_{0.20}\square_{0.40}NbO_3$, respectively. Furthermore, *in-situ* XRD showed that no new peak appears (and/or disappears), and existing peaks do not move, which indicates a solid solution type storage mechanism without much structural modifications upon Li^+ insertion. Therefore, it corresponds to zero-strain characteristics of materials as shown in Figure 2.5c and d. Due to low structural changes, electrodes exhibit good cycling stability after 800 cycles at 2mV.s^{-1} (Figure 2.5e). These results are in agreement with previous investigation of these materials synthesized by sol-gel route [1].

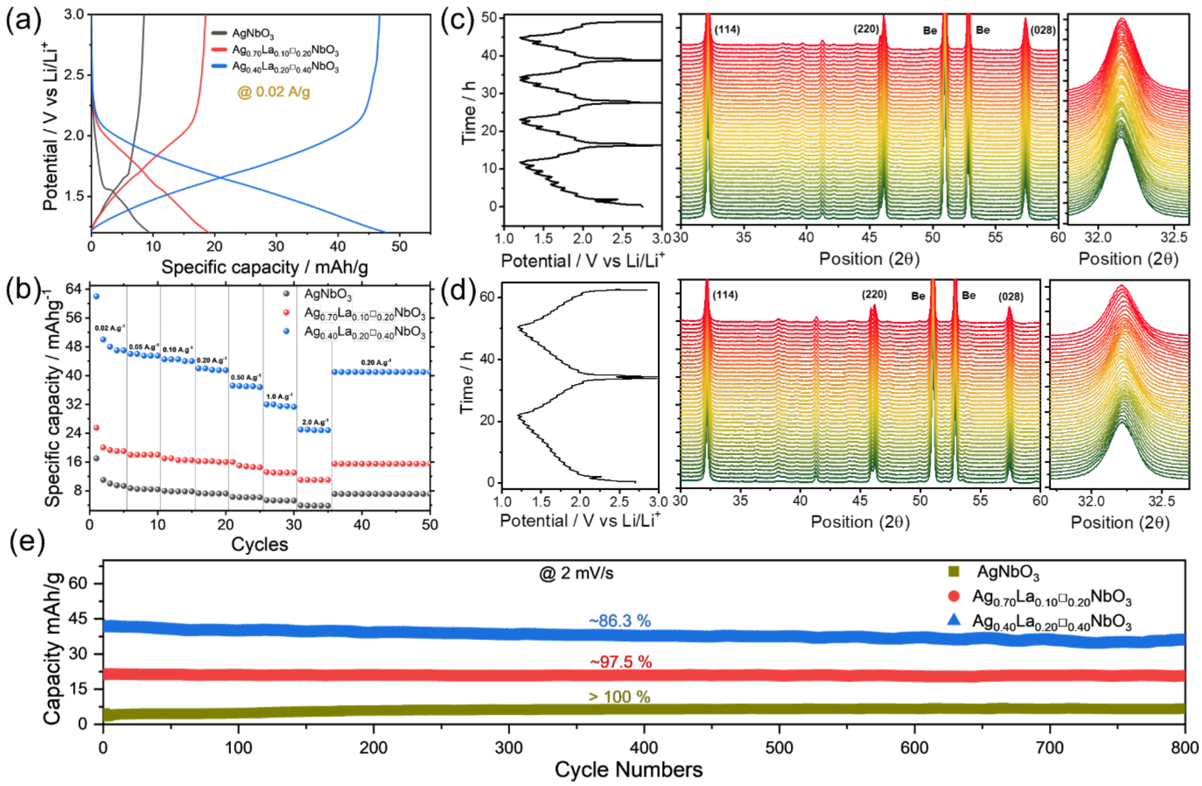

Figure 2.5. Ag$_{1-3x}$La$_x\square_{2x}$NbO$_3$ materials showing: (a) Charge/discharge curves at 0.02 A.g^{-1}. (b) Li$^+$ storage performance at different current densities. In situ XRD of substituted samples under 1.2 – 3.0 V vs Li$^+$/Li: (c) Ag$_{0.70}$La$_{0.10}\square_{0.20}$NbO$_3$ (d) Ag$_{0.40}$La$_{0.20}\square_{0.40}$NbO$_3$. (e) Cyclic stability of materials at 2 mV.s^{-1} for 800 cycles.

2.4 Li$^+$ storage in Ag$_{1-3x}$La$_x\square_{2x}$NbO$_3$ perovskites under extended potential windows

From the electrochemical point of view, the primary focus of this chapter is related to a detailed investigation of Li$^+$ storage in Ag$_{1-3x}$La$_x\square_{2x}$NbO$_3$ perovskites under extended potential windows (0.6 – 3.0V and 0.01 – 3.0V vs Li$^+$/Li). Electrochemical instability of Ag$_{1-3x}$La$_x\square_{2x}$NbO$_3$ perovskites was noticed at lower voltage cut-off potentials, where electrode material undergoes irreversible structural modifications during the first cycle, causing an enhanced and stable Li$^+$ storage in subsequent cycles. This interesting and unique activation process in these materials is studied in detail in the subsequent paragraphs.

Figure 2.6a-c shows the irreversible changes during first cycle of AgNbO$_3$, Ag$_{0.70}$La$_{0.10}\square_{0.20}$NbO$_3$ and Ag$_{0.40}$La$_{0.20}\square_{0.40}$NbO$_3$, respectively, under 0.6 – 3.0V potential window vs Li$^+$/Li. On the subsequent cycles, stable voltammograms are obtained, which indicates the reversible Li$^+$ storage in all the materials. The first cycle of AgNbO$_3$, Ag$_{0.70}$La$_{0.10}\square_{0.20}$NbO$_3$ and Ag$_{0.40}$La$_{0.20}\square_{0.40}$NbO$_3$ are compared in Figure 2.6d, where the irreversible effects are much pronounced for substituted samples. However, the zoomed inset of Figure 2.6d showed peaks in the range of 2.5 – 1.4V vs Li^+/Li, which are associated to impurity phases present in the materials. *Ex-situ* XRD were performed to track the structural changes during first cycle and results are presented in Figure 2.6e. Pristine $AgNbO_3$ preserved the global crystallinity with slightly reduced peak intensities and $Ag_2Nb_4O_{11}$ impurity removal (Figure 2.6f). However, substituted materials lose their crystallinity and no obvious peaks correspond to perovskite phase, indicating a structural collapse after reaching 0.6V cut-off potential. Regardless of these initial observations, it is interesting to check at firsthand (1) Li^+ storage capacity of the different materials compared to that measured using stable 1.2V cut-off potential (2) effect of irreversible structural transitions on rate performance and cyclic stability.

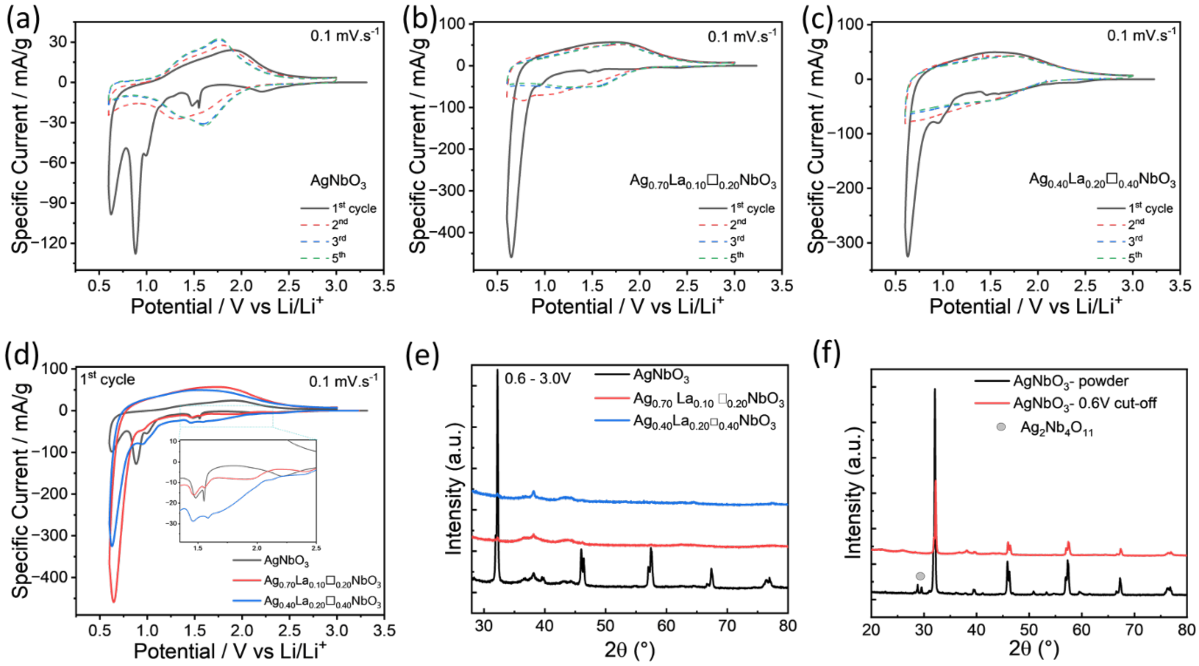

Figure 2.6. First five CV curves at 0.1 $mV.s^{-1}$ of (a) $AgNbO_3$. (b) $Ag_{0.70}La_{0.10}\square_{0.20}NbO_3$. (c) $Ag_{0.40}La_{0.20}\square_{0.40}NbO_3$. (d) First cycle comparison of all three samples. (e) Ex-situ XRD of samples after cycling at cut-off of 0.6V vs Li^+/Li.

The comparison of CV curves at 1.2V and 0.6V cut-off for $AgNbO_3$, $Ag_{0.70}La_{0.10}\square_{0.20}NbO_3$ and $Ag_{0.40}La_{0.20}\square_{0.40}NbO_3$ is presented in Figure 2.7a-c. At 0.6V cut-off, specific capacities of 74, 164 and 160 $mAh.g^{-1}$ were obtained at 0.1 $mV.s^{-1}$ for $AgNbO_3$, $Ag_{0.70}La_{0.10}\square_{0.20}NbO_3$ and $Ag_{0.40}La_{0.20}\square_{0.40}NbO_3$, respectively. In contrast, the maximum specific capacities at 1.2V cut-off were 12, 23, and 51 $mAh.g^{-1}$ for $AgNbO_3$, $Ag_{0.70}La_{0.10}\square_{0.20}NbO_3$ and $Ag_{0.40}La_{0.20}\square_{0.40}NbO_3$, respectively, under the same conditions. In addition, it is observed that the CV curves of substituted samples are much broadened than pristine sample, enabling them to deliver more capacity (Figure 2.7d). When cycled at higher scan rates (up to 50 $mV.s^{-1}$), $AgNbO_3$ retained highest specific capacity of 44% as shown in Figure 2.7e. $Ag_{0.70}La_{0.10}\square_{0.20}NbO_3$ and

$Ag_{0.40}La_{0.20}\square_{0.40}NbO_3$ delivered poor rate capability with capacity retention of 16% and 13%, respectively, at 50 mV.s^{-1}. This suggests that La-substituted samples possess large amount of A-site vacancies and an insufficient concentration of Ag cations at A-site to maintain the stability of perovskite framework, ultimately leading to a structure collapse. Consequently, this structural collapse results in a significant capacity decay in the substituted samples after 100 cycles, as shown in Figure 2.7f.

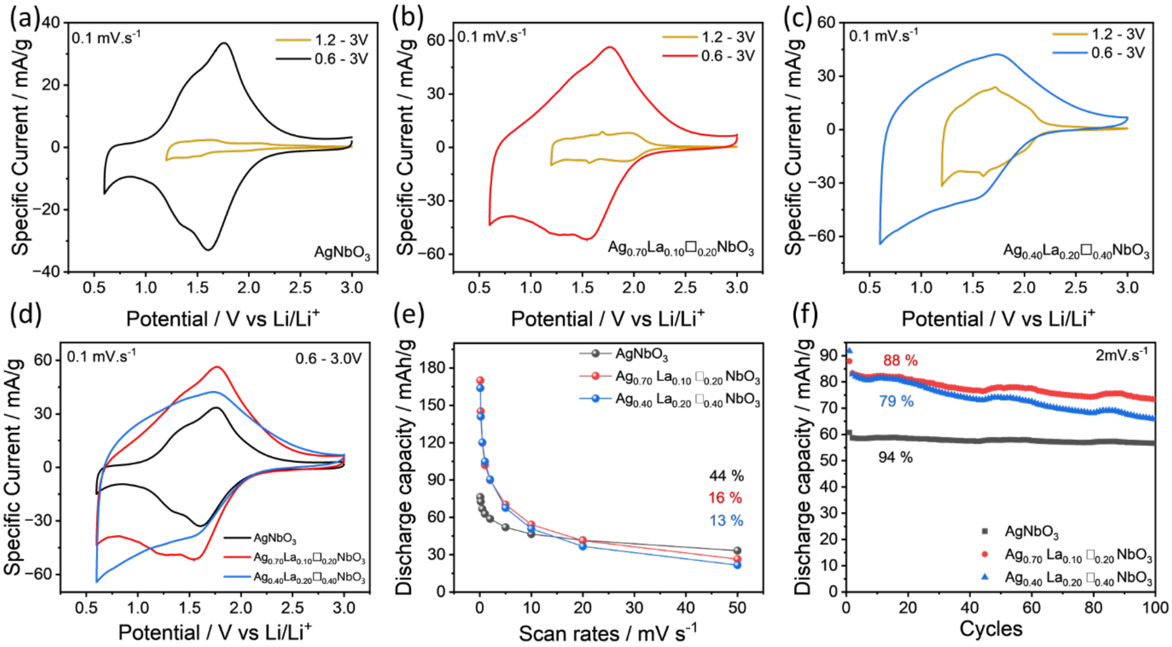

Figure 2.7. Comparison of CV curves at 1.2V and 0.6V cut-off potentials vs Li^+/Li (a) $AgNbO_3$. (b) $Ag_{0.70}La_{0.10}\square_{0.20}NbO_3$. (c) $Ag_{0.40}La_{0.20}\square_{0.40}NbO_3$. (d) CV curves of $AgNbO_3$, $Ag_{0.70}La_{0.10}\square_{0.20}NbO_3$, and $Ag_{0.40}La_{0.20}\square_{0.40}NbO_3$ at 0.6V cut-off. (e) Rate capability of $AgNbO_3$, $Ag_{0.70}La_{0.10}\square_{0.20}NbO_3$, and $Ag_{0.40}La_{0.20}\square_{0.40}NbO_3$ at 0.6V cut-off. (f) Cyclic stability of $AgNbO_3$, $Ag_{0.70}La_{0.10}\square_{0.20}NbO_3$, and $Ag_{0.40}La_{0.20}\square_{0.40}NbO_3$ at 0.6V cut-off for 100cycles.

These preliminary investigations provide a foundation for in-depth exploration of the intriguing electrochemical Li^+ storage activation behavior in pristine $AgNbO_3$ perovskite under extended potential windows. The results are detailed in our published paper entitled *"Lithium storage behaviour of $AgNbO_3$ perovskite: Understanding electrochemical activation and charge storage mechanisms", published in "Energy Storage Materials" 70 (2024): 103431*, presented in subsequent section.

2.5 Published paper

Here accepted version of published paper is presented. The open access published version of paper can be found on following link: https://doi.org/10.1016/j.ensm.2024.103431

The PDF version of paper is presented in annex at the end of the document.

Lithium storage behaviour of AgNbO$_3$ perovskite: Understanding electrochemical activation and charge storage mechanisms

Abbas Khan[1,2] $, Metin Orbay[3] $, Nicolas Dupré[1], Eric Gautron[1], Etienne Le Calvez[1,2], Andrea Balducci[3]*, Olivier Crosnier[1,2]*, Thierry Brousse[1,2]*

[1] *Nantes Université, CNRS, Institut des Matériaux de Nantes Jean Rouxel, IMN, F-44000 Nantes, France*

[2] *Réseau sur le Stockage Electrochimique de l'Energie (RS2E), CNRS FR 3459, 80039 Amiens, France*

[3] *Friedrich-Schiller-University Jena, Institute of Technical Chemistry and Environmental Chemistry and Center for Energy and Environmental Chemistry, Jena, Germany*

$ Equal Authors, Shared first authorship

* Corresponding Authors: Andrea Balducci (andrea.balducci@uni-jena.de) Thierry Brousse (Thierry.Brousse@univ-nantes.fr)

Graphical Abstract

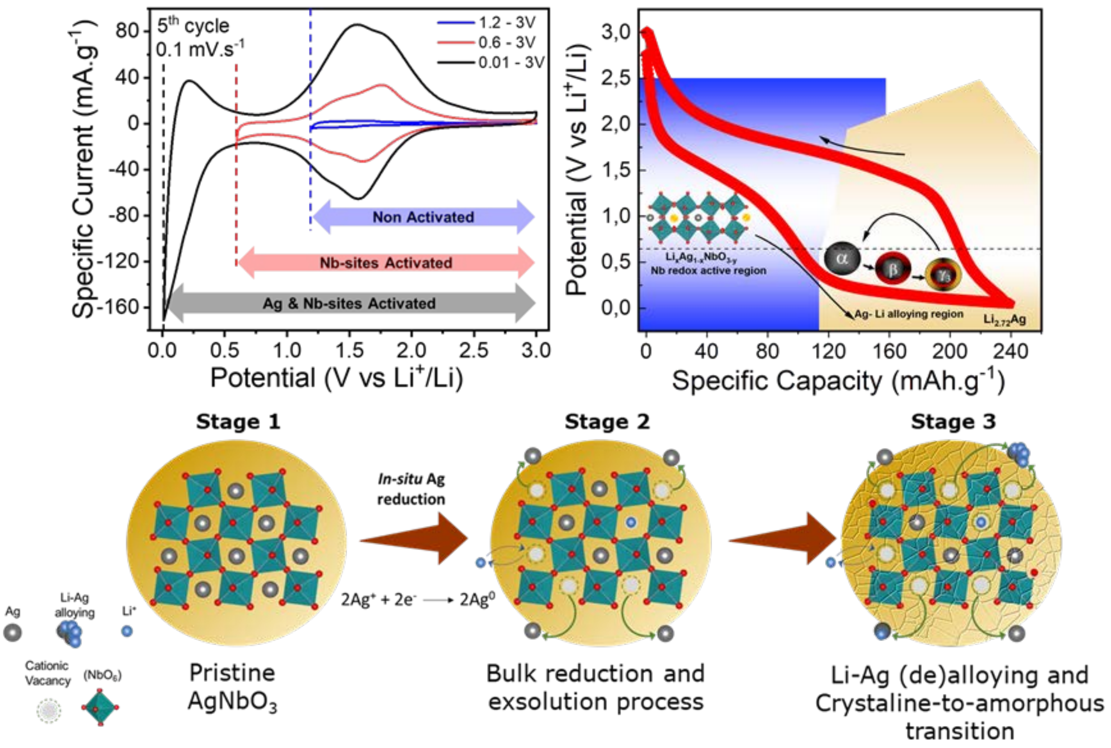

Abstract

In this study, a model AgNbO$_3$ perovskite is prepared via polyacrylamide synthesis technique, and the underlying unique Li$^+$ storage mechanism is studied. This structure is projected to provide low Li$^+$ storage capacity due to all occupied crystallographic sites. It delivered a specific capacity of 17 mAh.g^{-1} at 0.1A.g^{-1} within the potential range of 1.2-3.0V *vs.* Li$^+$/Li.

However, at lower potentials, the material undergoes activation for Li^+ storage by a multistep structural transition that included in-situ Ag-exsolution from the A-site of the lattice and an electrochemically induced crystalline-to-amorphous transition. At low potential the materials delivers high specific capacity (226 $mAh.g^{-1}$ at 0.1 $A.g^{-1}$ in 0.01-3V *vs.* Li^+/Li potential range) due to the contribution of improved Nb-redox activity and nanoscale Ag-Li (de)alloying mechanisms that were comprehensively examined utilizing advanced characterization tools. In addition, good capacity retention of 72 $mAh.g^{-1}$ at high current density of $2A.g^{-1}$ and an excellent cyclic stability with coulombic efficiencies above 99.9% are obtained for 2500 cycles at 1 $A.g^{-1}$ underlining the performance and the stability of $AgNbO_3$. This study introduces an alternative approach for tailoring electrode material using an electrochemically driven in-situ activation process. It also serves as a paradigm for the use of exsolved materials as negative electrodes in fast-charging batteries, paving the way for a better understanding of charge storage mechanisms in perovskites.

Introduction

With the successful commercialization of electric vehicles, the demand for energy storage devices is becoming increasingly critical [1]. Lithium-ion batteries (LIBs) are nowadays used in many applications, including several high-power applications. In these LIBs graphite is used as negative electrode material, and it is important to notice that despite the favorable feature of this type of anode, its use might not be an optimal choice when high current densities are applied [2]. As a matter of fact, the power performance of this material is rather different for the charge (intercalation) and the discharge (de-intercalation) process. It has been shown that during the discharge process graphite anodes retain well their capacity, but their performance during the charge process is strongly affected by the applied current [3]. Clearly, this represents a limitation associated to the use of this carbon electrode.

In the past years several alternative materials have been explored in literature. Among them, lithium titanium oxide ($Li_4Ti_5O_{12}$) has been one of the most widely investigated, and this anodic material is used as high-power alternative to graphite in commercial devices utilized for niche applications such as short-range buses but suffers from low energy density due to overall lower cell voltage [4]. Among other alternatives, niobium (Nb) containing oxides such as Nb_2O_5 and binary oxides L-Nb-O (where L is Ti, Fe, Zr, etc.), have gained an increasing attention in the last years. Anodes based on these materials display high specific capacity, originating from rich redox activity (Nb^{5+} to Nb^{4+}, Nb^{4+} to Nb^{3+}), fast charging capability, safety and excellent cyclic stability [5–8].

ABO_3 type perovskites such as $AgNbO_3$ are versatile materials because of their capacity to tolerate wide range of cation sizes, oxidation states, dopants and defects [9]. In this structure, A-site is filled by large radii cation in the center of perovskite cage with 12-fold coordination, and corner-shared BO_6 octahedral network giving a high packing factor [10]. The exploration of high voltage perovskite anodes [11] and exsolved perovskites for energy storage applications has shown promising results, yet the latter faces rapid capacity decline with cycling [12]. The challenge in utilizing ABO_3 type perovskites to their full potential lies in the difficulty of incorporating Li^+ ions into their structure due to limited interstitial sites and the constraint of fixed lattice spacing. Overcoming this obstacle is crucial for maximizing the energy storage capabilities of these materials.

One potential strategy to activate such materials is to partially substitute the A-site of the structure with cations at higher oxidation state to induce vacancies. Recently, it has been shown that this strategy can be successfully implemented through the substitution of Ag^+ cations by La^{3+}, leading to the creation of A-site vacancies in $Ag_{1-3x}La_x\square_{2x}NbO_3$ (with $x \leq 0.20$ and where $\square$ is a A-site vacancy) [13]. Moreover, the corresponding substituted materials have demonstrated fast Li^+ insertion and a dependence of the capacity with the number of created vacancies to a certain extent. Although the capacity of these materials is lower than that of other niobates such as T-Nb_2O_5, $CeNb_3O_9$, $Ti_2Nb_2O_9$, $TiNb_2O_7$, or $HTiNbO_5$ [14–18] the power capability of this compound made it of interest for further investigations.

An alternative appealing strategy which could be utilized to further improve the specific capacity of this type of material is the promotion of *in-situ* activation. Recently, it has been reported that *in-situ* amorphization can be an efficient way to generate defects by breaking the long-term crystal orders, hence enriching the Li^+ insertion sites to obtain enhanced specific capacity [19,20]. However, transitions from crystalline materials to amorphous ones are challenging to realize, especially in ABO_3 type perovskites (with ideal 1:1 cation ratio), due to strong structural stability and has rarely been achieved. It is also interesting to observe that ABO_3 type perovskites have received significant attention for realizing exsolution processes, a strategy to grow metallic nanoparticles from its host structure [21–24], especially for solid oxide fuel cells. The occurrence of this type of process could also be of interest in view of the use of ABO_3 type perovskites in LIBs.

In this study we report a detailed structural and electrochemical investigation on the storage mechanism occurring in a model ABO_3 type perovskite, namely $AgNbO_3$. The aim of this work is to evaluate whether it is possible to electrochemically promote, and possibly control, the occurrence of *in-situ* activation and exsolution processes in order to improve the capacity of $AgNbO_3$ based electrode as well as their behavior under high current density.

Experimental section

Material synthesis

$AgNbO_3$ perovskites were synthesized by polymerization assisted sol-gel route named polyacrylamide synthesis, which has been adopted previously for synthesis of transition metal oxides [25]. Stoichiometric amounts of silver nitrate ($AgNO_3$ by Alfa Aesar, 99.9%) and niobium oxalate hydrate ($C_{10}H_5NbO_{20}$. xH_2O by Alfa Aesar) precursors were dissolved in ethylene glycol (Alfa Aesar) and stirred at room temperature. Citric acid ($HOC(CH_2CO_2H)_2$ by Alfa Aesar, 99+%) was added to the solution in 1.5:1 cation molar ratio and stirred until transparent solution was obtained. Citric acid acted as a complexing agent of which carboxyl and hydroxyl groups were attached to Ag^+ and Nb^{5+}, respectively, through chelation reaction. Afterwards, acrylamide monomers (Alfa Aser) and N, N′-mesthylene-bisacrylamide (Alfa Aser) cross linkers were introduced to the solution in 9:1 cation molar ratio. The monomer radicals open up the double bonds of acrylamide and form a new activation site, which provides linkage to the second monomer unit and thus propagates the chain process by radical transfer process. Polyacrylamide grows in a linearly chained system. However, N, N' –methylene bisacrylamide acts as cross-linker and help to grow and develop a 3D network of interconnected loops. The solution was heated to 90 °C while stirring and hydrogen peroxide (30% w/w H_2O_2 in H_2O by Sigma Aldrich) was added to initiate the polymerization. Polymeric gel is formed after 20 min and converted to xerogel when kept in oven at 300 °C. The final $AgNbO_3$ materials were obtained by grounding xerogel and annealing at 650 °C in air for 12 hrs. The synthesis process is schematically illustrated in Fig. 1a.

Physical characterizations

Powder XRD measurements were carried out using PANalytical X'Pert Pro-diffractometer (Malvern PANalytical, Almelo, Netherlands). Cu-$K_{\alpha1}$-$K_{\alpha2}$ ($\lambda = 1.54060$ Å, 1.54443 Å) radiation source with acceleration voltage of 40 KV at a current 40 mA was used. XRD data were recorded in the 2θ range of 5° to 80°, scanning at a step size of 0.0170°. For *in-situ* XRD measurements, a specially designed Swagelok-type® cell with beryllium window on top was used [26]. The data were collected at different 2θ ranges between 20° and 80°. The applied current density, pattern acquisition and relaxation time varied depending on the selection of potential window for GCPL measurements. The BET specific surface area of the $AgNbO_3$

powder was calculated using N_2 adsorption–desorption isotherms at 77K with a Quantachrome Nova 4200e equipment (Anton Paar). The morphology study of $AgNbO_3$ powders and *post-mortem* analyses of cycled electrodes were performed by Zeiss MERLIN Instrument using in-Lens annular detector keeping an operating voltage of 20 kV. To prepare the samples, a small fraction of powder/electrode were affixed on carbon double tape. *Ex-situ* ^7Li and ^{93}Nb MAS NMR experiments were acquired on a Bruker Avance 500 spectrometer (B_0=11.75T), Larmor frequencies ν_0 (^{93}Nb = 122.41 MHz, ^7Li = 194.37 MHz) at RT. A Bruker MAS probe with a cylindrical 2.5 mm (o.d) zirconia rotor spun at a frequency of 25 kHz was used for spectral analyses. Spectra were obtained by applying a single pulse sequence, and a recycle delay (D_1) of 3 seconds ensuring the acquisition of quantitative spectra. The resulting integrated intensities were normalized with respect to the mass of the sample contained in the NMR rotor, the number of scans, and the receiver gain. Scanning/transmission electron microscopy (S/TEM) measurements were performed to characterize the morphological modification and Nb oxidation states of the pristine sample and after cycling (0.01V *vs.* Li+/Li). For both samples, the powder has been brought into contact with a holey carbon film-coated copper grid in a glove box (Ar atmosphere). The grid was inserted in an aberration-corrected S/TEM Themis Z G3 (Thermo Fisher Scientific) using an atmosphere-controlled sample holder. All S/TEM experiments were performed at 300 kV.

High-angle annular dark-field (HAADF-STEM) images were acquired with 21.4 mrad convergence angle and 63–200 mrad collection angles. A Super-X system (four energy-dispersive X-ray detectors) allowed to acquire elemental maps.

Electron energy loss spectroscopy (EELS) was performed with a GIF Quantum ERS 966 imaging filter (Gatan) in Dual-EELS mode (for simultaneous acquisition of low loss and high loss spectra) in STEM mode (21.4 mrad convergence angle and 36 mrad collection angle, probe current ~50 pA). The spectra presented here were integrated on spectral image areas. A power law was used to subtract the background before core edges.

Electrochemical measurements

Slurries containing 85% wt. active material ($AgNbO_3$), 10% wt. conducting agent (Imerys Super C65) and 5% wt. binder (Walocel sodium carboxymethyl cellulose CMC2000) were prepared and cast onto either copper or aluminum foil *via* doctor blading. $AgNbO_3$ electrode mass loadings ranged from 1.2 to 2.5 mg.cm^{-2}. For *in-situ* XRD, free standing electrodes were prepared by mixing $AgNbO_3$, conductive agent (Carbon Black by Superior Graphite, Chicago, IL, USA) and poly (1,1,2,2-tetrafluoroethylene (PTFE, Sigma Aldrich) in a %wt. of 75, 15, and

10, respectively. Few drops of ethanol were added, and the mixture was grounded until get homogenous paste. The paste was processed via cold-rolling until it became an electrode of around 5–10 mg.cm^{-2}. Propylene Carbonate (PC) anhydrous 99.7 % was purchased from Sigma Aldrich. Lithium bis(trifluoromethanesulfonyl)imide (LITFSI) (99.9 %), lithium bis(fluorosulfonyl)imide (LIFSI) (99.9 %) and 1-Butyl-1-methylpyrrolidinium bis (trifluoromethanesulfonyl)imide (Pyr$_{1,4}$TFSI) were purchased from Solvionic and used to prepare the electrolytes at room temperature whereas LP30 (Solvionic) was used as is. Swagelok-type® cells were used to study the electrochemical performance of $AgNbO_3$ electrodes in a three-electrode cell setup. The working electrode (WE) was $AgNbO_3$, whereas the reference electrode (Ref) and the counter electrode (CE) was lithium metal. Biologic VMP-3 and MPG-200 potentiostats were used for all electrochemical studies. The total area of all electrodes was 1.13 cm^2. Diffusion coefficient of $AgNbO_3$ electrodes were measured using the galvanostatic intermittent titration technique (GITT), using a previously described protocol [27]. Cell assembly and electrolyte preparation were carried out in an argon-filled glovebox (O_2 and H_2O <1 ppm).

Results and Discussions

Crystal structure and characterizations of $AgNbO_3$

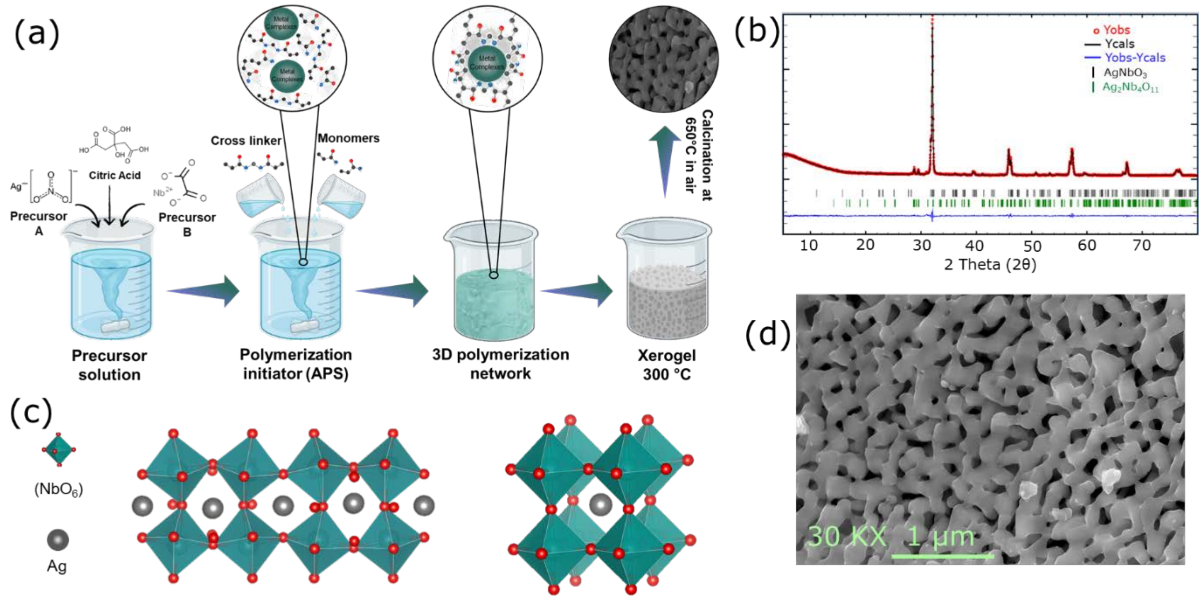

Figure 1. (a) Schematic illustration of polyacrylamide synthesis of $AgNbO_3$ perovskites. (b) Rietveld refined XRD profile of $AgNbO_3$ powder with experimental and calculated patterns, as well as the difference between the two patterns. Bragg reflection of the $AgNbO_3$ perovskite phase is denoted by black bars. $AgNbO_3$ crystalized in an orthorhombic perovskite phase (Pbcm space group with cell parameters a = 5.5485(16) Å, b = 5.6001(14) Å, and c = 15.6475(4) Å). Few impurities (mass percentage of ~11%) with main diffraction peaks around 29° corresponds to $Ag_2Nb_4O_{11}$ phase denoted by green bars. (c) Top and 3D view of crystal structure of $AgNbO_3$ based on refinement results. (d) SEM image of material showing well-defined and uniform morphology of $AgNbO_3$.

An overview of the synthesis of $AgNbO_3$ is presented in Fig.1a. Rietveld refinement of powder X-ray diffraction pattern revealed the formation of orthorhombic perovskite phase (Pbcm space group) with lattice parameters a = 5.54857(16) Å, b = 5.60010(14) Å, and c = 15.6475(4) Å (Fig. 1b). The cell parameters indicate a clear difference between the a and b parameters, validating the use of orthorhombic space group [28]. The perovskite structure of $AgNbO_3$ is built by Ag^+ cations in the center of the perovskite cage with a coordination number of 12 while Nb^{5+} with coordination number of 6 form corner-shared tilted $[NbO_6]$ octahedra as shown in Fig. 1c. The average crystallite size obtained is 76.8 nm, calculated by using Scherrer equation. The detailed Rietveld refinement results are presented in supplementary information (Table S1). Small impurity peaks (diffraction peak at 29°) of $Ag_2Nb_4O_{11}$ can be found in $AgNbO_3$ X-Ray diffraction pattern of the corresponding powder. The main reason of this is the thermodynamic instability of Ag^+ at higher temperatures (conversion to Ag^0 at 150°C), which is causing a phase formation competition between $AgNbO_3$ and $Ag_2Nb_4O_{11}$ [28,29]. Taking these results into account, it is evident that the realization of a single phased $AgNbO_3$ with uniform morphology via conventional solid-state reaction routes is rather challenging. Approaches such as keeping slight excess of Ag_2O precursor during synthesis or sintering in high-pressure O_2 environment has been reported to favor the homogeneity and improved phase quality of $AgNbO_3$ [29]. We recently reported the synthesis of $Ag_{1-3x}La_x\square_{2x}NbO_3$ (with $0 \leq x \leq 0.20$) perovskites by sol-gel method with fewer impurities [13]. However, to avoid particle agglomeration and to obtain a uniform morphology, polyacrylamide synthesis route was adopted for $AgNbO_3$ material [30]. The polymerization step during synthesis process helps to bind the metal complexes in solution with even distribution leading to the formation of interconnected porous network of particles with a uniform morphology, as shown in Fig. 1d. The BET surface area of the $AgNbO_3$ synthesized by polyacrylamide route was 6.7 m^2g^{-1}, which represents a twofold increase compared to materials synthesized by sol-gel method [13]. The electrochemical behavior of composite electrodes containing the synthesized $AgNbO_3$ was initially investigated in half-cell configuration (the details are reported in the experimental part). Preliminary measurements were performed in the potential range between 1.2 – 3.0V *vs.* Li^+/Li, which the electrochemical window mostly used to investigate electrodes containing Nb-based oxides [31]. Due to the 100% occupancy of the A site by Ag^+ cations in the $AgNbO_3$ structure, there are no open channels in the structure for Li^+ diffusion, nor well-defined empty sites to welcome them. Hence, no significant redox activity is observed in the CV within such potential window and the electrode displays a very limited specific capacity of 17 $mAh.g^{-1}$(Fig. 2a). This capacity mostly originated from surface charge storage processes rather than insertion of Li^+

into the structure. To confirm any structural changes in the material upon cycling, *in-situ* XRD experiments were carried out. The crystallographic peaks of perovskite structure do not deviate from their original positions, and no additional peaks appear upon charge/discharge processes, as shown in Fig. 2b. These results indicate that in the investigated potential range (1.2 – 3.0V *vs.* Li^+/Li) the electrode is displaying a stable structure containing Ag^+ and Nb^{5+}. It is interesting to notice, however, that a prolonged cycling process is leading to the formation of few nanoparticles on the surface (probably Ag^+ to Ag^0 conversion), although the morphology is retained. This latter point is well visible from the differences of the surface on *ex-situ* SEM observations reported in Fig. 2c and in Fig. 2d.

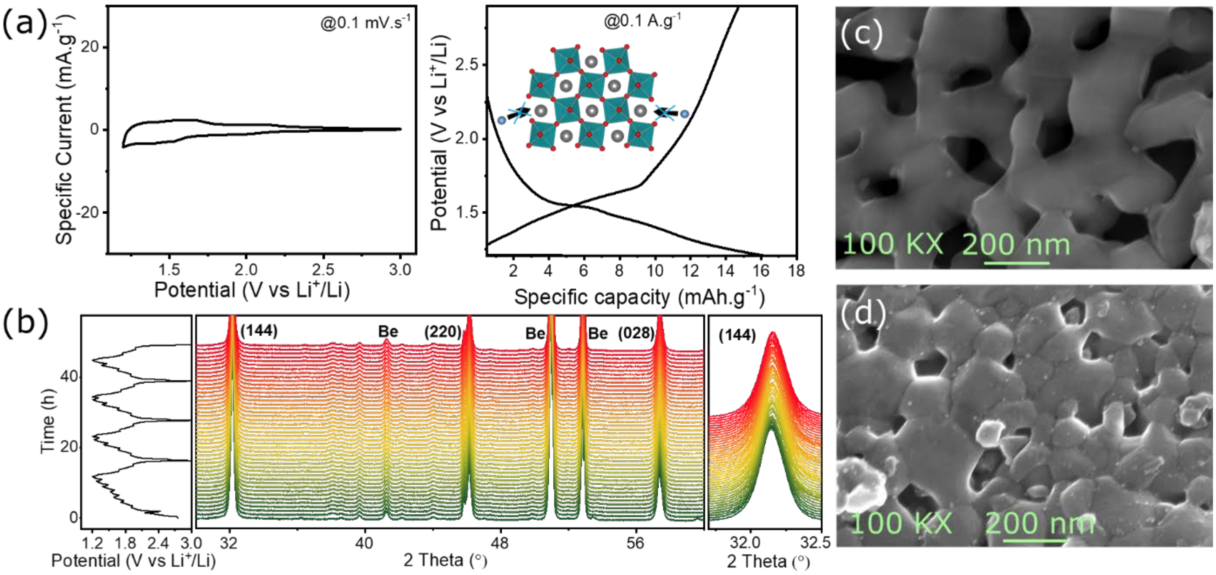

Figure 2. (a) Li^+ storage behavior of $AgNbO_3$ electrode in 1.2 – 3.0V potential window with Cyclic voltammetry and charge/discharge showing limited capacity. (b) In-situ XRD depicting no structural evolution and zero strain behavior upon cycling. SEM images of (c) Pristine electrode. (d) Cycled electrode showing morphology retention and surface Ag reduction (small white dots on the surface).

Ag reduction and exsolution process in $AgNbO_3$ crystal lattice

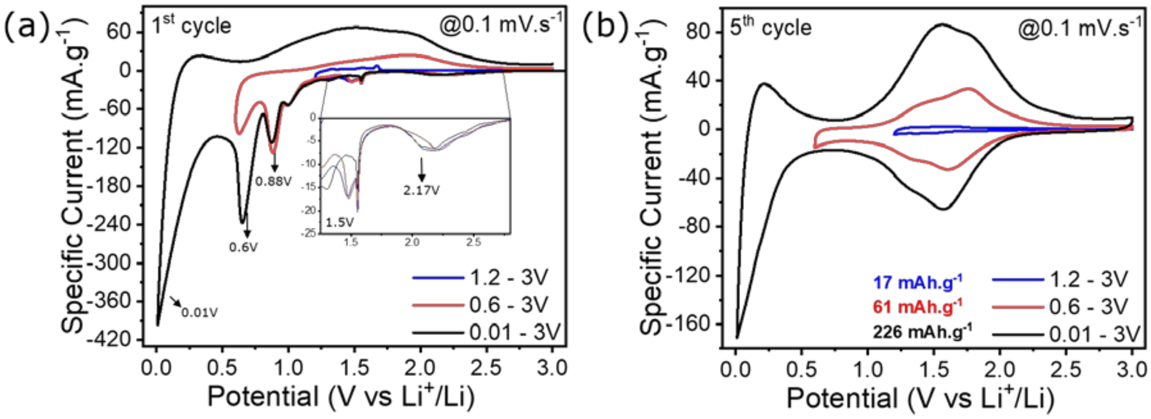

Figure 3. (a) 1st cycle of $AgNbO_3$ electrode in different potential windows using decreasing cut-off potential (1.2/0.6/0.01-3V vs. Li^+/Li) evidencing the activation region (0.6-0.9V) and emphasizing the appearance of irreversible activation peaks. (b) 5th cycle showing stable CV signature of the same electrodes after activation at 1.2,0.6 and 0.01V vs. Li^+/Li and related specific capacity values.

As mentioned in the introduction, the occurrence of *in-situ* activation as well as exsolution processes could positively contribute to the capacity of $AgNbO_3$-electrodes. Although similar process have been explored in the past for layered oxides by Morcrette [32] and Rozier *et al.*[33], where lithium-driven displacement process allows the growth and disappearance of copper dendrites, to the best of our knowledge, the possibility to induce/promote them electrochemically in ABO_3-type structures has not yet been considered for energy storage applications. With the aim to verify this possibility, the $AgNbO_3$-based electrodes were cycled in extended potential ranges compared to the one typically used for these materials (1.2 – 3.0V *vs.* Li^+/Li), namely from 0.6 – 3.0V *vs.* Li^+/Li and from 0.01 – 3.0V *vs.* Li^+/Li.

Fig. 3a depicts the first cycles of $AgNbO_3$ in these two potential windows and, for comparison, also in the “standard” one. The tests were carried out utilizing 1M lithium bis(fluorosulfonyl)imide (LiFSI) in propylene carbonate (PC) as the electrolyte. When the potential is stopped at 1.2V *vs.* Li^+/Li, the $AgNbO_3$-based electrode displays a weak reduction peak between 2.5-2V, which is identified as the initial reduction process of surface Ag^+ in $AgNbO_3$ and can be observed in SEM imaging as clustering is starting to appear (Fig. 2d). However, it is clear that the initial reduction of silver ions is not sufficient in terms of enhancement of storage capabilities and creation of relevant sites for Li^+ insertion in $AgNbO_3$, resulting in negligible reversible capacity value (17 $mAh.g^{-1}$).

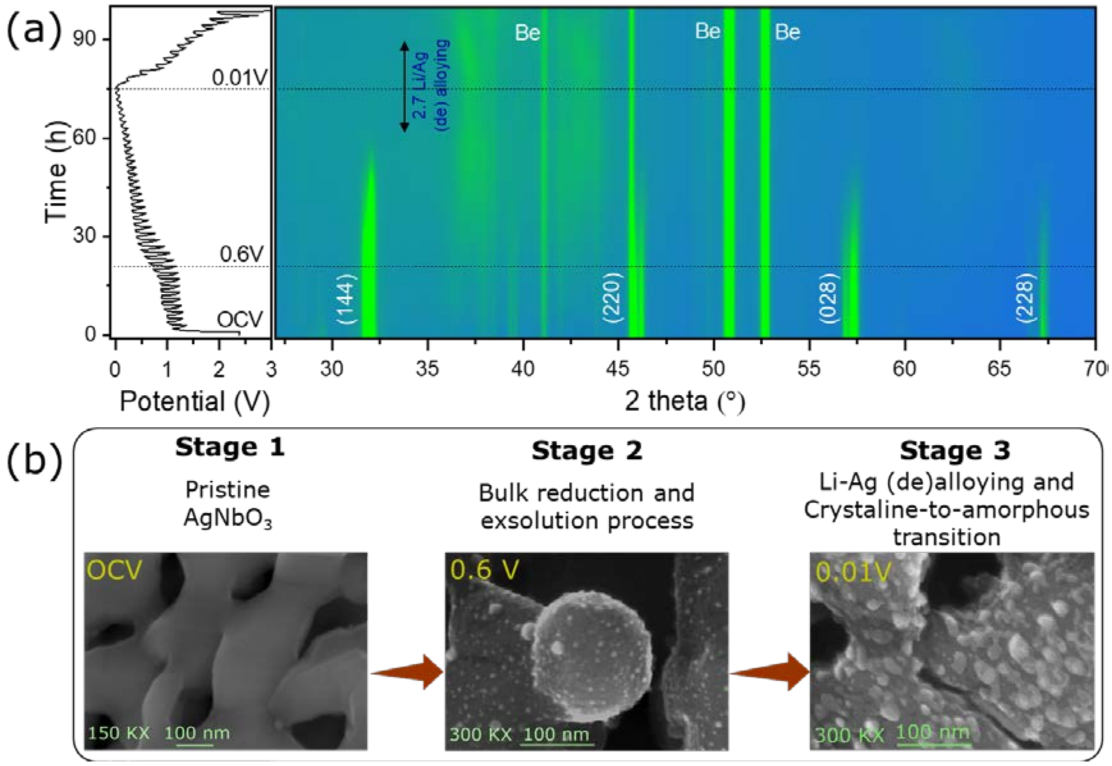

Figure 4. Li^+ storage mechanism investigation of $AgNbO_3$ electrode in 0.01 – 3.0V potential window. (a) In-situ XRD patterns of 1st charge/discharge cycles at 0.1 C. (b) Ex-situ SEM images of cycled electrode corresponding to different stages of material transition.

This value corresponds to 15% of the A-site accessible to Li^+ cations which is consistent with a partial reduction and exsolution of Ag^+ cations thus leaving empty A sites in the $AgNbO_3$ structure at the surface of the particles.

Lowering the electrodes cutoff potential to 0.6V *vs.* Li^+/Li resulted in the emergence of two consecutive peaks at 0.88V and 0.6V *vs.* Li^+/Li. These two peaks are also apparent when employing alternative electrolytes, some of which are known not to have SEI-forming capabilities (e.g., ionic liquid-based) (see figure S1 in SI). Therefore, it is reasonable to assume that they do not originate from interphase processes between electrode and electrolyte and/or decomposition processes on the latter, but rather come from structural processes occurring to $AgNbO_3$. Furthermore, at 0.6V *vs.* Li^+/Li, the electrochemical behavior of the electrodes changes considerably. Indeed, one can observe an enhancement of the reduction current at the same peak positions as depicted in the former 1.6-1.2V *vs.* Li^+/Li potential window (Fig. 3b), resulting in a much higher capacity (61 $mAh.g^{-1}$) (Fig. S2 & S3). *In-situ* XRD measurements, coupled with postmortem SEM and XRD (Fig. S4 & S5) indicate that the perovskite phase is preserved in the potential range between 0.6 – 3.0V *vs.* Li^+/Li. No new peaks were observed during cycling process which supports a solid solution-type mechanism occurring upon the charging process, as observed in the case of T-Nb_2O_5 [7]. Moreover, during the 1st lithiation cycle, XRD patterns above 1 V *vs.* Li^+/Li reveal the disappearance of peaks at around $2\theta = 29°$, corresponding to $Ag_2Nb_4O_{11}$ phase impurity. This suggests that a reductive potential serves as a stimulus for the impurity removal and phase purification. The mitigation of such impurities in $AgNbO_3$ perovskites has been reported previously through fine grinding process, because this impurity is typically localized within the surface layer, attributed to high-temperature melting/decomposition that initiates at the surface [34]. Furthermore, an irreversible decrease in intensity of all the crystallographic peaks is observed during 1st lithiation process (Fig. 4a) indicates that the perovskite structure is maintained at least down to 0.6V *vs.* Li^+/Li, while SEM imaging at this potential reveals an amplification of silver exsolution process at the surface of $AgNbO_3$ particles (Fig. 4b).

Alternatively, the exsolution of silver in $AgNbO_3$ can be obtained when the material is thermally reduced at 250 ˚C under Ar/H_2 atmosphere (Fig. S6a). However, thermal processes agglomerate silver particles into bulk-silver in comparison to the silver nanoparticles distribution obtained electrochemically (Fig. S6b). Metallic silver is detected by XRD (Fig. S6c) and concomitantly the pristine perovskite structure is still observed after thermal treatment. To summarize, decreasing the lower cut-off potential from 1.2 down to 0.6V *vs.*

Li^+/Li improves the capacity of the electrode while promoting the exsolution of nanosized silver particles.

Further advantage can be taken of this peculiar microstructure by decreasing the cut-off potential down to 0.01V *vs*. Li^+/Li. Indeed, when the $AgNbO_3$-based electrodes were cycled down to 0.01V *vs*. Li^+/Li their electrochemical behavior also changed significantly. As shown in Fig. 3a, the electrodes cycled in this potential range display a capacity of 226 $mAh.g^{-1}$, which is one order of magnitude higher than that displayed by the same electrodes when a cutoff voltage at 1.2V is applied and nearly quadrupled the capacity in comparison to 0.6V cut-off (it must be said that the contribution of the conducting agent to the observed capacity is negligible, S15). It is known that silver extrusion might destabilize the framework [35] and lead to structural failure and subsequent loss of capacity of the material. This is not the case for the investigated $AgNbO_3$-based electrode until the potential reaches 0.3V *vs*. Li^+/Li. Below 0.3V *vs*. Li^+/Li, and thus in the potential region considered in the test, the $AgNbO_3$ becomes amorphous with a clear loss of the diffraction peaks of the related phase (Fig. 4a). Moreover, the formation of Li-Ag alloy take place concomitantly [36,37]. However, the reversibility of this last process for bulk Ag particles is quite poor. $AgNbO_3$-based electrodes, on the contrary, display very high reversibility and stability (Fig. S2). This latter behavior might be related to the size of the Ag particles, which are only a few nm in diameter (Fig. S6b), and might improve the reversibility of the alloying reaction due to nanosizing effect [38].

The results discussed above indicate that the perovskite structure may intrinsically stabilize Nb and generate a wide operating window for lithium-ion intercalation into the $AgNbO_3$ host structure which exhibits a lot of vacancies once silver has been exsoluted.

A summary of all these processes can be depicted from *in-situ* XRD measurements performed in the potential window between 0.01 – 3.0V *vs*. Li^+/Li (Fig. 4a). During 1st lithiation, a gradual decrease in intensity of all the crystallographic peaks occurs, till their complete disappearance, thus indicating electrochemically induced crystalline-to-amorphous transition of $AgNbO_3$. Upon delithiation, the initial peaks are not reappearing, indicating that the amorphous phase is preserved. The Ag-exsolution process causes a deviation from the ideal $AgNbO_3$ (1:1 cation) stoichiometry to A-site deficient configuration. The SEM images of cycled electrode (0.01 – 3.0V *vs*. Li^+/Li) show the growth of enlarged Ag particles on the surface compared to what is observed at 0.6 and 3.0V (Fig. 4b). It is reasonable to assume that the surface exsoluted Ag can promote the formation of diffusion channels in the structure, allowing Li^+ to freely move in as the potential decreases. The removal of Ag^+ and subsequent insertion of Li^+ cations make possible the reversible reduction of Nb^{5+} that were previously inaccessible due to the presence of silver on all the A sites of the perovskite structure.

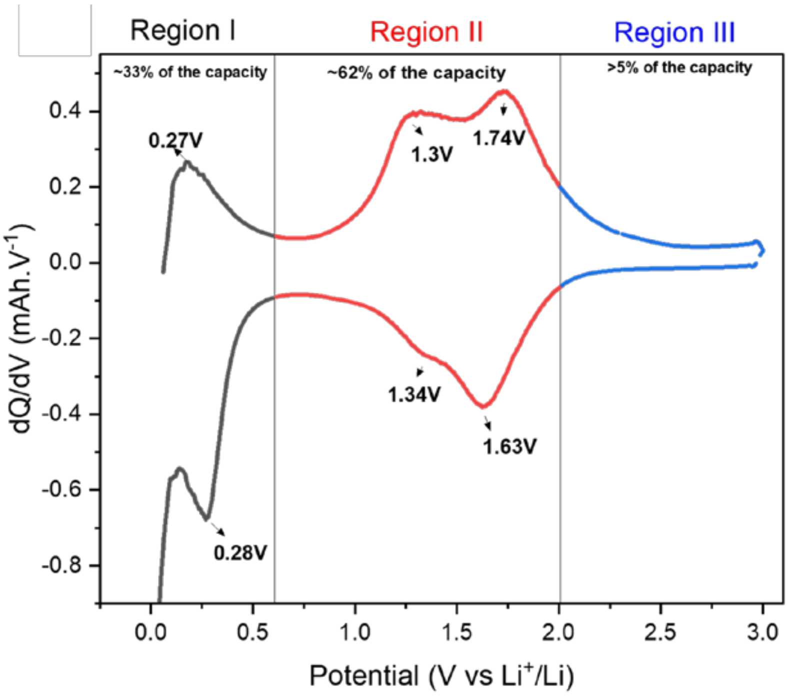

Figure 5. Differential capacity plot depicting 3 reversible redox peaks associated to region I and II respectively. Two redox peaks located at 1.74/1.63 V and 1.3/1.34 V vs. Li^+*/Li and single peak at 0.28 V/0.27 V vs.* Li^+*/Li could be attributed to the reduction of* Nb^{5+} *into* Nb^{3+} *as well as Li-Ag alloying reaction respectively.*

Further investigations of the $AgNbO_3$ electrode upon cycling were performed. Fig. 5 shows the variation of the differential capacity of $AgNbO_3$-based electrodes in the potential range between 0.01V-3V *vs.* Li^+/Li obtained from charge-discharge cycle (Fig. S7) carried out at a current density of 0.01A.g^{-1}. It is possible to identify three distinct regions, which are contributing to the total capacity of the electrode. In the potential range between 3-2V *vs.* Li^+/Li (Region III) a flat signal output is observed, indicating that no significant electrochemical process is occurring and, thus, that $AgNbO_3$ is inactive in this region. However, as the potential decreases, $AgNbO_3$ starts to exhibit prominent activity with two active redox peaks at 1.74/1.63V corresponding to Nb^{5+}/Nb^{4+} [39] and 1.3/1.34V indicating reduced Nb^{4+}/Nb^{3+} [40] are observed (Region II). To back up the above assertions, it is critical to describe the oxidation state of various elements using advanced characterization tools.

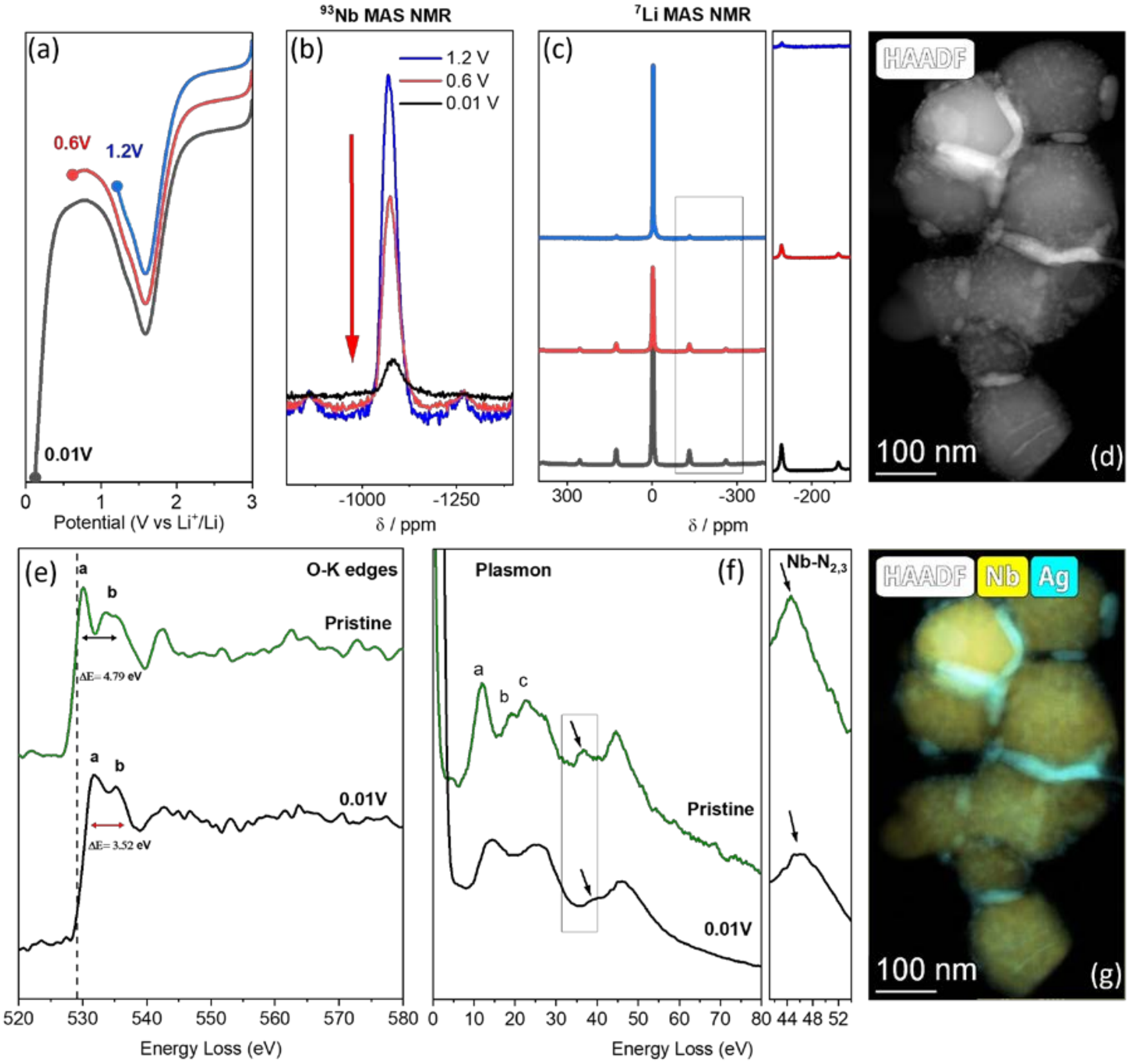

Figure 6. (a) cutoff potential for each of the associated ex-situ NMR mesurement. (b) ^{93}Niobium NMR at 1.2V (blue), 0.6V (red) and 0.01V (black) *vs.* Li^+/Li. (c) ^{7}Lithium NMR at 1.2,0.6 and 0.01V *vs.* Li^+/Li with zoom at 200 ppm. (d) and (g) HAADF-EDS mapping of $AgNbO_3$ electrode at 0.01V *vs.* Li^+/Li showing silver exsolution and contact between particles, as well as nanoclusters on its surface with homogeneous Niobium distribution in the particles. (e) EELS after background subtraction Fourier transformation showing the O-K edges of Pristine and Electrode at 0.01V *vs.* Li^+/Li. (f) plasmon region and Nb-$N_{2,3}$ edges.

Figure 6a depicts the cut-off potential for each mass normalized ^{93}Nb and ^{7}Li NMR spectra obtained from $AgNbO_3$-based electrodes during the first discharge and plotted consecutively in Figure 6b and c stopped at 1.2, 0,6 and 0.01V *vs.* Li^+/Li, respectively. Because of the diamagnetic state of Niobium (Nb^{5+}, d^0), NMR is a powerful technique for tracking niobium reduction in $AgNbO_3$, and any change in ^{93}Nb peak intensity can be correlated to the paramagnetic compounds of Nb^{3+} and Nb^{4+} (d^2 and d^1) that are not detectable by NMR, providing evidence of the change in Nb oxidation state in $AgNbO_3$-based electrodes during reduction. At 1.2V *vs.* Li^+/Li the ^{93}Nb NMR signal is clearly visible along with the corresponding sidebands which is an indication of presence of Nb^{5+} (Fig. 6b). At 0.6V, the same Nb signal is observed but the intensity is lower and suggests that some of the Nb^{5+} have been reduced along with Li^+ intercalation and thus became invisible to ^{93}Nb NMR. At 0.01V, the Nb^{5+} signal is still visible, but the signal is significantly reduced. It may indicate that the lithiation is not complete. Moreover, at 0.01V, the Nb signal appears to be broader with the beginning of a shoulder on the right side and a slight apparent shift of the maximum from -1070 to -1080 ppm. This can be an indication that the remaining Nb^{5+} are surrounded by reduced Nb^{4+} or Nb^{3+} that may provoke local distortions and modify the Nb^{5+} local environment. Fig. 6c shows^{7}Li NMR spectra at different potentials. At 1.2V *vs.* Li^+/Li, $AgNbO_3$-based electrodes display at least three resonances. Two sharp resonances at -3.3 and 0 ppm relate to Li species most likely originating from residual electrolyte/salt in our samples; these sharp signals do not match to intercalation compounds arising from Lithium-ion. However, at 0.6 and 0.01 V *vs.* Li^+/Li, there is a noticeable increase in a ^{7}Li NMR resonance signal which is consistent with the presence of Li^+ providing us an indication of intercalation into the active material.

Further investigations were then carried out using electron energy loss spectroscopy (EELS). Figure 6e shows O-K edges for $AgNbO_3$-based electrodes in pristine (Nb^{+5}) and electrodes cycled at 0.01V *vs.* Li^+/Li to highlight the potential difference in niobium oxidation state. First, O-K edge is characterized by a typical double-peak feature near the peak onset, which is characteristic of transition metal oxides [41]. This suggests that the investigated sample is not reduced to Nb^0, in agreement with the NMR results. Furthermore, in comparison to pristine $AgNbO_3$-based electrodes, a shift in peak onset as well as a peak intensity reduction between peak a and b, associated with the O-K edge of Nb at 0.01V *vs.* Li^+/Li, was observed. The energy difference ΔE between these two peaks was also reduced from 4.79eV for the pristine sample (Nb^{5+}) to 3.52eV in the electrode cycled at 0.01V *vs.* Li^+/Li. This behavior is comparable to that observed by Bach *et al.* and Tao *et al.* for niobium oxides and derivatives [42,43]. Furthermore, Nb-$N_{2,3}$ edges that appear in the low-loss region can be attributed to transitions of Nb 4p electrons to unoccupied 4d and 5s. This lead to a peak broadening with the appearance of a shoulder at around 44eV (Fig. 6f), which was also previously correlated to a decrease of Nb valence in niobium oxides [42,44]. These results indicate the occurrence of a shift in the oxidation state of Nb towards lower valence states. However, to determine the exact degree of oxidation is difficult. Nonetheless, the ΔE energy difference on the O-K edges in reduced $AgNbO_3$ electrode (ΔE=3.52eV) can be linearly associated with valence states of niobium oxides [42], suggesting an averaged out +3.66 oxidation state for Nb in the $AgNbO_3$-based electrode at 0.01V *vs.* Li^+/Li ($Nb^{+3.66}$) (Fig. S8) which is in agreement with the electrochemical results.

Finally, below 0.6V *vs.* Li^+/Li, a new reaction seems to take place. It leads to approximately 70 mAh.g^{-1} , which accounts for 2.72 lithium per silver atom, as depicted from Figure 5. According to previous studies on Li-Ag alloying [45] as well as to the Li-Ag binary diagram (Fig. S9), one can suspect that Ag-Li alloying reactions are taking place at such low potential region. In the lithium-silver binary diagram, 2.72 lithium per silver atom corresponds to the γ_3 phase with redox peaks at 0.28/0.27 V *vs.* Li^+/Li associated to Li-Ag alloying [36,46]. An indirect approach is adopted to confirm these results, where Ag-nanoparticles electrode were cycled vs. metallic Li keeping the same experimental conditions. The findings reveal a Li/Ag ratio of 2.61 in the alloying process, indicating that the system falls between the γ_3 and γ_2 phases (Fig. S9 & S10) in agreement with Ag-Li alloying obtained in $AgNbO_3$. Finally, HAADF-EDS imaging of $AgNbO_3$-based electrodes at 0.01V *vs.* Li^+/Li were carried out. As shown in Fig. 6d and g, the occurrence of silver extrusion in the cycled electrode compared to the pristine one (Fig. S11 and S12), takes place without affecting Niobium concentration in the material (Fig. 6g). Silver can be seen to percolate particles and grain boundaries but also cluster as nanoparticles at the surface (Fig. 6d and g), which could potentially play a substantial role in increasing the power capability of $AgNbO_3$-based electrodes by improving the electronic conductivity between the grains and further contributes to improved reversibility of electrochemical Ag-Li alloying reaction.

Moreover, According to [36,45,46] and [47,48], the theoretical capacity of $AgNbO_3$ (including a full reduction of Ag^+ to Ag^0 and Nb^{5+} to Nb^{3+}, and the formation of $Li_{2.72}Ag$ alloy) should reach 604 mAh.g^{-1}. The maximum capacity obtained upon the first reduction is 450 mAh.g^{-1}, thus suggesting only a partial reduction of Nb^{5+} to Nb^{3+}, and some Ag^0 particles not involved in alloying reaction with lithium. It can be noted that the maximum capacity for 12 wt% $Ag_2Nb_4O_{11}$ impurity leads to a contribution to the overall capacity of max. 24 mAh/g, i.e. 5% of the $AgNbO_3$ maximum capacity.

Considering the results discussed above, it appears that the $AgNbO_3$-based electrodes undergo a transition from pristine state (Fig. 7a, stage 1) to Ag-exsolution from A-site of the lattice (Stage 2), and finally to a crystalline-to-amorphous transition and concomitant Li-Ag alloying reaction (stage 3). Fig. 7b and c indicate what occurs to the $AgNbO_3$ electrode from a structural and electrochemical point of view. Undoubtfully, the silver exsolution process accounts for a major part to the reversibility of further reversible reactions.

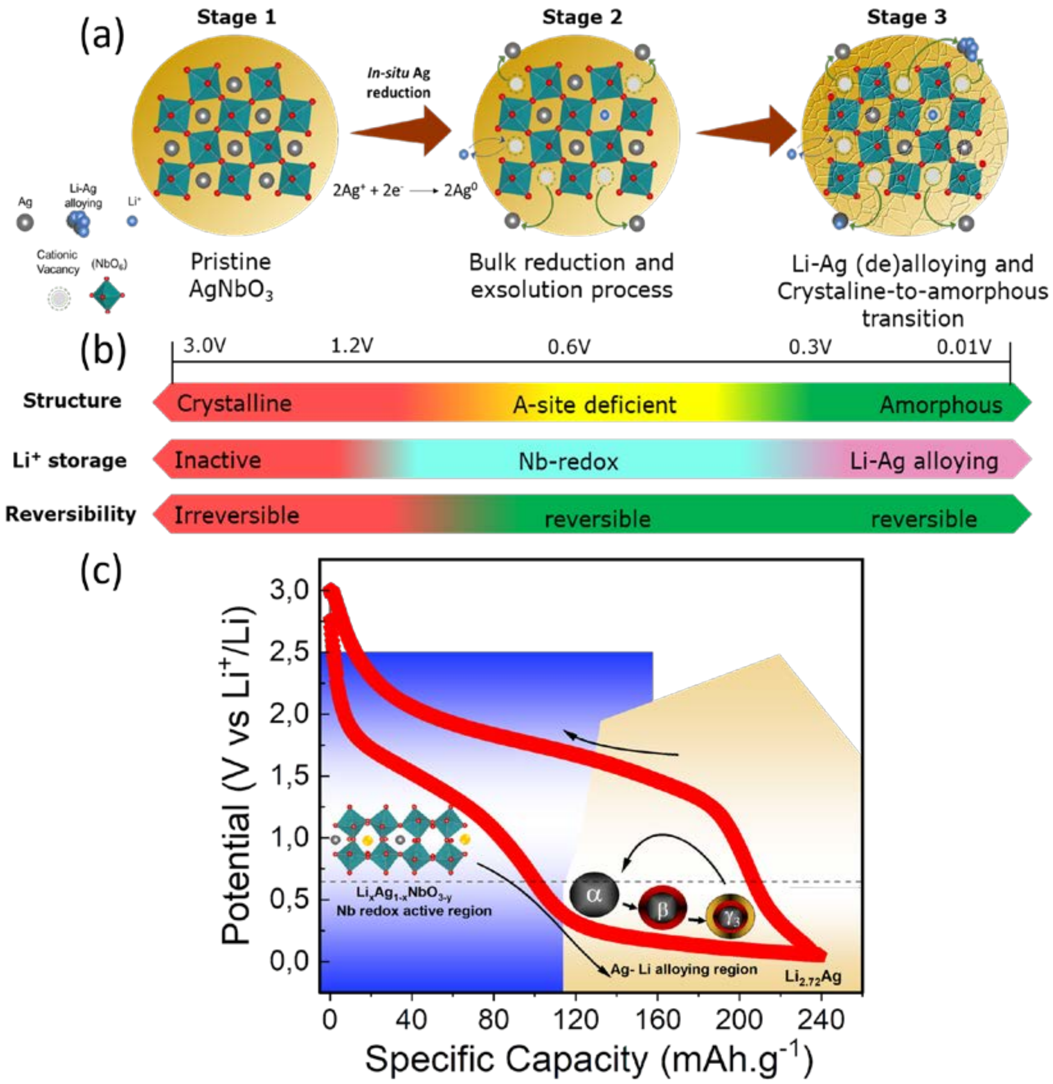

Figure 7. (a) Schematic representation of whole in-situ material transformation due to surface and bulk Ag reduction, exsolution of Ag nanoparticles, crystalline-to-amorphous transformation, and nanoscale Ag-Li alloying process. (b) Overall summary of material transition and Li$^+$ storage mechanisms involved in AgNbO$_3$ material. (c) AgNbO$_3$ specific capacity and its associated schematic redox activity and phase changes according to Li-Ag binary phase diagram at room temperature. As the potential decreases, Li-Ag alloying undergoes several phases transitions until γ_3 phase.

Electrochemical performance characterization

To understand the impact of the structural changes discussed above, the electrochemical performances of the AgNbO$_3$-based electrodes were investigated at various cutoff potentials. Fig. 8a shows the specific capacity of AgNbO$_3$-based electrode before and after activation with galvanostatic cycling at 1.2, 0.6, and 0.3 V *vs.* Li$^+$/Li, respectively. As shown, AgNbO$_3$-based electrodes achieve activation which allows a significant and permanent increase of their capacity. *e.g.*, from 14 mAh.g^{-1} at 0.3 V before activation to 55 mAh.g^{-1} at 0.3 V after activation. This activation behavior is seen to improve capacity continuously as the potential decreases up to 0.01V *vs.* Li$^+$/Li, in agreement with previous discussions regarding vacancies for lithium intercalation once silver has been exsoluted from the structure. To better understand the effect of activation on the power performance and diffusion kinetics of AgNbO$_3$, time-rate dependency was studied, where different current densities were applied at different cutoff potentials (Fig. 8b). From this study, it is obvious that the activation process is significantly enhancing the energy density of the $AgNbO_3$-based electrodes. Furthermore, discharge cycles can be carried out in less than 2 minutes while maintaining a capacity of 72 mAh.g^{-1}.

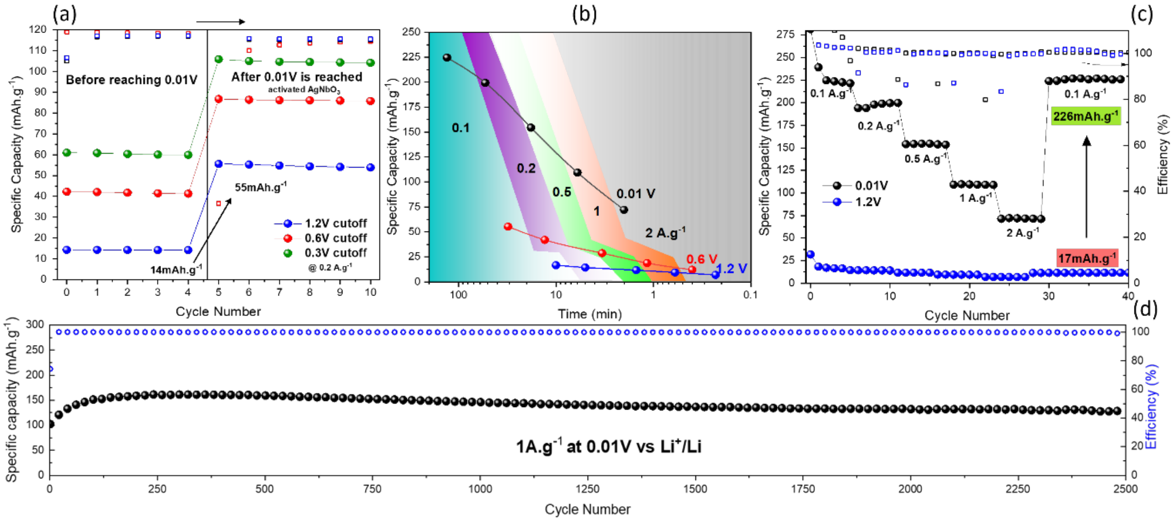

Figure 8 (a) specific capacity of $AgNbO_3$ electrode before activation (left) and after activation (right) at 0.2 A.g^{-1}. (b) Specific capacity versus discharge time for $AgNbO_3$ electrode at 1.2, 0.6, and 0.3 V vs. Li^+/Li. (c) rate test of $AgNbO_3$ at 0.01V (black) and 1.2V (blue) vs. Li^+/Li. The capacity has been multiplied by 13 for the same electrode at the same current density. (d) Stability test at 1 A.g^{-1} charge/discharge for 2500 cycles. These plots have been recorded after the initial cycles reported in Fig. 3.

The lithium diffusion coefficient calculated for the activated $AgNbO_3$ electrode from GITT measurements (Fig. S13) is in the order ~10^{-11}-10^{-12} cm^2 s^{-1}, which is a value comparable to the reported high-rate intercalation type anode materials [49,50]. Another important parameter to consider when studying high-rate anode materials is their stability under severe current load conditions. Fig. 8c depicts rate performance of $AgNbO_3$-based electrodes at 0.01V and 1.2V *vs.* Li^+/Li. As shown, the activated $AgNbO_3$-based electrodes display remarkable efficiency and fair rate performance, with capacities reaching 226 mAh.g^{-1}, 200 mAh.g^{-1}, 155 mAh.g^{-1}, 110 mAh.g^{-1} and 72 mAh.g^{-1} at 0.1 A.g^{-1}, 0.2 A.g^{-1}, 0.5 A.g^{-1}, 1 A.g^{-1}, and 2 A.g^{-1}, respectively. Moreover, when the current density is reduced again to 0.1 A.g^{-1}, the initial capacity is fully recovered, demonstrating the high reversibility and stability of the system to various current densities.

Finally, cycling stability of the $AgNbO_3$-based electrodes has been investigated carrying out charge-discharge cycles at 1A.g^{-1}. As shown in Fig. 8d, $AgNbO_3$-based electrodes display very high cycling efficiency (higher than 99,9%) as they go through activation, and they retain all their initial capacity after 2500 cycles. The good performance of the electrode is also maintained when is used in a proof-of-concept lab scale LIB cell (see figure S14). These results indicate that the investigated electrodes are a promising model electrode for high-power applications and pave the way for novel *exsoluted* and stable ABO_3-type electrodes for high-power lithium storage.

Conclusion

This work reported the preparation and investigation of perovskite type $AgNbO_3$ as a model material for negative electrode in LIBs. During 1st lithiation, a unique activation process is observed due to Ag-exsolution from A-site of structure causing A/B non-stoichiometry, which results in a compensation of Ag^+ by Li^+ cation intercalation to a certain extent. Structural transition between crystalline to amorphous oxide is observed below 0.3V *vs.* Li^+/Li. Lithium insertion is accompanied by Nb^{5+} reduction down to an average value of $Nb^{+3.66}$. Moreover, we have demonstrated the reversible Li-Ag nano (de)alloying charge storage mechanisms in this perovskite material at the end of the reduction process. Overall, $AgNbO_3$ delivered a specific capacity of 226 $mAh.g^{-1}$ in extended potential window (0.01 – 3.0V), which is thirteen-fold compared to the capacity of material in its electrochemically stable potential window (1.2 – 3.V) and 4 folds capacity in comparison to the Nb-electrochemically active (0.6-3V) region. Furthermore, the outstanding capabilities of such electrode in high-power conditions with a capacity retention of 72 $mAh.g^{-1}$ at $2A.g^{-1}$ and a very good cycling stability and efficiency at $1A.g^{-1}$ after 2500 cycles were demonstrated. This work opens the way for exploring the fascinating properties of exsolved ABO_3 type perovskites and provides a foundation for their utilization as design material for high power Lithium-ion intercalating perovskite anodes.

Acknowledgments

The authors wish to thank the Université de Nantes and Friedrich-Schiller University Jena for their financial support. Abbas Khan and Metin Orbay, as a part of the DESTINY PhD programme (Doctorate programme on Emerging battery Storage Technologies INspiring Young scientists) acknowledge funding from the European Union's Horizon 2020 research and innovation programme under the Marie Skłodowska-Curie Actions Cofund Grant Agreement No: 945357. Measurements which were performed on IMN's equipment(s) platform, PLASSMAT, Nantes, France. Funded by the French Contrat Plan Etat-Région and the European Regional Development Fund of Pays de la Loire, the CIMEN Electron Microscopy Center in Nantes, France, is greatly acknowledged. The authors are deeply thankful to Dr. Eric Quarez (from Institut des Matériaux de Nantes Jean Rouxel, IMN) for performing Rietveld refinements presented in this research paper.

References related to paper

[1] M. Armand, J.-M. Tarascon, Building better batteries, Nature 451 (2008) 652–657. https://doi.org/10.1038/451652a.

[2] B. Babu, P. Simon, A. Balducci, Fast Charging Materials for High Power Applications, Advanced Energy Materials 10 (2020) 2001128. https://doi.org/10.1002/aenm.202001128.

[3] M. Schroeder, S. Menne, J. Ségalini, D. Saurel, M. Casas-Cabanas, S. Passerini, M. Winter, A. Balducci, Considerations about the influence of the structural and electrochemical properties of carbonaceous materials on the behavior of lithium-ion capacitors, Journal of Power Sources 266 (2014) 250–258. https://doi.org/10.1016/j.jpowsour.2014.05.024.

[4] T.-F. Yi, S.-Y. Yang, Y. Xie, Recent advances of $Li_4Ti_5O_{12}$ as a promising next generation anode material for high power lithium-ion batteries, J. Mater. Chem. A 3 (2015) 5750–5777. https://doi.org/10.1039/C4TA06882C.

[5] T. Wang, T. Ge, S. Shi, M. Wu, G. Yang, Synthesis of wolframite $FeNbO_4$ nanorods as a novel anode material for improved lithium storage capability, Journal of Alloys and Compounds 740 (2018) 7–15. https://doi.org/10.1016/j.jallcom.2017.12.369.

[6] T. Takashima, T. Tojo, R. Inada, Y. Sakurai, Characterization of mixed titanium–niobium oxide $Ti_2Nb_{10}O_{29}$ annealed in vacuum as anode material for lithium-ion battery, Journal of Power Sources 276 (2015) 113–119. https://doi.org/10.1016/j.jpowsour.2014.11.109.

[7] J. Come, V. Augustyn, J.W. Kim, P. Rozier, P.-L. Taberna, P. Gogotsi, J.W. Long, B. Dunn, P. Simon, Electrochemical Kinetics of Nanostructured Nb_2O_5 Electrodes, J. Electrochem. Soc. 161 (2014) A718. https://doi.org/10.1149/2.040405jes.

[8] K.J. Griffith, Y. Harada, S. Egusa, R.M. Ribas, R.S. Monteiro, R.B. Von Dreele, A.K. Cheetham, R.J. Cava, C.P. Grey, J.B. Goodenough, Titanium Niobium Oxide: From Discovery to Application in Fast-Charging Lithium-Ion Batteries, Chem. Mater. 33 (2021) 4–18. https://doi.org/10.1021/acs.chemmater.0c02955.

[9] G.A. Samara, The relaxational properties of compositionally disordered ABO_3 perovskites, J. Phys.: Condens. Matter 15 (2003) R367. https://doi.org/10.1088/0953-8984/15/9/202.

[10] N. Ramadass, ABO_3-type oxides—Their structure and properties—A bird's eye view, Materials Science and Engineering 36 (1978) 231–239. https://doi.org/10.1016/0025-5416(78)90076-9.

[11] L. Zhang, X. Zhang, G. Tian, Q. Zhang, M. Knapp, H. Ehrenberg, G. Chen, Z. Shen, G. Yang, L. Gu, F. Du, Lithium lanthanum titanate perovskite as an anode for lithium ion batteries, Nat Commun 11 (2020) 3490. https://doi.org/10.1038/s41467-020-17233-1.

[12] A. Chaupatnaik, P. Barpanda, Perovskite lead-based oxide anodes for rechargeable batteries, Electrochemistry Communications 127 (2021) 107038. https://doi.org/10.1016/j.elecom.2021.107038.

[13] E. Le Calvez, J.C. Espinosa-Angeles, G.J. Whang, N. Dupré, B.S. Dunn, O. Crosnier, T. Brousse, Investigating the Perovskite $Ag_{1-3x}La_xNbO_3$ as a High-Rate Negative Electrode for Li-Ion Batteries, Front. Chem. 10 (2022) 873783. https://doi.org/orb.

[14] J.W. Kim, V. Augustyn, B. Dunn, The Effect of Crystallinity on the Rapid Pseudocapacitive Response of Nb_2O_5, Advanced Energy Materials 2 (2012) 141–148. https://doi.org/10.1002/aenm.201100494.

[15] L. Yang, X. Xiong, G. Liang, X. Li, C. Wang, W. You, X. Zhao, X. Liu, R. Che, Atomic Short-Range Order in a Cation-Deficient Perovskite Anode for Fast-Charging and Long-Life Lithium-Ion Batteries, Advanced Materials 34 (2022) 2200914. https://doi.org/10.1002/adma.202200914.

[16] Y. Zhou, E. Le Calvez, S.W. Baek, M. Frajnkovič, C. Douard, E. Gautron, O. Crosnier, T. Brousse, L. Pilon, Effect of particle size on thermodynamics and lithium ion transport in electrodes made of $Ti_2Nb_2O_9$ microparticles or nanoparticles, Energy Storage Materials 52 (2022) 371–385. https://doi.org/10.1016/j.ensm.2022.08.010.

[17] V. Aravindan, J. Sundaramurthy, A. Jain, P.S. Kumar, W.C. Ling, S. Ramakrishna, M.P. Srinivasan, S. Madhavi, Unveiling $TiNb_2O_7$ as an Insertion Anode for Lithium Ion Capacitors with High Energy and Power Density, ChemSusChem 7 (2014) 1858–1863. https://doi.org/10.1002/cssc.201400157.

[18] E.L. Calvez, N. Dupré, É. Gautron, C. Douard, O. Crosnier, T. Brousse, Effect of particle microstructure and the role of proton on the lithium insertion properties of $HTiNbO_5$ electrode material, Electrochimica Acta 455 (2023) 142432. https://doi.org/10.1016/j.electacta.2023.142432.

[19] X. Li, Z. Lin, N. Jin, L. Sun, X. Yang, Y. Liu, High-capacity anode materials for lithium-ion batteries: perovskite strontium vanadate with crystalline-amorphous dual-phase structure, Materials Today Chemistry 30 (2023) 101542. https://doi.org/10.1016/j.mtchem.2023.101542.

[20] X. Li, Z. Lin, N. Jin, L. Sun, X. Yang, Y. Liu, Electrochemically Induced Crystalline-to-Amorphous Transition of Dinuclear Polyoxovanadate for High-Rate Lithium-Ion Batteries, Advanced Functional Materials 33 (2023) 2214667. https://doi.org/10.1002/adfm.202214667.

[21] D. Neagu, V. Kyriakou, I.-L. Roiban, M. Aouine, C. Tang, A. Caravaca, K. Kousi, I. Schreur-Piet, I.S. Metcalfe, P. Vernoux, M.C.M. van de Sanden, M.N. Tsampas, In Situ Observation of Nanoparticle Exsolution from Perovskite Oxides: From Atomic Scale Mechanistic Insight to Nanostructure Tailoring, ACS Nano 13 (2019) 12996–13005. https://doi.org/10.1021/acsnano.9b05652.

[22] K. Kousi, C. Tang, I.S. Metcalfe, D. Neagu, Emergence and Future of Exsolved Materials, Small 17 (2021) 2006479. https://doi.org/10.1002/smll.202006479.

[23] H. Jeong, Y.H. Kim, B.-R. Won, H. Jeon, C. Park, J. Myung, Emerging Exsolution Materials for Diverse Energy Applications: Design, Mechanism, and Future Prospects, Chem. Mater. 35 (2023) 3745–3764. https://doi.org/10.1021/acs.chemmater.3c00004.

[24] J.H. Kim, J.K. Kim, J. Liu, A. Curcio, J.-S. Jang, I.-D. Kim, F. Ciucci, W. Jung, Nanoparticle Ex-solution for Supported Catalysts: Materials Design, Mechanism and Future Perspectives, ACS Nano 15 (2021) 81–110. https://doi.org/10.1021/acsnano.0c07105.

[25] S. Wang, D. Li, C. Yang, G. Sun, J. Zhang, Y. Xia, C. Xie, G. Yang, M. Zhou, W. Liu, A novel method for the synthesize of nanostructured $MgFe_2O_4$ photocatalysts, J Sol-Gel Sci Technol 84 (2017) 169–179. https://doi.org/10.1007/s10971-017-4471-3.

[26] J.B. Leriche, S. Hamelet, J. Shu, M. Morcrette, C. Masquelier, G. Ouvrard, M. Zerrouki, P. Soudan, S. Belin, E. Elkaïm, F. Baudelet, An Electrochemical Cell for Operando Study of Lithium Batteries Using Synchrotron Radiation, J. Electrochem. Soc. 157 (2010) A606. https://doi.org/10.1149/1.3355977.

[27] C. Leibing, A. Balducci, Glyoxylic-Acetal-Based Electrolytes in Combination with Soft and Hard Carbon Electrodes for Lithium-Ion Batteries: An Evaluation of Room and High Temperature Performance, J. Electrochem. Soc. 168 (2021) 090533. https://doi.org/10.1149/1945-7111/ac23a2.

[28] P. Sciau, A. Kania, B. Dkhil, E. Suard, A. Ratuszna, Structural investigation of $AgNbO_3$ phases using x-ray and neutron diffraction, J. Phys.: Condens. Matter 16 (2004) 2795. https://doi.org/10.1088/0953-8984/16/16/004.

[29] Y. Tian, P. Song, G. Viola, J. Shi, J. Li, L. Jin, Q. Hu, Y. Xu, W. Ge, Z. Yan, D. Zhang, N.V. Tarakina, I. Abrahams, X. Wei, H. Yan, Silver niobate perovskites: structure, properties and multifunctional applications, J. Mater. Chem. A 10 (2022) 14747–14787. https://doi.org/10.1039/D2TA00905F.

[30] S.F. Wang, H.B. Lv, X.S. Zhou, Y.Q. Fu, X.T. Zu, Magnetic Nanocomposites Through Polyacrylamide Gel Route, Nanoscience and Nanotechnology Letters 6 (2014) 758–771. https://doi.org/10.1166/nnl.2014.1796.

[31] Y. Yang, J. Zhao, Wadsley–Roth Crystallographic Shear Structure Niobium-Based Oxides: Promising Anode Materials for High-Safety Lithium-Ion Batteries, Advanced Science 8 (2021) 2004855. https://doi.org/10.1002/advs.202004855.

[32] M. Morcrette, P. Rozier, L. Dupont, E. Mugnier, L. Sannier, J. Galy, J.-M. Tarascon, A reversible copper extrusion–insertion electrode for rechargeable Li batteries, Nature Mater 2 (2003) 755–761. https://doi.org/10.1038/nmat1002.

[33] P. Rozier, M. Morcrette, O. Szajwaj, V. Bodenez, M. Dolle, C. Surcin, L. Dupont, J.M. Tarascon, Li-Driven Copper Extrusion/Re-injection in Various Cu-based Oxides and Sulfides, Israel Journal of Chemistry 48 (2008) 235–249. https://doi.org/10.1560/IJC.48.3-4.249.

[34] Y. Tian, P. Song, G. Viola, J. Shi, J. Li, L. Jin, Q. Hu, Y. Xu, W. Ge, Z. Yan, D. Zhang, N.V. Tarakina, I. Abrahams, X. Wei, H. Yan, Silver niobate perovskites: structure, properties and multifunctional applications, J. Mater. Chem. A 10 (2022) 14747–14787. https://doi.org/10.1039/D2TA00905F.

[35] J.H. Kim, J.K. Kim, J. Liu, A. Curcio, J.-S. Jang, I.-D. Kim, F. Ciucci, W. Jung, Nanoparticle Ex-solution for Supported Catalysts: Materials Design, Mechanism and Future Perspectives, ACS Nano 15 (2021) 81–110. https://doi.org/10.1021/acsnano.0c07105.

[36] J.S. Corsi, A.K. Ng, Y. Huang, E. Detsi, Impact of the Gibbs–Thomson Effect on Lithium Solubility in Silver Used as an Alloy Lithium-Ion Battery Anode, ACS Appl. Energy Mater. 5 (2022) 4547–4555. https://doi.org/10.1021/acsaem.1c04127.

[37] S. Jin, Y. Ye, Y. Niu, Y. Xu, H. Jin, J. Wang, Z. Sun, A. Cao, X. Wu, Y. Luo, H. Ji, L.-J. Wan, Solid–Solution-Based Metal Alloy Phase for Highly Reversible Lithium Metal Anode, J. Am. Chem. Soc. 142 (2020) 8818–8826. https://doi.org/10.1021/jacs.0c01811.

[38] X. Li, G. Yang, S. Zhang, Z. Wang, L. Chen, Improved lithium deposition on silver plated carbon fiber paper, Nano Energy 66 (2019) 104144. https://doi.org/10.1016/j.nanoen.2019.104144.

[39] C. Yang, S. Yu, C. Lin, F. Lv, S. Wu, Y. Yang, W. Wang, Z.-Z. Zhu, J. Li, N. Wang, S. Guo, $Cr_{0.5}Nb_{24.5}O_{62}$ Nanowires with High Electronic Conductivity for High-Rate and Long-Life Lithium-Ion Storage, ACS Nano 11 (2017) 4217–4224. https://doi.org/10.1021/acsnano.7b01163.

[40] M. Yang, S. Li, J. Huang, Three-Dimensional Cross-Linked Nb_2O_5 Polymorphs Derived from Cellulose Substances: Insights into the Mechanisms of Lithium Storage, ACS Appl. Mater. Interfaces 13 (2021) 39501–39512. https://doi.org/10.1021/acsami.1c11720.

[41] F.M.F. de Groot, M. Grioni, J.C. Fuggle, J. Ghijsen, G.A. Sawatzky, H. Petersen, Oxygen 1s x-ray-absorption edges of transition-metal oxides, Phys. Rev. B 40 (1989) 5715–5723. https://doi.org/10.1103/PhysRevB.40.5715.

[42] D. Bach, R. Schneider, D. Gerthsen, J. Verbeeck, W. Sigle, EELS of Niobium and Stoichiometric Niobium-Oxide Phases—Part I: Plasmon and Near-Edges Fine Structure, Microscopy and Microanalysis 15 (2009) 505–523. https://doi.org/10.1017/S143192760999105X.

[43] R. Tao, R. Todorovic, J. Liu, R.J. Meyer, A. Arnold, W. Walkosz, P. Zapol, A. Romanenko, L.D. Cooley, R.F. Klie, Electron energy-loss spectroscopy study of metallic Nb and Nb oxides, Journal of Applied Physics 110 (2011) 124313. https://doi.org/10.1063/1.3665193.

[44] D. Bach, R. Schneider, D. Gerthsen, EELS of Niobium and Stoichiometric Niobium-Oxide Phases—Part II: Quantification, Microscopy and Microanalysis 15 (2009) 524–538. https://doi.org/10.1017/S1431927609991061.

[45] C.-M. Park, H. Jung, H.-J. Sohn, Electrochemical Behaviors and Reaction Mechanism of Nanosilver with Lithium, Electrochem. Solid-State Lett. 12 (2009) A171. https://doi.org/10.1149/1.3152570.

[46] H. Okamoto, Supplemental Literature Review of Binary Phase Diagrams: Ag-Li, Ag-Sn, Be-Pu, C-Mn, C-Si, Ca-Li, Cd-Pu, Cr-Ti, Cr-V, Cu-Li, La-Sc, and Li-Sc, J. Phase Equilib. Diffus. 38 (2017) 70–81. https://doi.org/10.1007/s11669-016-0504-9.

[47] T. Brousse, D. Defives, L. Pasquereau, S.M. Lee, U. Herterich, D.M. Schleich, Metal oxide anodes for Li-ion batteries, Ionics 3 (1997) 332–337. https://doi.org/10.1007/BF02375707.

[48] G. Taillades, J. Sarradin, Silver: high performance anode for thin film lithium ion batteries, Journal of Power Sources 125 (2004) 199–205. https://doi.org/10.1016/j.jpowsour.2003.07.004.

[49] K.J. Griffith, K.M. Wiaderek, G. Cibin, L.E. Marbella, C.P. Grey, Niobium tungsten oxides for high-rate lithium-ion energy storage, Nature 559 (2018) 556–563. https://doi.org/10.1038/s41586-018-0347-0.

[50] X. Li, Z. Lin, N. Jin, X. Yang, Y. Du, L. Lei, P. Rozier, P. Simon, Y. Liu, Perovskite-Type $SrVO_3$ as High-Performance Anode Materials for Lithium-Ion Batteries, Advanced Materials 34 (2022) 2107262. https://doi.org/10.1002/adma.202107262.

2.6 Supplementary information associated to research paper

Table S1. Results of the Rietveld refinement of $AgNbO_3$ powder pattern. The $Ag_2Nb_4O_{11}$ phase (Cc space group, a = 10.7749(17) Å, b = 6.2101(7) Å, c = 12.839(11) Å, β = 106.25(17), V = 824.8(10) $Å^3$) is impurity present on the pattern.

$AgNbO_3$		**Reference pattern**
Parameters	**Pbcm**	**Pbcm (DOI: 10.1088/0953-8984/16/16/004)**
a (Å)	5.5485(16)	5.5468(3)
b (Å)	5.6001(14)	5.6038(3)
c (Å)	15.6475(4)	15.642(1)
V ($Å^3$)	486.21(2)	486.20(5)
R(obs) % $AgNbO_3$	1.97	
R(obs) % $Ag_2Nb_4O_{11}$	4.54	
GOF	1.38	
Rp %	2.84	
wRp %	3.81	
Crystallite size (nm)	76.8(6)	
$Ag_2Nb_4O_{11}$ (Impurity phase)		**CC (DOI: 10.1039/b921115b)**
Mass% $AgNbO_3$ / $Ag_2Nb_4O_{11}$	88.2(2) / 11.8(2)	
Crystallite size (nm)	102.6(9)	

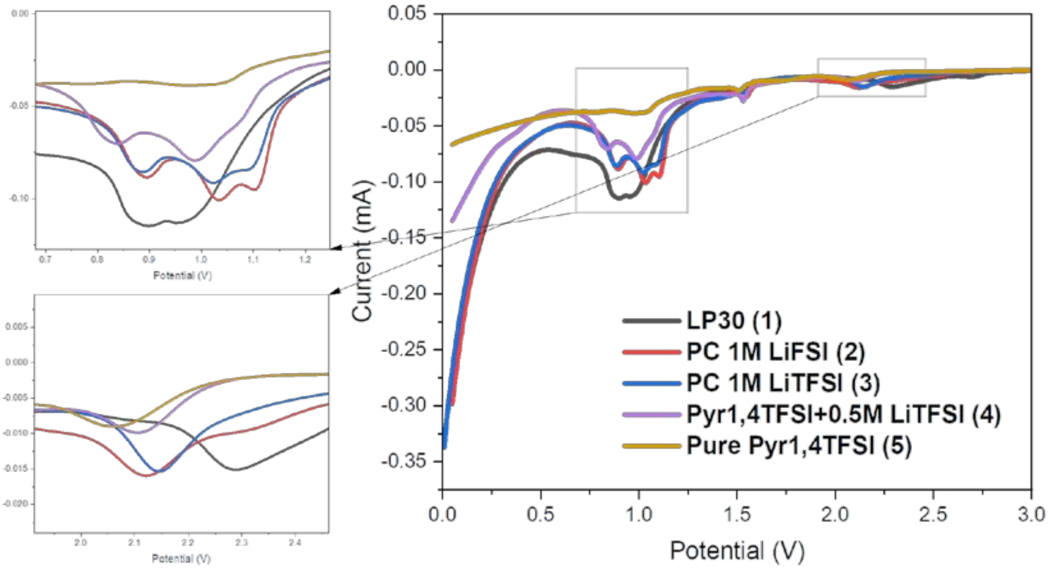

Figure S1. Current Vs Potential on the first reduction of $AgNbO_3$ in LP30(1), PC 1M LIFSI(2), PC 1M LITFSI(3), Pyr1,4TFSI+0.5M LITFSI(4) and Pure Pyr1,4TFSI(5).

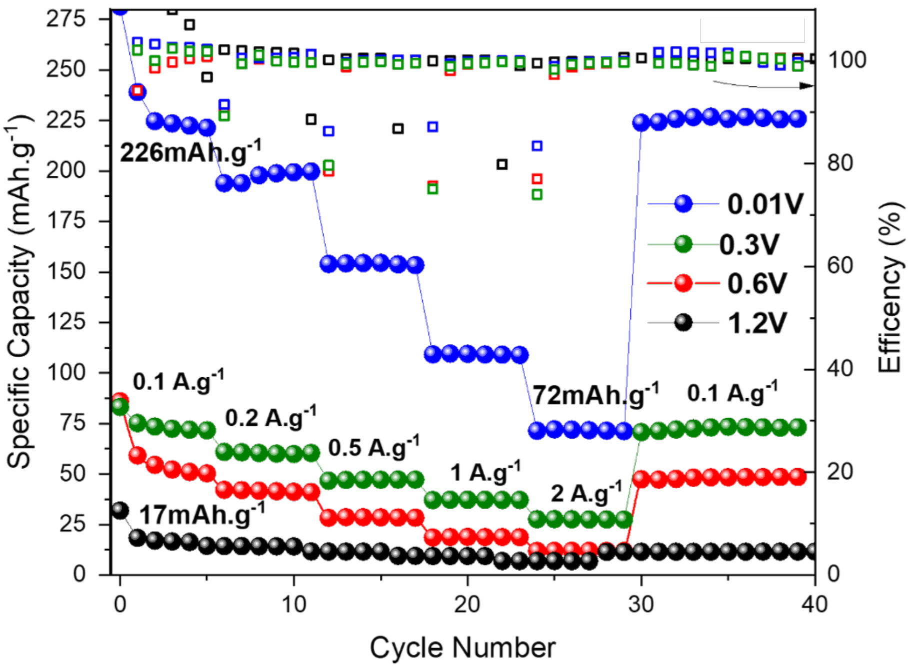

Figure S2. Galvanostatic charge discharge profile of AgNbO$_3$ with its associated regions (I,II,III) and rate performance at different cutoff voltages and current densities.

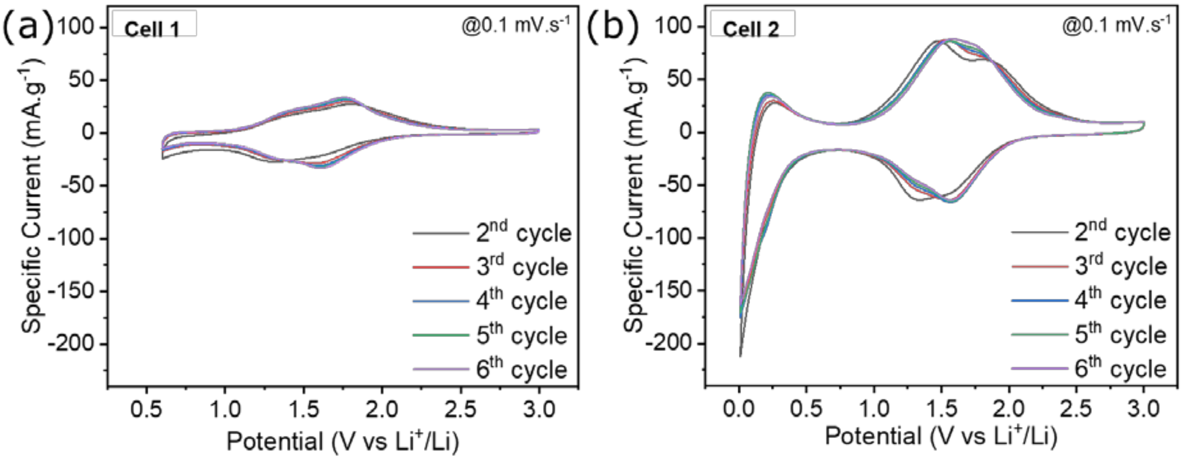

Figure S3. Cyclic voltammograms of AgNbO$_3$ from 2nd to 6th cycles in: (a) 0.6 – 3.0V. (b) Extended potential window of 0.01 – 3.0V.

Peaks arising around 41°, 50.8°, and 52.6° indicate metallic Be. It is noted that during the 1st lithiation cycle, the XRD patterns above 1 V *vs.* Li^{+}/Li reveal the disappearance of peaks at around 2θ = 29°, corresponding to Ag$_2$Nb$_4$O$_{11}$ phase impurity. This implies that a reducing potential serves as a stimulus for the impurity removal and phase purification. The mitigation of such impurities in ANO perovskites has been reported previously through fine grinding process because these impurities are typically localized within the surface layers, attributed to high-temperature melting/decomposition that initiates at the surface [1]. In addition, an irreversible decrease in intensity of all the crystallographic peaks is observed during 1st lithiation process.

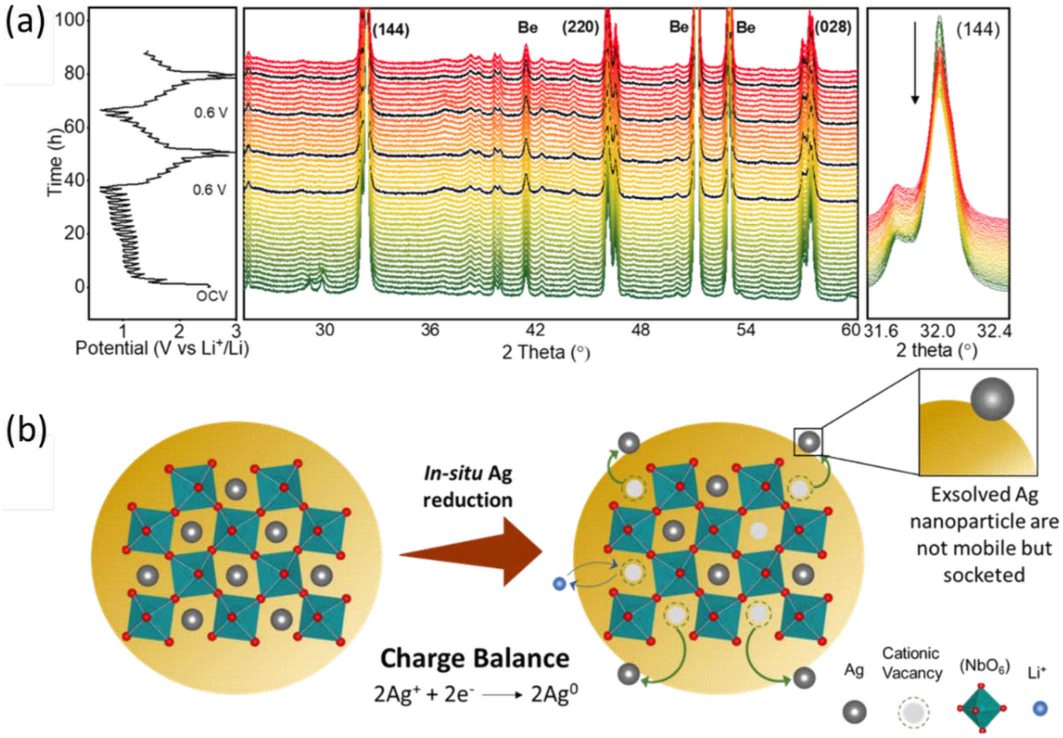

Figure S4. Li$^+$ storage mechanism investigation of AgNbO$_3$ in 0.6 – 3.0V potential window. (a) In-situ xrd profile of first two charge/discharge cycles at 0.1 C. (b) Schematic representation of in-situ material transformation due to surface and bulk Ag reduction and exsolution of Ag nanoparticles in the lattice.

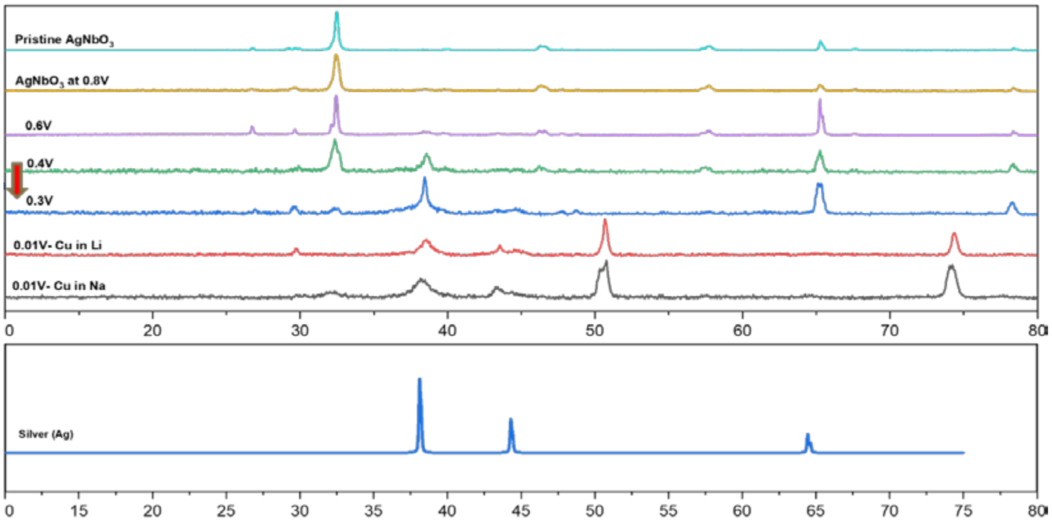

Figure S5. Ex situ XRD at each cut-off potential of cycled AgNbO$_3$ electrode (Al current collector up to 0.3V – Cu current collector for samples below 0.3V). Silver reference as a benchmark. Silver residues can be observed at 0.01V, indicating the presence of silver nanoparticles due to the broad shape of the XRD signal.

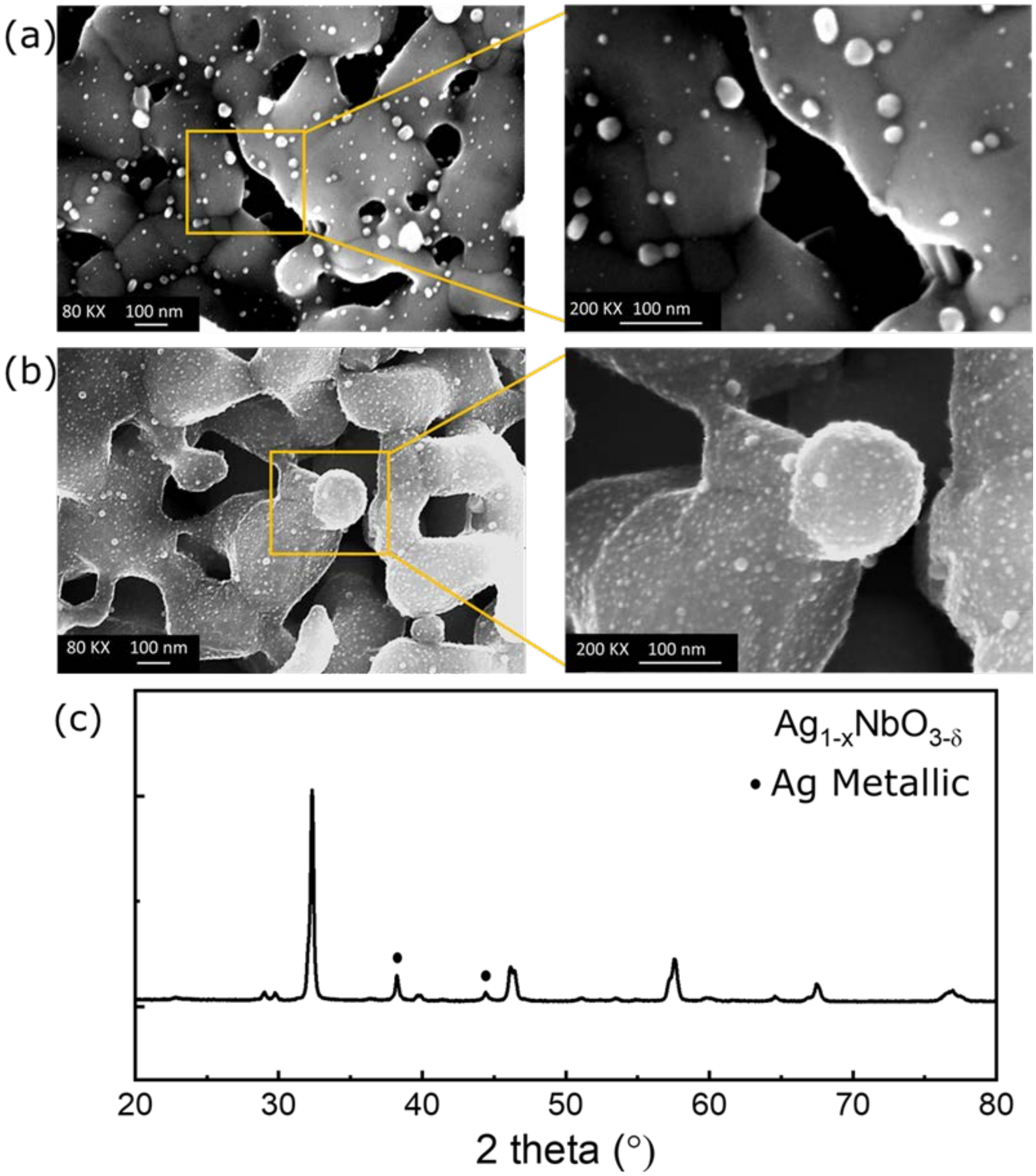

Figure S6. (a) SEM image of thermally reduced $AgNbO_3$ powder at 250 °C under Ar/H_2 environment. (b) Ex-situ SEM image of cycled electrodes in 0.6 – 3V, showing electrochemically induced Ag-exsolution. Selected area zoomed images are presented on the right side of each image. (c) XRD pattern of thermally reduced $AgNbO_3$ powder.

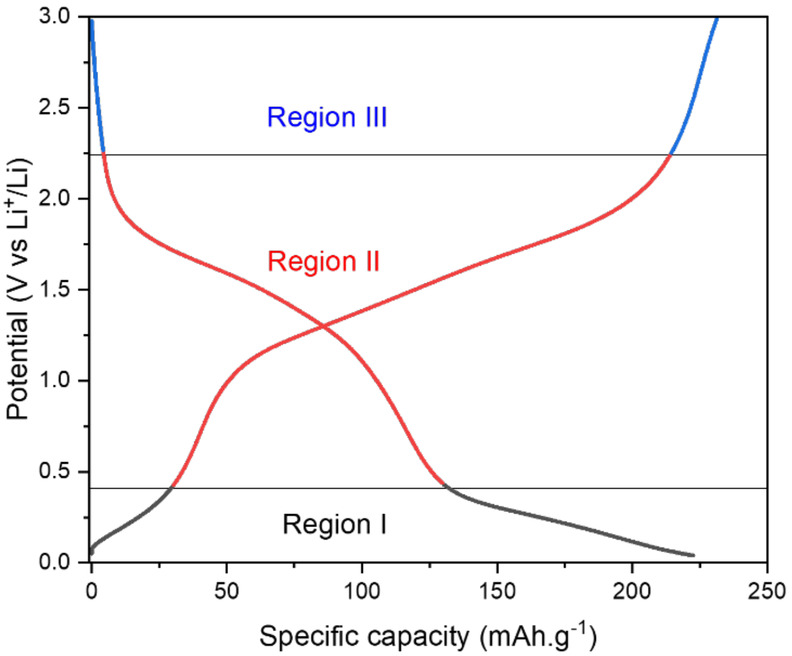

Figure S7. Galvanostatic charge discharge profile of AgNbO$_3$ with its associated regions (I,II,III).

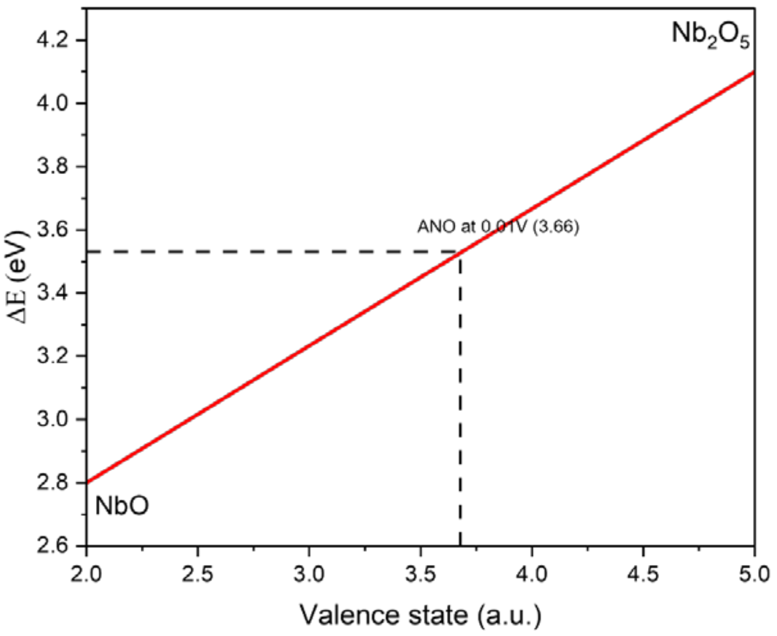

Figure S8. Plot for energy difference reference (ΔE) between a and b peaks at O-K edge for different Nb valence states [2].

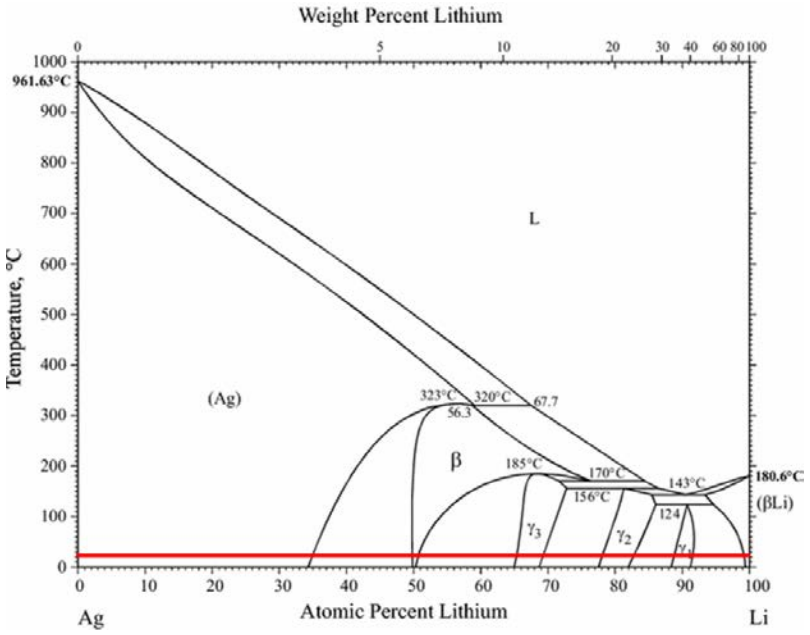

Figure S9. Silver (Ag) - Lithium (Li) binary diagram from 0 to 1000°C. Red line indicates room temperature.

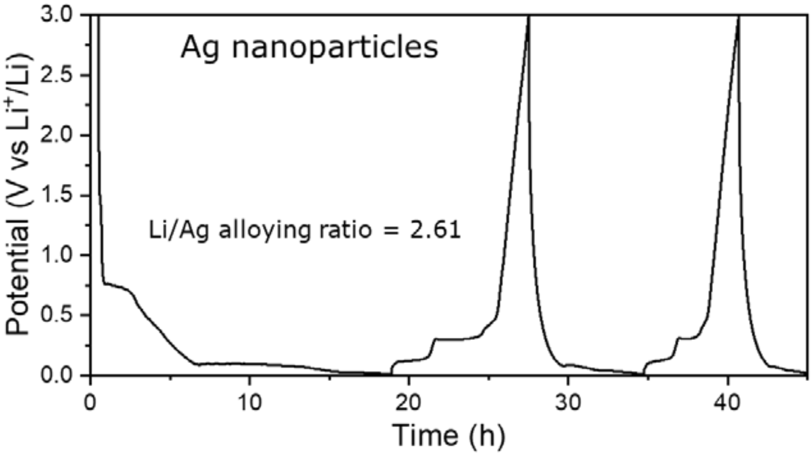

Figure S10. Silver Nanoparticles lithiation up to 0.01V showing different plateaus of Ag-Li Alloying formation with Li/Ag alloying ratio up to 2.61.

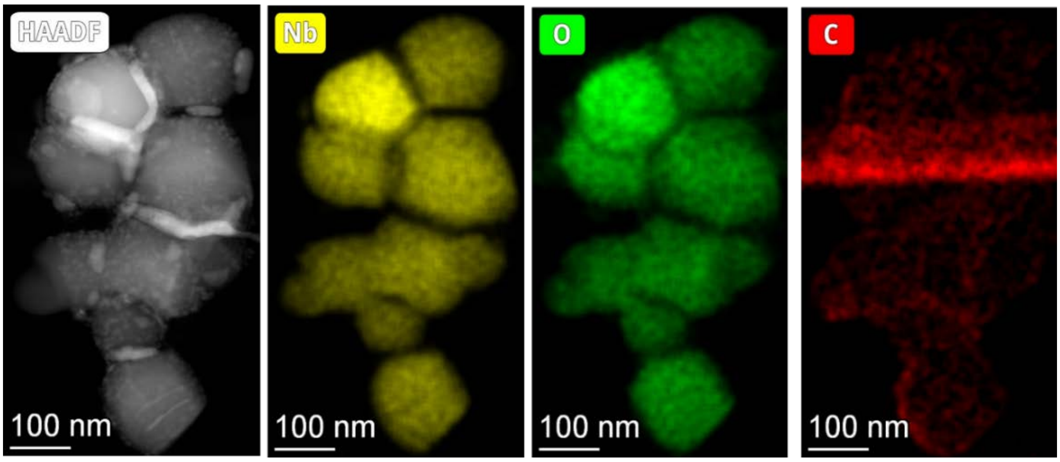

Figure S11. $AgNbO_3$ HAADF-EDS mapping for 0.01V cutoff electrode.

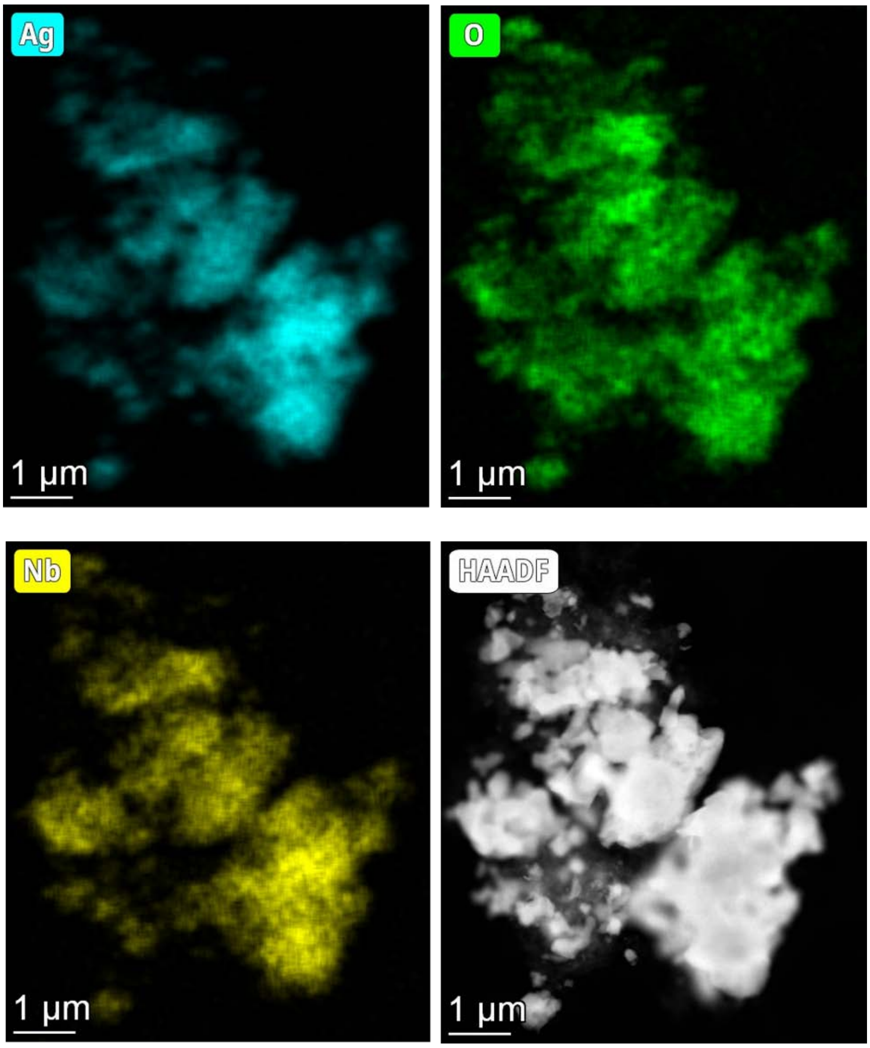

Figure S12. $AgNbO_3$ HAADF-EDS mapping for pristine electrode showing homogenous distribution of Ag.

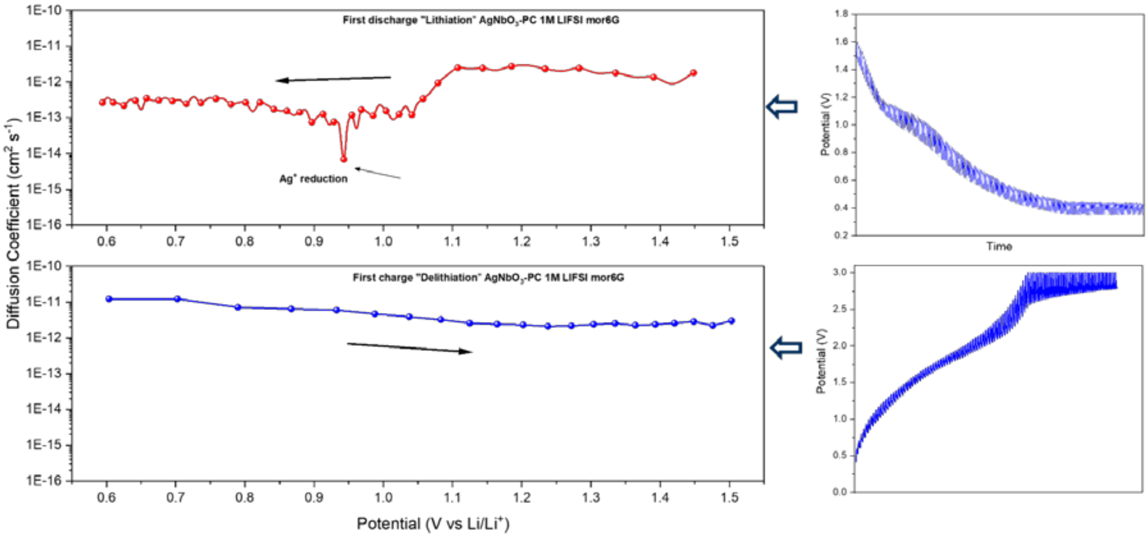

Figure S13. Diffusion coefficient vs Potential (left) during first lithiation and delithiation of $AgNbO_3$ and its associated stepwise potential ramp (right). The coefficient was calculated up to 0.6V cut-off potential to closely estimate lithium diffusion in $AgNbO_3$ for Nb redox using GITT measurements without solicitating Ag-Li alloying reaction

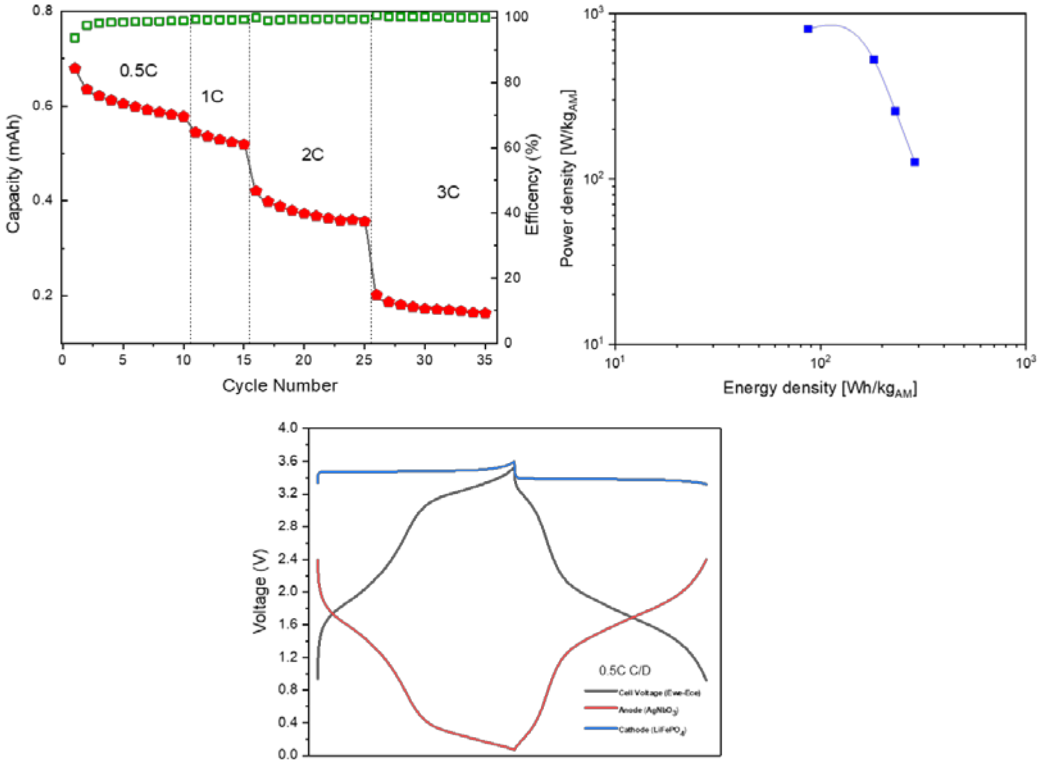

Figure S14. (top left) Rate test for $AgNbO_3$-$LiFePO_4$ full cell configuration. Calculated ragone plot for the full cell (top right). Charge discharge profile showing the potential sweep of the anode, cathode, and full cell (bottom center)

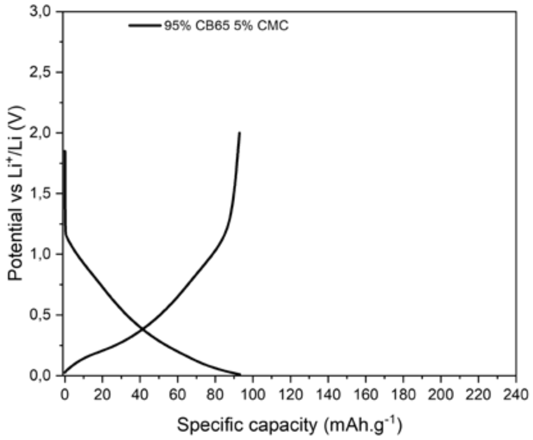

Figure S15. GCPL showing capacity values obtained for an electrode with 95% CB65 at the current density of 0.1A.g^{-1}. The materials signature is significantly different, contributing to less than 4% of the total capacity (226mAh.g^{-1}) observed in $AgNbO_3$.

References related to SI of paper

[1] T.-F. Yi, S.-Y. Yang, Y. Xie, Recent advances of $Li_4Ti_5O_{12}$ as a promising next generation anode material for high power lithium-ion batteries, J. Mater. Chem. A. 3 (2015) 5750–5777. https://doi.org/10.1039/C4TA06882C.

[2] D. Bach, R. Schneider, D. Gerthsen, J. Verbeeck, W. Sigle, EELS of Niobium and Stoichiometric Niobium-Oxide Phases—Part I: Plasmon and Near-Edges Fine Structure, Microscopy and Microanalysis. 15 (2009) 505–523. https://doi.org/10.1017/S143192760999105X.

2.7 Intrinsic A-site deficient $Ag_{1-x}\square_xNbO_{3-\delta}$: Synthesis and Li^+ storage performance

2.7.1 Synthesis and powder XRD characterizations

In this section, we explore the feasibility of Ag deficiency in $AgNbO_3$ perovskite without substitution and we investigate the effect of vacancies on Li^+ storage performance. As discussed earlier, Ag exsolution is the initial step in the electrochemical activation process, indicating that the perovskite structure retains its stability even with Ag deficiency in the lattice. Motivated by this observation, non-stoichiometric structures with general formula $Ag_{1-x}\square_xNbO_{3-\delta}$ ($0 < x < 0.55$) were designed to achieve controlled Ag deficiency by regulating Ag/Nb cation ratio. Figure 2.8a illustrate the crystal structure of the studied materials and the concept of Ag and O vacancies. The materials were synthesized by sol-gel synthesis route with without controlled environment calcination, which indicate that $AgNbO_3$ perovskite structure has an intrinsic ability to hold A-site deficiency.

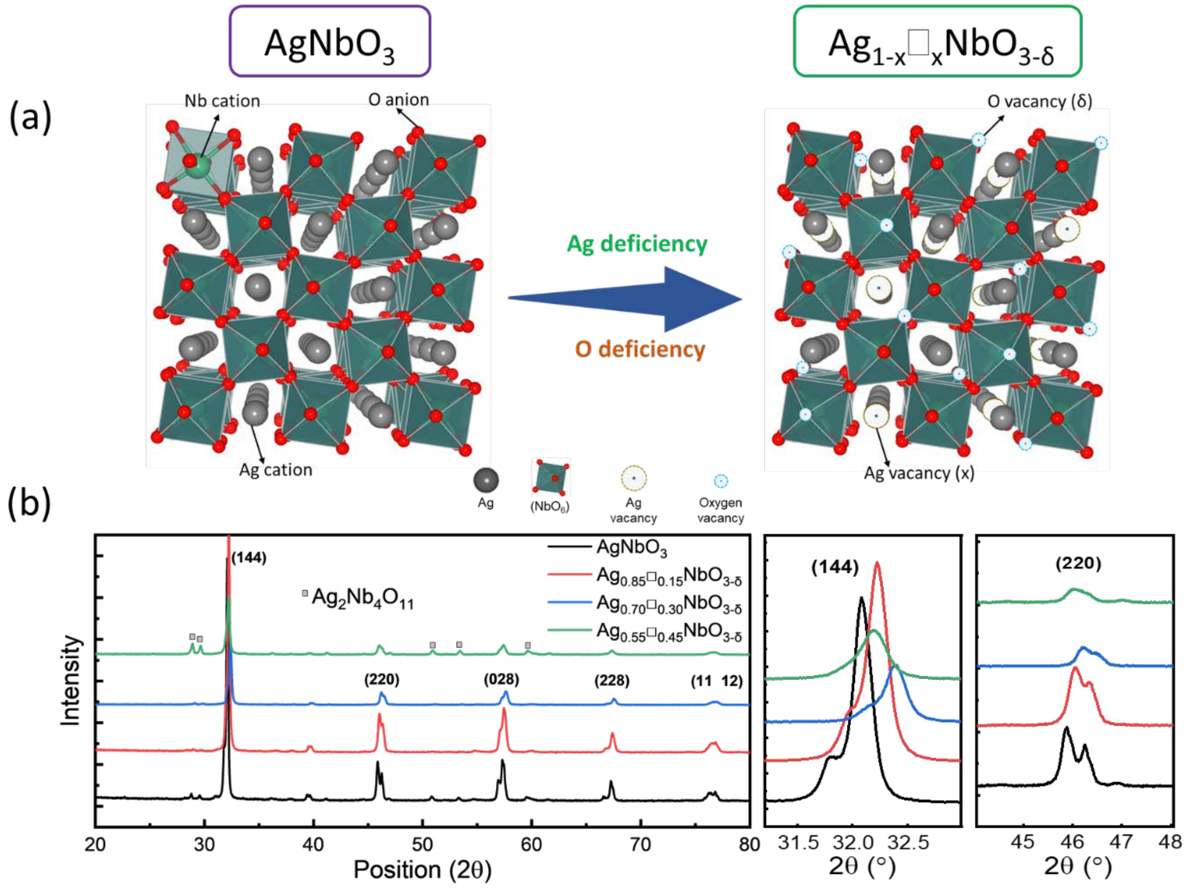

Figure 2.8. (a) Crystal structure representation of pristine $AgNbO_3$ to A-site deficient $Ag_{1-x}\square_xNbO_{3-\delta}$ transition. (b) Powder XRD patterns of $Ag_{1-x}\ \square_xNbO_{3-\delta}$ ($x = 0, 0.15, 0.30, 0.55$) perovskites. Zoomed images (right) of (144) and (200) peaks comparison.

The x values depend on Ag to Nb precursor molar ratios, though neither δ nor the exact nature of the gases released during calcination can be accurately determined. In this case, Ag deficiency can be compensated either by oxygen deficiencies ($Ag_{1-x}NbO_{3-x}$) or by change in oxidation state of Nb at B-site. However, the later is unlikely, as Nb^{5+} cannot transition to a higher oxidation state.

Powder XRD patterns shown in Figure 2.8b indicate that perovskite structure remains intact even with significant Ag and O vacancies and maintained up to 30% A-site vacancies without any significant contributions of secondary phases, although peak splitting remains persistent in all the samples. Interestingly, the $Ag_2Nb_4O_{11}$ impurity phase that appeared in small concentration while keeping Ag/Nb precursor ratio 1 (pristine sample), diminished significantly as x increased, indicating a phase purification trend. This suggests that a slightly reduced Ag concentration during sol-gel synthesis yield a phase pure $AgNbO_3$ perovskite. However, when the Ag concentration decreased below 0.70, the $Ag_2Nb_4O_{11}$ impurity phase reappeared, as observed in $Ag_{0.55}\square_{0.45}NbO_{3-\delta}$ sample. In this case, impurity phase arises from an insufficient Ag concentration, making conditions favorable for the formation of $Ag_2Nb_4O_{11}$ phase (Ag/Nb = 0.5). This phenomenon is similar to that observed in case of A-site substitutions in $AgNbO_3$ [7,8]. For A-site deficient structures, the main crystallographic peaks shifted towards higher 2θ as shown for (144) and (220) peaks in zoom on the right panel of Figure 2.8b. It indicates that a lattice contraction occurs due to a decrease of Ag content and the possible increased interaction between the remaining cations and oxygen anions as depicted in the literature [9]. Another possible reason can be an increased defect density due to vacancies, which alters the local bonding environment, causing atoms to adjust their positions slightly and further contributing to the higher 2θ shift. Additionally, the peak intensity decreases with increasing x value, which may be attributed to a suppressed long-range ordering caused by the randomly distributed cation vacancies [10,11]. The absence of additional reflections in the patterns may indicate that samples do not reveal superstructure formation. This discussion highlights that as Ag is progressively removed from the structure, a more defective and contracted lattice is formed. However, a consistent peak splitting indicate that the crystal symmetry and phase composition seems preserved, even with Ag deficiency.

2.7.2 Li^+ storage performance of $Ag_{1-x}\square_xNbO_{3-\delta}$ perovskite system

To investigate the electrochemical activity of the materials during the first cycle, cyclic voltammetry was first performed in two electrode half-cell configuration using metallic Li as counter and reference electrode. The structural activation and underlying Li^+ storage mechanisms that has been detailed in previous section for pristine $AgNbO_3$ perovskite is taken as a reference. Figure 2.9a shows the first cycle comparison of all the samples. At higher potentials (1.2 – 1.9V vs Li^+/Li), the pristine $AgNbO_3$ showed peaks of $Ag_2Nb_4O_{11}$ impurity, as highlighted in zoomed inset of Figure 2.9a. However, in samples with 15% and 30% A-site deficiency those peaks are not observed which clarifies the phase purity of samples. The irreversible peak that appeared just below 1.0V in pristine $AgNbO_3$ indicates the onset of structural activation process. In A-site deficient samples, this peak becomes broader and shifts toward higher potentials. This behavior is also evidenced in the first cycle during GCPL measurements, as shown in Figure 2.9b, where the sharp plateau observed in pristine $AgNbO_3$ turns into a uniformly distributed broad plateau (with more specific capacity) as the x value increases. It suggests that with increasing vacancies in the structure, Li^+ insertion increases as well. The vacancies filled lithiated $Ag_{1-x}Li_xNbO_3$ structure with enormous defects facilitate Ag-exsolution from the lattice, which subsequently leads to a structural collapse. Below 0.3V, the Li-Ag alloying process followed the similar trend to that of pristine sample, but with a systematic reduction in peak current as x value increased.

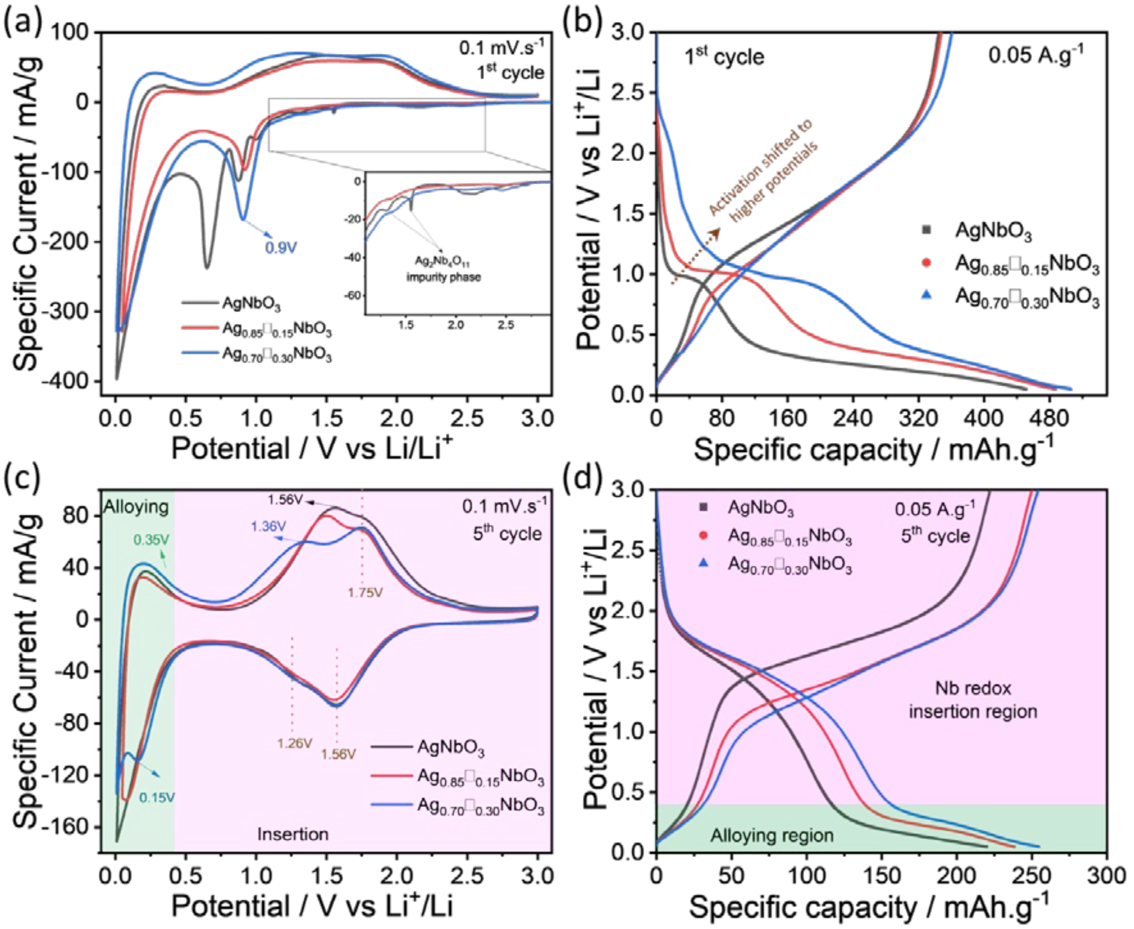

Figure 2.9. Electrochemistry comparisons of $Ag_{1-x}\,\square_xNbO_{3-\delta}$ (x = 0, 0.15, 0.30) perovskites in half cell (a) 1st cycle CVs. Inset shows the peaks associated to $Ag_2Nb_4O_{11}$. (b) 1st cycle GCPL curves. (c) 5th cycle CVs. (d) 5th cycle GCPL curves. CV measurements were performed at $0.1mV.s^{-1}$ and GCPL measurements at $0.05A.g^{-1}$.

First discharge capacity obtained in galvanostatic lithiation/delithiation curves were 451, 488, and 505 mAh.g^{-1} for $AgNbO_3$, $Ag_{0.85}\square_{0.15}NbO_{3-\delta}$, $Ag_{0.70}\square_{0.30}NbO_{3-\delta}$, respectively. However, initial Coulombic efficiencies of about 70% were obtained for all the samples, indicating solid electrolyte interphase (SEI) formation and structural activation during the first cycle. Upon subsequent cycles, materials maintained stable Coulombic efficiencies of above 99% due to stable SEI formation, which provides dynamic stability and ensures long term cycling stability similar to other negative electrode materials [11–13]. The CV results for stabilized cycle (5th cycle) are compared in Figure 2.9c, where two main regions are identified based on the results of pristine $AgNbO_3$. The first region at higher potentials (0.3 – 3.0V) is attributed to insertion region in which Nb^{5+}/Nb^{4+} and Nb^{4+}/Nb^{3+} reversible redox couples are identified in the range of 2.0 – 1.0 V vs Li^+/Li [14]. The structural changes with increasing x values could contribute to the observed changes in the redox behavior shown in the CV curves. Ag vacancies alters the electrochemical environment around the Nb-sites that may affect the energy levels associated with lithium insertion and extraction, which is reflected by shifts in peak positions and changes in intensities as the degree of Ag-deficiency increases. However, shifts are more pronounced during Li^+ extraction. These shifts suggest that the energy barrier for lithium insertion decreases, leading to enhanced redox activity. Additionally, suppression of long-range order may correlate with the broadening and reduction of peak intensity, particularly at lower potentials where the material transitions to a more amorphous state. This broadening is often linked to improved Li^+ diffusion and storage, as amorphous structures provide more disordered and accessible Li^+ insertion pathways, leading to enhanced electrochemical performance [15–17]. The second region below 0.3V is Li-Ag alloying which contribute to the total capacity of the materials. At the end of lithiation, the peak intensity associated to Li-Ag alloying decreases with increasing x values, likely due to unavailability of sufficient Ag content. Nonetheless, the reversibility of alloying and de-alloying reactions improves with regulation of Ag-vacancies and may contribute to improved rate performance. Figure 2.9d compares the 5th cycle charge/discharge curves of $Ag_{1-x}\square_xNbO_{3-\delta}$ electrodes at 0.05A.g^{-1}. By increasing x value, the maximum specific capacity increases systematically from 223 mAh.g^{-1} for pristine $AgNbO_3$ to 255 mAh.g^{-1} for $Ag_{0.70}\square_{0.30}NbO_{3-\delta}$ (30% A-site deficiency). The enhanced lithiation capacity is primarily distributed within insertion region under wide potential window of 0.5–3.0 V versus Li^+/Li, which is attributed to availability of more Nb-redox sites due to Ag-vacancies.

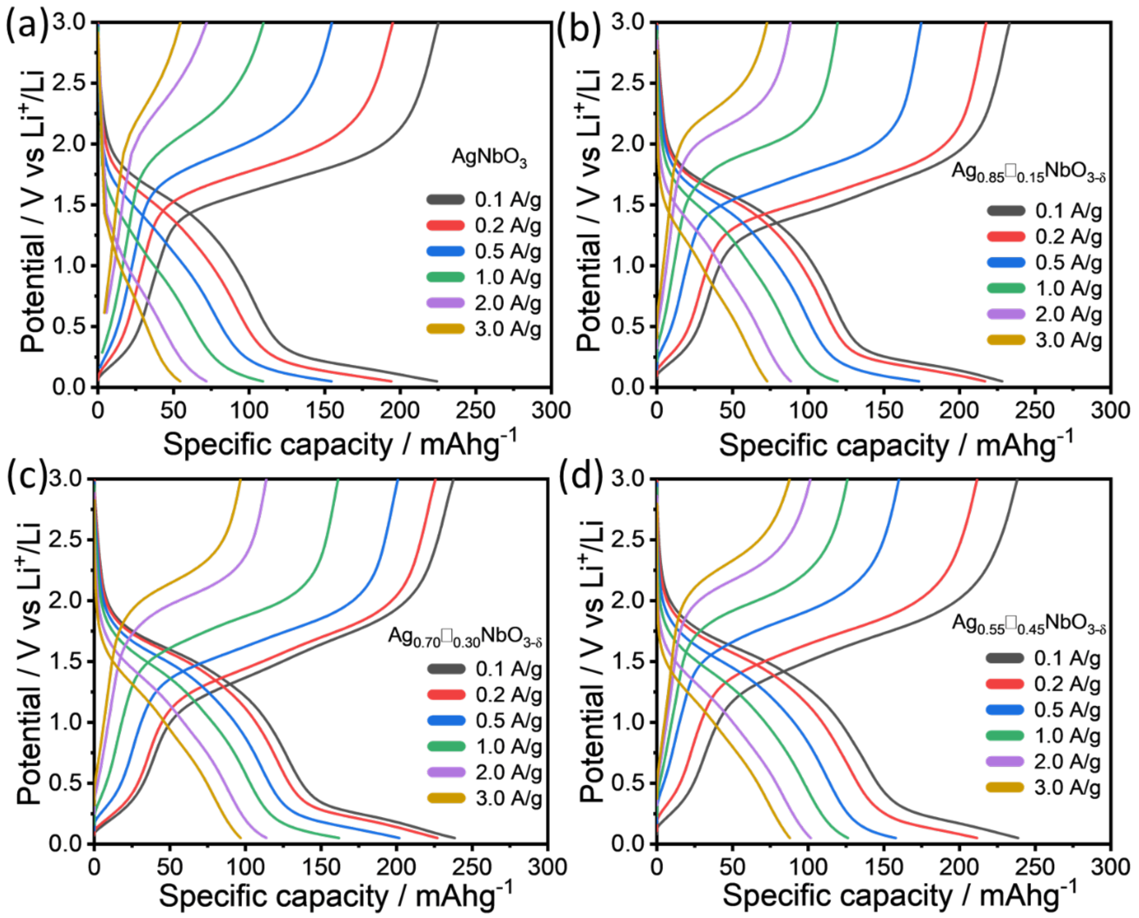

Figure 2.10. Galvanostatic lithiation/delithiation curves of $Ag_{1-x}\square_xNbO_{3-\delta}$ electrodes at different current densities (a) Pristine $AgNbO_3$. (b) $Ag_{0.85}\square_{0.15}NbO_{3-\delta}$. (c) $Ag_{0.70}\square_{0.30}NbO_{3-\delta}$. (d) $Ag_{0.55}\square_{0.45}NbO_{3-\delta}$.

The galvanostatic litiation/delithiation plots of pristine $AgNbO_3$, $Ag_{0.85}\square_{0.15}NbO_{3-\delta}$, $Ag_{0.70}\square_{0.30}NbO_{3-\delta}$, $Ag_{0.55}\square_{0.45}NbO_{3-\delta}$ electrodes at current densities ranging from 0.1 – 3.0 A.g^{-1} are presented in Figure 2.10 (a-d). Although all the materials withstand high current densities, their performances are different. Figure 2.11 shows the specific capacity vs number of cycles at different current densities. $Ag_{0.70}\square_{0.30}NbO_{3-\delta}$ delivers high capacity retention of 40% at 3.0 A.g^{-1} (97 mAh.g^{-1} in 2 min of charge), nearly double as compared to pristine $AgNbO_3$, making it the best rate performance sample among all. Such a high rate performance can be attributed to increased electrical conductivity of A-site deficient structures, due to induced oxygen vacancies. In addition, it also maintained its high maximum capacity upon subsequent cycling at 0.1 A.g^{-1}. The maximum specific capacity and rate performance of $Ag_{0.55}\square_{0.45}NbO_{3-\delta}$ is comparable to $Ag_{0.70}\square_{0.30}NbO_{3-\delta}$, but it has significant contributions of $Ag_2Nb_4O_{11}$ secondary phase.

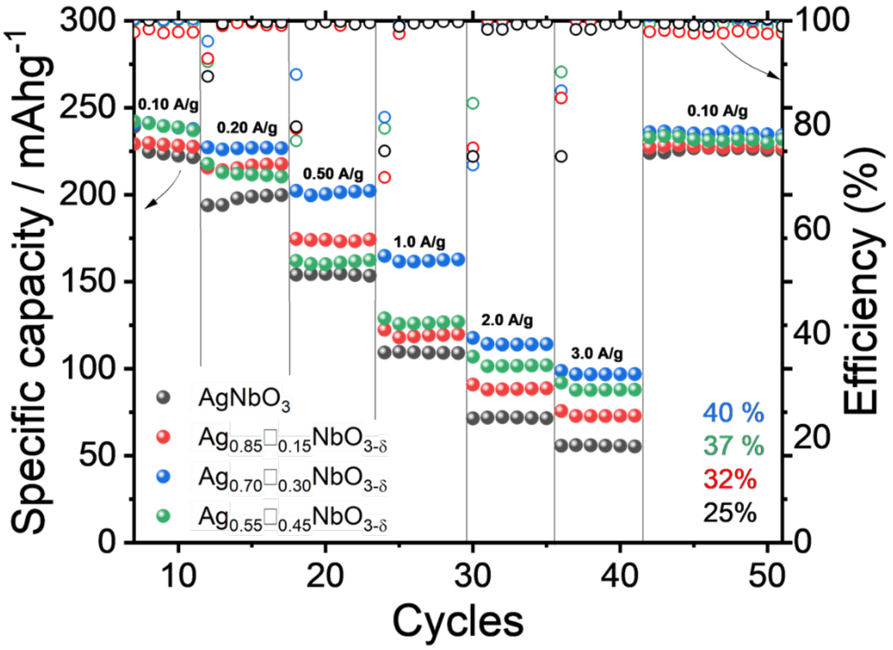

Samples	0.1 A/g	1 A/g	2 A/g	3 A/g
AgNbO$_3$	224 mAhg^{-1}	109 mAhg^{-1}	72 mAhg^{-1}	56 mAhg^{-1}
Ag$_{0.85}$□$_{0.15}$NbO$_{3-\delta}$	229 mAhg^{-1}	118 mAhg^{-1}	88 mAhg^{-1}	73 mAhg^{-1}
Ag$_{0.70}$□$_{0.30}$NbO$_{3-\delta}$	**240 mAhg^{-1}**	**162 mAhg^{-1}**	**114 mAhg^{-1}**	**97 mAhg^{-1}**
Ag$_{0.55}$□$_{0.45}$NbO$_{3-\delta}$	242 mAhg^{-1}	126 mAhg^{-1}	101 mAhg^{-1}	87 mAhg^{-1}

Figure 2.11. Li$^+$ storage performance of Ag$_{1-x}$□$_x$NbO$_{3-\delta}$ (0 < x < 0.55) electrodes at different current densities.

Based on literature, it can be hypothesized that creating Ag-vacancies may not significantly impact the electrical conductivity, as density of state likely remains unaffected [11]. However, it enhances the Li$^+$ ion conductivity and allows to manage Nb^{5+}/Nb^{4+} and Nb^{4+}/Nb^{3+} reversible redox couples more effectively as compared to pristine AgNbO$_3$, thereby contributing to an enhanced capacity [18]. In contract, oxygen vacancies (induced as a result of charge compensation) might improve electrical conductivity, ultimately contributing to a high rate performance [9]. Nonetheless, these hypotheses require verification through density functional theory (DFT) calculations.

To confirm the effect of A-site deficiency on cycling stability, the highly deficient and phase pure Ag$_{0.70}$□$_{0.30}$NbO$_{3-\delta}$ materials was selected. As depicted in Figure 2.12, the Ag$_{0.70}$□$_{0.30}$NbO$_{3-\delta}$ follows a similar trend as of pristine AgNbO$_3$, delivering 92% capacity retention after 2000 cycles at 1.0 A.g^{-1}, with a stable Coulombic efficiency close to 100%.

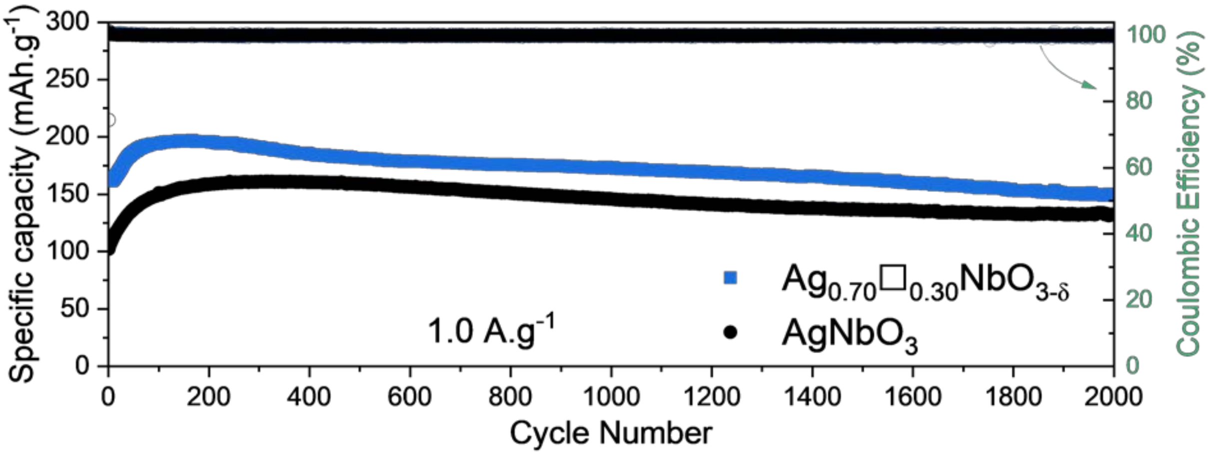

Figure 2.12. Cyclic stability of $Ag_{0.70}\square_{0.30}NbO_{3-\delta}$ electrodes at 1.0 A.g^{-1} for 2000 cycles.

2.8 Conclusion

In this chapter, $AgNbO_3$ perovskite, La-substituted $Ag_{1-3x}La_x\square_{2x}NbO_3$ ($x \leq 0.20$) perovskites and un-doped A-site deficient $Ag_{1-x}\square_xNbO_{3-\delta}$ ($0 < x < 0.55$) have been designed, synthesized and investigated as model negative electrode materials for Li^+ storage.

Firstly, polyacrylamide synthesis route was developed for synthesis of pristine $AgNbO_3$ and La-substituted $Ag_{1-3x}La_x\square_{2x}NbO_3$ ($x \leq 0.20$) perovskites that have never been reported before. Compared to sol-gel route, polyacrylamide synthesis yield materials with uniform and well-defined morphology without particle agglomeration, and good compositional uniformity. It has been demonstrated that the formation of vacancies in a perovskite through La-substitution enables the insertion of Li^+. Under the electrochemically stable potential window of 1.2 – 3.0V, Li^+ insertion in the structures increases with increasing concentration of vacancies. The overall Li^+ storage performance of $Ag_{1-3x}La_x\square_{2x}NbO_3$ ($x \leq 0.20$) perovskites was comparable to materials that have been synthesized by sol-gel route and investigated by our group previously [1].

Secondly, the electrochemical behavior of Li^+ storage in $Ag_{1-3x}La_x\square_{2x}NbO_3$ ($x \leq 0.20$) perovskites is investigated in detail under extended potential windows, focusing on the impact of lower cut-off potentials on material stability and performance. It is observed that at a lower cut-off of 0.6V vs Li^+/Li, these materials undergo irreversible structural changes during the first cycle, leading to enhanced and stable Li^+ storage in subsequent cycles. Specifically, the substituted samples $Ag_{0.70}La_{0.10}\square_{0.20}NbO_3$ and $Ag_{0.40}La_{0.20}\square_{0.40}NbO_3$ display significant higher specific capacities of 164 mAh.g^{-1} and 160 mAh.g^{-1}, respectively, compared to 74 mAh.g^{-1} for pristine $AgNbO_3$. However, the crystalline structure rapidly deteriorates with increasing La content, severely affecting their cyclic stability and resulting in poor rate capability (16% and 13% retention at 50 mV.s^{-1}). In contrast, $AgNbO_3$ retains 44% of its capacity at 50 mV.s^{-1}, while maintaining 94% of its initial specific capacity after 100 cycles under 0.6-3.0V vs Li^+/Li. Further investigations of $AgNbO_3$ show an overall specific capacity of 226 mAh.g^{-1} in an extended potential window (0.01–3.0V), which is thirteen-fold compared to the capacity of the material in its electrochemically stable potential window (1.2–3.0V) and four-fold compared to the Nb-electrochemically active (0.6–3.0V) region. During the first lithiation, $AgNbO_3$ undergoes Ag-exsolution from the A-site of the structure, causing A/B non-stoichiometry, which results in the compensation of Ag^+ by Li^+ intercalation to a certain extent. A structural transition from crystalline to amorphous oxide is observed below 0.3V vs. Li^+/Li. Lithium insertion is accompanied by Nb^{5+} reduction down to an average value of $Nb^{3.66+}$ as estimated by ^{93}Nb MAS NMR. At the end of the reduction (below 0.3V), a reversible Li-Ag (de)alloying charge storage mechanism is observed. Furthermore, outstanding performance under high-power conditions is demonstrated, with a capacity retention of 72 mAh.g^{-1} at 2 A.g^{-1} (2.2 min of charge) and good cycling stability and efficiency at 1 A.g^{-1} after 2500 cycles.

Thirdly, by regulating the Ag/Nb cation ratio, we successfully designed non-stoichiometric structures ($Ag_{1-x}\square_xNbO_{3-\delta}$, $0 < x < 0.55$) that exhibit enhanced Li^+ storage capabilities. It is demonstrate that the $AgNbO_3$ perovskite lattice can sustain significant A-site deficiencies while retaining its crystallographic integrity and phase composition. Specifically, the $Ag_{0.70}\square_{0.30}NbO_{3-\delta}$ sample exhibited the highest specific capacity of 255 mAh.g^{-1} at 0.05A.g^{-1} and a high rate performance with 40% capacity retention at 3 A.g^{-1}, alongside excellent long-term cycling stability, achieving 92% capacity retention over 2000 cycles at 1.0 A.g^{-1}. Such improved performance is attributed to the induced Ag and O vacancies, which facilitate Li^+ insertion and enhance the electronic conductivity, particularly at higher degrees of deficiency. Ag vacancies enhance the redox activity, particularly in insertion region by regulating Nb^{5+}/Nb^{4+} and Nb^{4+}/Nb^{3+} couples, resulting in higher specific capacity and better rate performance. Highly deficient $Ag_{0.70}\square_{0.30}NbO_{3-\delta}$ follows a similar trend as of pristine $AgNbO_3$, delivering 92% capacity retention after 2000 cycles at 1.0 A.g^{-1}, with a stable Coulombic efficiency close to 100%.

Overall, these findings suggest that the precise control of A-site deficiencies and the introduction of dopants like La are critical strategies to optimize the electrochemical performance of model $AgNbO_3$ perovskites for Li^+ storage. The developed strategies not only contributes to the fundamental understanding of defect chemistry in perovskites but also provide a foundation for further exploration of Nb-based ABO_3 perovskite materials consisting low cost cations for designing anode materials for next-generation LIBs. Based on these interesting results of model system, next chapter will continue to investigate such approaches to relatively low cost alkali metal based niobate perovskites.

References related to chapter 2

[1] E. Le Calvez, J.C. Espinosa-Angeles, G.J. Whang, N. Dupré, B.S. Dunn, O. Crosnier, T. Brousse, Investigating the Perovskite $Ag_{1-3x}La_xNbO_3$ as a High-Rate Negative Electrode for Li-Ion Batteries, Front. Chem. 10 (2022) 873783. https://doi.org/10.3389/fchem.2022.873783.

[2] L.L. Hench, J.K. West, The sol-gel process, Chem. Rev. 90 (1990) 33–72. https://doi.org/10.1021/cr00099a003.

[3] S.F. Wang, H.B. Lv, X.S. Zhou, Y.Q. Fu, X.T. Zu, Magnetic Nanocomposites Through Polyacrylamide Gel Route, Nanosci Nanotechnol Lett 6 (2014) 758–771. https://doi.org/10.1166/nnl.2014.1796.

[4] N. Masó, A.R. West, A new family of ferroelectric materials: $Me_2Nb_4O_{11}$ (Me = Na and Ag), J. Mater. Chem. 20 (2010) 2082. https://doi.org/10.1039/b921115b.

[5] N. Masó, D.I. Woodward, P.A. Thomas, A. Várez, A.R. West, Structural characterisation of ferroelectric $Ag_2Nb_4O_{11}$ and dielectric $Ag_2Ta_4O_{11}$, J. Mater. Chem. 21 (2011) 2715. https://doi.org/10.1039/c0jm02540b.

[6] P. Sciau, A. Kania, B. Dkhil, E. Suard, A. Ratuszna, Structural investigation of $AgNbO_3$ phases using x-ray and neutron diffraction, J. Phys.: Condens. Matter 16 (2004) 2795–2810. https://doi.org/10.1088/0953-8984/16/16/004.

[7] Y. Juang, S.-Y. Chu, K.S. Wang, Phase transition and dielectric properties of Sr-doped $AgNbO_3$ ceramics, Ferroelectrics 493 (2016) 54–61. https://doi.org/10.1080/00150193.2016.1133216.

[8] G. Li, T. Kako, D. Wang, Z. Zou, J. Ye, Enhanced photocatalytic activity of La-doped $AgNbO_3$ under visible light irradiation, Dalton Trans. (2009) 2423. https://doi.org/10.1039/b810126d.

[9] Y. Zhu, W. Zhou, J. Yu, Y. Chen, M. Liu, Z. Shao, Enhancing Electrocatalytic Activity of Perovskite Oxides by Tuning Cation Deficiency for Oxygen Reduction and Evolution Reactions, Chem. Mater. 28 (2016) 1691–1697. https://doi.org/10.1021/acs.chemmater.5b04457.

[10] K. V., K. A., T. E., V. A., N. E., J. J., F. J., Mixed conductivity and stability of A-site-deficient $Sr(Fe,Ti)O_{3-\delta}$ perovskites, Journal of Solid State Electrochemistry 7 (2002) 30–36. https://doi.org/10.1007/s10008-002-0286-3.

[11] X. Li, Z. Lin, N. Jin, X. Yang, L. Sun, Y. Wang, L. Xie, X. Chen, L. Lei, P. Rozier, P. Simon, Y. Liu, Boosting the lithium-ion storage performance of perovskite $SrVO_{3-\delta}$ via Sr

cation and O anion deficient engineering, Science Bulletin 67 (2022) 2305–2315. https://doi.org/10.1016/j.scib.2022.11.006.

[12] C.-Z. Ke, F. Liu, Z.-M. Zheng, H.-H. Zhang, M.-T. Cai, M. Li, Q.-Z. Yan, H.-X. Chen, Q.-B. Zhang, Boosting lithium storage performance of Si nanoparticles via thin carbon and nitrogen/phosphorus co-doped two-dimensional carbon sheet dual encapsulation, Rare Met. 40 (2021) 1347–1356. https://doi.org/10.1007/s12598-021-01716-1.

[13] C. Ke, R. Shao, Y. Zhang, Z. Sun, S. Qi, H. Zhang, M. Li, Z. Chen, Y. Wang, B. Sa, H. Lin, H. Liu, M. Wang, S. Chen, Q. Zhang, Synergistic Engineering of Heterointerface and Architecture in New-Type ZnS/Sn Heterostructures In Situ Encapsulated in Nitrogen-Doped Carbon Toward High-Efficient Lithium-Ion Storage, Adv Funct Materials 32 (2022) 2205635. https://doi.org/10.1002/adfm.202205635.

[14] A. Khan, M. Orbay, N. Dupré, E. Gautron, E.L. Calvez, O. Crosnier, A. Balducci, T. Brousse, Lithium storage behaviour of $AgNbO_3$ perovskite: Understanding electrochemical activation and charge storage mechanisms, Energy Storage Materials 70 (2024) 103431. https://doi.org/10.1016/j.ensm.2024.103431.

[15] V. Augustyn, P. Simon, B. Dunn, Pseudocapacitive oxide materials for high-rate electrochemical energy storage, Energy Environ. Sci. 7 (2014) 1597. https://doi.org/10.1039/c3ee44164d.

[16] M.-X. Shi, M. Wu, S.-S. Xiao, S.-P. Liu, R.-Q. Yao, Y.-Q. Li, Y.-H. Wang, Y.-G. Li, H.-Q. Tan, Amorphous $NiMo_3S_{13}$/nickel foam integrated anode for lithium-ion batteries, Tungsten 6 (2024) 438–446. https://doi.org/10.1007/s42864-022-00201-1.

[17] P. Jing, M. Liu, H.-P. Ho, Y. Ma, W. Hua, H. Li, N. Guo, Y. Ding, W. Zhang, H. Chen, B. Zhao, J. Wang, M. Liu, Tailoring the Wadsley–Roth crystallographic shear structures for high-power lithium-ion batteries, Energy Environ. Sci. (2024) 10.1039.D4EE02293A. https://doi.org/10.1039/D4EE02293A.

[18] C. Chen, Ionic conductivity, lithium insertion and extraction of lanthanum lithium titanate, Solid State Ionics 144 (2001) 51–57. https://doi.org/10.1016/S0167-2738(01)00884-0.

Chapter 3: Study of Li^+ storage in tailored perovskite $K_{1-3x}La_x\square_{2x}NbO_3$ ($0 \leq x \leq 0.15$) negative electrode materials

3.1 Introduction

As discussed in Chapter 1, ABO_3 perovskites are versatile structures that can be modified in numerous ways to enhance their properties. The studies presented in Chapter 2 on the $Ag_{1-3x}La_x\square_{2x}NbO_3$ perovskite system demonstrate the significant impact of substitution-driven vacancies on Li^+ storage performance. Specifically, this modification results in increased specific capacity, improved fast-charging capabilities, and enhanced cycling stability. However, the electrochemical reduction of Ag from the A-site of the $Ag_{1-3x}La_x\square_{2x}NbO_3$ structure restricts the cycling stability to a narrow potential window of 1.2–3.0 V vs. Li^+/Li. Extending the cycling beyond this potential range leads to structural collapse and poor cyclic stability. Therefore, it is essential to explore alternative hosts to $AgNbO_3$ perovskites for more robust and stable electrochemical performance.

Interestingly, there are several other thermodynamically stable Nb-based cubic perovskites with monovalent A-site cations in the form of $A^{1+}Nb^{5+}O_3$. These primarily include alkali metal-based perovskites such as $LiNbO_3$, $KNbO_3$, $NaNbO_3$, and $RbNbO_3$ [1,2]. All of these materials form a perovskite structure with Nb^{5+} as the B-site cation, similar to $AgNbO_3$ although alternative crystallographic structures can be obtained. This structural similarity contributes to their closely related chemical and electronic properties. The presence of Nb^{5+} in all these compounds is expected to build comparable bonding environment and electronic structure. However, due to the differing A-site cations, the thermodynamic stability and the effects of substitution may vary significantly. Additionally, their Li^+ storage behavior and performance could differ as well because the variations in the A-site cation can influence factors such as ion mobility, defect formation, and overall electrochemical stability. Therefore, detailed investigations are required to fully understand and optimize their performance.

Alkali metal-based niobates are cost-effective and sustainable alternatives to $AgNbO_3$. In terms of abundance, Na and K are the most readily available, followed by Li, which is moderately abundant compared to Ag. For instance, according to Mineral Commodity Summaries 2024, the abundance of Li is about 20 parts per million (ppm), Na is 23,000 ppm, and K is 15,000 ppm, whereas Ag is only about 0.075 ppm [3]. This abundance directly impacts the cost, For example, when comparing the costs of the pure metals, Li is priced at approximately \$100 to

$150 per kilogram (kg), Na is about $2 to $3 per kg, and K costs around $35 to $40 per kg. In contrast, Ag is much more expensive, at approximately $752 per Kg [3,4]. This cost difference directly impacts the feasibility of using $AgNbO_3$ versus alkali niobates like $LiNbO_3$, $NaNbO_3$, and $KNbO_3$ in large-scale applications. While $AgNbO_3$ offer advantageous properties such as good electrical conductivity, which enable its fast Li^+ storage behavior, its high cost makes it less attractive for commercial battery applications. Tailoring cheaper alkali metal niobates for such applications may provide economically viable alternatives with similar functionality.

Based on the above discussion, the $KNbO_3$ host perovskite structure was chosen to extend the developed strategy from the model system to a more cost-effective and practical system. Designing $K_{1-3x}La_x\square_{2x}NbO_3$ ($0 \leq x \leq 0.15$) perovskite system is expected to offer multiple advantages in creating a versatile material. This system is expected to enhance Li^+ storage performance due to the presence of vacancies in its structure. Furthermore, the appropriate size of the K vacancies may enable compatibility with K^+ insertion, a feature that was not achievable with $Ag_{1-3x}La_x\square_{2x}NbO_3$ when used for Na^+ storage [5]. Therefore, $K_{1-3x}La_x\square_{2x}NbO_3$ ($0 \leq x \leq 0.15$) perovskite system is designed, synthesized and structure-property relationship as negative electrode for Li^+ storage is investigated in detail. The next section present the main results about this new compounds which have also been reported in the manuscript entitled “Effect of A-site deficiency on Li^+ storage in tailored perovskite $K_{1-3x}La_x\square_{2x}NbO_3$ ($0 \leq x \leq 0.15$) negative electrode” which is submitted for publication.

3.2 Submitted paper

Effect of A-site deficiency on Li^+ storage in tailored perovskite $K_{1-3x}La_x\square_{2x}NbO_3$ ($0 \leq x \leq 0.15$) negative electrode

Abbas Khan[1,2], Eric Quarez[1], Nicolas Dupré[1], Eric Gautron[1], Andrea Balducci[3], Olivier Crosnier[1,2], Thierry Brousse[1,2]*

[1]*Nantes Université, CNRS, Institut des Matériaux de Nantes Jean Rouxel, IMN, F-44000 Nantes, France*
[2]*Réseau sur le Stockage Electrochimique de l’Energie (RS2E), CNRS FR 3459, 80039 Amiens, France*
[3]*Friedrich-Schiller-University Jena, Institute of Technical Chemistry and Environmental Chemistry and Center for Energy and Environmental Chemistry, Philosophenweg 7a, 07743 Jena, Germany*

* Corresponding Author

Graphical Abstract

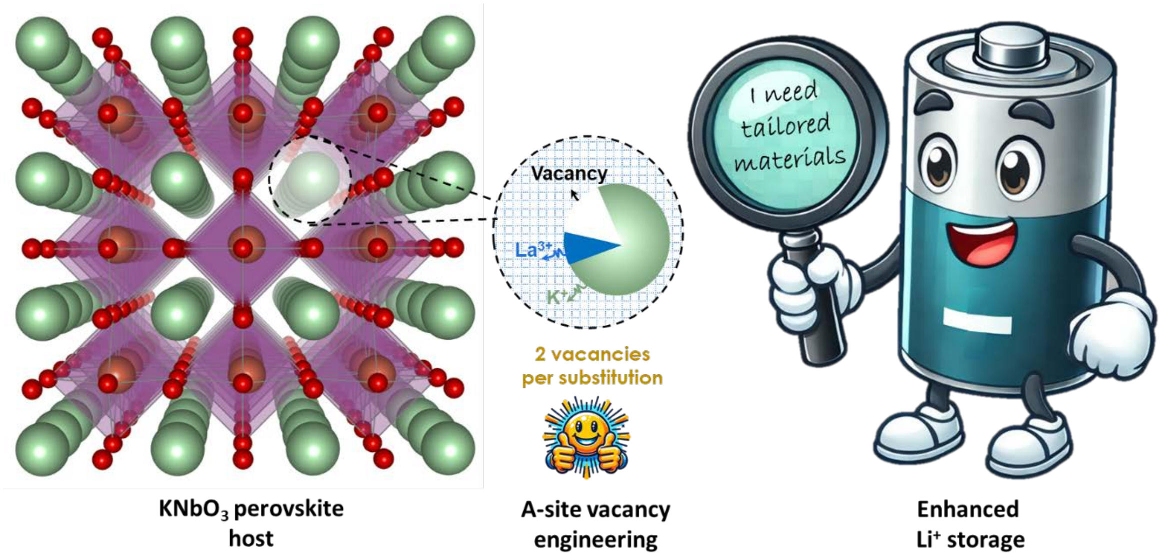

Abstract

Design of tailored materials using innovative approaches that allow faster charging/discharging processes could be the key for improvement of electric mobility. In this work, a strategy is developed to modify $KNbO_3$ perovskite structure by partially substituting K^+ with La^{3+} at A-site of structure, creating two cationic vacancies per cationic substitution in the lattice. Materials according to general formula $K_{1-3x}La_x\square_{2x}NbO_3$ (with $0 \leq x \leq 0.15$; $\square$ is an A-site vacancy) have been synthesized by sol-gel method. With La-substitution and creation of artificial vacancies in the structure, $KNbO_3$ become activated for Li^+ insertion. The highly substituted $K_{0.55}La_{0.15}\square_{0.30}NbO_3$ (30% atomic A-site vacancies) exhibited 164 mAh g^{-1} at 0.02 $A.g^{-1}$ in 0.05 – 3.0 V vs Li^+/Li potential window. *Ex situ* ^7Li and ^{93}Nb MAS NMR confirmed an increased Li^+ insertion in relation to vacancies and corresponding changes in Nb^{5+} local environment, respectively. *In situ* XRD analysis revealed a solid solution type storage mechanism with a maximum volume change of only 1.3% upon Li^+ insertion. This accounts for the remarkable capacity retention obtained after 900 cycles at 0.1 $A.g^{-1}$. Diverged from the classical design of insertion materials, this study presents an alternative approach of creating vacancies without sacrificing the pristine phase, with a possibility to use not so common class of ABO_3-type perovskites as battery electrode.

Key words: Transition metal oxide, negative electrode, lithium ion battery, perovskite, vacancies

Introduction

The advancement of electric cars and autonomous vehicles for future mobility necessitates the emergence of novel electrode materials that can sustain fast charge/discharge rates in Li-ion batteries (LIBs). Design of new materials and strategies could be the key that allow faster charging/discharging processes [1,2]. Graphite being the commercially known negative electrode material for LIBs, has major issues against fast charging. It has an average lithiation potential of approximately 0.1 V vs. Li^+/Li, which poses a risk of lithium plating at high current rates, potentially leading to a short circuit in battery cell [3,4]. In this regard, spinel $Li_4Ti_5O_{12}$ (LTO) has been successfully implemented as an alternative to graphite for fast charging applications. It can reversibly store Li^+ in the structure at quite high average potential of 1.55 V vs. Li^+/Li, while exhibiting nearly zero-strain characteristics [5,6]. Recently, Nb-based Wadsley-Roth phases with 3D open structures such as $TiNb_2O_7$ [7], $Nb_{16}W_5O_{55}$ [8] and, PNb_9O_{25} [9] have gained great interest as high power negative electrode owing to their fast kinetics, robust ion diffusion, and good structural stability. Among other transition metal oxides with open crystallographic structures and high specific capacities, ReO_3 perovskite stands out delivering a specific capacity of 228 $mAh.g^{-1}$ thanks to 2 Li^+ inserted per transition metal cation [10]. However, Li^+ insertion in the structure built by corner-shared $[ReO_6]$ octahedra causes a significant volume change due to octahedral distortions and results in low cyclability. Therefore, the urge of insertion hosts materials with tailored structures and fast Li^+ diffusion is growing rapidly, together with a need of a deeper understanding of charge storage mechanism in such structures.

To relieve the lattice strain induced upon Li^+ insertion and avoid structural collapse in BO_3-type structures, ABO_3-type perovskites can be an interesting choice where the presence of an A-site atom in the center of the perovskite cage can enhance structural stability. However, due to all crystallographic sites being occupied, such structures are expected to exhibit only negligible Li^+ storage capacity. Our group recently demonstrated a strategy to tailor ABO_3-type perovskite structure, by partially substituting A-site to create vacancies, thus activating the structures for Li^+ insertion. Based on general formula $Ag_{1-3x}La_x\square_{2x}NbO_3$, (with $x \leq 0.20$; where $\square$ is a A-site vacancy), model materials were designed with artificial vacancies in the structure that allow fast Li^+ insertion following a solid-solution type mechanism [11]. The highly substituted ($x = 0.15$) material achieved a maximum specific capacity of 35 $mAh.g^{-1}$ at a scan rate of 0.1 $mV.s^{-1}$, with 95% capacity retention after 800 cycles within a potential window of 1.2 – 3.0 V vs. Li^+/Li. Moreover, when charge/discharge at a constant current of 2 $A.g^{-1}$, the capacity is still 30 mAh.g^{-1}. However, these structures have quite a narrow stability potential window. This is primarily due to silver cation (Ag^+) sensitivity towards external stimuli, which results in its reduction followed by exsolution from the structure of metallic silver when exposed to extended potential windows [12]. Subsequently, we initiated a study to transfer the concept from the model $AgNbO_3$ structure to a more cost-effective and abundantly available $KNbO_3$. Additionally, the stability of K^+ in the structure can be leveraged to extend the potential window range versus Li^+/Li. To the best of our knowledge, this material has never been investigated as a LIB electrode.

$KNbO_3$ has been widely studied as lead-free ferroelectric, piezoelectric, and electro-optic perovskite material [13–15]. Cation doping in the structure reported significantly enhanced structural and functional properties. Structurally, $KNbO_3$ is built by K^+ cations in the center of the perovskite cage with a coordination number (CN) of 12 and Nb^{5+} with CN of 6 form corner-shared $[NbO_6]$ octahedral. For given coordination, the ionic radius of K^+ is 1.64 Å, whereas that of Nb^{5+} is 0.64 Å [16]. The structure has an ability to accommodate other cations of slightly different sizes and varied oxidation states at A-site. For example, monovalent Li^+ or Na^+, divalent Ca^{2+}, and trivalent Sm^{3+} substitutions at A-site of the structure have been reported previously [17–20]. While monovalent dopants induce strains in the structure due to size mismatch and favored a phase stabilization, di- or trivalent dopant requires an additional charge compensation. Notably, in most of the cases, the charge compensation has been reported because of oxygen vacancies. Specifically, Dudhe *et al.*, studied the cubic-orthorhombic phase transition in $KNbO_3$ by varying oxygen vacancies through La-doping at A-site [21]. However, effect of substitution dependent cation vacancies on the structure of $KNbO_3$ has rarely been examined.

In the present study, we propose a strategy to create A-site vacancies in $KNbO_3$ by partial substitution of K^+ with La^{3+} according to general formula $K_{1-3x}La_x\square_{2x}NbO_3$ (with $0 \leq x \leq 0.15$; $\square$ is an A-site vacancy). Pure phase compounds were synthesised by sol-gel method. In-depth analysis of the effect of cation substitutions on the structure was investigated through X-ray diffraction refinements coupled with observation of microstrutural changes. Subsequently, the effect of A-site vacancies on Li^+ storage behaviour was investigated using different degree of substitution. The compounds with vacancies exhibited a solid-solution type mechanism upon lithiation with low volume expansion, which leads to a good cycling stability of $K_{1-3x}La_x\square_{2x}NbO_3$ electrodes.

Experimental

Material synthesis

$K_{1-3x}La_x\square_{2x}NbO_3$ perovskites were synthesized by sol-gel route. Stoichiometric amounts of potassium nitrate (KNO_3 by Alfa Aesar, 99.9%), lanthanum nitrate hexahydrated (La $(NO_3)_3.6H_2O$ by Sigma Aldrich, 99.99% trace metals basis) and niobium (V) ammonium oxalate hydrate ($C_4H_4NNbO_9{\cdot}xH_2O$ by Sigma Aldrich, 99.99% trace metals basis) were dissolved in 30 ml 30% (w/w) H_2O_2 in DI water (Sigma Aldrich) and stirred at room temperature. Citric acid monohydrated ($HOC(COOH)(CH_2COOH)_2 \cdot H_2O$ by Sigma Aldrich, ≥ 98% GC/titration) was added to the solution in 2:1 cation molar ratio and stirred until transparent solution was obtained. Citric acid acted as a complexing agent of which carboxyl and hydroxyl groups were occupied by K^+ and Nb^{5+}, respectively, through chelation reaction. The pH of reaction was adjusted to 6.5 by ammonium hydroxide (NH_3(aq), Sigma Aldrich). The solution was heated to 90 °C while stirring. Wet gel was obtained and converted to xerogel when kept in oven at 250 °C. The final materials were obtained by grinding xerogel and annealing at 600 °C in air for 2 hrs. The samples with varied La content were prepared and named as pristine $KNbO_3$, $K_{0.85}La_{0.05}\square_{0.10}NbO_3$, $K_{0.70}La_{0.10}\square_{0.20}NbO_3$, $K_{0.55}La_{0.15}\square_{0.30}NbO_3$, and $K_{0.40}La_{0.20}\square_{0.40}NbO_3$. Schematic illustration of synthesis route is presented in Figure S1.

Physical characterizations

XRD measurements were performed on powder samples using PANalytical X'Pert Pro-diffractometer (Malvern Panalytical, Almelo, Netherlands) with Cu-Kα1-Kα2 (λ = 1.54060 Å, 1.54443 Å) radiation source and acceleration voltage of 40 kV at a current of 40 mA. Data were recorded in the 2 theta range of 20° - 80°. For *in situ* XRD measurements, a Swagelok-type cell with beryllium window on top was used (Leriche *et al.*, 2010). The data were collected at 2 theta range between 20° and 70°. The BET specific surface area of powders were calculated using N_2 adsorption–desorption isotherms at 77K with a Quantachrome Nova 4200e equipment (Anton Paar). The SEM of powders and cycled electrodes and EDX were performed by Zeiss MERLIN Instrument using in-Lens annular detector at an operating voltage of 20 kV. To prepare the samples, a small fraction of powder/electrode was sticked on carbon tape. *Ex situ* ^7Li and ^{93}Nb MAS NMR experiments were acquired on a Bruker Avance-500 spectrometer (B_0=11.75T), Larmor frequencies ν_0 were 122.41 MHz and 194.37 MHz at room temperature for ^{93}Nb and ^7Li, respectively. A spectral analysis carried out using Bruker MAS probe with a cylindrical 2.5 mm o.d zirconia rotor at a spinning frequency of 25 kHz. NMR spectra was obtained by applying a single pulse sequence, and a recycle delay (D_1) of 3 sec. to guarantee quantitative spectra. The resulting integrated intensities were normalized with respect to number of counts, mass of the sample, and receiver gain. Transmission electron microscopy (TEM) was performed with an aberration-corrected S/TEM Themis Z G3 (Thermo Fisher Scientific) microscope. Powder samples dispersed in ethanol were spread on a holey carbon coated Cu grids. High-angle annular dark-field (HAADF) STEM images of the pristine sample were recorded at 300 kV, with 21.4 mrad convergence angle and 65–200 mrad collection angles. A Super-X system (four energy-dispersive X-ray detectors) was used to obtain atomic scale elemental maps. Due to the degradation of substituted sample under the beam at 300 kV, attempts were made to obtain TEM results at 80 kV.

Electrochemical measurements

Free standing electrodes (WE) containing 75% wt. active material, 15% wt. conducting agent (Carbon Black by Superior Graphite, Chicago, IL, United States) and 10% wt. binder (poly (1,1,2,2-tetrafluoroethylene - PTFE in H_2O, Sigma Aldrich) were fabricated *via* cold rolling by using few drops of ethanol as solvent. Electrode mass loadings ranged from 5 – 8 $mg.cm^{-2}$. 1M $LiPF_6$ dissolved in 1:1 %wt. EC/DMC (Solvionic, France, battery grade) was selected as the electrolyte. Two terminal Swagelok cells were used to study the electrochemical behavior of $K_{1-3x}La_x\square_{2x}NbO_3$ electrodes in WE/electrolyte soaked in separator/Li metal configuration. GF/D Whatman glass fiber membrane of 10 mm diameter was used as separator. Electrochemical studies were performed using VMP-3 and MPG-200 potentiostats (Biologic with ECLab software). Cell assembly and postmortem experiments were conducted in an argon-filled glovebox (O_2 and H_2O <1 ppm). *In situ* XRD measurements were performed at a low current density of 0.01 Ag^{-1} with a 1 hour pattern acquisition and relaxation time, and under 0.05 – 3.0V potential window *vs.* Li^+/Li. For *ex situ* NMR measurements, electrodes were cycled at different cut-off potentials vs Li^+/Li using cyclic voltammetry at a low scan rate of 0.1 $mV.s^{-1}$. An open circuit potential step (OCP) of 40 hours was performed at each cut-off. For *ex situ* analysis, cells were disassembled in glove box and electrodes were washed in DMC solution.

Results and Discussion

Crystal structure and physical characterizations

XRD analysis of $KNbO_3$, $K_{0.85}La_{0.05}\square_{0.10}NbO_3$ and $K_{0.55}La_{0.15}\square_{0.30}NbO_3$ powders was performed to investigate the changes in the crystal structure upon substitution. All the samples exhibited single phase with no discernible impurity phases. Rietveld refinements confirmed the orthorhombic structure of $KNbO_3$ (Amm2 space group) as reported previously [22,23]. The refinements using a higher symmetry space group (R3m) have been performed as well; however, they did not give a good agreement, validating the use of orthorhombic space group. As La^{3+} has an ionic radius of 1.36 Å for the given coordination, it can effectively substitute K^+ with ionic radius of 1.64 Å at the A-site. Therefore, partial substitution according to general formula $K_{1-3x}La_x\square_{2x}NbO_3$ is systematically introduced into the structure until the appearance of any secondary phase. Reaction for K^+ to La^{3+} substitution is described by Eq. 1:

$$La_2O_3 \rightarrow\ 2La_K^{\cdot\cdot} +\ 3O_O^x + 4V_K' \tag{1}$$

Considering charge neutrality, the effect of substitution at the same Wyckoff position is compensated by generating cationic vacancies, without altering the anion concentration. The diffractograms of $KNbO_3$, $K_{0.85}La_{0.05}\square_{0.10}NbO_3$, and $K_{0.55}La_{0.15}\square_{0.30}NbO_3$ indicate the phase-pure synthesis of materials with a successful La substitution up to x = 0.15. The Goldschmidt tolerance factor (t) calculated for $KNbO_3$ was 1.06. Such value suggests the formation of stable perovskite structure [24,25]. However, due to vacancies in the La-substituted structures, the t values decreased to 0.99 and 0.87 for x = 0.05 and x = 0.15, respectively. Considering the smaller ionic radius of La^{3+} compared to K^+ as well as the presence of vacancies, these values still corresponds to a perovskite structure. These values may correspond to a perovskite structure with reduced stability of perovskite cage. This was confirmed in case of materials synthesized with La-substitutions above 15% where perovskite structure was eventually disturbed and for which a secondary phase of $K_2Nb_6O_{17}$ was detected (Figure S2a).

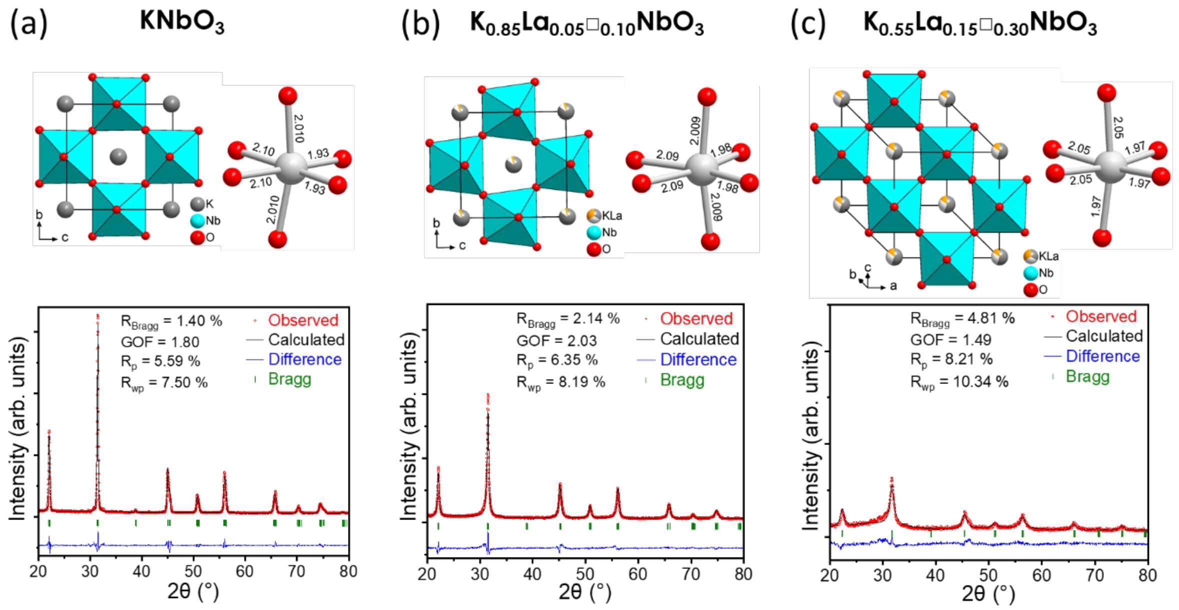

Figure 1. Crystal structure illustration and Rietveld refinement results of powder XRD patterns with experimental, calculated, and difference of (a) Pristine $KNbO_3$ (b) $K_{0.85}La_{0.05}\square_{0.10}NbO_3$ (c) $K_{0.55}La_{0.15}\square_{0.30}NbO_3$ materials. Bond lengths in the $[NbO_6]$ octahedra are given in angstroms (Å). Bond valence sums derived from these bond lengths yield values of 4.70(15), 4.50(17), and 4.6(4) for the Nb1 site, respectively.

Rietveld refinements analysis showed that by increasing La-substitution, the structure transforms to a more symmetrical space group (from Amm2 to R3m in case of higher substitution) as shown in Figure 1a-c. This is mainly due to a reduced $[NbO]_6$ octahedra distortion, which stabilizes the local structure by increasing configuration entropy. With La-substitution at A-site, the reflections of diffraction patterns systematically transformed to a broader full widths at half-maxima and lower intensities indicating a stress caused by substitution of La atom in the lattice, which limits the grain growth. This difference implies that there is a trend of reduced crystallite size concomitant with La substitution, which is in agreement with SEM observations. A ~90% reduction of crystallite size is obtained for 15% La substitution compared to pristine material (from 125 nm to 10 nm) which is a significant change unlike what is commonly reported in the literature [19,21]. $K_{1-3x}La_x\square_{2x}NbO_3$ system inhibits more disorder due to a cumulative effect of La substitution and cationic vacancies. This can be possibly explained in two ways: i) partially replacing K^+ with La^{3+} creates a mismatch in ionic radii, as a result the structure attempts to accommodate the size difference, which causes local distortions in the lattice due to substitution-induced strain effect, and ii) The creation of cation vacancies disrupts the long-range order, increasing the number of grain boundaries within the material. Furthermore, the artificial vacancies and La-substitution might not be uniformly distributed, leading to the regions with varying degrees of strains and defects. This inhomogeneous strain distribution contributes to the observed peak asymmetry in substituted compounds. The details of space group, lattice parameters, cell volume and crystallite sizes of all the samples obtained through refinements are presented in Table 1.

Table 1. Crystal structure, lattice parameters, and crystallite size details of $K_{1-3x}La_x\square_{2x}NbO_3$ for $0 \leq x \leq 0.15$ samples obtained by Rietveld refinements.

Formula	**Space group**	**a (Å)**	**b (Å)**	**c (Å)**	**V (Å³)**	**Crystallite size (nm)**
$KNbO_3$	Amm2	3.99562(16)	5.6870(4)	5.6999(4)	129.520(14)	125(2)
$K_{0.85}La_{0.05}\square_{0.10}NbO_3$	Amm2	4.0011(5)	5.6716(11)	5.6878(11)	129.07(4)	26(1)
$K_{0.55}La_{0.15}\square_{0.30}NbO_3$	R3m	5.670(7)	-	6.930(18)	192.9(6)	10(1)

According to Figure S2b, the (101) and (200) main peaks position shifted toward higher 2θ, which represent a contraction of unit cell volume upon La-substitution. This decrease in cell volume is consistent with the replacement of K^+ ions by La^{3+} ions, which have a smaller ionic radius [26]. Specifically, the cell volumes for the structures with $x = 0$, $x = 0.05$ and $x = 0.15$ are 129.52 Å³, 129.07 Å³, and 128.6 Å³ (calculated as 192.9 Å³ × 2/3 for $x = 0.15$), respectively.

The aliovalent substitution of K^+ by La^{3+} leads either to the formation of cationic vacancies in the A site, or to the introduction of interstitial oxygen sites, although the latter is structurally unlikely to happen in our case. Further details of adopted refinement model and obtained results are presented in Table S1 in supplementary information.

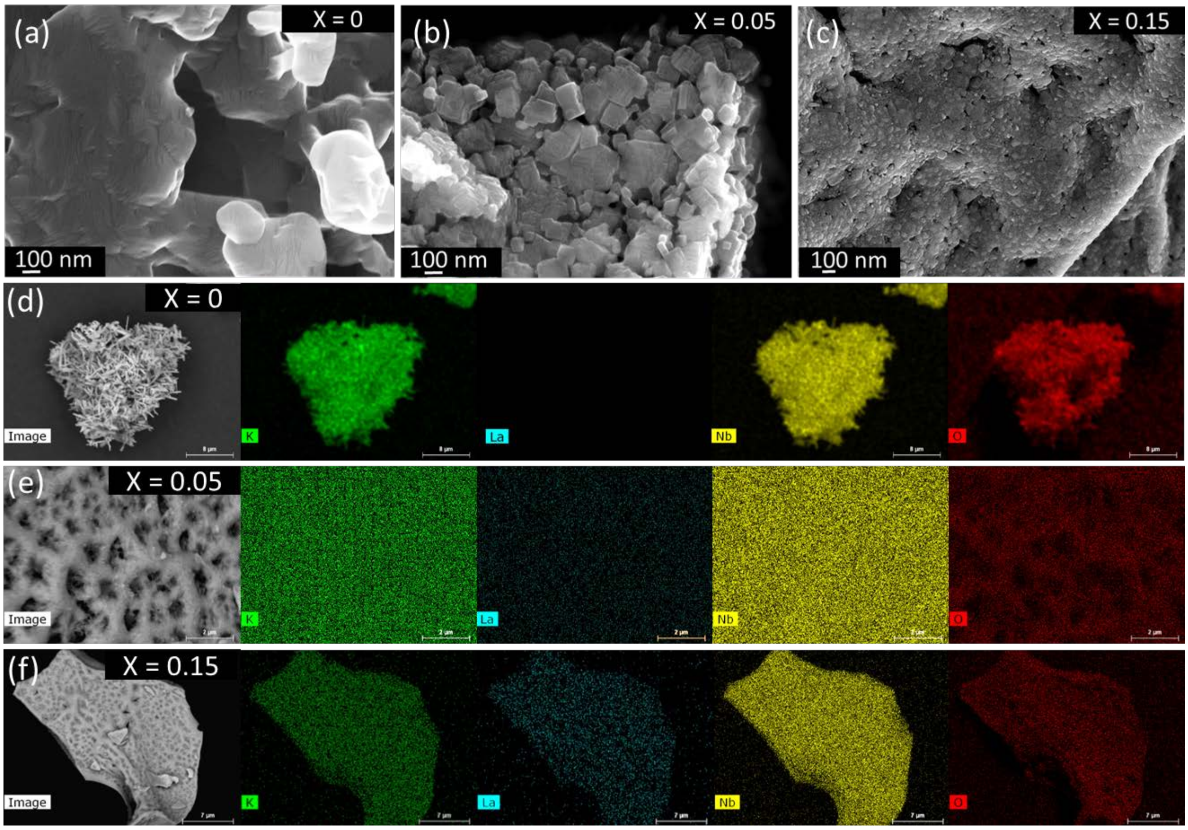

Figure 2. Effect of La substitution on morphology of materials. SEM images of (a) $KNbO_3$ *(Pristine) (b)* $K_{0.85}La_{0.05}\square_{0.10}NbO_3$ *(5% La substitution) (c)* $K_{0.55}La_{0.15}\square_{0.30}NbO_3$ *(15% La substitution). EDX mapping showing a uniform distribution of elements in (d)* $KNbO_3$ *(Pristine) (e)* $K_{0.85}La_{0.05}\square_{0.10}NbO_3$ *(5% La substitution) (f)* $K_{0.55}La_{0.15}\square_{0.30}NbO_3$ *(15% La substitution).*

La substitutions affects the morphology of the material as observed by SEM analysis. Figure 2a shows the $KNbO_3$ pristine material with lamellar textured rod shaped particles, which are necked together and agglomerated. Materials synthesized by sol-gel route typically exhibits agglomeration of smaller individual particles. With 5% of La substitution, the lamellar morphology becomes more pronounced into well-connected and stacked platelets (Figure 2b). However, at 15% La substitutions, the particles grow into spherical shape uniform morphology (Figure 2c). Further, the morphology at 10% La substitution is given in Figure S3. These results show a decrease in particle size by increasing La concentration, which is in agreement with XRD analysis. In addition, the EDX mapping in Figure 2d-f indicate the homogeneous distribution of cations in the materials.

To visualize the vacancies and their ordering in the structures, HAADF-STEM observations were attempted. Figure S4a shows HAADF-STEM image of $KNbO_3$ at low magnification which clearly evidences the absence of any defects or impurity in the material. In high resolution image, a well-defined atomic periodicity can be seen (Figure S4b). In Figure S4c, corresponding EDX map exhibits a uniform distribution of K and Nb atoms in agreement with crystal structure of a perovskite oxide. Individual EDX elemental distributions for K, Nb, and O are also shown in Figure S4d-f. Unfortunately, we were unsuccessful to attain such atomic maps for substituted samples because of phase change in materials under the electron beam (see Figure S5).

Due to decrease in particle size, the specific surface area of substituted materials increases, a characteristic confirmed by nitrogen adsorption BET measurements. As shown in Figure 3a, the surface area values obtained are 3, 15 and 18 $m^2.g^{-1}$ for $KNbO_3$, $K_{0.85}La_{0.05}\square_{0.10}NbO_3$ and $K_{0.55}La_{0.15}\square_{0.30}NbO_3$, respectively. In addition, these materials exhibit mesoporosity with an average pore size of 2 nm, and La-substitution has no significant effect on this value. The EDX elemental analysis of K, La, and Nb presented as bar chart in Figure 3b confirms the target composition in agreement with proposed chemical formula. The A to B-site cation ratios indicate the presence of vacancies in the substituted materials.

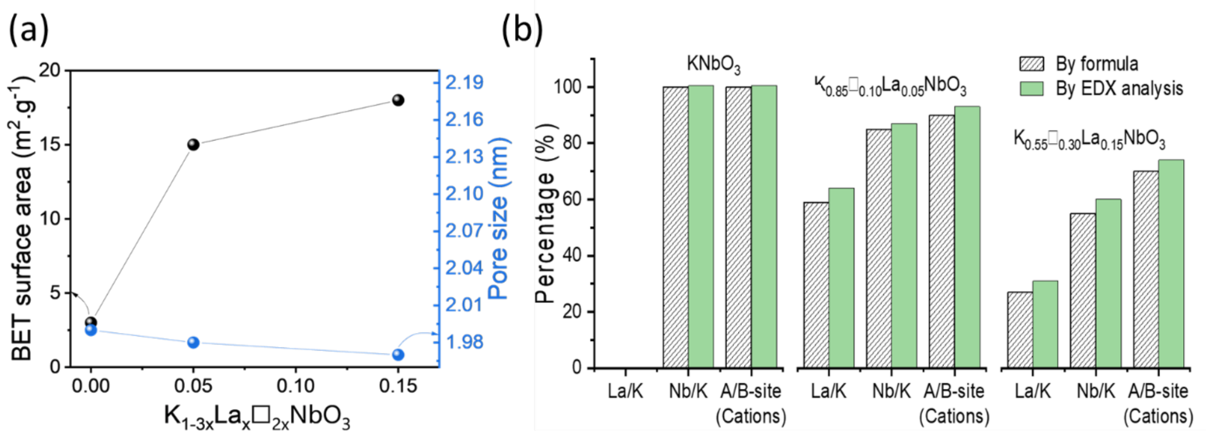

Figure 3. $K_{1-3x}La_x\square_{2x}NbO_3$ (x = 0, 0.01, 0.15) materials with: (a) Elemental contribution obtained by EDX and comparison with corresponding theoretical values. A-site/B-site confirms the presence of vacancies in the substituted structures. (b) Effect of La-substitution on BET surface area and pore size.

Li^+ storage behaviour of $K_{1-3x}La_x\square_{2x}NbO_3$ materials

The electrochemical measurements of $K_{1-3x}La_x\square_{2x}NbO_3$ materials at x = 0, 0.05, and 0,15 were performed to investigate the ability of the related structures to reversibly intercalate Li^+ cations. Cyclic voltammetry (CV) at low scan rate of 0.1 $mV.s^{-1}$ (which corresponds to 5 h of charge) within potential window of 1.2 – 3.0V vs. Li^+/Li was initially chosen based on the electrochemical stability window of typical Nb-based oxide materials reported in literature [27]. As shown in Figure 4a, the pristine $KNbO_3$ structure is closely packed and has no open channels whereas in case of La-substituted materials, vacancies exist and concomitantly Li^+ insertion can be expected. According to the results depicted in Figure 4b, $KNbO_3$ only exhibits negligible electrochemical activity, which corresponds to a specific capacity of 3 mAh.g^{-1}. The substituted materials at x = 0.05 and 0.15 show electrochemical activity with enhanced specific current giving a specific capacity of 12 and 30 mAh.g^{-1}, respectively. This indicates that the specific capacity increases with the amount of A site vacancies in the perovskite structure. Based on one lithium insertion per vacancy, the calculated theoretical capacities are 0, 15 and 43 mAh.g^{-1} for $KNbO_3$, $K_{0.85}La_{0.05}\square_{0.10}NbO_3$ and $K_{0.55}La_{0.15}\square_{0.30}NbO_3$, respectively, which are comparable with experimental values except for the $K_{0.55}La_{0.15}\square_{0.30}NbO_3$. The discrepancy observed for this latter compound can be attributed to the significantly reduced crystallinity and shrinkage of the unit cell due to higher La-substitution, which also affects vacancy concentration. Consequently, the consideration of one Li^+ insertion/vacancy is compromised. Li^+ insertion in the substituted structures can be considered by following reaction (Eq. 2):

$$K_{1-3x}La_{2x}\square_{2x}NbO_3 + yLi_x + ye^- \rightarrow Li_yK_{1-3x}La_{2x}\square_{2x}NbO_3 \tag{2}$$

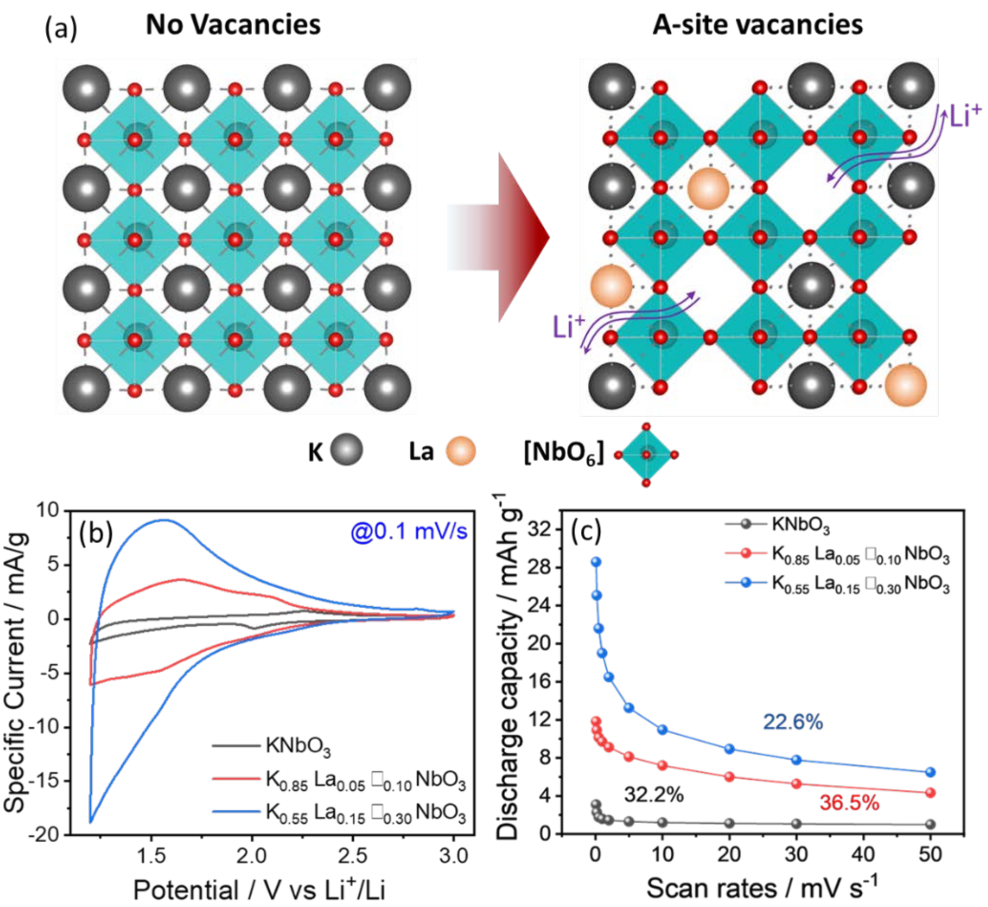

Figure 4. $K_{1-3x}La_x\square_{2x}NbO_3$ (x = 0, 0.05, 0.15) materials with (a) Structural representation, where A-site vacancies act as Li^+ insertion sites. (b) Cyclic voltamograms at 0.1 mV.s^{-1} in potential windows 1.2 – 3.0V vs. Li (c) Comparison of capacity retention at different scan rates.

With increasing sweep rate, the specific capacity decreases as shown in Figure 4c. At 2 mV.s^{-1} (15 min of oxidation or reduction scan), materials retained specific capacity with 50%, 75%

and 55% retention for $KNbO_3$, $K_{0.85}La_{0.05}\square_{0.10}NbO_3$ and $K_{0.55}La_{0.15}\square_{0.30}NbO_3$, respectively. CVs at different scan rates for all the samples are compared in Figure S6. In addition, at extremely high scan rate of 50 $mV.s^{-1}$ (36 sec of charge), a capacity retention of 32%, 36% and 23% were obtained for $KNbO_3$, $K_{0.85}La_{0.05}\square_{0.10}NbO_3$ and $K_{0.55}La_{0.15}\square_{0.30}NbO_3$, respectively. Despite low capacity values, these compounds are still able to intercalate Li^+ even at very fast scan rates.

To gain further insights about Li^+ storage behavior, electrochemical stability of these structures was investigated under extended potential windows *vs.* Li^+/Li. Interestingly, the materials withstand well for the reducing potentials up to 10 mV *vs.* Li. Although the CV shapes are well recovered after reaching lower cutoff potentials without significant electrochemical activity loss for pristine $KNbO_3$, a slight reduction in electrochemical activity was observed for highly substituted $K_{0.55}La_{0.15}\square_{0.30}NbO_3$, as shown in Figure S7. This implies that the substituted structures should undergo significant changes. This hypothesis has been investigated through *in situ* XRD analysis, which is provided in next section.

Crystal structure evolution during charge/discharge

In situ XRD analysis was performed to better understand the structural changes upon lithium (de) insertion into the different structures in order to elucidate underlying lithiation mechanism. Following the electrochemistry, two substituted samples ($K_{0.85}La_{0.05}\square_{0.10}NbO_3$ and $K_{0.55}La_{0.15}\square_{0.30}NbO_3$) were initially investigated in galvanostatic conditions at 0.01 $A.g^{-1}$ under extended potential window (0.05 – 3.0V vs. Li). To better visualize the patterns, the peaks associated to beryllium window were removed from the XRD patterns. Results in Figure 5a show that i) existing peaks do not disappear and no new peaks appear during the lithiation and delithiation processes, indicating that $K_{0.85}La_{0.05}\square_{0.10}NbO_3$ follows a solid solution mechanism as previously reported for other compounds in the literature, [28,29] and ii) the structure exhibits no significant peak shift for the (101), (200), (022), and (222) peaks, which implies that lattice parameters are not significantly affected during Li^+ insertion into vacancies. These characteristics confirm the "zero strain" nature of the $K_{0.85}La_{0.05}\square_{0.10}NbO_3$ material, similar to the A-site vacant structures reported by Le Calvez *et al.* [11] However, upon further investigation, a slight reduction in diffraction peak intensities with a minor shift in peak positions was observed during lithiation. While it was difficult to accurately determine and compare the peak shifts along the preferred direction due to minimal shift, Rietveld refinements were performed to obtain deeper insights.

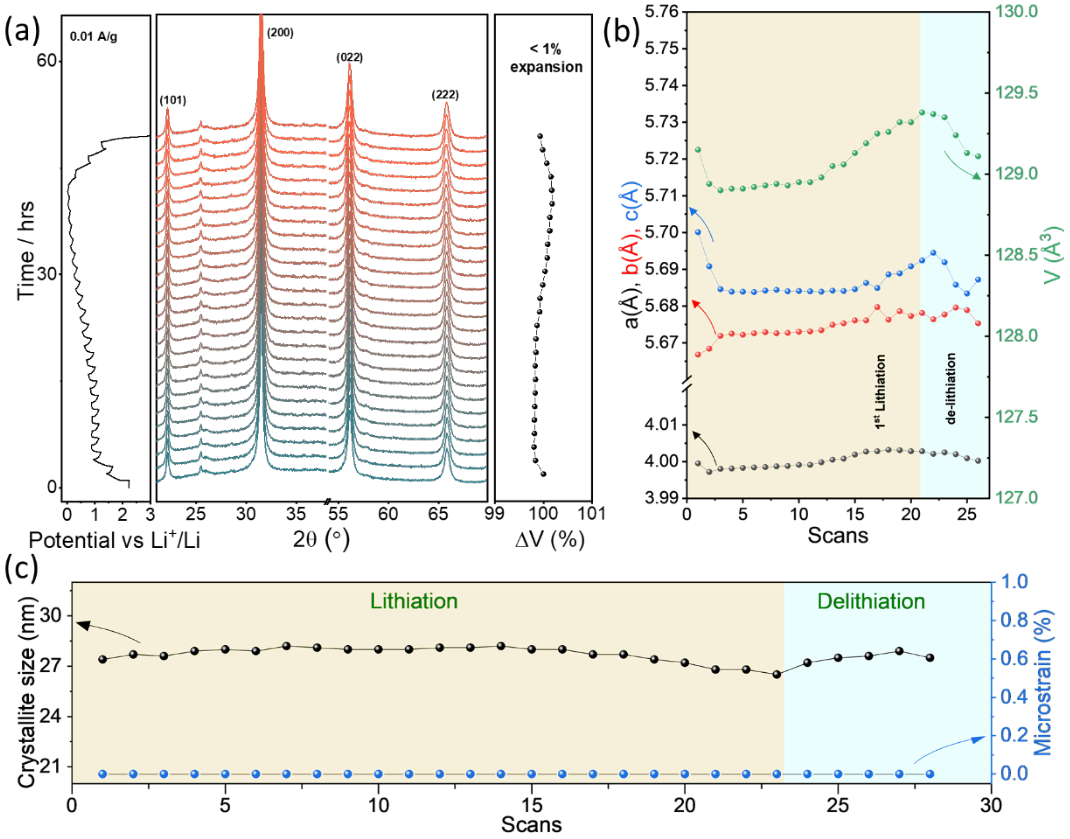

Figure 5. In situ XRD characterizations of $K_{0.85}La_{0.05}\square_{0.10}NbO_3$ sample at 0.01 A.g^{-1} (a) XRD patterns with corresponding potential-time curve and percentage volume variations upon 1st cycle. (b) Rietveld refinement results showing lattice parameter and cell volume evolution. (c) Crystallite size and microstrain evolution upon 1st cycle lithiation-delithiation. No change in microstrains indicate "zero-strain" characteristics of $K_{0.85}La_{0.05}\square_{0.10}NbO_3$ material.

The refinements were successful and results at OCP were in agreement with the pristine powder samples, which indicate that electrode preparation process did not affect the structural integrity of the materials. $K_{0.85}La_{0.05}\square_{0.10}NbO_3$ shows a slight increase in lattice parameters indicating a volume expansion upon lithiation. However, the variations are quite small, with "c" parameter changing slightly more, as can be seen from Figure 5b. At the end of lithiation, a maximum volume expansion of less than 1% was obtained. During delithiation, almost a complete reversibility of lattice parameters towards the original state was achieved. In addition, lithiation-delithiation process causes a reversible change in apparent particle size without inducing any macrostrains (Figure 5c). This confirms that vacancies play a crucial role in balancing local strains, thereby enabling the material to achieve a "zero strain" characteristic. Such a behavior suggests that the structure remains intact upon reversible Li^+ insertion, which has significant effects on electrochemical performance, particularly cyclic stability.

The *in situ* XRD performed for $K_{0.55}La_{0.15}\square_{0.30}NbO_3$ and patterns are depicted in Figure 6a. It follows a structural evolution during (de) lithiation similar to $K_{0.85}La_{0.05}\square_{0.10}NbO_3$, however with more pronounced effects. At the end of lithiation, a noticeable peak shift is observed on the patterns unlike $K_{0.85}La_{0.05}\square_{0.10}NbO_3$, confirming an increased lithium insertion due to higher concentration of A-site vacancies (30%) in $K_{0.55}La_{0.15}\square_{0.30}NbO_3$. The refinement results in Figure 6b shows the variations in cell parameters during a complete lithiation-delithiation cycle. It can be noted that no preferential Li^+ insertion occurs as both “a” and “c” parameter evolve equally. It means that vacancies are distributed in a disordered fashion providing random pathways for Li^+ transport into the bulk of the electrode material. Interestingly, the volume expansion was still small with ~1.3% value obtained at the end of lithiation. However, the cell parameters and volume variations were irreversible upon delithiation, an effect that was less prominent in case of $K_{0.85}La_{0.05}\square_{0.10}NbO_3$.

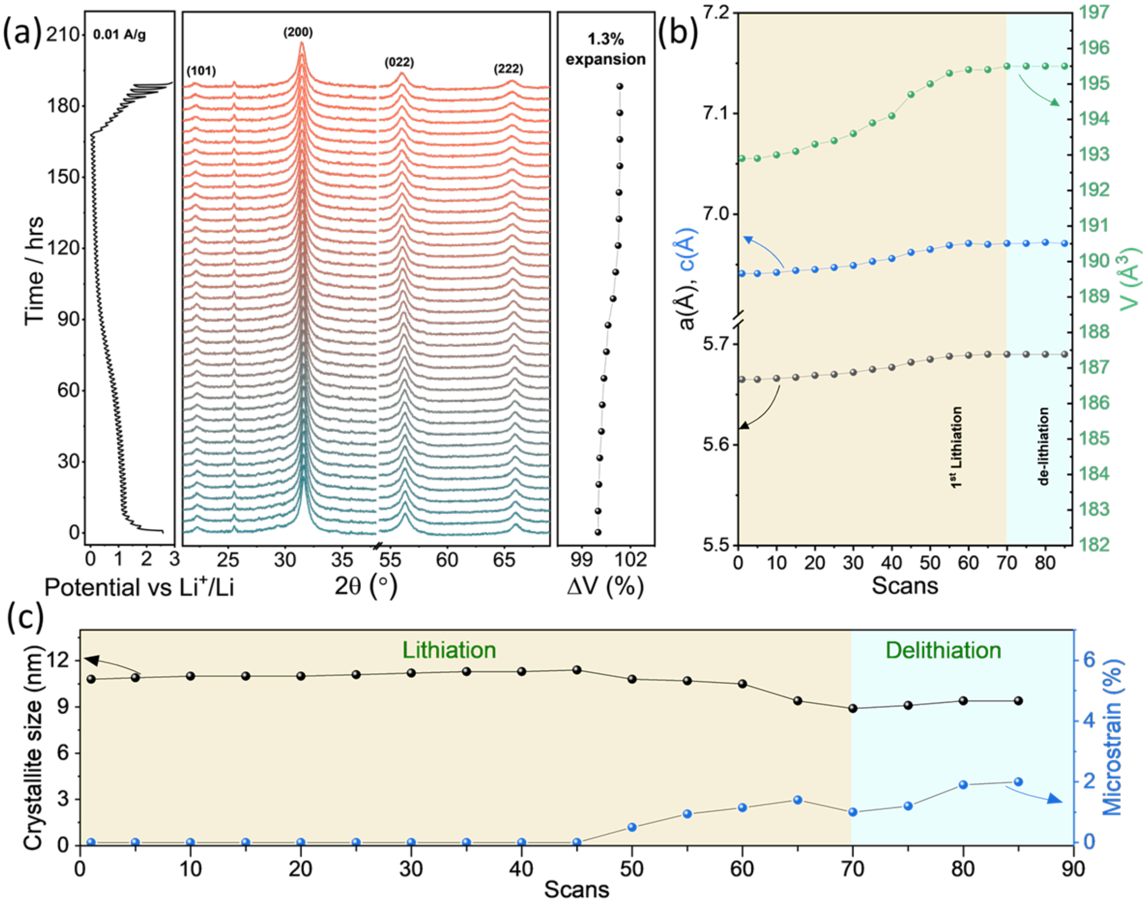

Figure 6. In situ XRD characterizations of $K_{0.55}La_{0.15}\square_{0.30}NbO_3$ sample at 0.01 $A.g^{-1}$ (a) XRD patterns with corresponding potential-time curve and percentage volume variations upon 1st cycle. (b) Rietveld refinement results showing lattice parameter and cell volume evolution. (c) Crystallite size and microstrain evolution upon 1st cycle lithiation-delithiation.

Additionally, Figure 6c shows that the local microstrains started to appear after 0.5V during 1st lithiation (a region with relatively enhanced ΔV), which were irreversible upon delithiation. One possible explanation can be that the Li^+ extraction from the structure upon delithiation is incomplete and some lithium irreversibly trapped in the structure during first cycle. Secondly, the crystallite size of material decreases, while cell volume and microstrain increases. This indicates that the particles undergo an irreversible and partial extrusion during lithiation, which helped to compensate the stresses induced by formation of lithiated phase

$Li_xK_{0.55}La_{0.15}\square_{0.30}NbO_3$. This effect has been reported in certain transition metal oxides, [30,31] where electrochemically induced partial amorphization enhances Li^+ storage performance. Albeit, since the global crystallinity of the material was preserved even under extreme reducing conditions (50 mV vs. Li^+/Li), the structure is expected to exhibit superior electrochemical cyclic stability. As a baseline, *in situ* XRD of pristine $KNbO_3$ was performed, and results are presented in Figure S8. It shows that the structural integrity is intrinsic to pristine material and well preserved in substituted material.

Li^+ insertion into the structure and changes in the Nb local environment are further supported by ^7Li and ^{93}Nb MAS NMR performed in *ex situ* mode. Solid-state NMR spectroscopy has been used as a powerful tool, which provides insights about electrochemical processes in battery materials [32–34]. Figure 7a corresponds to the cyclic voltammetry of $K_{0.85}La_{0.05}\square_{0.10}NbO_3$ electrodes whose cycling has been stopped at OCP (before any cycling), the end of lithiation (0.05 V vs Li^+/Li), and the end of delithiation (3.0 V vs Li^+/Li) after one complete cycle. A low scan rate of 0.1 $mV.s^{-1}$ was selected to ensure complete Li^+ insertion/extraction into the structure and the electrodes were subsequently polarized to allow thermodynamic equilibrium.

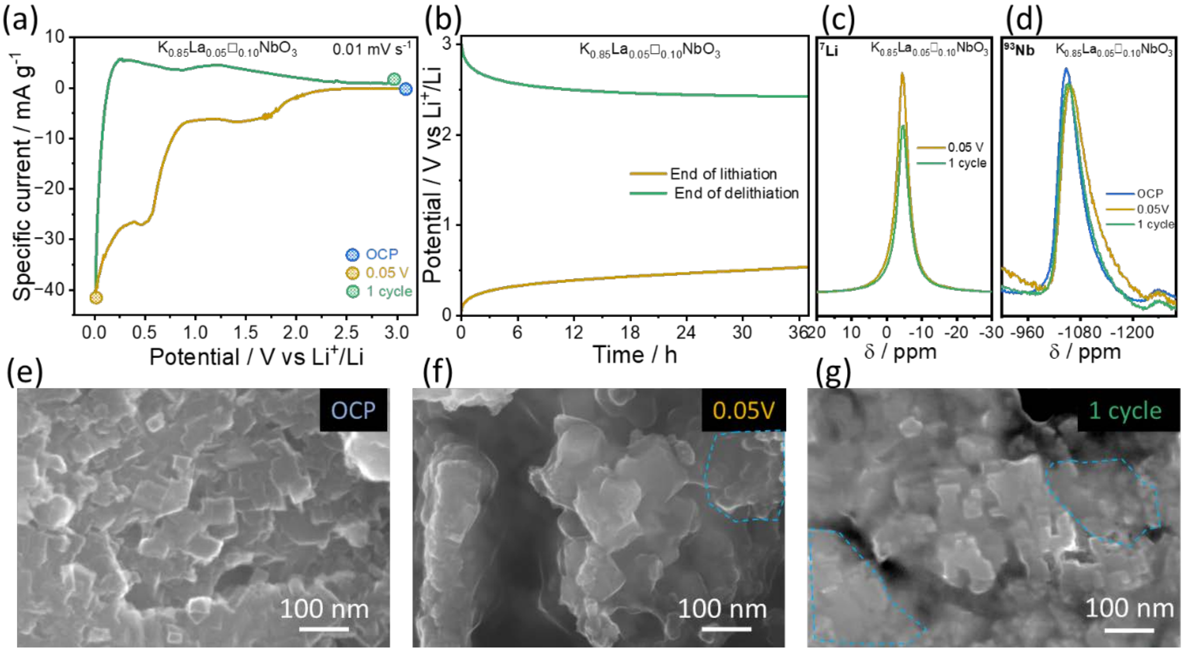

Figure 7. 1st cycle post-mortem diagnosis of $K_{0.85}La_{0.05}\square_{0.10}NbO_3$ through Ex situ NMR and ex situ SEM (a) Cyclic voltammetry of three cells cycled at different cut-off potentials OCP, 0.05V, and 1 complete cycle, respectively. (b) Self discharge curves after cut-off at 0.05V and 1 cycle. (c) ^7Li MAS NMR at 0.05V and 1 cycle cut-off. (d) ^{93}Nb MAS NMR at OCV, 0.05V and 1 cycle cut-off. Ex situ SEM at (e) OCP. (f) 0.05V cut-off. (g) After 1 complete cycle. Blue dotted area represent the SEI coverage on the particles.

After 36 hours under OCP conditions, the cells showed variations in potentials as they reached equilibrium. Specifically, the electrode at the 0.05 V cut-off potential stabilized at 0.5 V vs. Li^+/Li, while the electrode at the 3.0 V cut-off stabilized at 2.5 V vs. Li^+/Li, as illustrated in Figure 7b.The ^7Li MAS NMR results depicted in Figure 7c show the appearance of a sharp

NMR resonance signal at -5 ppm for the sample recovered at 0.05 V cut-off potential, indicating the presence of Li^+ in the structure. The peak intensity, normalized to the mass and number of scans, is directly proportional to the amount of Li^+ inserted. Upon delithiation to 3.0 V cut-off potential, a slight decrease in intensity occurs, indicating that only a partial extraction of Li^+ is observed, validating our hypothesis of Li^+ cations trapping during the first cycle as observed in other compounds [35]. Hence, this justifies the low coulombic efficiency during the first cycle as a combinatorial effect of incomplete Li^+ extraction. At the same time, main peak in ^{93}Nb MAS NMR spectrum slightly broadened with a reduced intensity at 0.05 V cut-off potential (Figure 7d). Due to partial Li^+ insertion, some Nb^{5+} (diamagnetic, electronic configuration in d^0) are reduced, probably to Nb^{4+} which are paramagnetic and display one localized electron. Due to the significant electron-nucleus dipolar interaction between the Nb nucleus and the unpaired localized electron at the same site, Nb^{4+} are typically unobservable by ^{93}Nb NMR. Therefore, only the remaining Nb^{5+} can still be detected. This explains the slightly reduced intensity in the ^{93}Nb MAS NMR spectrum. In addition, the formation of some Nb^{4+} will introduce structural distortions in Li and Nb local environments causing a peak broadening. It is accompanied by slight apparent shift in peak position (-1047 to -1054 δ/ppm), which is not completely reversible upon delithiation and may be assigned to the local distortions due to trapped Li cations in the vicinity of [Nb_6] octahedron. However, these effects are less prominent and almost reversible upon delithiation at 3.0 V vs Li^+/Li. Nevertheless, these results indicate that most of the Nb remains unreacted, maintaining 5+ oxidation state. Therefore, a moderated specific capacity is expected for $K_{0.85}La_{0.05}\square_{0.10}NbO_3$. Figure 7e-g show *ex situ* SEM of electrodes at OCV, 0.05 V, and 3.0 V cut-off, respectively. Compared to image at OCV, particles in lithiated and delithiated electrodes are covered with a thin blurry layer which is prominent in blue dotted regions and can be referred as SEI. However, the morphology appears to be unaffected. This analysis provides a basis for explaining the Li^+ insertion behavior of $K_{0.55}La_{0.15}\square_{0.30}NbO_3$. Figure 8a and 8b compare the CV curves at 0.05 V cut-off potential and ^7Li MAS NMR spectra of $K_{0.85}La_{0.05}\square_{0.10}NbO_3$ and $K_{0.55}La_{0.15}\square_{0.30}NbO_3$, respectively. ^7Li MAS NMR results reveal a 2.5-fold increase in lithium insertion into the $K_{0.55}La_{0.15}\square_{0.30}NbO_3$ structure upon lithiation, highlighting the role of high vacancy concentration. Simultaneously, ^{93}Nb MAS NMR confirms the significant reduction of Nb from 5+ to lower oxidation states, as resonance peak intensity significantly decreased (Figure 8c). Only a very low intensity and broad signal can still be observed, indicating that Nb^{5+} remains in very low concentration. However, direct observation of reduced Nb^{4+} and/or Nb^{3+} as well as the identification of nominal oxidation state is not realized, as no new peaks are detectable due to paramagnetic nature of Nb^{4+} (d^1) and Nb^{3+} (d^2) making them invisible to ^{93}Nb NMR in these experimental conditions.

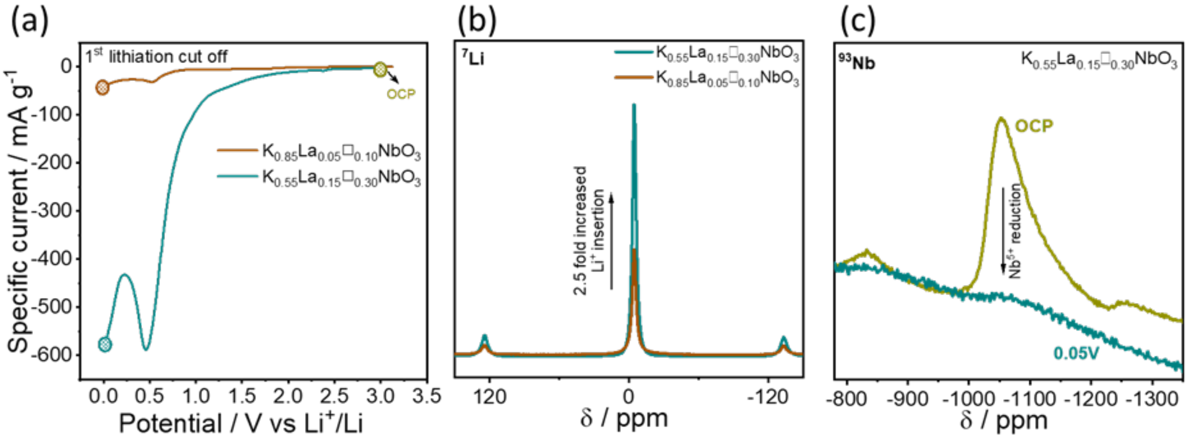

Figure 8. Ex situ NMR comparison for $K_{0.85}La_{0.05}\square_{0.10}NbO_3$ and $K_{0.55}La_{0.15}\square_{0.30}NbO_3$ at the end of lithiation (0.05V cut-off) (a) Cyclic voltammetry of $K_{0.85}La_{0.05}\square_{0.10}NbO_3$ and $K_{0.55}La_{0.15}\square_{0.30}NbO_3$ at 0.05V. (b) ^{7}Li MAS NMR comparison of $K_{0.85}La_{0.05}\square_{0.10}NbO_3$ and $K_{0.55}La_{0.15}\square_{0.30}NbO_3$ at 0.05V. (c) ^{93}Nb MAS NMR at OCP and 0.05V for $K_{0.55}La_{0.15}\square_{0.30}NbO_3$.

Li^+ storage performance under extended potential window

Li^+ storage performance of $K_{1-3x}La_x\square_{2x}NbO_3$ (x = 0, 0.05, 0.15) was investigated under extended potential window (0.05 – 3.0V vs Li^+/Li) in two electrode Swagelok cells. The cyclic voltammetry (CV) comparison at 0.5 mV.s^{-1} is presented in Figure 9a, where substituted materials exhibit more pronounced activity than the pristine perovskite compound, as evidenced by an increase in current response and broadening of CV shape. For $K_{0.55}La_{0.15}\square_{0.30}NbO_3$, a pair of broad redox peaks appears around 1.2 V in addition to much broadened redox peaks at lower potentials vs Li^+/Li, which could be associated to Nb-redox activity [28,36,37]. These redox peaks are less prominent and appears at lower potential in case of $K_{0.85}La_{0.05}\square_{0.10}NbO_3$ and $KNbO_3$. This indicates that A-site vacancies enhance the Li^+ accessibility to the perovskite cage and concomitantly the vicinity of [NbO_6] octahedra. Nonetheless, the Nb activity is moderate, with redox potentials exhibiting slight shifts. These shifts are likely attributed to the local chemical environment and the disordered distribution of vacancies. Galvanostatic charge-discharge (GCPL) measurements were carried out and comparison of 1st lithiation curves are presented in Figure 9b. The plateau at 0.75 V becomes more prominent with La-substitution. It indicates slight irreversible changes in electrode materials during the 1st cycle as emphasized by *in situ* XRD analysis. Additionally, the effect might combined with electrolyte degradation and formation of passivation layer (SEI formation) as previously described [37,38]. It can be pointed out that a relatively higher particle extrusion effect in the $K_{0.55}La_{0.15}\square_{0.30}NbO_3$ material during the first cycle caused unstable SEI formation, an effect that persists in subsequent cycles as well. Figure 9c-e show the charge-discharge plots of pristine $KNbO_3$, $K_{0.85}La_{0.05}\square_{0.10}NbO_3$, and $K_{0.55}La_{0.15}\square_{0.30}NbO_3$ materials, respectively. The measurements were recorded at current densities ranging from 0.02 A.g^{-1} to 3.0 A.g^{-1}. Pristine $KNbO_3$ delivers 41 mAh.g^{-1} at 0.02 A.g^{-1} and 5 mAh.g^{-1} at 3 A.g^{-1}. Partially substituted $K_{0.85}La_{0.05}\square_{0.10}NbO_3$ delivered 80 mAh.g^{-1} at 0.02 A.g^{-1} and 21 mAh.g^{-1} at 3 A.g^{-1}, while highly substituted $K_{0.55}La_{0.15}\square_{0.30}NbO_3$ exhibited 164 mAh.g^{-1} at 0.02 A.g^{-1} and 20 mAh.g^{-1} at 3 A.g^{-1} (charge and discharge in 24s). This indicates at such high current density a capacity retention of 12, 26, and 12 % for $KNbO_3$, $K_{0.85}La_{0.05}\square_{0.10}NbO_3$, and $K_{0.55}La_{0.15}\square_{0.30}NbO_3$, respectively. The moderate rate performance of $KNbO_3$ could be due to intrinsic low electronic conductivity the host structure, as it has been widely known for semiconducting properties [39,24]. Overall performance comparison is shown in Figure 9f, where an unstable capacity was obtained during initial cycling as explained previously. The detailed comparison of capacity decay from cycle 2 to 7 is presented in Figure S9. It was observed that the relative capacity decay for all samples was the same, indicating that the presence of La in the structure does not have a detrimental effect on the electrochemical stability. Nevertheless, all the materials showed stable cycling afterwards while maintaining a high coulombic efficiency. Long term cycling of all the materials were investigated through galvanostatic charge-discharge at 0.1 A.g^{-1} for 900 cycles. Initially, cycling was started without constant temperature, which caused a capacity fluctuation and a constant temperature of 25 °C was adopted afterward. The results in Figure 9g depicts an initial capacity decay followed by stable cycling up to first 100 cycles. Interestingly, a constant increase in capacity over cycling is observed for all the three materials, which can be explained by the formation of stable electrode-electrolyte interphase. At the end of the cycling process, the specific capacities of $KNbO_3$, $K_{0.85}La_{0.05}\square_{0.10}NbO_3$, and $K_{0.55}La_{0.15}\square_{0.30}NbO_3$ were 49, 75, and 119 mAh.g^{-1}, respectively. These values indicate an increase of 39, 33, and 27% in specific capacity after 900 cycles considering the stable capacity values after initial decay. Postmortem analysis of cycled electrodes was performed using *ex situ* SEM. Given that all the materials exhibited similar trends in cyclic stability, $K_{0.55}La_{0.15}\square_{0.30}NbO_3$ was selected for further investigation due to its high performance. The results in Figures S10a and S10b show SEM images of cycled electrodes taken immediately under the electron beam and after a few seconds of focused exposure, respectively. The area highlighted by the green circle indicates the beam damage to the encapsulation layer, termed the SEI. The morphology of pristine $K_{0.55}La_{0.15}\square_{0.30}NbO_3$ powder in Figure S10c can be compared with the zoomed-in image of the cycled electrode in Figure S10d, where particles appear after the removal of the thick SEI under the beam. This observation explains the significant irreversible capacity in the first cycle and a capacity decay over subsequent cycles, which thickened the SEI until it became stable. Once stabilized, the material tends to regain capacity over extended cycling.

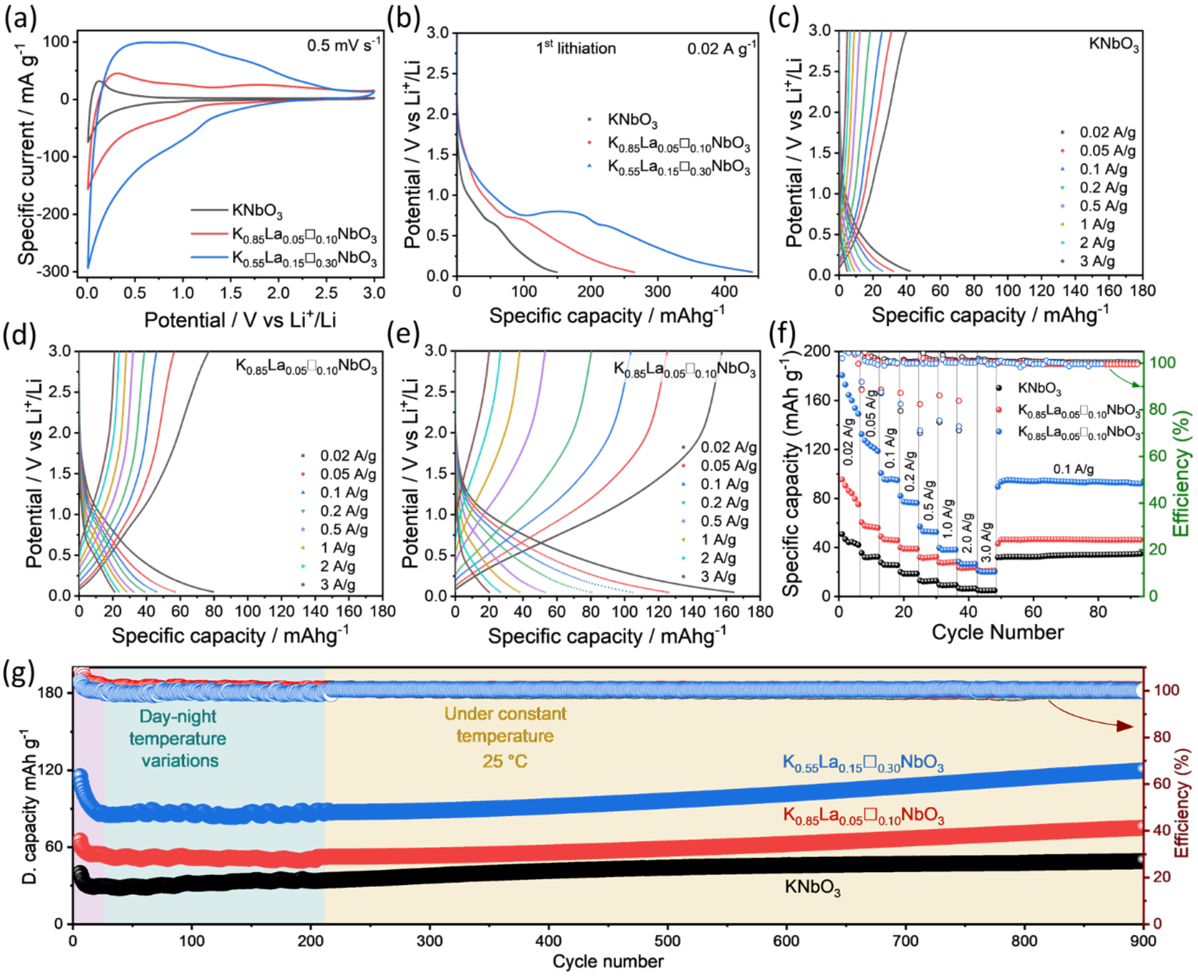

Figure 9. Li$^+$ storage performance of $K_{1-3x}La_x□_{2x}NbO_3$ (x = 0, 0.05, 0.15) materials under extended potential windows vs Li in half cell configurations. (a) CV comparison at 0.5 mV.s^{-1}. (b) 1st lithiation curve of GCPL measurements at 0.02 A.g^{-1}. GCPL curves at different current densities for: (c) pristine $KNbO_3$ electrode. (d) $K_{0.85}La_{0.05}□_{0.10}NbO_3$ electrode. (e) $K_{0.55}La_{0.15}□_{0.30}NbO_3$ electrode. (f) Overall performance comparison of all the samples. (g) Cyclic stability for 900 cycles at 0.1A.g^{-1}.

Conclusion

In our approach, we developed a strategy of creating artificial vacancies on atomic level in the lattice of a structure. $KNbO_3$ host structure is tailored by partial substitution of K$^+$ from A-site with La^{3+}, generating two vacancies per substitution. The materials were successfully synthesized and effect of substitutions on the structure was accurately investigated. An increase in lattice symmetry was obtained with La-substitutions on K$^+$ occupied A-site of the perovskite structure which results in transformation of space group from Amm2 of pristine $KNbO_3$ to R3m for $K_{0.55}La_{0.15}□_{0.30}NbO_3$. Electrochemical measurements confirmed an increase in performance of substituted material for Li$^+$ storage with 3-fold improvement of the specific capacity and better rate capability compared to pristine structure. Artificial vacancies in the structure acted as a Li^+ insertion sites that facilitated Li^+ accessibility to the perovskite cage and concomitantly the vicinity of $[NbO_6]$ octahedral. The structures exhibited enhanced electrochemical stability, as evidenced by a 50 mV vs Li^+/Li cut-off potential, a feature uncommon in Nb-based oxides. *In situ* XRD revealed a solid-solution mechanism with Li^+ migration in the structure without causing significant lattice disturbance. We chose a host structure with relatively low cost cations and importantly a cubic perovskite structure class that are not supposedly meant for ion storage. Vacancies in $K_{1-3x}La_x\square_{2x}NbO_3$ (x = 0, 0.05, 0.15) structure helped in enhanced Li^+ insertion and an increase in performance was achieved.

Acknowledgments

Abbas Khan as a part of the DESTINY PhD programme (Doctorate programme on Emerging battery Storage Technologies INspiring Young scientists) acknowledges funding from the European Union’s Horizon 2020 research and innovation programme under the Marie Skłodowska-Curie Actions Cofund Grant Agreement No: 945357. The authors also thank Nicolas Stephant for SEM images and Stéphane Grolleau for BET measurements. Measurements were performed using the IMN’s characterisation platform, PLASSMAT, Nantes, France.

References related to Paper

[1] M. Armand, J.-M. Tarascon, Building better batteries, Nature 451 (2008) 652–657. https://doi.org/10.1038/451652a.

[2] Y. Liu, Y. Zhu, Y. Cui, Challenges and opportunities towards fast-charging battery materials, Nat Energy 4 (2019) 540–550. https://doi.org/10.1038/s41560-019-0405-3.

[3] C. Uhlmann, J. Illig, M. Ender, R. Schuster, E. Ivers-Tiffée, In situ detection of lithium metal plating on graphite in experimental cells, Journal of Power Sources 279 (2015) 428–438. https://doi.org/10.1016/j.jpowsour.2015.01.046.

[4] C. Choi, D.S. Ashby, D.M. Butts, R.H. DeBlock, Q. Wei, J. Lau, B. Dunn, Achieving high energy density and high power density with pseudocapacitive materials, Nat Rev Mater 5 (2019) 5–19. https://doi.org/10.1038/s41578-019-0142-z.

[5] T. Ohzuku, A. Ueda, N. Yamamoto, Zero-Strain Insertion Material of $Li[Li_{1/3}Ti_{5/3}]O_4$ for Rechargeable Lithium Cells, J. Electrochem. Soc. 142 (1995) 1431–1435. https://doi.org/10.1149/1.2048592.

[6] A.S. Prakash, P. Manikandan, K. Ramesha, M. Sathiya, J.-M. Tarascon, A.K. Shukla, Solution-Combustion Synthesized Nanocrystalline $Li_4Ti_5O_{12}$ As High-Rate Performance Li-Ion Battery Anode, Chem. Mater. 22 (2010) 2857–2863. https://doi.org/10.1021/cm100071z.

[7] X. Lu, Z. Jian, Z. Fang, L. Gu, Y.-S. Hu, W. Chen, Z. Wang, L. Chen, Atomic-scale investigation on lithium storage mechanism in TiNb2O7, Energy Environ. Sci. 4 (2011) 2638. https://doi.org/10.1039/c0ee00808g.

[8] K.J. Griffith, K.M. Wiaderek, G. Cibin, L.E. Marbella, C.P. Grey, Niobium tungsten oxides for high-rate lithium-ion energy storage, Nature 559 (2018) 556–563. https://doi.org/10.1038/s41586-018-0347-0.

[9] M. Saber, M.B. Preefer, S.K. Kolli, W. Zhang, G. Laurita, B. Dunn, R. Seshadri, A. Van Der Ven, Role of Electronic Structure in Li Ordering and Chemical Strain in the Fast Charging Wadsley–Roth Phase PNb_9O_{25}, Chem. Mater. 33 (2021) 7755–7766. https://doi.org/10.1021/acs.chemmater.1c02059.

[10] N.H. Bashian, S. Zhou, M. Zuba, A.M. Ganose, J.W. Stiles, A. Ee, D.S. Ashby, D.O. Scanlon, L.F.J. Piper, B. Dunn, B.C. Melot, Correlated Polyhedral Rotations in the Absence of Polarons during Electrochemical Insertion of Lithium in ReO_3, ACS Energy Lett. 3 (2018) 2513–2519. https://doi.org/10.1021/acsenergylett.8b01179.

[11] E. Le Calvez, J.C. Espinosa-Angeles, G.J. Whang, N. Dupré, B.S. Dunn, O. Crosnier, T. Brousse, Investigating the Perovskite $Ag_{1-3x}La_xNbO_3$ as a High-Rate Negative Electrode for Li-Ion Batteries, Front. Chem. 10 (2022) 873783. https://doi.org/10.3389/fchem.2022.873783.

[12] A. Khan, M. Orbay, N. Dupré, E. Gautron, E.L. Calvez, O. Crosnier, A. Balducci, T. Brousse, Lithium storage behaviour of $AgNbO_3$ perovskite: Understanding electrochemical activation and charge storage mechanisms, Energy Storage Materials 70 (2024) 103431. https://doi.org/10.1016/j.ensm.2024.103431.

[13] D. Wang, G. Wang, Z. Lu, Z. Al-Jlaihawi, A. Feteira, Crystal Structure, Phase Transitions and Photoferroelectric Properties of $KNbO_3$-Based Lead-Free Ferroelectric Ceramics: A Brief Review, Front. Mater. 7 (2020) 91. https://doi.org/10.3389/fmats.2020.00091.

[14] M. Waqar, H. Wu, J. Chen, K. Yao, J. Wang, Evolution from Lead-Based to Lead-Free Piezoelectrics: Engineering of Lattices, Domains, Boundaries, and Defects Leading to Giant Response, Advanced Materials 34 (2022) 2106845. https://doi.org/10.1002/adma.202106845.

[15] M. Dubernet, M.J. Pitcher, M. Zaghrioui, M. Bah, J. Bustillo, F. Giovannelli, I. Monot-Laffez, Synthesis routes for enhanced piezoelectric properties in spark plasma sintered Ta-doped KNN ceramics, Journal of the European Ceramic Society 42 (2022) 2188–2194. https://doi.org/10.1016/j.jeurceramsoc.2021.12.030.

[16] R.D. Shannon, C.T. Prewitt, Effective ionic radii in oxides and fluorides, Acta Crystallogr B Struct Sci 25 (1969) 925–946. https://doi.org/10.1107/S0567740869003220.

[17] V.A. Trepakov, M.E. Savinov, V. Železný, P.P. Syrnikov, A. Deyneka, L. Jastrabik, Li doping effect on properties and phase transfomations of $KNbO_3$, Journal of the European Ceramic Society 27 (2007) 4071–4073. https://doi.org/10.1016/j.jeurceramsoc.2007.02.113.

[18] S.R. Burns, M.R. Dolgos, Sizing up $(K_{1-x}Na_x)NbO_3$ films: a review of synthesis routes, properties & applications, New J. Chem. 45 (2021) 7408–7436. https://doi.org/10.1039/D1NJ01092A.

[19] G. Song, Y. Song, J. Su, K. Zhang, L. Xing, H. Yang, N. Zhang, High temperature dielectric properties and magnetic behavior of $K_{1-x}Ca_xNbO_3$ ceramic, Physica B: Condensed Matter 602 (2021) 412593. https://doi.org/10.1016/j.physb.2020.412593.

[20] P.D. Durugkar, A.G. Katpatal, Growth and characterization of pure, and doped crystals of potassium niobate, Journal of Crystal Growth 162 (1996) 161–166. https://doi.org/10.1016/0022-0248(95)00924-8.

[21] C.M. Dudhe, S.J. Khambadkar, Oxygen vacancy dependent structural phases in $KNbO_3$, Materials Letters 216 (2018) 97–100. https://doi.org/10.1016/j.matlet.2018.01.011.

[22] S. Kawamura, E. Magome, C. Moriyoshi, Y. Kuroiwa, N. Taniguchi, H. Tanaka, S. Maki, M. Takata, S. Wada, Electronic Polarization in $KNbO_3$ Visualized by Synchrotron Radiation Powder Diffraction, Jpn. J. Appl. Phys. 52 (2013) 09KF04. https://doi.org/10.7567/JJAP.52.09KF04.

[23] A.W. Hewat, Cubic-tetragonal-orthorhombic-rhombohedral ferroelectric transitions in perovskite potassium niobate: neutron powder profile refinement of the structures, J. Phys. C: Solid State Phys. 6 (1973) 2559–2572. https://doi.org/10.1088/0022-3719/6/16/010.

[24] L. Zhou, Z. Bai, G. Wang, J. Li, M. Jin, X. Zhang, H. Peng, H. Zhao, Q. Fan, J. Zhou, X. Pan, Perovskite $KNbO_3$ nanostructure for high-response photoelectrochemical ultraviolet detector, J Mater Sci: Mater Electron 34 (2023) 2259. https://doi.org/10.1007/s10854-023-11699-7.

[25] X. Wang, Y. Huan, S. Ji, Y. Zhu, T. Wei, Z. Cheng, Ultra-high piezoelectric performance by rational tuning of heterovalent-ion doping in lead-free piezoelectric ceramics, Nano Energy 101 (2022) 107580. https://doi.org/10.1016/j.nanoen.2022.107580.

[26] X. Zhang, R. Qi, S. Dong, S. Yang, C. Jing, L. Sun, Y. Chen, X. Hong, P. Yang, F. Yue, J. Chu, Modulation of Ferroelectric and Optical Properties of La/Co-Doped $KNbO_3$ Ceramics, Nanomaterials 11 (2021) 2273. https://doi.org/10.3390/nano11092273.

[27] L. Yan, X. Rui, G. Chen, W. Xu, G. Zou, H. Luo, Recent advances in nanostructured Nb-based oxides for electrochemical energy storage, Nanoscale 8 (2016) 8443–8465. https://doi.org/10.1039/C6NR01340F.

[28] J. Come, V. Augustyn, J.W. Kim, P. Rozier, P.-L. Taberna, P. Gogotsi, J.W. Long, B. Dunn, P. Simon, Electrochemical Kinetics of Nanostructured Nb_2O_5 Electrodes, J. Electrochem. Soc. 161 (2014) A718–A725. https://doi.org/10.1149/2.040405jes.

[29] Q. Zhang, S. Ma, W. Wang, S. Gao, Y. Ou, S. Li, X. Liu, C. Lin, “Zero-strain” $K_2SrV_4O_{12}$ as a high-temperature friendly Li+-storage material, Energy Storage Materials 52 (2022) 637–645. https://doi.org/10.1016/j.ensm.2022.08.023.

[30] J. Wu, H.-W. Liu, A. Tang, W. Zhang, H.-S. Sheu, J.-F. Lee, Y.-F. Liao, S. Huang, M. Wei, N.-L. Wu, Unexpected reversible crystalline/amorphous (de)lithiation transformations enabling fast (dis)charge of high-capacity anatase mesocrystal anode, Nano Energy 102 (2022) 107715. https://doi.org/10.1016/j.nanoen.2022.107715.

[31] Z. Huang, H. Gao, Z. Yang, W. Jiang, Q. Wang, S. Wang, J. Ju, Y.-U. Kwon, Y. Zhao, Improved capacity and cycling stability of SnO_2 nanoanode induced by amorphization during cycling for lithium ion batteries, Materials & Design 180 (2019) 107973. https://doi.org/10.1016/j.matdes.2019.107973.

[32] O. Pecher, J. Carretero-González, K.J. Griffith, C.P. Grey, Materials' Methods: NMR in Battery Research, Chem. Mater. 29 (2017) 213–242. https://doi.org/10.1021/acs.chemmater.6b03183.

[33] C.P. Grey, N. Dupré, NMR Studies of Cathode Materials for Lithium-Ion Rechargeable Batteries, Chem. Rev. 104 (2004) 4493–4512. https://doi.org/10.1021/cr020734p.

[34] A. Kuhn, J.C. Pérez-Flores, M. Hoelzel, C. Baehtz, I. Sobrados, J. Sanz, F. García-Alvarado, Comprehensive investigation of the lithium insertion mechanism of the $Na_2Ti_6O_{13}$ anode material for Li-ion batteries, J. Mater. Chem. A 6 (2018) 443–455. https://doi.org/10.1039/C7TA09150H.

[35] E.L. Calvez, N. Dupré, É. Gautron, C. Douard, O. Crosnier, T. Brousse, Effect of particle microstructure and the role of proton on the lithium insertion properties of $HTiNbO_5$ electrode material, Electrochimica Acta 455 (2023) 142432. https://doi.org/10.1016/j.electacta.2023.142432.

[36] S. Liu, J. Zhou, Z. Cai, G. Fang, A. Pan, S. Liang, Nb_2O_5 microstructures: a high-performance anode for lithium ion batteries, Nanotechnology 27 (2016) 46LT01. https://doi.org/10.1088/0957-4484/27/46/46LT01.

[37] T. Yan, R. Ding, D. Ying, Y. Huang, Y. Huang, C. Tan, X. Sun, P. Gao, E. Liu, An intercalation pseudocapacitance-driven perovskite $NaNbO_3$ anode with superior kinetics and stability for advanced lithium-based dual-ion batteries, J. Mater. Chem. A 7 (2019) 22884–22888. https://doi.org/10.1039/C9TA09233A.

[38] T. Wang, T. Ge, S. Shi, M. Wu, G. Yang, Synthesis of wolframite $FeNbO_4$ nanorods as a novel anode material for improved lithium storage capability, Journal of Alloys and Compounds 740 (2018) 7–15. https://doi.org/10.1016/j.jallcom.2017.12.369.

[39] C.L. Diao, H.W. Zheng, The preparation and surface photovoltage characterization of $KNbO_3$ powder, J Mater Sci: Mater Electron 26 (2015) 3108–3111. https://doi.org/10.1007/s10854-015-2803-z.

Supplementary information associated to submitted paper

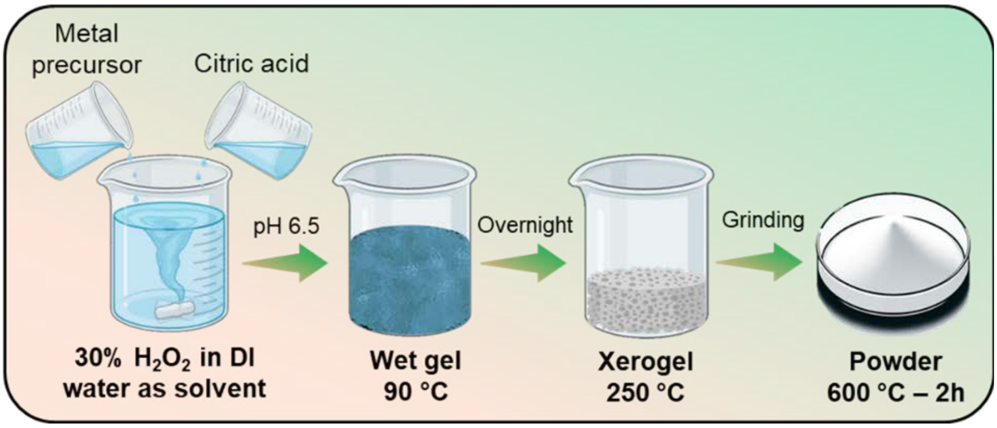

Figure S1. General schematic illustration of sol gel synthesis route for preparation of $K_{1-3x}La_x\square_{2x}NbO_3$ *at* $0 \leq x \leq 0.20$ *series of samples*

Table S1. Results of the Rietveld refinement of powder XRD patterns of $K_{1-3x}La_x\square_{2x}NbO_3$ *(with* $0 \leq x \leq 0.15$*;* $\square$ *is an A-site vacancy) materials.*

$KNbO_3$ – Amm2

Atoms	Wyckoff	x	y	z	Occ.	U_{iso} (Å^2)
K1	2a	0	0	-0.013(2)	1	0.0027(18)
Nb1	2b	1/2	0	0.5108(4)	1	0.0062(6)
O1	2a	0	0	0.471(6)	1	0.003(6)
O2	4e	1/2	0.253(7)	0.243(5)	1	0.011(3)

$K_{0.85}La_{0.05}\square_{0.10}NbO_3$ – Amm2

Atoms	Wyckoff	x	y	z	Occ.	U_{iso} (Å^2)
K1	2a	0	0	0.0024(17)	0.85	0.005
La1	2a	0	0	0.0024(17)	0.05	0.005
Nb1	2b	1/2	0	0.509(3)	1	0.0196(8)
O1	2a	0	0	0.541(12)	1	0.005
O2	4e	1/2	0.217(8)	0.212(7)	1	0.005

$K_{0.55}La_{0.15}\square_{0.30}NbO_3$ – R3m

Atoms	Wyckoff	x	y	z	Occ.	U_{iso} (Å^2)
K1	2a	0	0	0.009(3)	0.55	0.01
La1	2b	0	0	0.009(3)	0.15	0.01
Nb1	2a	0	0	0.510(6)	1	0.0184
O1	4e	0.159(6)	0.317(12)	0.319(14)	1	0.014(5)

Bond lengths and angles

Bonds	$KNbO_3$	$K_{0.85}La_{0.05}\square_{0.10}NbO_3$	$K_{0.55}La_{0.15}\square_{0.30}NbO_3$
Nb1–O1 x2	2.010(4)	2.009(7)	-
Nb1–O2 x2	1.93(3)	1.98(4)	-
Nb1–O2 x2	2.10(3)	2.09(4)	-
Nb1–O1 x3	-	-	1.97(7)
Nb1–O1 x3	-	-	2.05(8)
O–Nb1–O cis x12	85.3(7) – 94.4(7)	72.1(17) – 108.6(18)	82(3) – 98(3)
O–Nb1–O trans x3	167.2(14) – 176.7(13)	161.7(18) – 169(3)	169(4) x3

Distances (Å) and angle range (°) in [NbO_6] octahedral

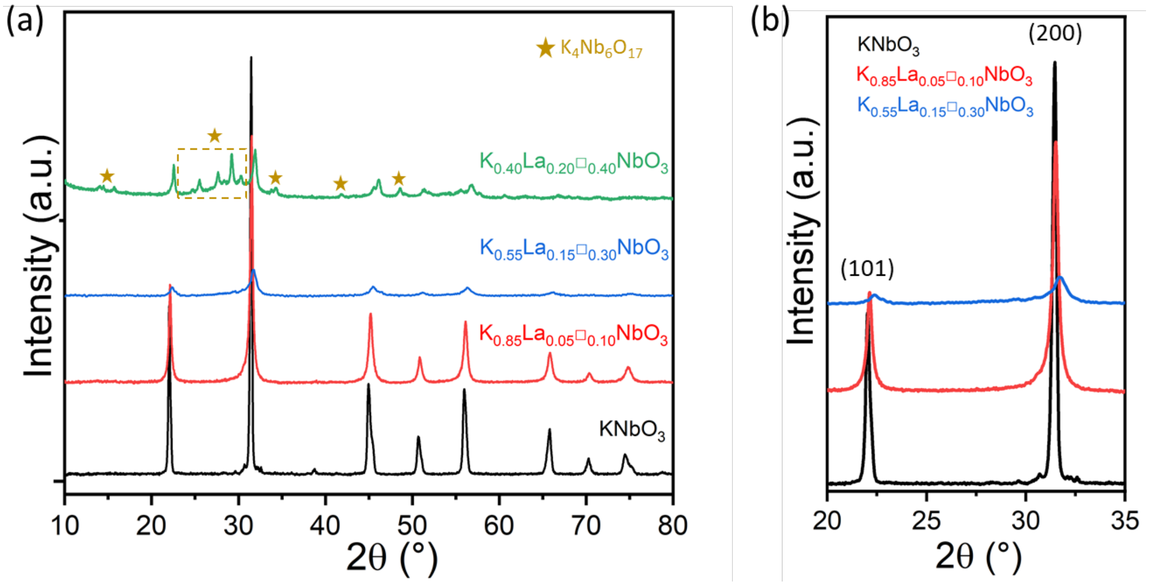

Figure S2. Powder XRD patterns of all the samples in $K_{1-3x}La_x\square_{2x}NbO_3$ *for* $0 \leq x \leq 0.20$ *series prepared by sol gel synthesis route. After 15% of La substitution, the perovskite structure started destabilizing with a significant appearance of secondary phase* $K_2Nb_6O_{17}$*. (b) Peak shift corresponding (101) and (200) planes toward higher 2θ with L-substitutions.*

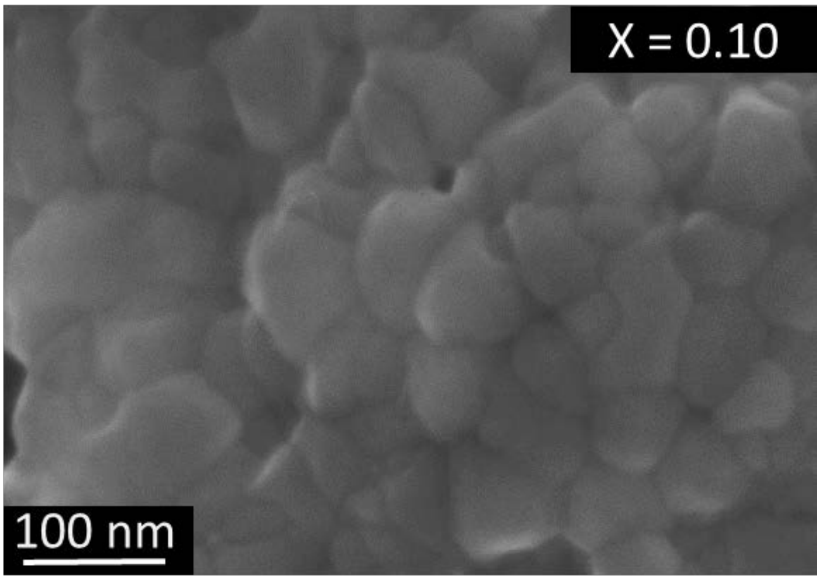

Figure S3. SEM images of $K_{0.70}La_{0.10}\square_{0.20}NbO_3$ (10% La substitution) showing a well-defined spherical particle growth.

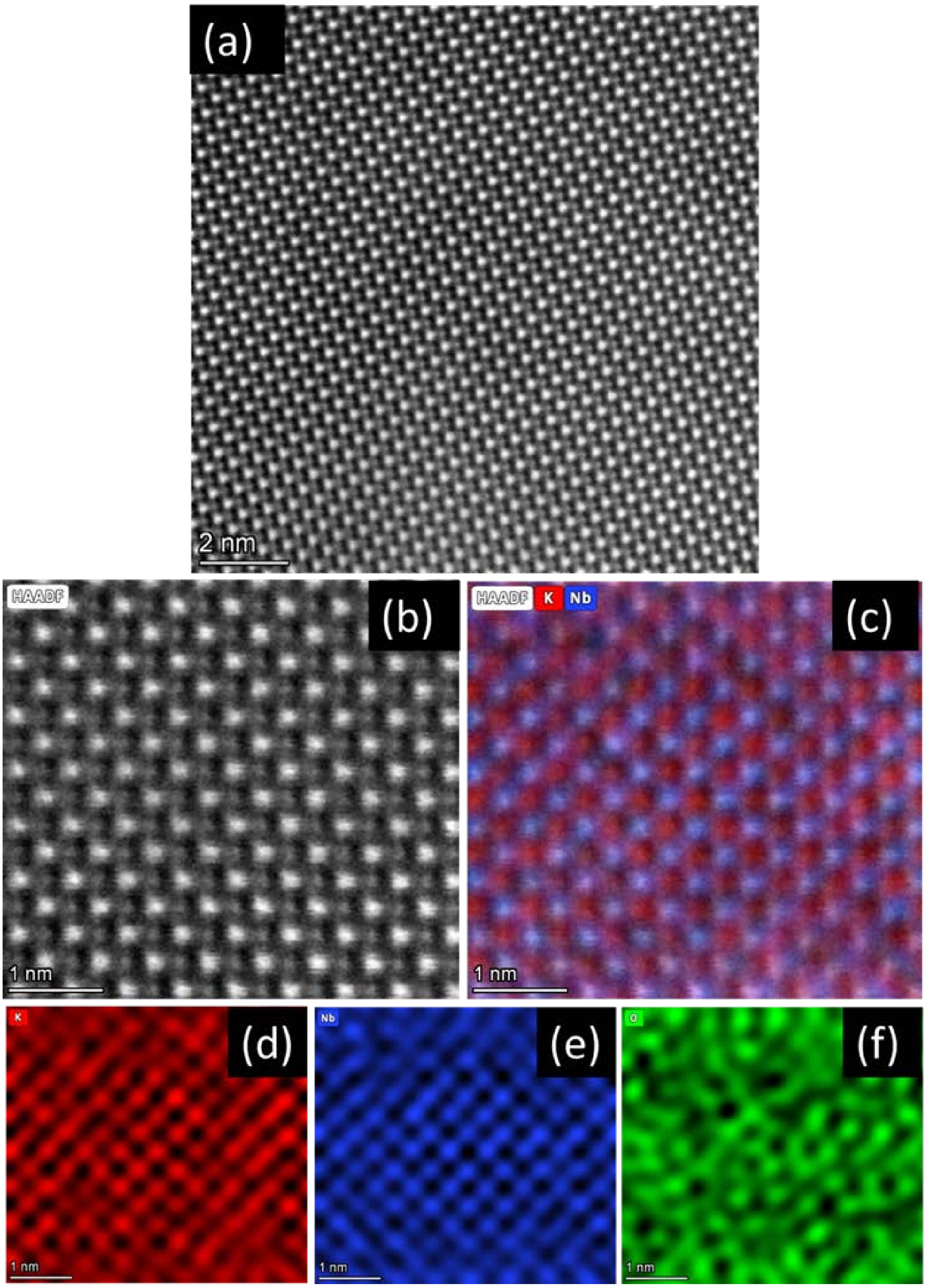

Figure S4. KNbO$_3$ (a) Experimental HAADF-STEM image (radial Wiener filtered) along [100] indicating absence of any defects. (b) At high resolution (c) Overlay of HAADF EDX image with K and Nb maps (d-f) EDX maps of KNbO$_3$ showing atomic distributions (K: red, Nb: blue, and O: green).

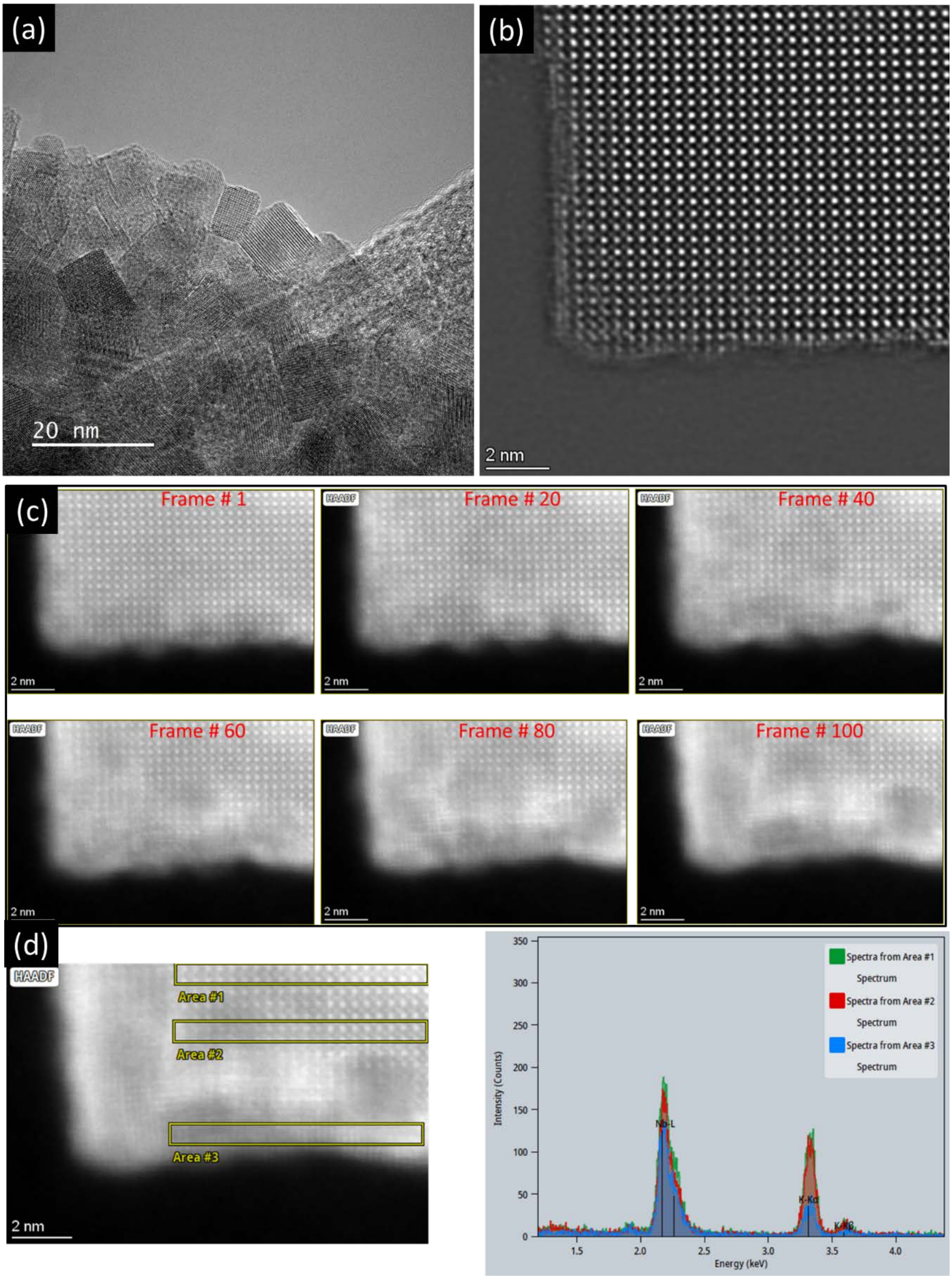

Figure S5. (a) TEM image of $K_{0.85}La_{0.05}\square_{0.10}NbO_3$. (b) HAADF-STEM image (High pass and Gaussian blur filtered) of a single crystal. c) evidence of $K_{0.85}La_{0.05}\square_{0.10}NbO_3$ sample degradation during EDX mapping (from 1st frame to 100th frame). d) EDX spectra integrated in different area of the particle after 100 frames. K atomic percentage decreases in the most degraded area (surface of the particle).

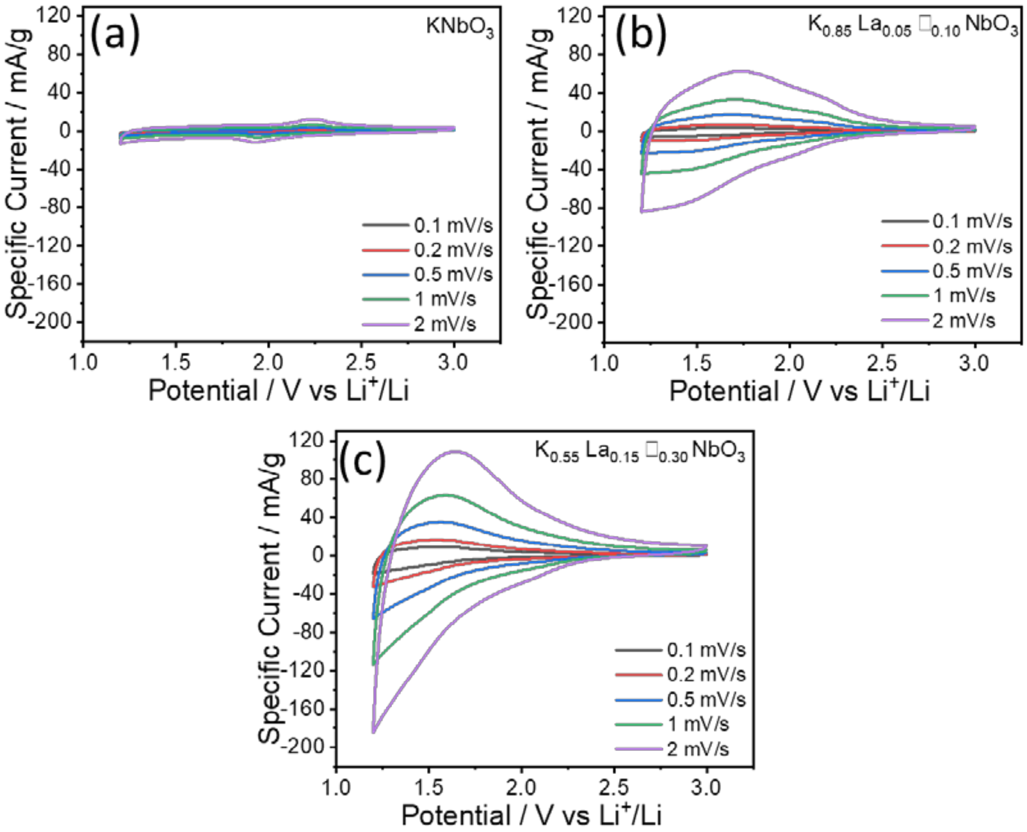

Figure S6. CVs at different scan rates in potential window 1.2 – 3.0V vs. Li. (a) Pristine $KNbO_3$ (b) $K_{0.85}La_{0.05}\square_{0.10}NbO_3$ (c) $K_{0.55}La_{0.15}\square_{0.30}NbO_3$.

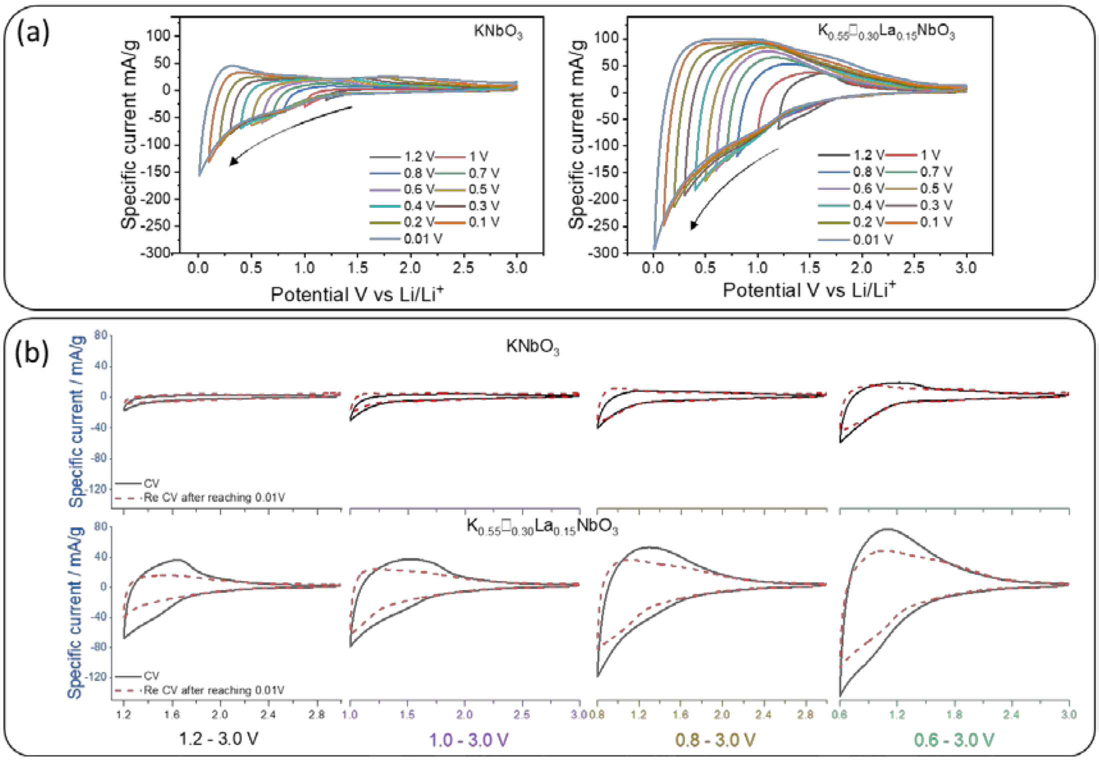

Figure S7. CV of pristine $KNbO_3$ and $K_{0.55}La_{0.15}\square_{0.30}NbO_3$ at 10 mV.s^{-1} (a) CVs under different potential windows (b) comparison of CV before and after reaching 10 mV cut-off potential for both samples.

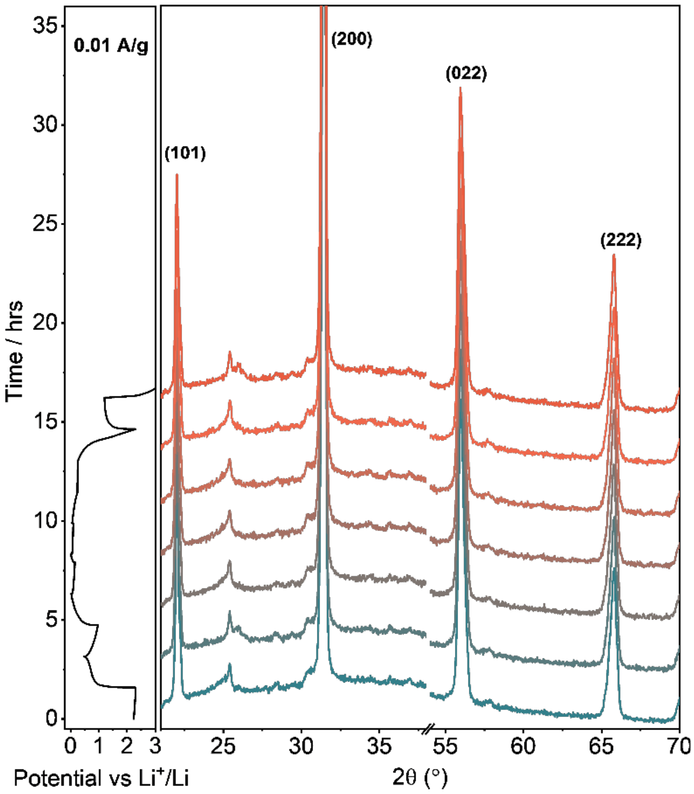

Figure S8. In situ XRD of pristine $KNbO_3$ sample at 0.01 $A.g^{-1}$.

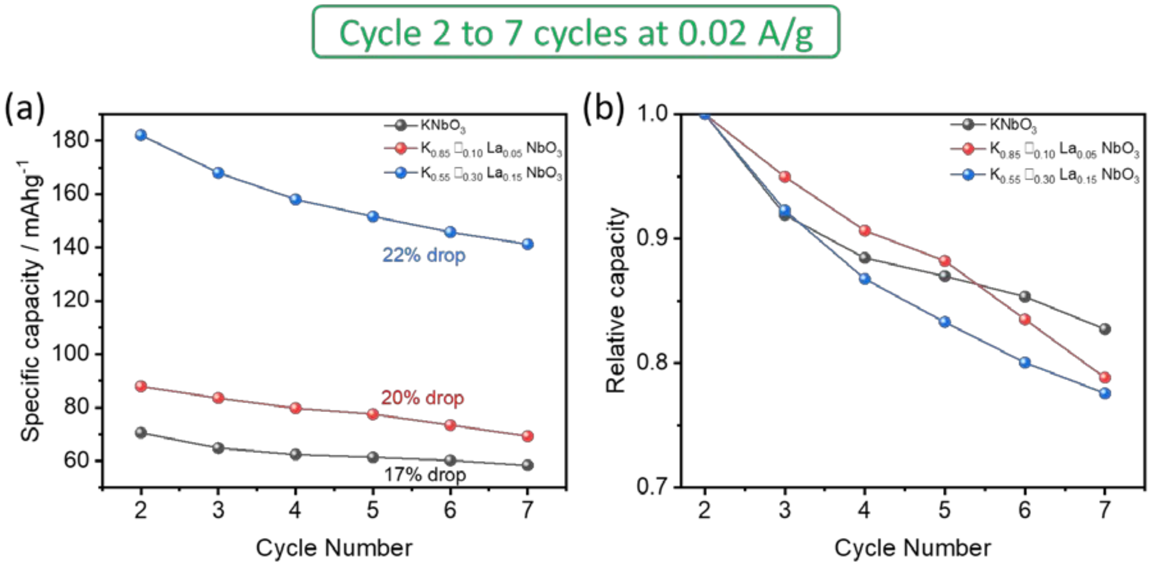

Figure S9. Capacity during initial 7 cycles of all three samples obtained by GCPL measurements (a) specific capacity drop comparison (b) Relative capacity drop comparison.

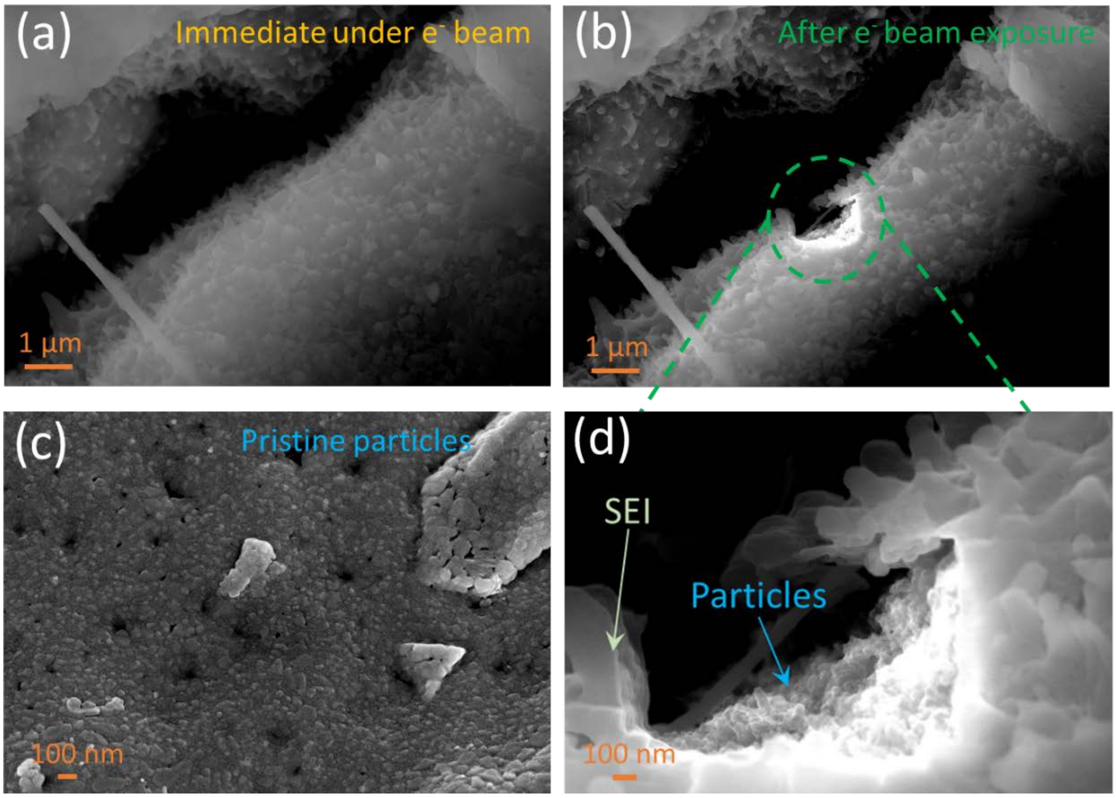

Figure S10. Cycled $K_{0.55}La_{0.15}\square_{0.30}NbO_3$ *with: (a) Postmortem SEM of electrode after 900 cycles captured immediately. (b) After electron beam exposure on particular area indicated by green circle indicating beam damage. (c) Pristine powder particles (d) Zoomed image of focused area indicating the burning of thick SEI layer under electron beam exposing active material particles afterward. All the measurements are performed at constant accelerating voltage of 20 KV.*

3.3 Conclusion

In this chapter, La-substituted, A-site-deficient perovskites with the composition $K_{1-3x}La_x\square_{2x}NbO_3$ ($0 \leq x \leq 0.15$) were designed, synthesized, and investigated as negative electrode materials for Li+ storage. First, a sol-gel method was adopted for synthesizing pristine $KNbO_3$ and La-substituted $K_{1-3x}La_x\square_{2x}NbO_3$ perovskites, achieving successful substitution up to x = 0.15. While samples for higher x values were also synthesized, they resulted in the destabilization of the perovskite structure and the formation of the secondary $K_4Nb_6O_{17}$ phase. The evolution of the crystal structure and the effects of La substitution were thoroughly studied *via* XRD analysis. La substitution at the K^+ A-site led to increased lattice symmetry, transforming the space group from Amm2 in pristine $KNbO_3$ to R3m in $K_{0.55}La_{0.15}\square_{0.30}NbO_3$. The global effect of La^{3+} substitution in $KNbO_3$ perovskites is consistent with findings in the $Ag_{1-3x}La_x\square_{2x}NbO_3$ ($x \leq 0.20$) model system in which La substitution stabilizes the structure by reducing $[NbO_6]$ octahedral distortions, resulting in a more symmetric Pm-3m space group. This indicates a universal tendency in cubic perovskite structures to stabilize when smaller cations are substituted at the A-site. However, the substitution threshold and its effects vary between systems due to differences in A-site cation size and the nature of the pristine phases. The evolution of lattice parameters and the stress-induced reduction in particle size indicate that $K_{1-3x}La_x\square_{2x}NbO_3$ system is more sensitive to La substitution than $Ag_{1-3x}La_x\square_{2x}NbO_3$.

The Li^+ storage behavior of $K_{1-3x}La_x\square_{2x}NbO_3$ ($0 \leq x \leq 0.15$) materials was initially evaluated within a 1.2–3.0 V vs. Li^+/Li potential window to compare it with the $Ag_{1-3x}La_x\square_{2x}NbO_3$ ($x \leq 0.20$) model system. $KNbO_3$, $K_{0.85}La_{0.05}\square_{0.30}NbO_3$, and $K_{0.55}La_{0.15}\square_{0.30}NbO_3$ delivered specific capacities of 3, 12, and 30 $mAh.g^{-1}$, respectively, at 0.1 $mV.s^{-1}$. The increase in capacity with substitution confirms the role of A-site vacancies. However, the rate performance of $K_{1-3x}La_x\square_{2x}NbO_3$ ($0 \leq x \leq 0.15$) was lower compared to $Ag_{1-3x}La_x\square_{2x}NbO_3$ ($x \leq 0.20$), likely due to the higher conductivity of Ag cations in the structure.

Additionally, the electrochemical behavior of Li^+ storage in $K_{1-3x}La_x\square_{2x}NbO_3$ ($0 \leq x \leq 0.15$) was investigated under extended potential windows, focusing on the effects of voltage cut-offs on material stability and performance. Notably, $K_{1-3x}La_x\square_{2x}NbO_3$ ($0 \leq x \leq 0.15$) retained structural stability across all samples, while maintaining the trend of increasing capacity with substitution. This behavior differed from that of $Ag_{1-3x}La_x\square_{2x}NbO_3$ ($x \leq 0.20$) under similar conditions. The highly substituted $K_{0.55}La_{0.15}\square_{0.30}NbO_3$ (with 30% atomic A-site vacancies) exhibited a capacity of 164 $mAh.g^{-1}$ at 0.02 $A.g^{-1}$ in a 0.05 –3.0 V *vs* Li^+/Li potential window. *In situ* XRD analyses revealed a solid solution-type storage mechanism, with a maximum volume change of only 1.3% upon Li^+ insertion in the highly substituted $K_{0.55}La_{0.15}\square_{0.30}NbO_3$, accounting for the remarkable capacity retention observed after 900 cycles at 0.1 $A.g^{-1}$.

This study diverged from the classical design of insertion materials by developing a strategy of creating vacancies on atomic level within the host lattice. We selected a host structure with relatively low-cost cations and importantly a cubic perovskite structure class that is not supposedly meant for ion storage. Vacancies in $K_{1-3x}La_x\square_{2x}NbO_3$ ($x = 0, 0.05, 0.15$) structure facilitated the creation of potential Li^+ insertion sites, leading to enhanced performance. This strategy highlights the effectiveness of vacancy engineering in enhancing Li^+ storage capabilities of perovskite oxides.

References related to chapter 3

[1] S.K. Sahu, S. Zlotnik, A. Navrotsky, P.M. Vilarinho, Thermodynamic stability of lead-free alkali niobate and tantalate perovskites, J. Mater. Chem. C 3 (2015) 7691–7698. https://doi.org/10.1039/C5TC01308A.

[2] A. Yamamoto, K. Murase, T. Sato, K. Sugiyama, T. Kawamata, Y. Inaguma, J. Yamaura, K. Shitara, R. Yokoi, H. Moriwake, Crystal structure and properties of perovskite-type rubidium niobate, a high-pressure phase of $RbNbO_3$, Dalton Trans. 53 (2024) 7044–7052. https://doi.org/10.1039/D4DT00190G.

[3] Mineral commodity summaries 2024, 2024. https://doi.org/10.3133/mcs2024.

[4] P. Agnese, P. Garcia Del Barrio, L.A. Gil-Alana, F. Perez De Gracia, Precious metal prices: a tale of four US recessions, SEF (2024). https://doi.org/10.1108/SEF-09-2023-0550.

[5] E. Le Calvez, J.C. Espinosa-Angeles, G.J. Whang, N. Dupré, B.S. Dunn, O. Crosnier, T. Brousse, Investigating the Perovskite $Ag_{1-3x}La_xNbO_3$ as a High-Rate Negative Electrode for Li-Ion Batteries, Front. Chem. 10 (2022) 873783. https://doi.org/10.3389/fchem.2022.873783.

Chapter 4: Wet chemical synthesis approach for Ti_3AlC_2 MAX phases and their Li^+ storage performance

4.1 Introduction

In the previous chapters, the focus has been on the study of oxide perovskite structures and their potential for Li^+ storage through substitution strategies and vacancy engineering. In Chapter 2, polyacrylamide gel method was successfully applied to the synthesis of $Ag_{1-3x}La_x\square_{2x}NbO_3$ perovskites, demonstrating its potential for precise control over particle morphology and compositional uniformity. Capitalizing on these findings, this chapter shifts the focus toward another class of materials with significant potential in energy storage: ternary carbides known as MAX phases. This chapter presents an innovative use of the polyacrylamide-based wet chemical route to synthesize carbides, more precisely Ti_3AlC_2 MAX phases. This transition is motivated by the promising applications of MAX phases in energy storage, particularly in their potential to form MXenes, a material class showing excellent performance as electrode materials in high power electrochemical energy storage systems.

Polymeric gel synthesis route have been studied in literature for synthesis of various metal oxide nanoparticles, where it provide advantage of molecular-level mixing of precursors resulting in a superior compositional uniformity, low agglomeration, size and shape control, and a high surface area [1–3]. On the other hand, this route has not fully optimized for synthesis of metal carbide, particularly MAX phases, with only a few studies addressing this challenge.

Mardali *et al.* directly adopted this route for co-synthesis of tungsten carbide–cobalt nanopowders (WC-Co) [4]. Acrylamide monomer primarily acted as carbon source. Following a simultaneous carburization-reduction reaction between 900 and 1100°C in Ar/H_2, W_2C, Co_3W_3C, and Co_6W_6C intermediate phases formed. The reaction finally leads to the formation of WC, with cobalt acting as a catalyst. For titanium based carbides, the direct use of polymeric gel route for synthesis of titanium carbides (TiC) powders with a fine particle size and narrow distribution is reported as well. It involve either using polymeric compounds as a source of carbon to directly grow TiC particles, or synthesis of TiO_2 by polyacrylamide gel route followed by carbothermal reduction to form TiC particles, while releasing carbon monoxide (CO) as a byproduct [5,6]. The gel provides a scaffold that facilitates the intimate mixing of the carbon source and the titanium precursor, enhancing the efficiency of the TiC synthesis.

In context of ternary carbides, sol-gel routes has been recently developed by the Birkel's group, where they mainly focused Cr and V based magnetic MAX phases [7,8]. However, wet chemical synthesis route for development of Ti_3AlC_2 MAX phase has not been reported in the literature. This ternary compound was first synthesized by Pietzka and Schuster in 1994 through the sintering of cold-compacted powder mixtures of Ti, TiAl, Al_4C_3, and C in pure hydrogen for 20 hours [9]. In addition, Tzenov and Barsoum developed reactively hot isostatically pressing route for synthesis of bulk polycrystalline samples of Ti_3AlC_2 by mixtures of Ti, graphite, and Al_4C_3 powders at 1400°C for 16 hours [10]. However, the development of highly pure Ti_3AlC_2 MAX phases by different routes has received enormous research interest after discovery of promising 2-dimentional $Ti_3C_2T_x$ MXene synthesized by etching of Ti_3AlC_2 MAX phase [11,12]. $Ti_3C_2T_x$ MXene have received enormous research interest as an electrode material for high performance ion batteries [13]. Therefore, in this chapter, we aimed to develop polyacrylamide synthesis route for synthesis of Ti_3AlC_2 MAX phase. In the later sections of this chapter, obtained materials were subsequently investigated as a negative electrode for Li^+ storage.

4.2 Polyacrylamide synthesis approach for Ti_3AlC_2 MAX phases

In polyacrylamide synthesis of Ti_3AlC_2, metal precursors Aluminum nitrate nonahydrate ($Al(NO_3)_3.9H_2O$, Sigma Aldrich, 99.99% trace metals basis) and Titanium (IV) n-butoxide $C_{16}H_{36}O_4Ti$ (Sigma Aldrich, reagent grade, 97%) or Titanium(IV) isopropoxide ($Ti[OCH(CH_3)_2]_4$, Sigma Aldrich, 99.99% trace metals basis) were dissolved in 60 ml of ethylene glycol (Sigma Aldrich, anhydrous, 99.8%). The selection of precursors and solvent was guided by their solubility properties and compatibility with the polyacrylamide method. Ti/Al precursor molar ration was adjusted to 3. Citric acid ($HOC(CH_2CO_2H)_2$, Alfa Aesar, 99+%) was then added to the solution at a cation molar ratio of 1.5:1, and the mixture was stirred until a transparent solution was achieved. Temperature kept at 40 °C. Citric acid served as a complexing agent, with its carboxyl and hydroxyl groups binding to Ti^{4+} and Al^{3+}, through chelation. Next, acrylamide monomers (Alfa Aesar, ≥ 99%) and N,N′-methylene-bisacrylamide (Alfa Aesar, 99%) cross-linkers were introduced into the solution at a cation molar ratio of 9:1. The monomers are primarily act as a source of carbon in synthesis. The monomer radicals open the double bonds of acrylamide, creating new activation sites that link to subsequent monomer units, propagating the chain through radical transfer. Polyacrylamide forms a linear chain structure, while N,N′-methylene-bisacrylamide acts as a cross-linker, promoting the development of a 3D network of interconnected loops. Wet gel was developed in around 1 hour, after adding H_2O_2 as polymerization initiator.

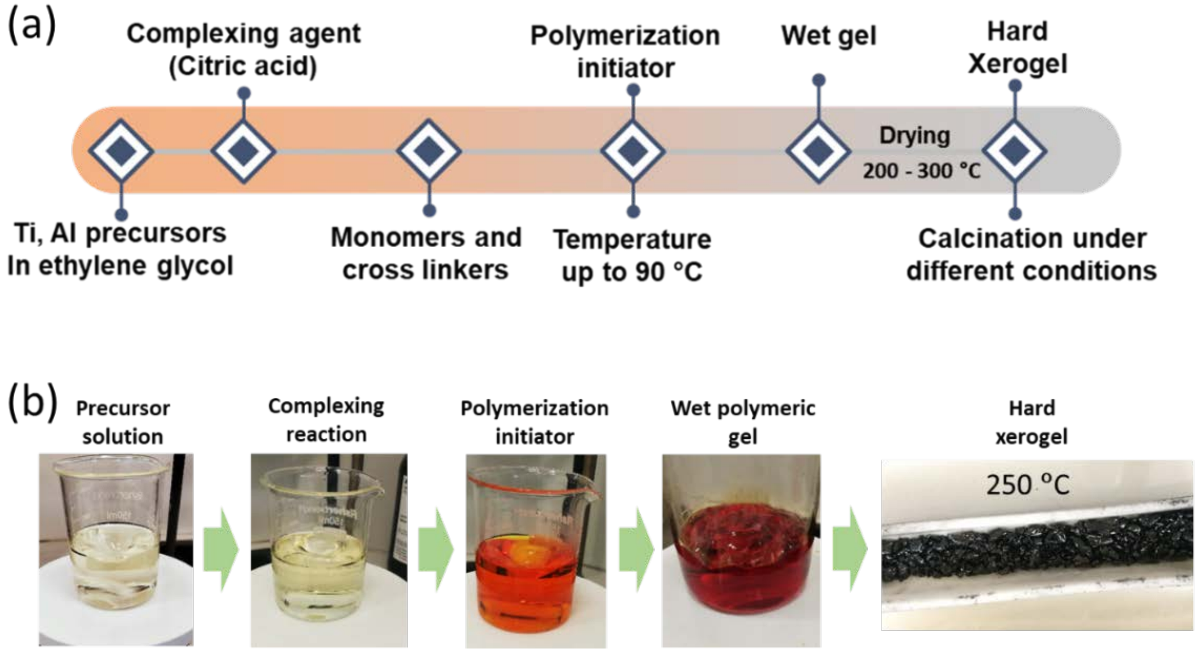

Figure 4.1. (a) Schematic illustration of each step of synthesis route. (b) Photographic images at different stages during reaction.

Wet polymeric gel was dried in oven under 200 °C – 300 °C temperature range to obtain xerogel. The hardness and grinding of xerogel depends on drying temperature. Between 150 °C - 250 °C drying temperature, the obtained xerogel was extremely hard and difficult to grind due to polymeric organic contents. However, by increasing temperature to 300 °C, grinding became relatively easier. Based on removal temperature of carbon sources, the drying temperature was set at 300 °C for all the further experiments. The scheme of synthesis route along with photographic images at each stage of reaction is depicted in Figure 4.1.

4.3 Crystallization approaches for achieving Ti_3AlC_2 MAX phase

To crystallize the product in Ti_3AlC_2 MAX phase, the challenging step is to optimize the carbon content by considering its sources from the precursors. To address this challenge, several approaches have been carried out before calcining the product to higher temperatures. The thermal decomposition and oxidation of each organic compound (or source of carbons) is crucial for selectively removing carbon from the final product by thermal treatment, which are summarized in Table 4.1.

Tableau 4.1. Decomposition and oxidation temperature of various carbon sources used during synthesis.

Carbon Source	Decomposition Temperature (°C)	Oxidation Temperature (°C)	References
Citric Acid	150 - 200	200 - 300	[14]
Acrylamide	250 - 300	300 - 400	[15]
N,N′-methylene-bisacrylamide	250 - 300	350 - 450	[16]
Titanium isopropoxide	150 - 200	200 - 300	[17]
Ethylene Glycol	200 - 250	300 - 400	[14]

Thermogravematric analysis (TGA) was performed under combined argon and oxygen environment at 50 and 40 ml/min gas flow rate, respectively. Selective carbon removal region was identified by weight loss estimation as shown in Figure 4.2a. A rapid weight loss of around 90% was obtained in a narrow temperature window of 300°C – 470°C. Increasing the temperature further to 1000 °C did not result in significant additional changes. Based on TGA experiment, a temperature of 400 °C was selected for further treatments, which showed around 50% weight loss primarily due to the removal of carbon from the product. However, under air, combustion of carbon may not be same due to difference in dynamics of the two processes. Therefore, detailed oxidation behavior of xerogel at different temperatures in air was carried out.

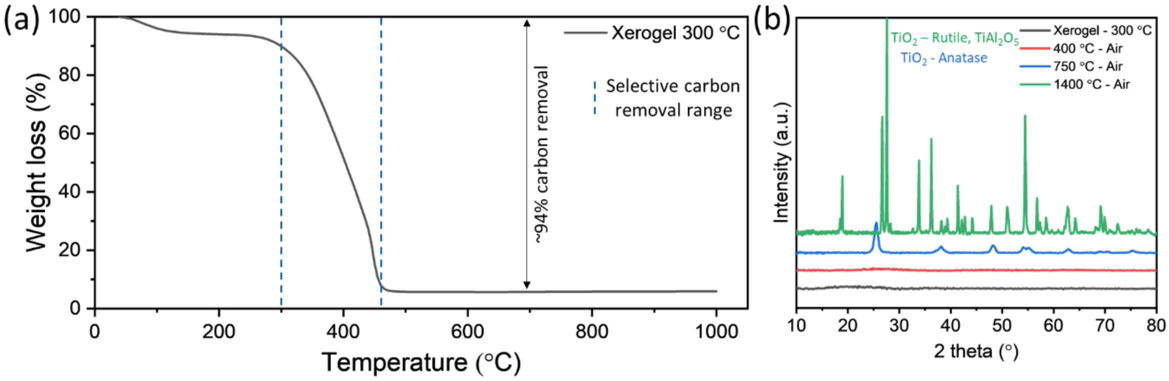

Figure 4.2. (a) TGA under Ar-O_2 environment at 2K.min^{-1} heating rate. (b) Powder XRD at different calcination temperature under air.

Xerogel was subjected to calcination at 400°C, 750°C, and 1400°C under air and results are compared in Figure 4.2b. Material exhibited overall an amorphous behavior at 400°C, which transitioned to crystalline structure at 750°C, as indicated by well-defined peaks associated to

TiO_2-Anatase phase formation [18]. The powder turned its colour from black to white. In addition, aluminum nitrate decomposes into aluminum oxide, which at temperatures up to 750 °C often remains in an amorphous or poorly crystalline state [19]. Amorphous Al_2O_3 does not show diffraction peaks but it contribute to the background signal. Further increasing temperature to 1400°C, material transform its crystallinity forming TiO_2-Rutile and $TiAl_2O_5$ phases [20,21]. This suggests that Ti cations are more readily oxidized compared to Al cations. Figure 4.3 illustrate the flow diagram of two adopted strategies towards for crystallizing Ti_3AlC_2 MAX phase.

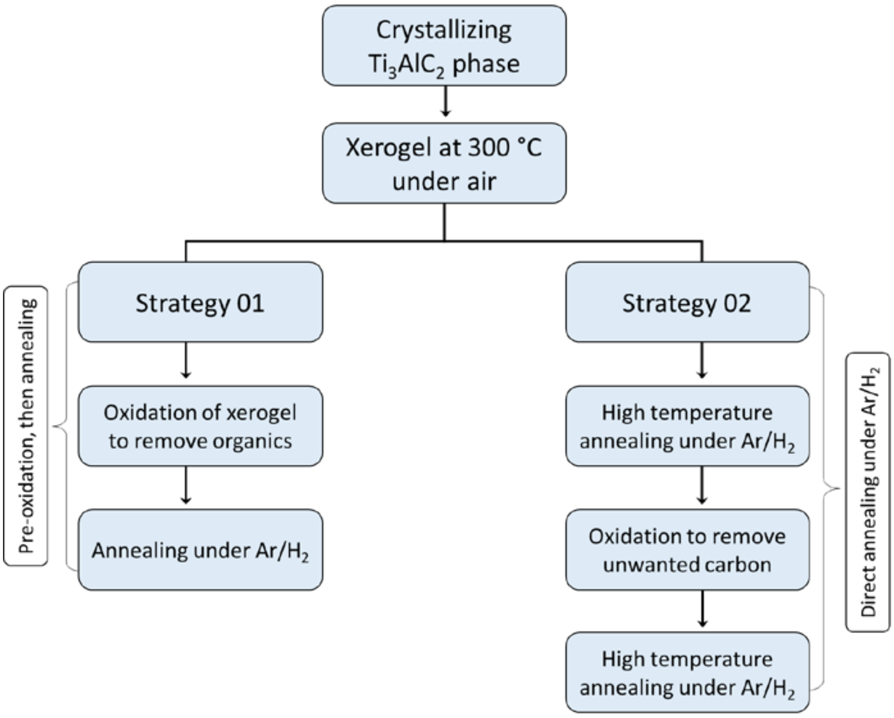

Figure 4.3. Flow chart of strategies to crystallize Ti_3AlC_2 phase.

4.3.1 Strategy 1: Pre-oxidation and subsequent annealing of xreogel in Ar/H_2

A close observation of xerogel dried at 300 °C in air showed the broad hump at $2\theta = 20$ in XRD pattern, which is a characteristic signature amorphous carbon material (Figure 4.4) [22]. It indicate the thermal decomposition of carbon sources (such as citric acid, acrylamide, and others), forming a disordered carbon matrix. When temperature increased to 400 °C under air at 300 °C/h rate, the broad hump shifts to $2\theta = 27°$. This shift could imply that some of the amorphous carbon is starting to organize into more structured or locally densified, yet still non-crystalline. The resulting material was easy to grind and colour of powder turned to dark brown.

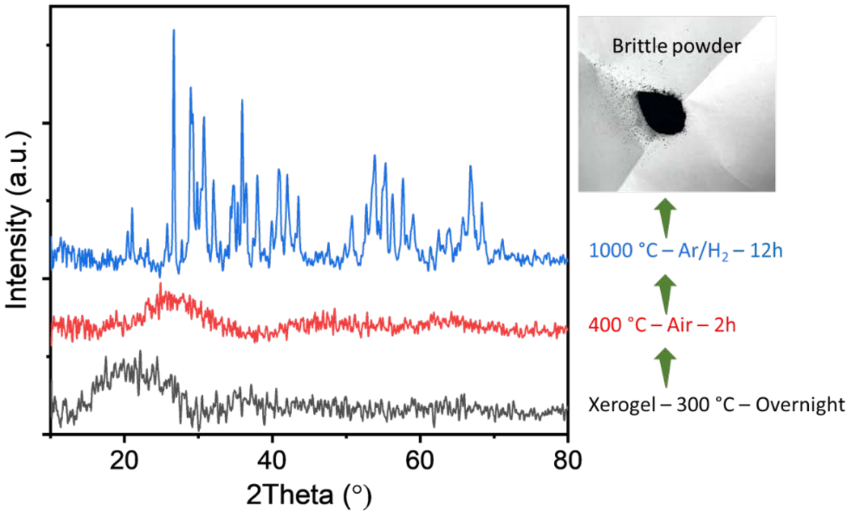

Figure 4.4. Powder XRD patterns of xerogel calcined at different temperature and atmosphere. Ar/H_2 *flow rate was 50 ml.min*$^{-1}$ *and ramp rate was 300 °C/h.*

On the other hand, Titanium isopropoxide decomposes at relatively low temperatures (150-200 °C), forming amorphous TiO_2 at low temperature [17,23]. At 400 °C, the amorphous TiO_2 might not yet crystallize but could affect the surrounding carbon matrix, leading to the observed shift in the XRD pattern [24,18]. When aluminum nitrate decomposes, highly dispersed amorphous aluminum oxide start forming at relatively low temperatures. The presence of amorphous Al_2O_3 might also facilitate the condensation and densification of the carbon matrix. Based on weight of sample before and after thermal treatment at 400 °C for 2h in air, around 80% weight loss was obtained, which is significantly different compared to TGA. One reason is the differences in heating rates and or longer periods at critical temperatures, allowing for more complete oxidation and resulting in greater weight loss. Another reason is presence of nitrogen along with oxygen in air that could lead to a different oxidation mechanism or enhanced diffusion effects, potentially causing more extensive carbon removal/cation oxidation.

Materials then subjected to higher temperatures in a tube furnace under Ar/H_2 at 1000 °C to crystallize the Ti_3AlC_2 phase. After grinding, the resulting black powder consisted of brittle, fine particles. However, powder XRD analysis showed slight increase in crystallinity, but the neither targeted phase was achieved nor other stable phase formed.

The SEM analysis was performed to get further insights about morphology transformation. Figure 4.5a show the formation of porous foam-like interconnected network of material calcined at 400 °C. The surface morphology is highly textured, with numerous round voids/bubbles, suggesting that the material underwent a partial oxidation and gas release due to decomposition of carbon sources and in accordance with previously observed [4]. Reduction annealing at 1000 °C, particles are regular shaped and appear to have a much smoother surface than material calcined at 400 °C Figure 4.5b. High temperature and reducing environment likely facilitated the densification process without evolving it to a desired lamellar morphology, which is typical for Ti_3AlC_2 phase [25,26].

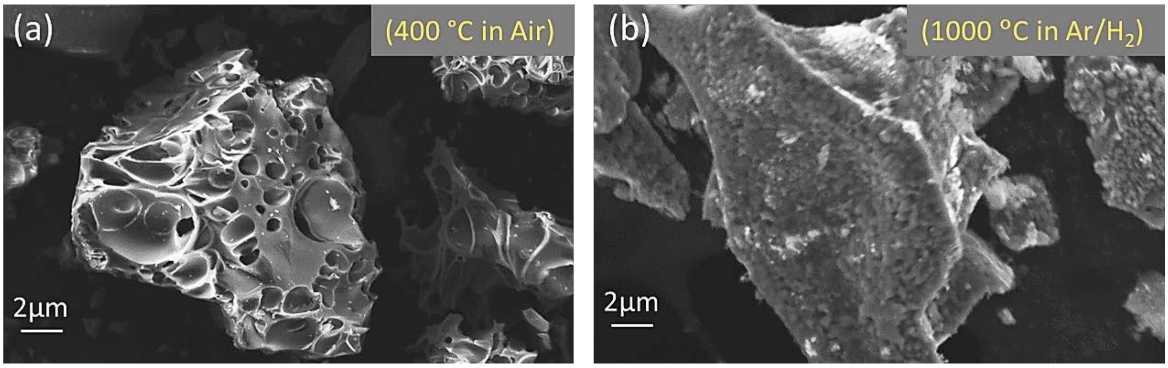

Figure 4.5. SEM images (a) Xerogel calcined at 400 °C in air. (b) Annealing of calcined sample under reducing environment at 1000 °C.

4.3.2 Strategy 2: Direct annealing of xreogel in Ar/H_2 atmosphere

In second approach, xerogel was directly annealed under reducing atmosphere at 900, 1000, 1100 and 1300 °C temperatures. In the xerogel state, the Al cations are likely dispersed within an amorphous matrix, possibly as part of an amorphous precursor or in a mixed oxide form with Ti. Set of broad peaks appeared on powder XRD patterns when xerogel annealed to 900 °C (Figure 4.6). At lower 2θ, the broad peak appears is observed that can be associated to amorphous carbon. However, this peak is relatively intense and shifted from 20 to 24.5° compared to xerogel, which indicate ordering and densification of carbon. Two broad and noticeable peaks also appeared at 43.5 and 63.4°, which are difficult to attribute any crystalline Ti-Al based carbide phase. Under the reducing atmosphere of Ar/H_2, some of the Al should start to reduce, making conditions sufficient to mobilize the Al cations for MAX phase formation. Al may either stay trapped in a mixed amorphous phase or partially diffuse into Ti based phases. In practice, the exact phase composition is difficult to know from XRD patterns because of unwanted carbon that dominate the underlying reduced Ti-Al-C phases in amorphous network. At 1000 and 1100 °C, the peaks progressively become sharper, indicating increased crystallinity. Under broad peaks, there are possibilities of three phases namely TiC cubic phase, Ti_3AlC cubic phase, and desired Ti_3AlC_2 MAX phase as mentioned in Figure 4.6 [27]. With temperature increases, aluminum has a high tendency to volatilize, especially in reducing atmospheres, potentially leading to its depletion from the system [27]. This would reduce the amount of available Al to participate in forming the Ti_3AlC_2 phase. Alternatively, Al could segregate into separate phases, like forming Ti_2AlC (211 MAX phase) or Al-rich intermetallic that are not being detected due to their low crystallinity or small quantity and the dominance of other phases [28,29]. TiC cubic phase becomes more prominent as the temperature increases to 1300 °C. The formation of TiC in the presence of carbon is favorable at this temperature [5].

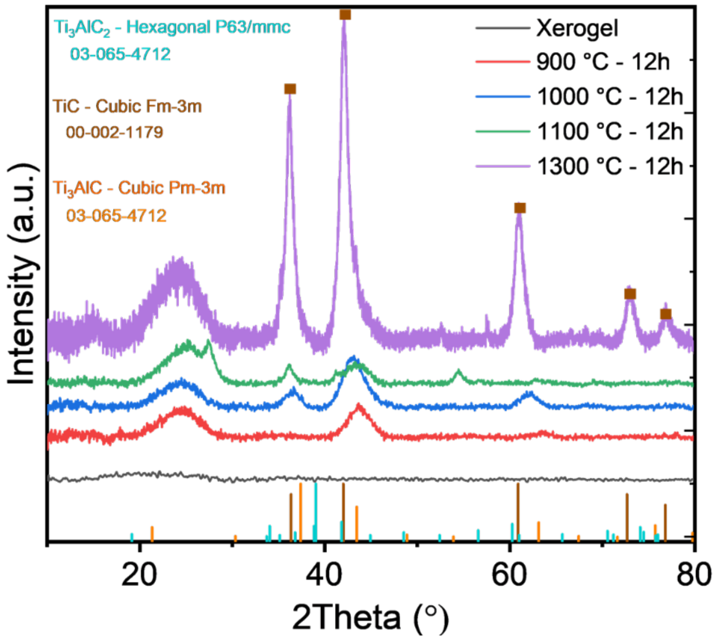

Figure 4.6. Powder XRD showing the evolution of different phases when xerogel directly annealed at 900, 1000, 1100, and 1300 °C in Ar/H_2 atmosphere.

The preferential formation of TiC over Ti_3AlC_2 in carbon-rich environments, especially under reducing conditions was reported [30]. The thermodynamics of Ti-C systems have been extensively studied, and TiC was recognized for its high stability, particularly when carbon is in excess and Al is depleted. While direct experimental confirmation of intermediate phase evolution in our case is difficult due to the complex interplay and excess carbon causing amorphous dominance in XRD patterns at low temperatures, the literature provides a strong basis for these mechanisms. If compared with traditional high temperature synthesis route, where a mixture of Ti, Al, and C is heated, two reactions occur: C + Ti = TiC (micro-crystal) and 2TiC + Al + TiC = Ti_3AlC_2. Here, TiC formed may act as seed crystals for the formation of Ti_3AlC_2 at temperature above 1300 °C [31,27]. It suggests that annealing of obtained powder at further higher temperatures may required. However, in the context of the wet chemical route, it is anticipated that the Ti_3AlC_2 phase can crystallize at lower temperatures. Additionally, due to the presence of excess carbon in the material, further high-temperature treatments were deemed unnecessary. Excess carbon, along with the reducing atmosphere, makes it more difficult for Al to form the desired Ti_3AlC_2 phase. Instead, carbon is preferentially consumed in forming TiC, which outcompetes the formation of any MAX phases that require a more precise stoichiometric balance of Ti, Al, and C.

According to literature, the TiC cubic phase (NaCl type structure) intrinsically exhibit non-lamellar morphologies, in contrast to the lamellar structure of Ti_3AlC_2 [32,6,33,34]. Consequently, SEM analysis is a valuable tool for tracking the formation and characteristics of these reaction products. Given that TiC is stable and a dominant phase at 1300 °C, SEM analysis of samples annealed at 900 and 1000 °C was performed because of possible expectation of Ti_3AlC_2 (312) or Ti_2AlC (211) phase formation.

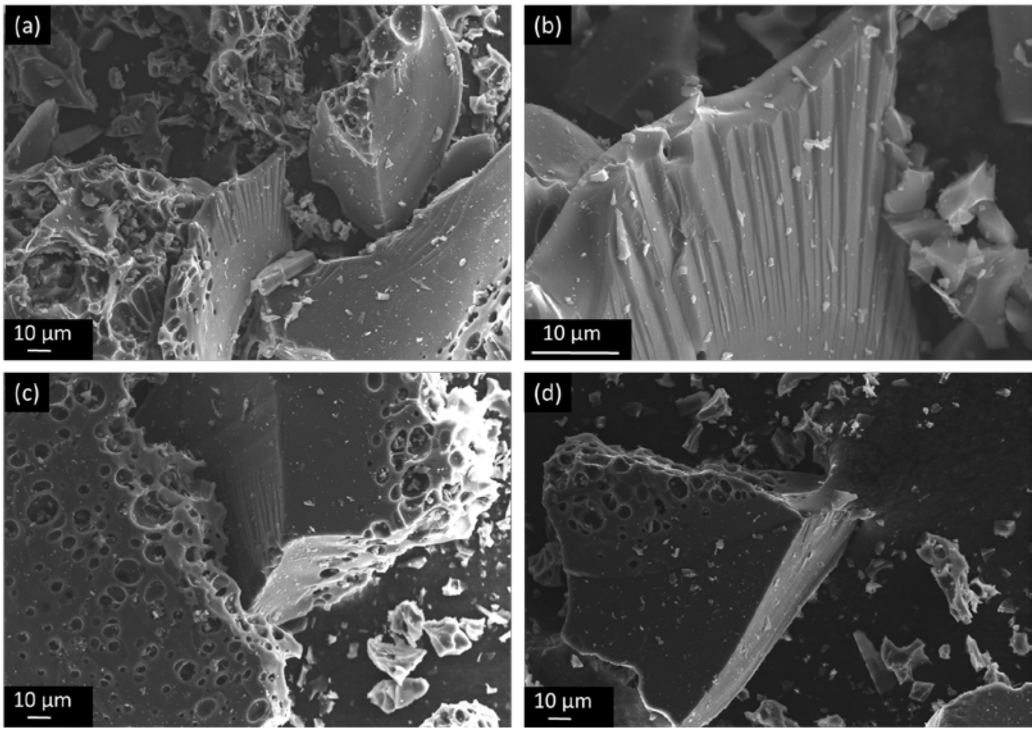

Figure 4.7. (a-d) SEM images of xerogel annealed directly at 900 °C under Ar/H_2 flow rate of 50 ml.min^{-1} and ramp rate 300 °C/h.

Morphology examination of product at 900 °C revealed the mixed porous network and growth of bulk irregular shaped large particles Figure 4.7a-d. It suggest an incomplete nucleation of possible phases containing Ti, Al and C inside the carbon matrix. However, at 1000 °C, the growth of micron-sized particles with dominant lamellar morphologies is achieved as shown in Figure 4.8a-f. The transformation of porous structures into layered morphology is a strong indication for the growth of targeted Ti_3AlC_2 MAX phase [35]. However, presence of excess carbon can be observed in on the layered structures as shown in Figure 4.8d. This suggests that not all carbon is consumed in formation of Ti_3AlC_2, but some carbon likely remains in its amorphous state or consumed in forming other secondary phases as discussed in XRD.

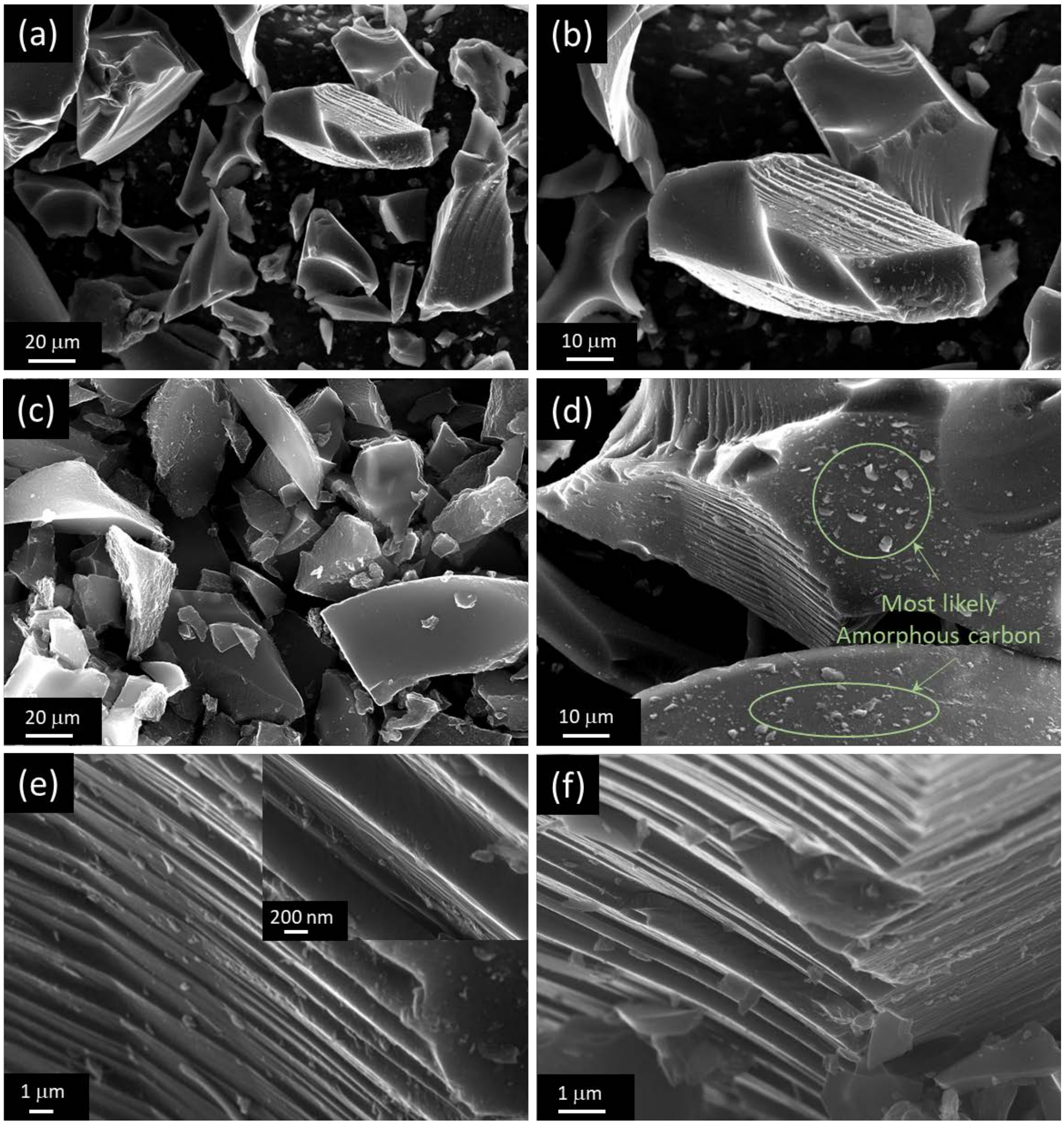

Figure 4.8. SEM images of xerogel annealed directly at 1000 °C under Ar/H_2 flow rate of 50 ml.min^{-1} and ramp rate 300 °C/h. (a & c) Low magnification images. (b & d) Corresponding high magnification images showing amorphous carbon on the surface. (e & f) High magnification images at different site of sample showing the thickness and stacking of layers.

To get further insights about the nature of the phases associated with these lamellar structures, elemental analysis was performed using EDX measurements. The analysis focused on cation and carbon stoichiometry at several locations within the sample. As a conclusion, mean Ti/Al ratio obtained at several areas of site 1 and site 2 were 2.83 and 3.05, respectively (Figure 4.9a & b). These results not only confirm the presence of Al but also align with cation stoichiometry characteristics of desired Ti_3AlC_2 phase.

Although estimating carbon stoichiometry via EDX is challenging, the Ti/C ratio can still provide some insights. The mean Ti/C ratio obtained at several areas of site 1 and site 2 were 0.067 and 0.073, respectively, much higher than required value of 1.5 in Ti_3AlC_2. This confirms the presence of excess carbon in the material, complementing the findings from XRD analysis and SEM observations. This carbon excess carbon is coming from organic sources used in synthesis. While carbon is crucial for achieving the desired carbide phases, it is important to regulate any excess carbon, which will be addressed in the subsequent section.

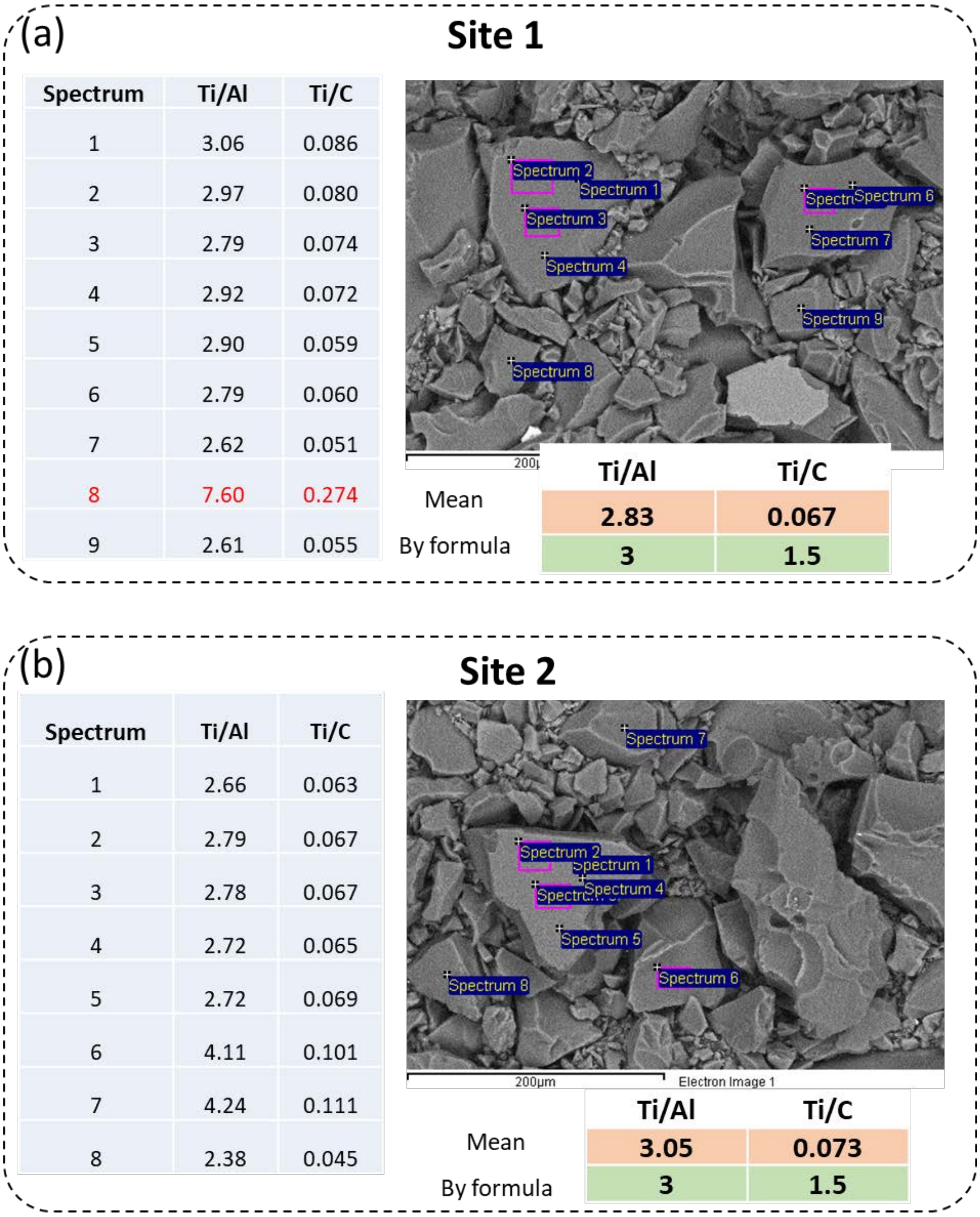

Spectrum	Ti/Al	Ti/C
1	3.06	0.086
2	2.97	0.080
3	2.79	0.074
4	2.92	0.072
5	2.90	0.059
6	2.79	0.060
7	2.62	0.051
8	7.60	0.274
9	2.61	0.055

	Ti/Al	Ti/C
Mean	2.83	0.067
By formula	3	1.5

Spectrum	Ti/Al	Ti/C
1	2.66	0.063
2	2.79	0.067
3	2.78	0.067
4	2.72	0.065
5	2.72	0.069
6	4.11	0.101
7	4.24	0.111
8	2.38	0.045

	Ti/Al	Ti/C
Mean	3.05	0.073
By formula	3	1.5

Figure 4.9. EDX elemental analysis and corresponding SEM images of xerogel directly annealed at 1000 °C in Ar/H_2 (a) Site 1. (b) Site 2.

4.3.2.1 Selective removal of extra carbon after formation of lamellar structures

An attempt to remove the excess carbon content was conducted for the sample directly annealed at 1000 °C and exhibited Ti_3AlC_2 like lamellar morphology. Here, the nature of carbon and its distribution can significantly differ as compared to strategy 01, adopted previously. Therefore, oxidation behavior of pre-annealed sample was investigated carrying out TGA under Ar/O_2

environment at 2K.min^{-1} heating rate up to 1000 °C. Although, overall TGA curve displayed a different oxidation behavior as indicated by weight loss, compared to xerogel oxidation, but major weight loss region (~78%) is almost similar (Figure 4.10a). Therefore, 400 °C temperature was selected for calcination of pre-annealed sample in air. The color of material remained unchanged, retaining its black appearance.

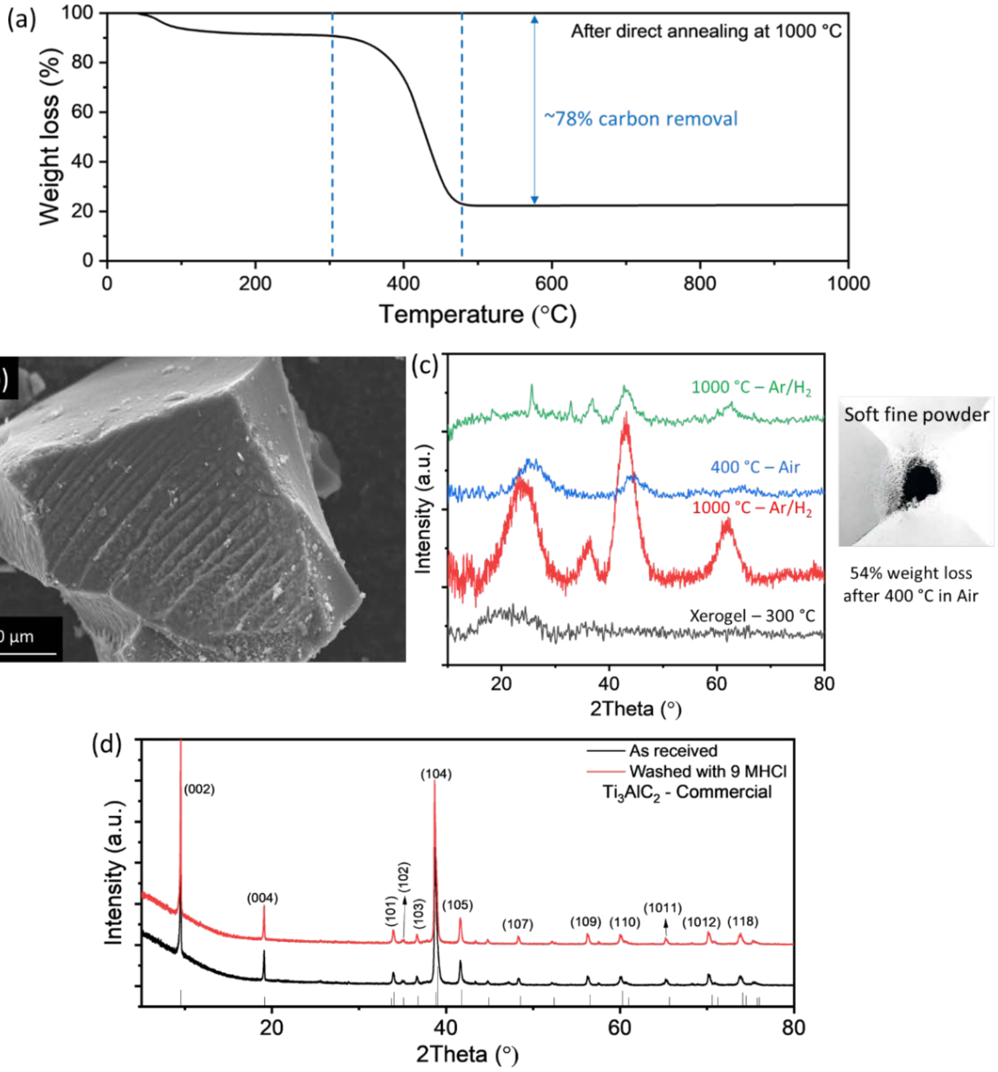

Figure 4.10. (a) TGA of pre-annealed xerogel at 1000 °C in Ar/H_2. Measurements performed in Ar-O_2 environment at 2K.min^{-1} heating rate. (b) SEM image taken after calcination of pre-annealed xerogel at 400 °C in air. (c) Powder XRD patterns comparing samples after different heat treatments according to strategy 02. (e) Powder XRD of commercial Ti_3AlC_2 MAX phase, as received and after washing before use.

Figure 4.10b depicts the SEM image taken after calcination showed that the global layered morphology is retained, while significantly disturbed by granular growth on surface. This effect persists even after post-annealing to 1000 °C (where soft fine powder obtained), indicating that instead of a selective carbon removal, oxidation process readily affected the layered structures with a possible secondary phase formation. Furthermore, powder XRD confirms the reduction of carbon as indicated by decrease in peak intensity around 23° after both calcination and post-annealing (Figure 4.10c). However, the desired Ti_3AlC_2 phase is not achieved. For comparison, the XRD pattern of commercial Ti_3AlC_2 powder (Sigma Aldrich, ≥ 90% purity and ≤ 200um particle size) is presented in Figure 4.10d.

4.4 Electrochemical characterizations of synthesized carbide materials

The direct annealed sample at 1000 °C in Ar/H_2 (from strategy 02), showed well-defined Ti_3AlC_2-like lamellar morphologies and selected to investigate as a negative electrode of LIBs. For simplicity, this sample hereafter named as Ti_3AlC_2@C. Free standing electrodes are prepared after grinding well the Ti_3AlC_2@C powder and mixing it in few drops of ethanol with conducting agent (Carbon Black by Superior Graphite, Chicago, IL, United States) and binder (poly (1,1,2,2-tetrafluoroethylene - PTFE in H_2O, Sigma Aldrich) in 75% /15% / 10% wt., respectively. Electrode mass loadings ranged from 5 – 8 mg cm^{-2}. 1M $LiPF_6$ dissolved in 1:1 %wt. EC/DMC (Solvionic, France, battery grade) was used as the electrolyte. GF/D Whatman glass fiber membrane of 10 mm diameter was used as separator. Electrochemical measurements were performed in half-cell configurations using two-electrode swagelok cell, where Li metal used as counter and reference electrode. For electrochemical behavior and performance comparison, commercial Ti_3AlC_2 material with ≥ 90% purity and ≤ 200um particle size (Sigma Aldrich) was used to fabricate the electrodes with same composition. Before electrode processing, as received Ti_3AlC_2 MAX phases were washed in 9M HCl solution to remove any unreacted titanium or aluminum present. To differentiate, commercial sample is named as Ti_3AlC_2 – commercial.

The Li^+ storage behavior of Ti_3AlC_2@C and Ti_3AlC_2-commercial MAX phase are compared. The galvanostatic charge-discharge profiles at 0.01A.g^{-1} (Figures 4.11a & c) reveal that Ti_3AlC_2@C delivered a higher 1st cycle specific capacity of 600 mAh.g^{-1} as compared to Ti_3AlC_2-commercial, which is 100 mAh.g^{-1}. On subsequent cycles, a stable cycling behavior was obtained for both materials. Discharge specific capacities of 200 and 33 mAh.g^{-1} were obtained at 0.01 A.g^{-1} for Ti_3AlC_2@C and Ti_3AlC_2-commercial, respectively. Figure 4.11b & d shows the charge discharge profile, where the average working potential and Li^+ storage behavior at low potential region are similar for both materials. This similarity is a further indication of the Ti_3AlC_2 MAX phase formation through the polyacrylamide synthesis route. However, a significantly enhanced specific capacity is obtained for Ti_3AlC_2@C indicating the contributions of excess carbon in addition to Ti_3AlC_2. In addition, the corresponding dQ/dV curves show that for Ti_3AlC_2@C, there is almost no activity in range of 1.0 – 3.0 V vs Li^+/Li, which is not exactly the case for Ti_3AlC_2-commercial.

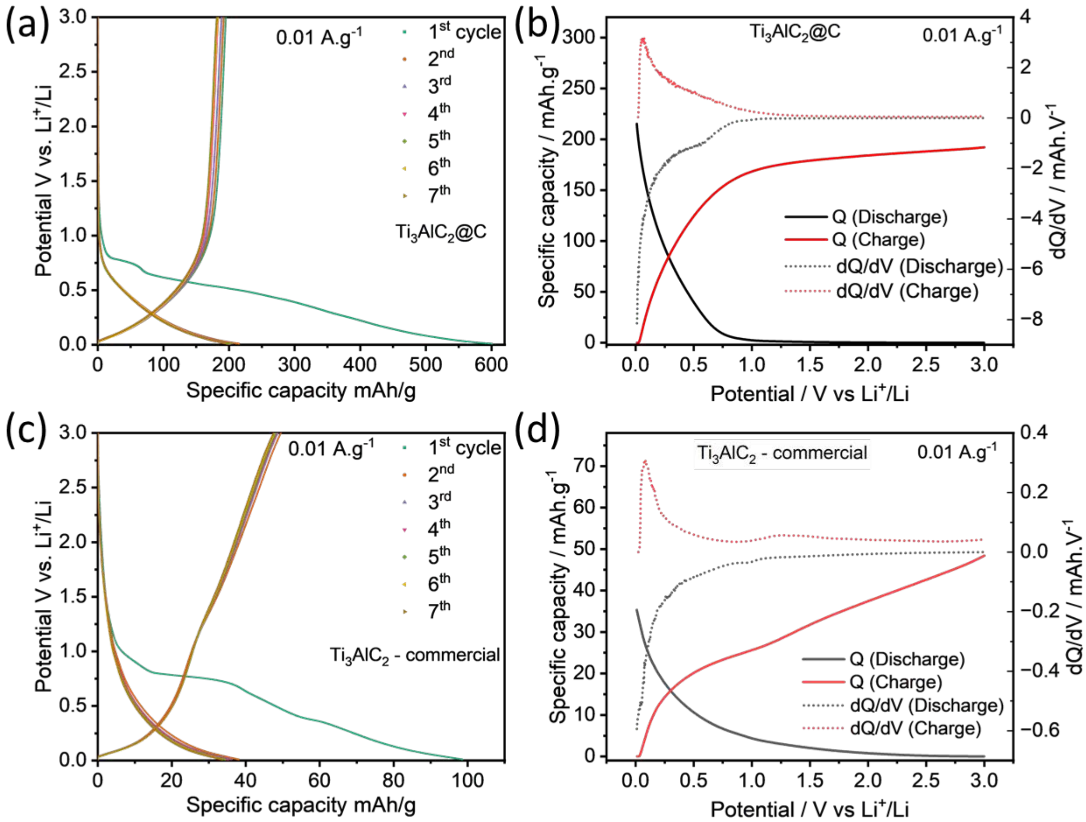

Figure 4.11. Electrochemical measurements of Ti_3AlC_2@C (a) Galvanostatic charge-discharge profiles of initial seven cycles at 0.01 $A.g^{-1}$. (b) Selected 3rd cycle and corresponding dQ/dV curves. Electrochemical measurements of reference Ti_3AlC_2-commercial sample (c) Galvanostatic charge-discharge profiles of initial seven cycles at 0.01 $A.g^{-1}$. (d) Selected 3rd cycle and corresponding dQ/dV curves.

The detailed Li^+ storage performance of Ti_3AlC_2@C and Ti_3AlC_2-commercial materials at different current densities (0.01 – 2.0 $A.g^{-1}$) was investigated. Ti_3AlC_2@C delivers 200 $mAh.g^{-1}$ at 0.01 $A.g^{-1}$ and 5 $mAh.g^{-1}$ at 2 $A.g^{-1}$. While Ti_3AlC_2-commercial delivered 33 $mAh.g^{-1}$ at 0.01 $A.g^{-1}$ and 4 $mAh.g^{-1}$ at 2 $A.g^{-1}$ as shown in Figure 4.12a & c. This indicates that at significantly high current density, a capacity retention of 2% and 15% for Ti_3AlC_2@C and Ti_3AlC_2-commercial, respectively. Overall performance comparison is shown in Figure 4.12b & d. The behavior of both the materials towards higher current densities and extended cycling is quite similar. The significant differences in charge and discharge specific capacities are observed at low current densities. However, Ti_3AlC_2@C exhibits higher and more stable efficiencies compared to the Ti_3AlC_2-commercial, suggesting a more stable and reversible electrochemical reaction. The efficiency of Ti_3AlC_2@C remains close to 100% or higher throughout the cycling, highlighting the advantage of the excess carbon. Contrary, Ti_3AlC_2-

commercial show a noticeable increase in efficiency at higher current densities. However, a clear decline in efficiency at low current densities and with cycling is observed.

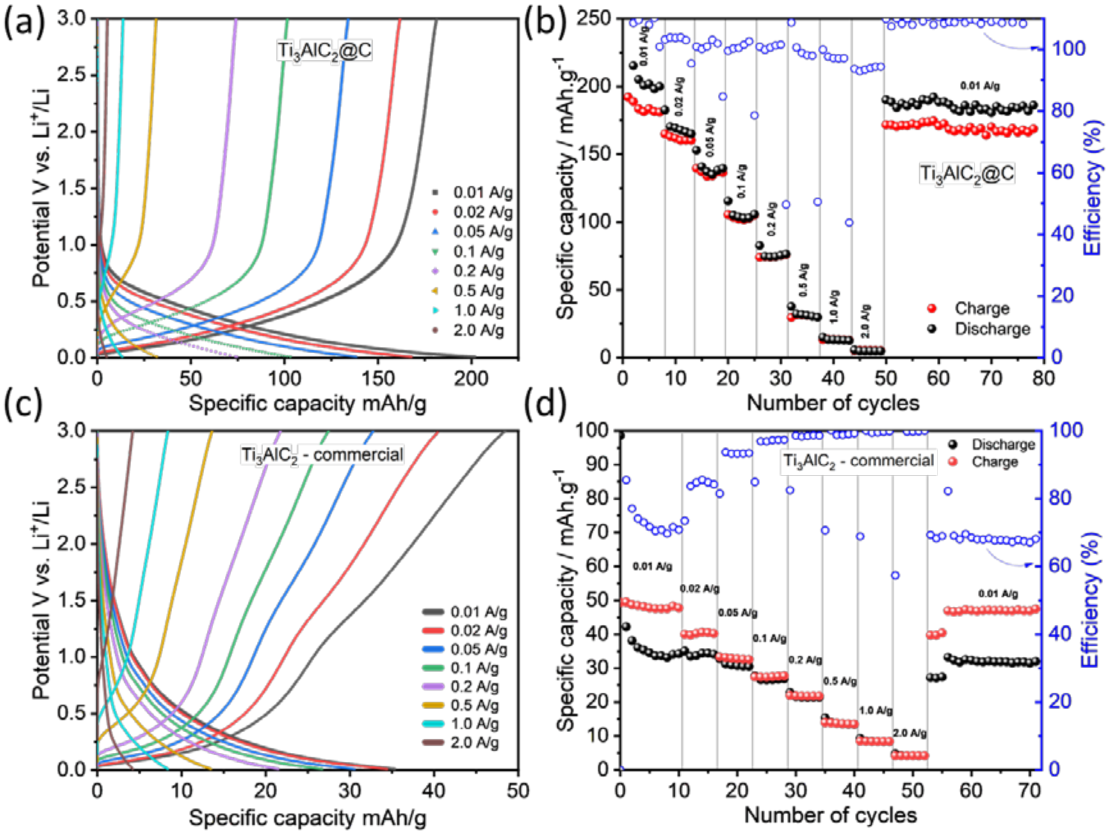

Figure 4.12. (a) Galvanostatic charge-discharge curves of Ti_3AlC_2@C at different current densities from 0.01 – 2.0 A.g^{-1}. (b) Li^+ storage perfromance of Ti_3AlC_2@C. (c) Galvanostatic charge-discharge curves of Ti_3AlC_2-commercial at different current densities from 0.01 – 2.0 A.g^{-1}. (d) Li^+ storage perfromance of Ti_3AlC_2-commercial.

4.5 Conclusion

This chapter presented an in-depth investigation into the wet chemical synthesis of Ti_3AlC_2 MAX phases using a polyacrylamide-based route and their subsequent evaluation as anodes for Li^+ storage. The synthesis process highlighted the critical role of controlling carbon content and the conditions of thermal treatment to achieve the desired Ti_3AlC_2 phase. Through a series of crystallization strategies, including pre-oxidation followed by annealing and direct annealing in a reducing atmosphere, we systematically explored the phase evolution and morphological transformations necessary for optimizing the Ti_3AlC_2 structure. However, the simultaneous occurrence of reduction and carburization reactions and residual carbon matrix complicated the process, specifically making it challenging to isolate and study intermediate phases. Despite the challenges in phase purity, particularly due to the excess carbon leading to the formation of TiC, the direct annealing method at 1000°C successfully produced Ti_3AlC_2-like lamellar morphologies.

The later part of this chapter discussed the Li^+ storage properties, which revealed that the synthesized Ti_3AlC_2@C material exhibited significantly higher specific capacities and better cycling stability at low current densities compared to commercial Ti_3AlC_2. The presence of excess carbon, while complicating phase purity, contributed to the improved electrochemical performance, suggesting a dual role of carbon in both enhancing conductivity and participating in Li^+ storage.

These findings underscore the potential of the polyacrylamide synthesis route in producing Ti_3AlC_2 MAX phases with tailored Li^+ storage properties. However, it also highlight the need for further optimization of the synthesis parameters to achieve phase purity without compromising the beneficial effects of carbon, particularly concerning the monomer concentrations, which are directly linked to the amount of residual carbon. Future work should focus on refining this synthesis to optimize phase purity and morphology, paving the way for the efficient production of Ti_3AlC_2 MAX phase. This advancement could potentially address the practical challenges associated with $T_{33}C_2T_x$ MXenes, a high-power electrode material.

References related to chapter 4

[1] S.F. Wang, H.B. Lv, X.S. Zhou, Y.Q. Fu, X.T. Zu, Magnetic Nanocomposites Through Polyacrylamide Gel Route, Nanosci Nanotechnol Lett 6 (2014) 758–771. https://doi.org/10.1166/nnl.2014.1796.

[2] S. Wang, D. Li, C. Yang, G. Sun, J. Zhang, Y. Xia, C. Xie, G. Yang, M. Zhou, W. Liu, A novel method for the synthesize of nanostructured MgFe2O4 photocatalysts, J Sol-Gel Sci Technol 84 (2017) 169–179. https://doi.org/10.1007/s10971-017-4471-3.

[3] X. Li, Z. Shao, Y. Zhang, W. Zhang, H. Shao, A facile polymeric gel route synthesis of high-voltage $LiNi_{0.5}Mn_{1.5}O_4$ cathode material for Lithium-ion batteries, Materials Letters 277 (2020) 128310. https://doi.org/10.1016/j.matlet.2020.128310.

[4] M. Mardali, R. Sarraf-Mamoory, B. Sadeghi, B. Safarbali, Acrylamide route for the co-synthesis of tungsten carbide–cobalt nanopowders with additives, Ceramics International 42 (2016) 9382–9386. https://doi.org/10.1016/j.ceramint.2016.02.152.

[5] H. Zhang, F. Li, Q. Jia, G. Ye, Preparation of titanium carbide powders by sol–gel and microwave carbothermal reduction methods at low temperature, J Sol-Gel Sci Technol 46 (2008) 217–222. https://doi.org/10.1007/s10971-008-1697-0.

[6] H.-P. Gou, G.-H. Zhang, K.-C. Chou, Formation of submicrometer titanium carbide from a titanium dioxide encapsulated in phenolic resin, J Mater Sci 51 (2016) 7008–7015. https://doi.org/10.1007/s10853-016-9989-1.

[7] J.P. Siebert, L. Bischoff, M. Lepple, A. Zintler, L. Molina-Luna, U. Wiedwald, C.S. Birkel, Sol–gel based synthesis and enhanced processability of MAX phase Cr_2GaC, J. Mater. Chem. C 7 (2019) 6034–6040. https://doi.org/10.1039/C9TC01416K.

[8] J.P. Siebert, K. Patarakun, C.S. Birkel, Mechanistic Insights into the Nonconventional Sol–Gel Synthesis of MAX Phase M_2GeC (M = V, Cr), Inorg. Chem. 61 (2022) 1603–1610. https://doi.org/10.1021/acs.inorgchem.1c03415.

[9] M.A. Pietzka, J.C. Schuster, Summary of constitutional data on the Aluminum-Carbon-Titanium system, JPE 15 (1994) 392–400. https://doi.org/10.1007/BF02647559.

[10] N.V. Tzenov, M.W. Barsoum, Synthesis and Characterization of Ti_3AlC_2, Journal of the American Ceramic Society 83 (2000) 825–832. https://doi.org/10.1111/j.1151-2916.2000.tb01281.x.

[11] M. Naguib, M. Kurtoglu, V. Presser, J. Lu, J. Niu, M. Heon, L. Hultman, Y. Gogotsi, M.W. Barsoum, Two-Dimensional Nanocrystals Produced by Exfoliation of Ti_3AlC_2, Advanced Materials 23 (2011) 4248–4253. https://doi.org/10.1002/adma.201102306.

[12] M. Naguib, V.N. Mochalin, M.W. Barsoum, Y. Gogotsi, 25th Anniversary Article: MXenes: A New Family of Two-Dimensional Materials, Advanced Materials 26 (2014) 992–1005. https://doi.org/10.1002/adma.201304138.

[13] D. Er, J. Li, M. Naguib, Y. Gogotsi, V.B. Shenoy, Ti_3C_2 MXene as a High Capacity Electrode Material for Metal (Li, Na, K, Ca) Ion Batteries, ACS Appl. Mater. Interfaces 6 (2014) 11173–11179. https://doi.org/10.1021/am501144q.

[14] V. Petrykin, M. Kakihana, Chemistry and Applications of Polymeric Gel Precursors, in: L. Klein, M. Aparicio, A. Jitianu (Eds.), Handbook of Sol-Gel Science and Technology, Springer International Publishing, Cham, 2018: pp. 81–112. https://doi.org/10.1007/978-3-319-32101-1_4.

[15] Y. Zheng, X. Wang, C. Zhang, L. Zong, Synthesis, characterization, and swelling behaviors of chitosan-g-poly (acrylic acid-co-acrylamide) superabsorbent using tetraallylammonium bromine as crosslinker, Polym. Bull. 80 (2023) 4443–4458. https://doi.org/10.1007/s00289-022-04289-w.

[16] D. Sternik, K. Szewczuk-Karpisz, O. Siryk, Y. Samchenko, A. Derylo-Marczewska, L. Kernosenko, E. Pakhlov, O. Goncharuk, Structure and thermal properties of acrylic copolymer gels: effect of composition and cross-linking method, J Therm Anal Calorim (2024). https://doi.org/10.1007/s10973-024-13430-y.

[17] D.A.H. Hanaor, I. Chironi, I. Karatchevtseva, G. Triani, C.C. Sorrell, Single and mixed phase TiO_2 powders prepared by excess hydrolysis of titanium alkoxide, Advances in Applied Ceramics 111 (2012) 149–158. https://doi.org/10.1179/1743676111Y.0000000059.

[18] O. Khatim, M. Amamra, K. Chhor, A.M.T. Bell, D. Novikov, D. Vrel, A. Kanaev, Amorphous–anatase phase transition in single immobilized TiO2 nanoparticles, Chemical Physics Letters 558 (2013) 53–56. https://doi.org/10.1016/j.cplett.2012.12.019.

[19] T.W. Simpson, Q. Wen, N. Yu, D.R. Clarke, Kinetics of the Amorphous→γ→α Transformations in Aluminum Oxide: Effect of Crystallographic Orientation, Journal of the American Ceramic Society 81 (1998) 61–66. https://doi.org/10.1111/j.1151-2916.1998.tb02296.x.

[20] D.A.H. Hanaor, C.C. Sorrell, Review of the anatase to rutile phase transformation, J Mater Sci 46 (2011) 855–874. https://doi.org/10.1007/s10853-010-5113-0.

[21] T. Ai, High-temperature oxidation behavior of un-dense Ti_3AlC_2 material at 1000°C in air, Ceramics International 38 (2012) 2537–2541. https://doi.org/10.1016/j.ceramint.2011.10.091.

[22] S. López-Romero, J. Chávez-Ramírez, Synthesis of TiC thin films by CVD from toluene and titanium tetrachloride with nickel as catalyst, Matéria (Rio J.) 12 (2007) 487–493. https://doi.org/10.1590/S1517-70762007000300009.

[23] S. Sun, P. Song, J. Cui, S. Liang, Amorphous TiO_2 nanostructures: synthesis, fundamental properties and photocatalytic applications, Catal. Sci. Technol. 9 (2019) 4198–4215. https://doi.org/10.1039/C9CY01020C.

[24] S.-K. Jerng, D. Seong Yu, J. Hong Lee, C. Kim, S. Yoon, S.-H. Chun, Graphitic carbon growth on crystalline and amorphous oxide substrates using molecular beam epitaxy, Nanoscale Res Lett 6 (2011) 565. https://doi.org/10.1186/1556-276X-6-565.

[25] Y. Liu, X. Zhang, S. Dong, Z. Ye, Y. Wei, Synthesis and tribological property of Ti_3C_2T X nanosheets, J Mater Sci 52 (2017) 2200–2209. https://doi.org/10.1007/s10853-016-0509-0.

[26] X.N. Li, P.Y. Li, Z.Q. Liu, K. Ma, Z.Y. Liu, B.L. Xiao, Z.Y. Ma, Microstructure and mechanical properties of Ti_3AlC_2 reinforced $Al_{4.5}Cu_{1.5}Mg$ composites fabricated by powder metallurgy, J Mater Sci 58 (2023) 2570–2580. https://doi.org/10.1007/s10853-023-08185-0.

[27] L.M. Peng, Preparation and Properties of Ternary Ti_3AlC_2 and its Composites from Ti–Al–C Powder Mixtures With Ceramic Particulates, Journal of the American Ceramic Society 90 (2007) 1312–1314. https://doi.org/10.1111/j.1551-2916.2007.01517.x.

[28] J. Zhu, J. Gao, J. Yang, F. Wang, K. Niihara, Synthesis and microstructure of layered-ternary Ti_2AlC ceramic by high energy milling and hot pressing, Materials Science and Engineering: A 490 (2008) 62–65. https://doi.org/10.1016/j.msea.2008.01.017.

[29] X.H. Wang, Y.C. Zhou, Layered Machinable and Electrically Conductive Ti_2AlC and Ti_3AlC_2 Ceramics: a Review, Journal of Materials Science & Technology 26 (2010) 385–416. https://doi.org/10.1016/S1005-0302(10)60064-3.

[30] G. Liu, Y. Li, L. Fan, M. Nath, Y. Xu, J. Liu, Formation mechanism of Ti_3AlC_2 in TiO_2–Al–C/TiC systems at high temperatures, Ceramics International 48 (2022) 2614–2624. https://doi.org/10.1016/j.ceramint.2021.10.044.

[31] A. Zhou, C.-A. Wang, Z. Ge, L. Wu, Preparation of Ti_3AlC_2 and Ti_2AlC by self-propagating high-temperature synthesis, Journal of Materials Science Letters 20 (2001) 1971–1973. https://doi.org/10.1023/A:1013147121618.

[32] M.W. Barsoum, The $M_{N+1}AX_N$ phases: A new class of solids, Progress in Solid State Chemistry 28 (2000) 201–281. https://doi.org/10.1016/S0079-6786(00)00006-6.

[33] X. Wang, H. Ding, F. Qi, Q. Liu, X. Fan, Y. Shi, Mechanism of in situ synthesis of TiC in Cu melts and its microstructures, Journal of Alloys and Compounds 695 (2017) 3410–3418. https://doi.org/10.1016/j.jallcom.2016.12.018.

[34] A.M. Stolin, P.M. Bazhin, M.I. Alymov, M.V. Mikheev, Self-Propagating High-Temperature Synthesis of Titanium Carbide Powder under Pressure–Shear Conditions, Inorg Mater 54 (2018) 521–527. https://doi.org/10.1134/S0020168518060146.

[35] C.E. Shuck, M. Han, K. Maleski, K. Hantanasirisakul, S.J. Kim, J. Choi, W.E.B. Reil, Y. Gogotsi, Effect of Ti_3AlC_2 MAX Phase on Structure and Properties of Resultant $Ti_3C_2T_x$ MXene, ACS Appl. Nano Mater. 2 (2019) 3368–3376. https://doi.org/10.1021/acsanm.9b00286.

General Conclusion

The aim of this thesis was to explore and develop novel electrode materials for LIBs with a focus on improving energy storage performance, particularly rate capability and cycling stability. Over the course of this work, various strategies were developed to synthesize and optimize materials, building on the background research established in the bibliographic chapter. The goal was to address existing challenges in the field by investigating new approaches to material design, structural modifications, and synthesis methods, ultimately contributing to the advancement of electrode materials for LIBs.

The first experimental investigation centered on $AgNbO_3$ perovskites as model negative electrode materials for LIBs. Through electrochemical cycling, it was demonstrated that an *in situ* activation process involving the exsolution of silver nanoparticles enhanced the Li^+ storage capacity of $AgNbO_3$. This work contributed to the understanding of how dynamic structural transformations during electrochemical processes can enhance the performance of perovskite-based electrodes. Although $AgNbO_3$ might not be used in practical LIBs, the insights gained from its behavior could pave the way for further studies on perovskite materials for high-power battery applications. Through several tailoring strategies such as La-substituted A-site deficient ($Ag_{1-3x}La_x\square_{2x}NbO_3$, $x \leq 0.20$) perovskites, and undoped A-site deficient ($Ag_{1-x}\square_xNbO_{3-\delta}$, $0 < x < 0.55$), it was demonstrated that ABO_3 perovskite material are versatile and promising host structures to build future cation storage electrode materials with desired properties.

In the second experimental study, alkali metal-based $K_{1-3x}La_x\square_{2x}NbO_3$ ($0 \leq x \leq 0.15$) perovskites were investigated as a cost-effective and sustainable alternative to ($Ag_{1-3x}La_x\square_{2x}NbO_3$ ($x \leq 0.20$) model material. The introduction of cationic vacancies through La substitution created additional Li^+ storage sites, resulting in improved cycling stability and rate performance. In connection to investigations of model $Ag_{1-3x}La_x\square_{2x}NbO_3$ ($x \leq 0.20$) system, this study further validate the significant role that controlled structural modifications can play in optimizing material performance for LIB electrodes, particularly in the context of vacancy engineering.

After a successful development of polyacrylamide route for multicationic oxides, the experimental work in this thesis further investigated the possibility of applying this synthesis route for preparing carbides, targeting the promising Ti_3AlC_2 MAX phase. Hence, third experimental chapter shifted focus on the development of challenging polyacrylamide-based wet chemical synthesis of Ti_3AlC_2 MAX phase. The successful synthesis of Ti_3AlC_2-like lamellar structures was achieved, and these materials were evaluated as negative electrode materials for LIBs. The results showed that Ti_3AlC_2@C exhibited higher specific capacities and better cycling stability compared to commercial Ti_3AlC_2, largely due to the beneficial role of excess carbon in enhancing conductivity and contributing to Li^+ storage. However, challenges related to phase purity and excess carbon were also observed, highlighting the need for further optimization of the synthesis process.

Across these studies, the common theme has been the importance of tailored oxides and carbides synthesis through several routes and structural control in enhancing the performance of LIB electrodes. The research presented in this thesis demonstrates that by employing different strategies, such as in-situ activation, cation substitution, and tailored synthesis techniques, it is possible to significantly improve Li^+ storage capacity, cycling stability, and overall performance. While each material system posed unique challenges, the collective findings offer valuable insights into the design principles that can guide the development of future high-performance electrode materials.

Overall, this thesis has made a meaningful contribution to the field of energy storage by exploring novel material systems and providing a deeper understanding of the structural and electrochemical properties that govern their performance in LIBs. The insights gained from the studies on perovskite oxides ($AgNbO_3$, $Ag_{1-3x}La_x\square_{2x}NbO_3$, $Ag_{1-x}\square_xNbO_{3-\delta}$, and $K_{1-3x}La_x\square_{2x}NbO_3$) and ternary carbides ($Ti_3AlC_2$ MAX phases) not only enhance the current knowledge of these materials but also provide a foundation for future research aimed at optimizing electrode materials for next-generation high power energy storage technologies.

Perspectives and Critical Reflections on this Thesis Work

In this final section, which is more personal and subjective, I will explore the future directions suggested by my thesis research, as well as offer a critical, personal reflection on the work conducted. As is often the case with research, while some questions have been resolved, many new ones have emerged, warranting further investigation. The following reflections aim to highlight these areas for consideration.

The research detailed about tailored oxide perovskite, such as successful implementation of structure-property relationship in La-substituted A-site deficient perovskites ($Ag_{1-3x}La_x\square_{2x}NbO_3$, $x \leq 0.20$ and $K_{1-3x}La_x\square_{2x}NbO_3$, $0 \leq x \leq 0.15$) could motivate for the future research in several ways.

1) By application prespective, $K_{1-3x}La_x\square_{2x}NbO_3$ could be studied as electrode material for sodium or potassium ion batteries. The appropriate size of the K vacancies may enable compatibility with higher sized K^+ or Na^+ insertion, a feature that was not achievable with $Ag_{1-3x}La_x\square_{2x}NbO_3$ when used for Na^+ storage. In this regard, a close collaboration with Prof. Balducci’s group has been established through the DESTINY PhD program, where fellow PhD student Metin Orbay has investigated these materials as electrodes for sodium and potassium ion batteries.
2) According to literature, $KNbO_3$ and related alkali niobates exhibits thermally insulating properties. $KNbO_3$ exhibits lowest thermal conductivity (1.2 $Wm^{-1}K^{-1}$ at 1000 K) reported for any oxide perovskites, which mainly originating from A-site deficiency. Therefore, it is worth exploring $K_{1-3x}La_x\square_{2x}NbO_3$ materials as negative electrodes for high temperature LIBs, using ionic liquids as electrolyte as developed in the lab of Prof. Balducci, a major collaborator of this project.
3) Given the structural flexibility of Nb-based perovskite structures, it is valuable to explore B-site substitutions as a strategy for creating vacancies. For instance, substituting Nb^{5+} with W^{6+} would require fewer A cations to equilibrate the positive charge such as $Ag_{1-x}(Nb_{1-x}W_x)O_3$ with x vacancies.
4) Many more studies could be conducted to highlight the interest of this approach and generalize it to other oxides. In addition to cost-effectiveness, optimizing A-site and/or B-site substitution in metallic perovskites of which some already already displayed amazing redox properties, such as $SrBO_3$, (SBO, B = V, Nb, Ta, Mo, etc.), is interesting to investigate. However, due to intrinsic defects related to the difficulty in synthesis of these

metastable phases, introducing intentional defects (La-substitutions) systematically with control and accuracy is challenging. According to conclusions of research done in this thesis, it can be proposed that a cation substitution could be a potential strategy to stabilize such phases by avoiding over-oxidized states, and retaining the expected metallicity. Thirdly, as a general perspective, such approach could be adopted for other perovskite systems ($A^{2+}B^{4+}O_3$ and $A^{3+}B^{3+}O_3$) to obtain novel tailored materials or for already known electrochemically active oxide materials to be considered promising for potential practical applications.

The research detailed about Ti_3AlC_2 MAX phase, hold promising future prospects. The wet chemical synthesis of the Ti_3AlC_2 MAX phase emphasizes the need for further optimization of synthesis parameters to achieve high phase purity while maintaining the beneficial properties of carbon. In particular, the concentration of monomers is closely tied to the amount of residual carbon, highlighting a key area for refinement. Future efforts should aim to fine-tune this synthesis process to enhance both phase purity and material morphology, facilitating more efficient production of the Ti_3AlC_2 MAX phase. This advancement could help address practical challenges in the development of $Ti_3C_2T_x$ MXenes, a promising material for high-power electrode applications.

As a critical reflection about work done in this thesis, there are two main concerns. Firstly, the environmental and economic analysis about choice of transition metals in the system is necessary from industrial as well as humanitarian point of view. Niobium, which is mainly used in experimental work of this thesis, is considered critical materials by the European Union, meaning there are concerns regarding their availability on earth, geographic distribution, and/or scarcity, which affects their price. Furthermore, extraction conditions in mining countries must be considered. For example, niobium is partially extracted in the Democratic Republic of the Congo (DRC) from illegal coltan mines that poses collapse risks. Often, children are exploited to extract this rock, and the sale of these minerals funds the purchase of weapons that fuel guerrilla warfare across the country. The lack of data and information on these issues calls for caution when considering the possible industrialization of niobium based oxides as negative electrode materials.

Secondly, for scaling up into higher quantity of materials, a synthesis method should be environmentally friendly and cost-effective. Although, polyacrylamide gel method can often be carried out at relatively lower temperatures, reducing energy costs. One significant issue with this method is the complexity and toxicity of the chemicals involved, such as acrylamide monomers and crosslinkers, which are more expensive and hazardous than the simpler metal alkoxides or salts used in sol-gel synthesis. From an environmental perspective, the polyacrylamide method generates organic residues during calcination, leading to carbon contamination and toxic fume emissions, requiring careful waste management. Additionally, the polyacrylamide gel method faces scalability challenges, particularly in handling toxic acrylamide on a larger scale.

Despite the challenges highlighted, the research presented in this thesis opens the door to exciting future possibilities. The breakthroughs in oxide perovskites and MAX phases have the potential to inspire innovative solutions in energy storage, high-performance materials, and beyond. This thesis not only contributes valuable insights to the field but also serves as a stepping stone toward transformative discoveries, promising a bright future for both scientific progress and real-world applications.

Annex

Energy Storage Materials 70 (2024) 103431

Contents lists available at ScienceDirect

Energy Storage Materials

journal homepage: www.elsevier.com/locate/ensm

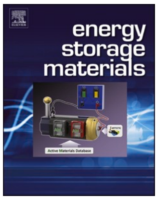

Lithium storage behaviour of $AgNbO_3$ perovskite: Understanding electrochemical activation and charge storage mechanisms

Abbas Khan [a,b,$], Metin Orbay [c,$], Nicolas Dupré [a], Eric Gautron [a], Etienne Le Calvez [a,b], Olivier Crosnier [a,b], Andrea Balducci [c,*], Thierry Brousse [a,b,*]

[a] Nantes Université, CNRS, Institut des Matériaux de Nantes Jean Rouxel, IMN, F-44000 Nantes, France
[b] Réseau sur le Stockage Electrochimique de l'Energie (RS2E), CNRS FR 3459, 80039 Amiens, France
[c] Friedrich-Schiller-University Jena, Institute of Technical Chemistry and Environmental, Chemistry and Center for Energy and Environmental Chemistry, Jena, Germany

ARTICLE INFO

Keywords:
Lithium-ion batteries
Perovskites
Anodes
Electrochemical activation

ABSTRACT

In this study, a model $AgNbO_3$ perovskite is prepared via polyacrylamide synthesis technique, and the underlying unique Li^+storage mechanism is studied. This structure is projected to provide low Li^+ storage capacity due to all occupied crystallographic sites. It delivered a specific capacity of 17 $mAh.g^{-1}$ at $0.1A.g^{-1}$ within the potential range of 1.2–3.0 V *vs.* Li^+/Li. However, at lower potentials, the material undergoes activation for Li^+ storage by a multistep structural transition that included in-situ Ag-exsolution from the A-site of the lattice and an electrochemically induced crystalline-to-amorphous transition. At low potential the materials delivers high specific capacity (226 $mAh.g^{-1}$ at 0.1 $A.g^{-1}$ in 0.01–3 V *vs.* Li^+/Li potential range) due to the contribution of improved Nb-redox activity and nanoscale Ag-Li (de)alloying mechanisms that were comprehensively examined utilizing advanced characterization tools. In addition, good capacity retention of 72 $mAh.g^{-1}$ at high current density of $2A.g^{-1}$ and an excellent cyclic stability with coulombic efficiencies above 99.9 % are obtained for 2500 cycles at 1 $A.g^{-1}$ underlining the performance and the stability of $AgNbO_3$. This study introduces an alternative approach for tailoring electrode material using an electrochemically driven in-situ activation process. It also serves as a paradigm for the use of exsolved materials as negative electrodes in fast-charging batteries, paving the way for a better understanding of charge storage mechanisms in perovskites.

1. Introduction

With the successful commercialization of electric vehicles, the demand for energy storage devices is becoming increasingly critical [1]. Lithium-ion batteries (LIBs) are nowadays used in many applications, including several high-power applications. In these LIBs graphite is used as negative electrode material, and it is important to notice that despite the favorable feature of this type of anode, its use might not be an optimal choice when high current densities are applied [2]. As a matter of fact, the power performance of this material is rather different for the charge (intercalation) and the discharge (de-intercalation) process. It has been shown that during the discharge process graphite anodes retain well their capacity, but their performance during the charge process is strongly affected by the applied current [3]. Clearly, this represents a limitation associated to the use of this carbon electrode.

In the past years several alternative materials have been explored in literature. Among them, lithium titanium oxide ($Li_4Ti_5O_{12}$) has been one of the most widely investigated, and this anodic material is used as high-power alternative to graphite in commercial devices utilized for niche applications such as short-range buses but suffers from low energy density due to overall lower cell voltage [4]. Among other alternatives, niobium (Nb) containing oxides such as Nb_2O_5 and binary oxides l-Nb-O (where L is Ti, Fe, Zr, etc.), have gained an increasing attention in the last years. Anodes based on these materials display high specific capacity, originating from rich redox activity (Nb^{5+} to Nb^{4+}, Nb^{4+} to Nb^{3+}), fast charging capability, safety and excellent cyclic stability [5–8].

ABO_3 type perovskites such as $AgNbO_3$ are versatile materials because of their capacity to tolerate wide range of cation sizes, oxidation states, dopants and defects [9]. In this structure, A-site is filled by large radii cation in the center of perovskite cage with 12-fold coordination, and corner-shared BO_6 octahedral network giving a high packing factor

---

* Corresponding authors.
E-mail addresses: andrea.balducci@uni-jena.de (A. Balducci), Thierry.Brousse@univ-nantes.fr (T. Brousse).
[$] Equal Authors, Shared first authorship.

https://doi.org/10.1016/j.ensm.2024.103431
Received 20 December 2023; Received in revised form 18 April 2024; Accepted 23 April 2024

[10].The exploration of perovskite anodes for energy storage applications has shown promising results, yet the latter faces rapid capacity decline with cycling [11,12]. The challenge in utilizing ABO_3 type perovskites to their full potential lies in the difficulty of incorporating Li^+ ions into their structure due to limited interstitial sites and the constraint of fixed lattice spacing. Overcoming this obstacle is crucial for maximizing the energy storage capabilities of these materials.

One potential strategy to activate such materials is to partially substitute the A-site of the structure with cations at higher oxidation state to induce vacancies. Recently, it has been shown that this strategy can be successfully implemented through the substitution of Ag^+ cations by La^{3+}, leading to the creation of A-site vacancies in $Ag_{1-3x}La_x\square_{2x}NbO_3$ (with $x \leq 0.20$ and where $\square$ is a A-site vacancy) [13]. Moreover, the corresponding substituted materials have demonstrated fast Li^+ insertion and a dependence of the capacity with the number of created vacancies to a certain extent. Although the capacity of these materials is lower than that of other niobates such as $T\text{-}Nb_2O_5$, $CeNb_3O_9$, $Ti_2Nb_2O_9$, $TiNb_2O_7$, or $HTiNbO_5$ [14–18] the power capability of this compound made it of interest for further investigations.

An alternative appealing strategy which could be utilized to further improve the specific capacity of this type of material is the promotion of *in-situ* activation. Recently, it has been reported that *in-situ* amorphization can be an efficient way to generate defects by breaking the long-term crystal orders, hence enriching the Li^+ insertion sites to obtain enhanced specific capacity [19,20]. However, transitions from crystalline materials to amorphous ones are challenging to realize, especially in ABO_3 type perovskites (with ideal 1:1 cation ratio), due to strong structural stability and has rarely been achieved. It is also interesting to observe that ABO_3 type perovskites have received significant attention for realizing exsolution processes, a strategy to grow metallic nanoparticles from its host structure [21–24], especially for solid oxide fuel cells. The occurrence of this type of process could also be of interest in view of the use of ABO_3 type perovskites in LIBs.

In this study we report a detailed structural and electrochemical investigation on the storage mechanism occurring in a model ABO_3 type perovskite, namely $AgNbO_3$. The aim of this work is to evaluate whether it is possible to electrochemically promote, and possibly control, the occurrence of *in-situ* activation and exsolution processes in order to improve the capacity of $AgNbO_3$ based electrode as well as their behavior under high current density.

2. Experimental section

2.1. Material synthesis

$AgNbO_3$ perovskites were synthesized by polymerization assisted sol-gel route named polyacrylamide synthesis, which has been adopted previously for synthesis of transition metal oxides [25]. Stoichiometric amounts of silver nitrate ($AgNO_3$ by Alfa Aesar, 99.9 %) and niobium oxalate hydrate ($C_{10}H_5NbO_{20}$. xH_2O by Alfa Aesar) precursors were dissolved in ethylene glycol (Alfa Aesar) and stirred at room temperature. Citric acid ($HOC\ (CH_2CO_2H)_2$ by Alfa Aesar, 99+%) was added to the solution in 1.5:1 cation molar ratio and stirred until transparent solution was obtained. Citric acid acted as a complexing agent of which carboxyl and hydroxyl groups were attached to Ag^+ and Nb^{5+}, respectively, through chelation reaction. Afterwards, acrylamide monomers (Alfa Aser) and N, N′-mesthylene-bisacrylamide (Alfa Aser) cross linkers were introduced to the solution in 9:1 cation molar ratio. The monomer radicals open up the double bonds of acrylamide and form a new activation site, which provides linkage to the second monomer unit and thus propagates the chain process by radical transfer process. Polyacrylamide grows in a linearly chained system. However, N, N' –methylene bisacrylamide acts as cross-linker and help to grow and develop a 3D network of interconnected loops. The solution was heated to 90 °C while stirring and hydrogen peroxide (30% w/w H_2O_2 in H_2O by Sigma Aldrich) was added to initiate the polymerization. Polymeric gel is formed after 20 min and converted to xerogel when kept in oven at 300 °C. The final $AgNbO_3$ materials were obtained by grounding xerogel and annealing at 650 °C in air for 12 hrs. The synthesis process is schematically illustrated in Fig. 1a.

2.2. Physical characterizations

Powder XRD measurements were carried out using PANalytical X'Pert Pro-diffractometer (Malvern PANalytical, Almelo, Netherlands). Cu-$K_{\alpha1}$-$K_{\alpha2}$ (λ = 1.54060 Å, 1.54443 Å) radiation source with acceleration voltage of 40 KV at a current 40 mA was used. XRD data were recorded in the 2θ range of 5° to 80°, scanning at a step size of 0.0170° For *in-situ* XRD measurements, a specially designed Swagelok-type® cell with beryllium window on top was used [26]. The data were collected at different 2θ ranges between 20° and 80° The applied current density, pattern acquisition and relaxation time varied depending on the selection of potential window for GCPL measurements. The BET specific surface area of the $AgNbO_3$ powder was calculated using N_2 adsorption–desorption isotherms at 77 K with a Quantachrome Nova 4200e equipment (Anton Paar). The morphology study of $AgNbO_3$ powders and *post-mortem* analyses of cycled electrodes were performed by Zeiss MERLIN Instrument using in-Lens annular detector keeping an operating voltage of 20 kV. To prepare the samples, a small fraction of powder/-electrode were affixed on carbon double tape. *Ex-situ* ^7Li and ^{93}Nb MAS NMR experiments were acquired on a Bruker Avance 500 spectrometer ($B_0 = 11.75T$), Larmor frequencies ν_0 ($^{93}Nb = 122.41$ MHz, $^7Li = 194.37$ MHz) at RT. A Bruker MAS probe with a cylindrical 2.5 mm (o.d) zirconia rotor spun at a frequency of 25 kHz was used for spectral analyses. Spectra were obtained by applying a single pulse sequence, and a recycle delay (D_1) of 3 s ensuring the acquisition of quantitative spectra. The resulting integrated intensities were normalized with respect to the mass of the sample contained in the NMR rotor, the number of scans, and the receiver gain. Scanning/transmission electron microscopy (S/TEM) measurements were performed to characterize the morphological modification and Nb oxidation states of the pristine sample and after cycling (0.01 V *vs.* Li+/Li). For both samples, the powder has been brought into contact with a holey carbon film-coated copper grid in a glove box (Ar atmosphere). The grid was inserted in an aberration-corrected S/TEM Themis Z G3 (Thermo Fisher Scientific) using an atmosphere-controlled sample holder. All S/TEM experiments were performed at 300 kV.

High-angle annular dark-field (HAADF-STEM) images were acquired with 21.4 mrad convergence angle and 63–200 mrad collection angles. A Super-X system (four energy-dispersive X-ray detectors) allowed to acquire elemental maps.

Electron energy loss spectroscopy (EELS) was performed with a GIF Quantum ERS 966 imaging filter (Gatan) in Dual-EELS mode (for simultaneous acquisition of low loss and high loss spectra) in STEM mode (21.4 mrad convergence angle and 36 mrad collection angle, probe current ~50 pA). The spectra presented here were integrated on spectral image areas. A power law was used to subtract the background before core edges.

2.3. Electrochemical measurements

Slurries containing 85% wt. active material ($AgNbO_3$), 10% wt. conducting agent (Imerys Super C65) and 5% wt. binder (Walocel sodium carboxymethyl cellulose CMC2000) were prepared and cast onto either copper or aluminum foil *via* doctor blading. $AgNbO_3$ electrode mass loadings ranged from 1.2 to 2.5 $mg.cm^{-2}$. For *in-situ* XRD, free standing electrodes were prepared by mixing $AgNbO_3$, conductive agent (Carbon Black by Superior Graphite, Chicago, IL, USA) and poly (1,1,2,2-tetrafluoroethylene (PTFE, Sigma Aldrich) in a%wt. of 75, 15, and 10, respectively. Few drops of ethanol were added, and the mixture was grounded until get homogenous paste. The paste was processed via cold-rolling until it became an electrode of around 5–10 $mg.cm^{-2}$. The

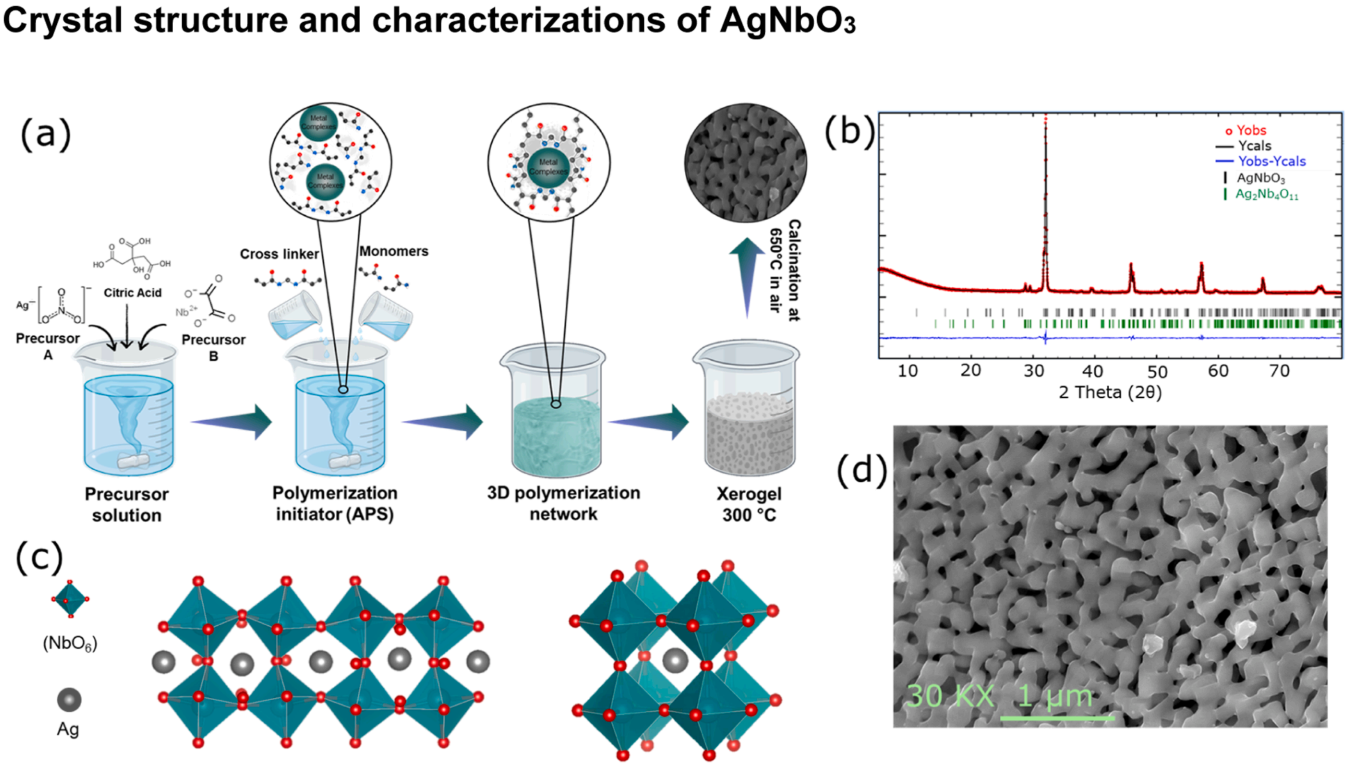

Fig. 1. (a) Schematic illustration of polyacrylamide synthesis of $AgNbO_3$ perovskites. (b) Rietveld refined XRD profile of $AgNbO_3$ powder with experimental and calculated patterns, as well as the difference between the two patterns. Bragg reflection of the $AgNbO_3$ perovskite phase is denoted by black bars. $AgNbO_3$ crystalized in an orthorhombic perovskite phase (Pbcm space group with cell parameters $a = 5.5485(16)$ Å, $b = 5.6001(14)$ Å, and $c = 15.6475(4)$ Å). Few impurities (mass percentage of ~11 %) with main diffraction peaks around 29° corresponds to $Ag_2Nb_4O_{11}$ phase denoted by green bars. (c) Top and 3D view of crystal structure of $AgNbO_3$ based on refinement results. (d) SEM image of material showing well-defined and uniform morphology of $AgNbO_3$.

latter formulation, different from the one used for electrochemical tests, was chosen to ensure high quality in-situ XRD measurements. Propylene Carbonate (PC) anhydrous 99.7 % was purchased from Sigma Aldrich. Lithium bis(trifluoromethanesulfonyl)imide (LITFSI) (99.9 %), lithium bis(fluorosulfonyl)imide (LIFSI) (99.9 %) and 1-Butyl-1-methylpyrrolidinium bis (trifluoromethanesulfonyl)imide ($Pyr_{1,4}TFSI$) were purchased from Solvionic and used to prepare the electrolytes at room temperature whereas LP30 (Solvionic) was used as is. Swagelok-type® cells were used to study the electrochemical performance of $AgNbO_3$ electrodes in a three-electrode cell setup. The working electrode (WE) was $AgNbO_3$, whereas the reference electrode (Ref) and the counter electrode (CE) was lithium metal. Biologic VMP-3 and MPG-200 potentiostats were used for all electrochemical studies. The total area of all electrodes was 1.13 cm^2. Diffusion coefficient of $AgNbO_3$ electrodes were measured using the galvanostatic intermittent titration technique (GITT), using a previously described protocol [27]. Cell assembly and electrolyte preparation were carried out in an argon-filled glovebox (O_2 and H_2O <1 ppm).

3. Results and discussions

3.1. *Crystal structure and characterizations of $AgNbO_3$*

An overview of the synthesis of $AgNbO_3$ is presented in Fig. 1a. Rietveld refinement of powder X-ray diffraction pattern revealed the formation of orthorhombic perovskite phase (Pbcm space group) with lattice parameters $a = 5.54857(16)$ Å, $b = 5.60010(14)$ Å, and $c = 15.6475(4)$ Å (Fig. 1b). The cell parameters indicate a clear difference between the a and b parameters, validating the use of orthorhombic space group [28]. The perovskite structure of $AgNbO_3$ is built by Ag^+ cations in the center of the perovskite cage with a coordination number of 12 while Nb^{5+} with coordination number of 6 form corner-shared tilted $[NbO_6]$ octahedra as shown in Fig. 1c. The average crystallite size obtained is 76.8 nm, calculated by using Scherrer equation. The detailed Rietveld refinement results are presented in supplementary information (Table S1). Small impurity peaks (diffraction peak at 29°) of $Ag_2Nb_4O_{11}$ can be found in $AgNbO_3$ X-Ray diffraction pattern of the corresponding powder. The main reason of this is the thermodynamic instability of Ag^+at higher temperatures (conversion to Ag^0 at 150 °C), which is causing a phase formation competition between $AgNbO_3$ and $Ag_2Nb_4O_{11}$ [28,29]. Taking these results into account, it is evident that the realization of a single phased $AgNbO_3$ with uniform morphology via conventional solid-state reaction routes is rather challenging. Approaches such as keeping slight excess of Ag_2O precursor during synthesis or sintering in high-pressure O_2 environment has been reported to favor the homogeneity and improved phase quality of $AgNbO_3$ [29]. We recently reported the synthesis of $Ag_{1-3x}La_x\square_{2x}NbO_3$ (with $0 \leq x \leq 0.20$) perovskites by sol-gel method with fewer impurities [13]. However, to avoid particle agglomeration and to obtain a uniform morphology, polyacrylamide synthesis route was adopted for $AgNbO_3$ material [30]. The polymerization step during synthesis process helps to bind the metal complexes in solution with even distribution leading to the formation of interconnected porous network of particles with a uniform morphology, as shown in Fig. 1d. The BET surface area of the $AgNbO_3$ synthesized by polyacrylamide route was 6.7 m^2g^{-1}, which represents a twofold increase compared to materials synthesized by sol-gel method [13]. The electrochemical behavior of composite electrodes containing the synthesized $AgNbO_3$ was initially investigated in half-cell configuration (the details are reported in the experimental part). Preliminary measurements were performed in the potential range between 1.2 – 3.0 V *vs.* Li^+/Li, which the electrochemical window mostly used to investigate electrodes containing Nb-based oxides [31]. Due to the 100 % occupancy of the A site by Ag^+ cations in the $AgNbO_3$ structure, there are no open channels in the structure for Li^+ diffusion, nor well-defined empty sites to welcome them. Hence, no significant redox activity is observed in the CV within such potential window and the electrode displays a very limited specific capacity of 17 mAh.g^{-1}(Fig. 2a). This capacity mostly originated from surface charge storage processes rather than insertion of Li$^+$ into the structure. To confirm any structural changes in the material upon cycling, *in-situ* XRD experiments were carried out. The crystallographic peaks of perovskite structure do not deviate from their original positions, and no additional peaks appear upon charge/discharge processes, as shown in Fig. 2b. These results indicate that in the investigated potential range (1.2 – 3.0 V *vs.* Li$^+$/Li) the electrode is displaying a stable structure containing Ag$^+$ and Nb^{5+}. It is interesting to notice, however, that a prolonged cycling process is leading to the formation of few nanoparticles on the surface (probably Ag$^+$ to Ag$^\circ$ conversion), although the morphology is retained. This latter point is well visible from the differences of the surface on *ex-situ* SEM observations reported in Fig. 2c and in Fig. 2d.

3.2. Ag reduction and exsolution process in AgNbO$_3$ crystal lattice

As mentioned in the introduction, the occurrence of *in-situ* activation as well as exsolution processes could positively contribute to the capacity of AgNbO$_3$-electrodes. Although similar process have been explored in the past for layered oxides by Morcrette [32] and Rozier et al.[33], where lithium-driven displacement process allows the growth and disappearance of copper dendrites, to the best of our knowledge, the possibility to induce/promote them electrochemically in ABO$_3$-type structures has not yet been considered for energy storage applications. With the aim to verify this possibility, the AgNbO$_3$-based electrodes were cycled in extended potential ranges compared to the one typically used for these materials (1.2 – 3.0 V *vs.* Li$^+$/Li), namely from 0.6 – 3.0 V *vs.* Li$^+$/Li and from 0.01 – 3.0 V *vs.* Li$^+$/Li.

Fig. 3a depicts the first cycles of AgNbO$_3$ in these two potential windows and, for comparison, also in the “standard” one. The tests were carried out utilizing 1 M lithium bis(fluorosulfonyl)imide (LiFSI) in propylene carbonate (PC) as the electrolyte. When the potential is stopped at 1.2 V *vs.* Li$^+$/Li, the AgNbO$_3$-based electrode displays a weak reduction peak between 2.5–2 V, which is identified as the initial reduction process of surface Ag$^+$ in AgNbO$_3$ and can be observed in SEM imaging as clustering is starting to appear (Fig. 2d). However, it is clear that the initial reduction of silver ions is not sufficient in terms of enhancement of storage capabilities and creation of relevant sites for Li$^+$ insertion in AgNbO$_3$, resulting in negligible reversible capacity value (17 mAh.g^{-1}). This value corresponds to 15 % of the A-site accessible to Li$^+$ cations which is consistent with a partial reduction and exsolution of Ag$^+$ cations thus leaving empty A sites in the AgNbO$_3$ structure at the surface of the particles.

Lowering the electrodes cutoff potential to 0.6 V *vs.* Li$^+$/Li resulted in the emergence of two consecutive peaks at 0.88 V and 0.6 V *vs.* Li$^+$/Li. These two peaks are also apparent when employing alternative electrolytes, some of which are known not to have SEI-forming capabilities (*e.g.*, ionic liquid-based) (see figure S1 in SI). Therefore, it is reasonable to assume that they do not originate from interphase processes between electrode and electrolyte and/or decomposition processes on the latter, but rather come from structural processes occurring to AgNbO$_3$. Furthermore, at 0.6 V *vs.* Li$^+$/Li, the electrochemical behavior of the electrodes changes considerably. Indeed, one can observe an enhancement of the reduction current at the same peak positions as depicted in the former 1.6–1.2 V *vs.* Li$^+$/Li potential window (Fig. 3b), resulting in a much higher capacity (61 mAh.g^{-1}) (Fig. S2 & S3). *In-situ* XRD measurements, coupled with postmortem SEM and XRD (Fig. S4 & S5) indicate that the perovskite phase is preserved in the potential range between 0.6 – 3.0 V *vs.* Li$^+$/Li. No new peaks were observed during cycling process which supports a solid solution-type mechanism occurring upon the charging process, as observed in the case of T-Nb$_2$O$_5$ [7]. Moreover, during the 1st lithiation cycle, XRD patterns above 1 V *vs.* Li$^+$/Li reveal the disappearance of peaks at around 2θ = 29°, corresponding to Ag$_2$Nb$_4$O$_{11}$ phase impurity. This suggests that a reductive potential serves as a stimulus for the impurity removal and phase purification. The mitigation of such impurities in AgNbO$_3$ perovskites has been reported previously through fine grinding process, because this impurity is typically localized within the surface layer, attributed to high-temperature melting/decomposition that initiates at the surface [29]. Furthermore, an irreversible decrease in intensity of all the crystallographic peaks is observed during 1st lithiation process (Fig. 4a) indicates that the perovskite structure is maintained at least down to 0.6 V *vs.* Li$^+$/Li, while SEM imaging at this potential reveals an amplification

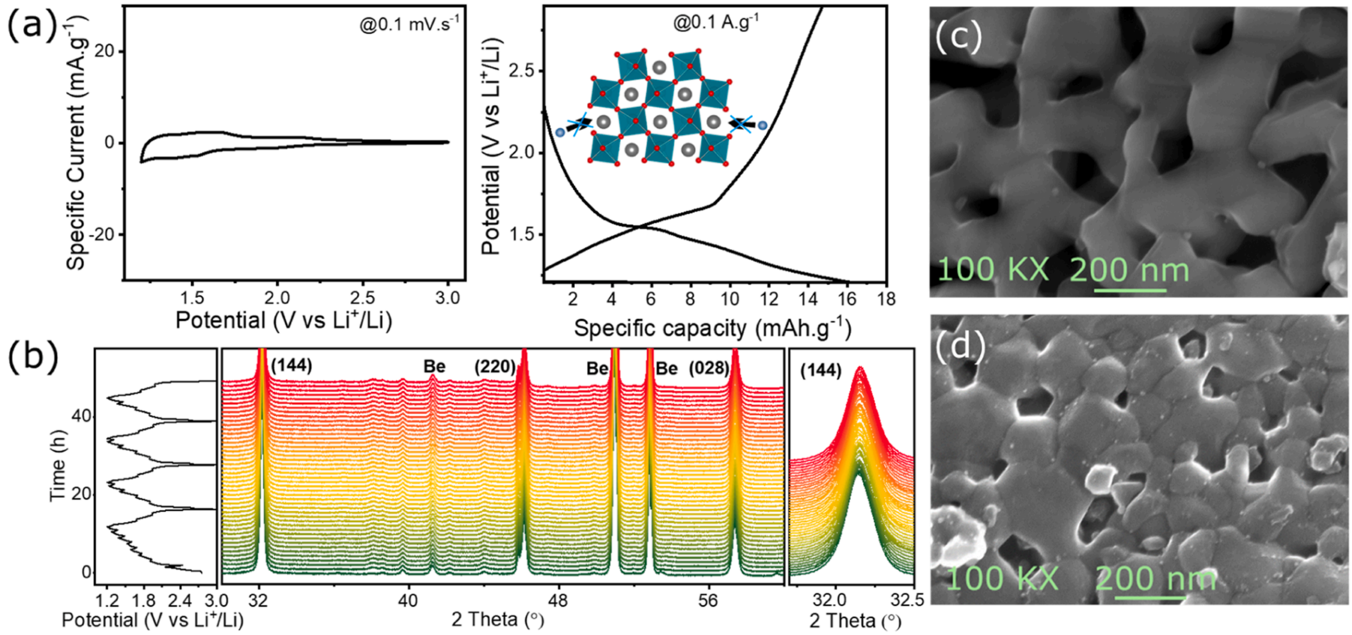

Fig. 2. (a) Li$^+$ storage behavior of AgNbO$_3$ electrode in 1.2 – 3.0 V potential window with Cyclic voltammetry and charge/discharge showing limited capacity. (b) *In-situ* XRD depicting no structural evolution and zero strain behavior upon cycling. SEM images of (c) Pristine electrode. (d) Cycled electrode showing morphology retention and surface Ag reduction (small white dots on the surface).

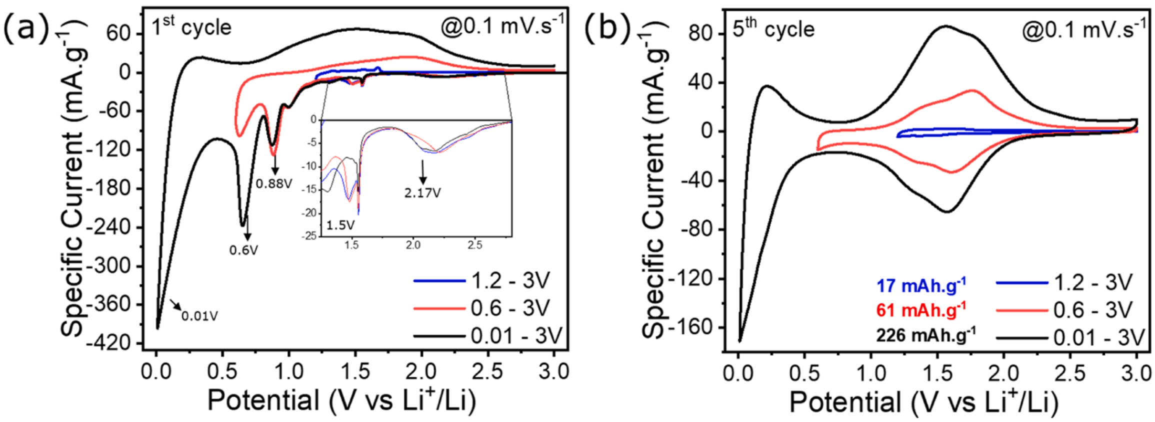

Fig. 3. (a) 1st cycle of $AgNbO_3$ electrode in different potential windows using decreasing cut-off potential (1.2/0.6/0.01–3 V *vs.* Li^+/Li) evidencing the activation region (0.6–0.9 V) and emphasizing the appearance of irreversible activation peaks. (b) 5th cycle showing stable CV signature of the same electrodes after activation at 1.2,0.6 and 0.01 V *vs.* Li^+/Li and related specific capacity values.

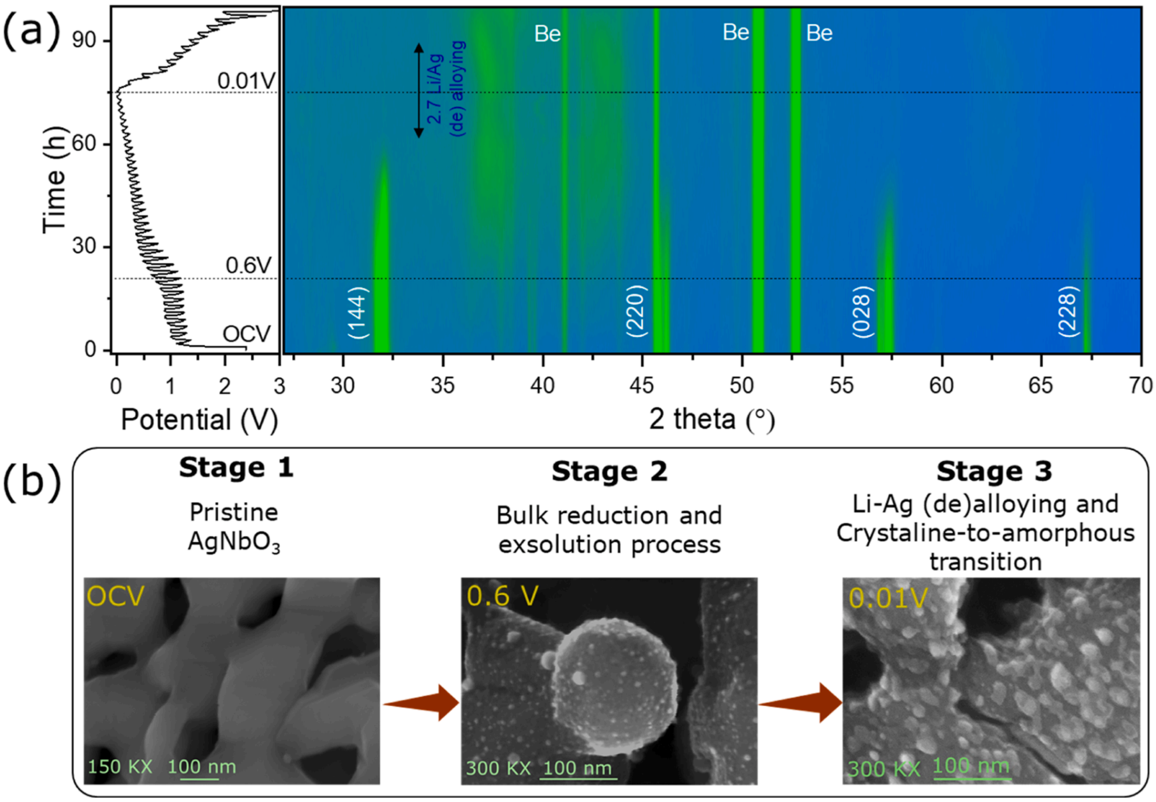

Fig. 4. Li^+ storage mechanism investigation of $AgNbO_3$ electrode in 0.01 – 3.0 V potential window. (a) In-situ XRD patterns of 1st charge/discharge cycles at 0.1 C. (b) Ex-situ SEM images of cycled electrode corresponding to different stages of material transition.

of silver exsolution process at the surface of $AgNbO_3$ particles (Fig. 4b).

Alternatively, the exsolution of silver in $AgNbO_3$ can be obtained when the material is thermally reduced at 250 °C under Ar/H_2 atmosphere (Fig. S6a). However, thermal processes agglomerate silver particles into bulk-silver in comparison to the silver nanoparticles distribution obtained electrochemically (Fig. S6b). Metallic silver is detected by XRD (Fig. S6c) and concomitantly the pristine perovskite structure is still observed after thermal treatment. To summarize, decreasing the lower cut-off potential from 1.2 down to 0.6 V *vs.* Li^+/Li improves the capacity of the electrode while promoting the exsolution of nanosized silver particles.

Further advantage can be taken of this peculiar microstructure by decreasing the cut-off potential down to 0.01 V *vs.* Li^+/Li. Indeed, when the $AgNbO_3$-based electrodes were cycled down to 0.01 V *vs.* Li^+/Li their electrochemical behavior also changed significantly. As shown in Fig. 3a, the electrodes cycled in this potential range display a capacity of 226 $mAh.g^{-1}$, which is one order of magnitude higher than that displayed by the same electrodes when a cutoff voltage at 1.2 V is applied and nearly quadrupled the capacity in comparison to 0.6 V cut-off (it must be said that the contribution of the conducting agent to the observed capacity is negligible, see figure S15 in SI). It is known that silver extrusion might destabilize the framework [24] and lead to structural failure and subsequent loss of capacity of the material. This is not the case for the investigated $AgNbO_3$-based electrode until the potential reaches 0.3 V *vs.* Li^+/Li. Below 0.3 V *vs.* Li^+/Li, and thus in the potential region considered in the test, the $AgNbO_3$ becomes amorphous with a clear loss of the diffraction peaks of the related phase (Fig. 4a). Moreover, the formation of Li-Ag alloy take place concomitantly [34, 35]. However, the reversibility of this last process for bulk Ag particles is quite poor. $AgNbO_3$-based electrodes, on the contrary, display very high reversibility and stability (Fig. S2). This latter behavior might be related to the size of the Ag particles, which are only a few nm in diameter (Fig. S6b), and might improve the reversibility of the alloying reaction due to nanosizing effect [36].

The results discussed above indicate that the perovskite structure may intrinsically stabilize Nb and generate a wide operating window for lithium-ion intercalation into the $AgNbO_3$ host structure which exhibits a lot of vacancies once silver has been exsoluted.

A summary of all these processes can be depicted from *in-situ* XRD measurements performed in the potential window between 0.01 – 3.0 V *vs.* Li^+/Li (Fig. 4a). During 1st lithiation, a gradual decrease in intensity of all the crystallographic peaks occurs, till their complete disappearance, thus indicating electrochemically induced crystalline-to-amorphous transition of $AgNbO_3$. Upon delithiation, the initial peaks are not reappearing, indicating that the amorphous phase is preserved. The Ag-exsolution process causes a deviation from the ideal $AgNbO_3$ (1:1 cation) stoichiometry to A-site deficient configuration. The SEM images of cycled electrode (0.01 – 3.0 V *vs.* Li^+/Li) show the growth of enlarged Ag particles on the surface compared to what is observed at 0.6 and 3.0 V (Fig. 4b). It is reasonable to assume that the surface exsoluted Ag can promote the formation of diffusion channels in the structure, allowing Li^+ to freely move in as the potential decreases. The removal of Ag^+ and subsequent insertion of Li^+ cations make possible the reversible reduction of Nb^{5+} that were previously inaccessible due to the presence of silver on all the A sites of the perovskite structure.

Further investigations of the $AgNbO_3$ electrode upon cycling were performed. Fig. 5 shows the variation of the differential capacity of $AgNbO_3$-based electrodes in the potential range between 0.01V-3 V *vs.* Li^+/Li obtained from charge-discharge cycle (Fig. S7) carried out at a current density of $0.01A.g^{-1}$. It is possible to identify three distinct regions, which are contributing to the total capacity of the electrode. In the potential range between 3 and 2 V *vs.* Li^+/Li (Region III) a flat signal output is observed, indicating that no significant electrochemical process is occurring and, thus, that $AgNbO_3$ is inactive in this region. However, as the potential decreases, $AgNbO_3$ starts to exhibit prominent activity with two active redox peaks at 1.74/1.63 V corresponding to Nb^{5+}/Nb^{4+} [37] and 1.3/1.34 V indicating reduced Nb^{4+}/Nb^{3+} [38] are observed (Region II). To back up the above assertions, it is critical to describe the oxidation state of various elements using advanced characterization tools.

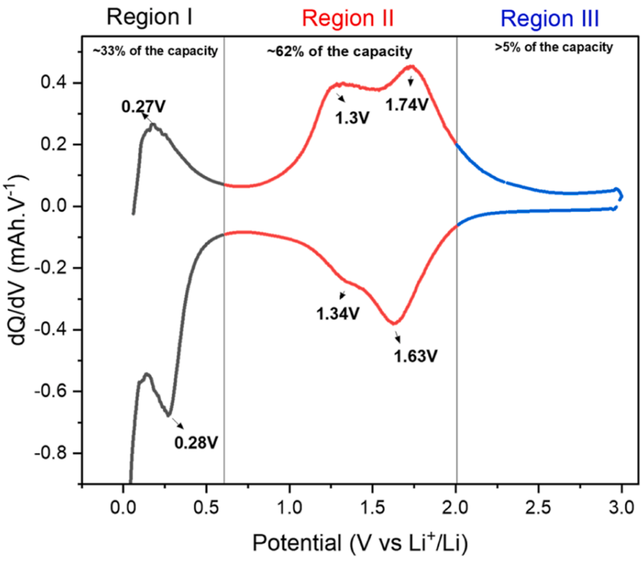

Fig. 5. Differential capacity plot depicting 3 reversible redox peaks associated to region I and II respectively. Two redox peaks located at 1.74/1.63 V and 1.3/1.34 V *vs.* Li^+/Li and single peak at 0.28 V/0.27 V *vs.* Li^+/Li could be attributed to the reduction of Nb^{5+} into Nb^{3+} as well as Li-Ag alloying reaction respectively.

Fig. 6a depicts the cut-off potential for each mass normalized ^{93}Nb and ^7Li NMR spectra obtained from $AgNbO_3$-based electrodes during the first discharge and plotted consecutively in Fig. 6b and c stopped at 1.2, 0,6 and 0.01 V *vs.* Li^+/Li, respectively. Because of the diamagnetic state of Niobium (Nb^{5+}, d^0), NMR is a powerful technique for tracking niobium reduction in $AgNbO_3$, and any change in ^{93}Nb peak intensity can be correlated to the paramagnetic compounds of Nb^{3+} and Nb^{4+} (d^2 and d^1) that are not detectable by NMR, providing evidence of the change in Nb oxidation state in $AgNbO_3$-based electrodes during reduction. At 1.2 V *vs.* Li^+/Li the ^{93}Nb NMR signal is clearly visible along with the corresponding sidebands which is an indication of presence of Nb^{5+} (Fig. 6b). At 0.6 V, the same Nb signal is observed but the intensity is lower and suggests that some of the Nb^{5+} have been reduced along with Li^+ intercalation and thus became invisible to ^{93}Nb NMR. At 0.01 V, the Nb^{5+} signal is still visible, but the signal is significantly reduced. It may indicate that the lithiation is not complete. Moreover, at 0.01 V, the Nb signal appears to be broader with the beginning of a shoulder on the right side and a slight apparent shift of the maximum from -1070 to -1080 ppm. This can be an indication that the remaining Nb^{5+} are surrounded by reduced Nb^{4+} or Nb^{3+}that may provoke local distortions and modify the Nb^{5+}local environment. Fig. 6c shows^7Li NMR spectra at different potentials. At 1.2 V *vs.* Li^+/Li, $AgNbO_3$-based electrodes display at least three resonances. Two sharp resonances at -3.3 and 0 ppm relate to Li species most likely originating from residual electrolyte/salt in our samples; these sharp signals do not match to intercalation compounds arising from Lithium-ion. However, at 0.6 and 0.01 V *vs.* Li^+/Li, there is a noticeable increase in a ^7Li NMR resonance signal which is consistent with the presence of Li^+ providing us an indication of intercalation into the active material.

Further investigations were then carried out using electron energy loss spectroscopy (EELS). Fig. 6e shows O-K edges for $AgNbO_3$-based electrodes in pristine (Nb^{+5}) and electrodes cycled at 0.01 V *vs.* Li^+/Li to highlight the potential difference in niobium oxidation state. First, O-K edge is characterized by a typical double-peak feature near the peak onset, which is characteristic of transition metal oxides [39]. This suggests that the investigated sample is not reduced to Nb^0, in agreement with the NMR results. Furthermore, in comparison to pristine $AgNbO_3$-based electrodes, a shift in peak onset as well as a peak intensity reduction between peak a and b, associated with the O-K edge of Nb at 0.01 V *vs.* Li^+/Li, was observed. The energy difference ΔE between these two peaks was also reduced from 4.79 eV for the pristine sample (Nb^{5+}) to 3.52 eV in the electrode cycled at 0.01 V *vs.* Li^+/Li. This behavior is comparable to that observed by Bach *et al.* and Tao et al. for niobium oxides and derivatives [40,41]. Furthermore, Nb-$N_{2,3}$ edges that appear in the low-loss region can be attributed to transitions of Nb 4p electrons to unoccupied 4d and 5 s. This lead to a peak broadening with the appearance of a shoulder at around 44 eV (Fig. 6f), which was also previously correlated to a decrease of Nb valence in niobium oxides [40, 42]. These results indicate the occurrence of a shift in the oxidation state of Nb towards lower valence states. However, to determine the exact degree of oxidation is difficult. Nonetheless, the ΔE energy difference on the O-K edges in reduced $AgNbO_3$ electrode (ΔE=3.52 eV) can be linearly associated with valence states of niobium oxides [40], suggesting an averaged out $+3.66$ oxidation state for Nb in the $AgNbO_3$-based electrode at 0.01 V *vs.* Li^+/Li ($Nb^{+3.66}$) (Fig. S8) which is in agreement with the electrochemical results.

Finally, below 0.6 V *vs.* Li^+/Li, a new reaction seems to take place. It leads to approximately 70 $mAh.g^{-1,}$ which accounts for 2.72 lithium per silver atom, as depicted from Fig. 5. According to previous studies on Li-Ag alloying [43] as well as to the Li-Ag binary diagram (Fig. S9), one can suspect that Ag-Li alloying reactions are taking place at such low

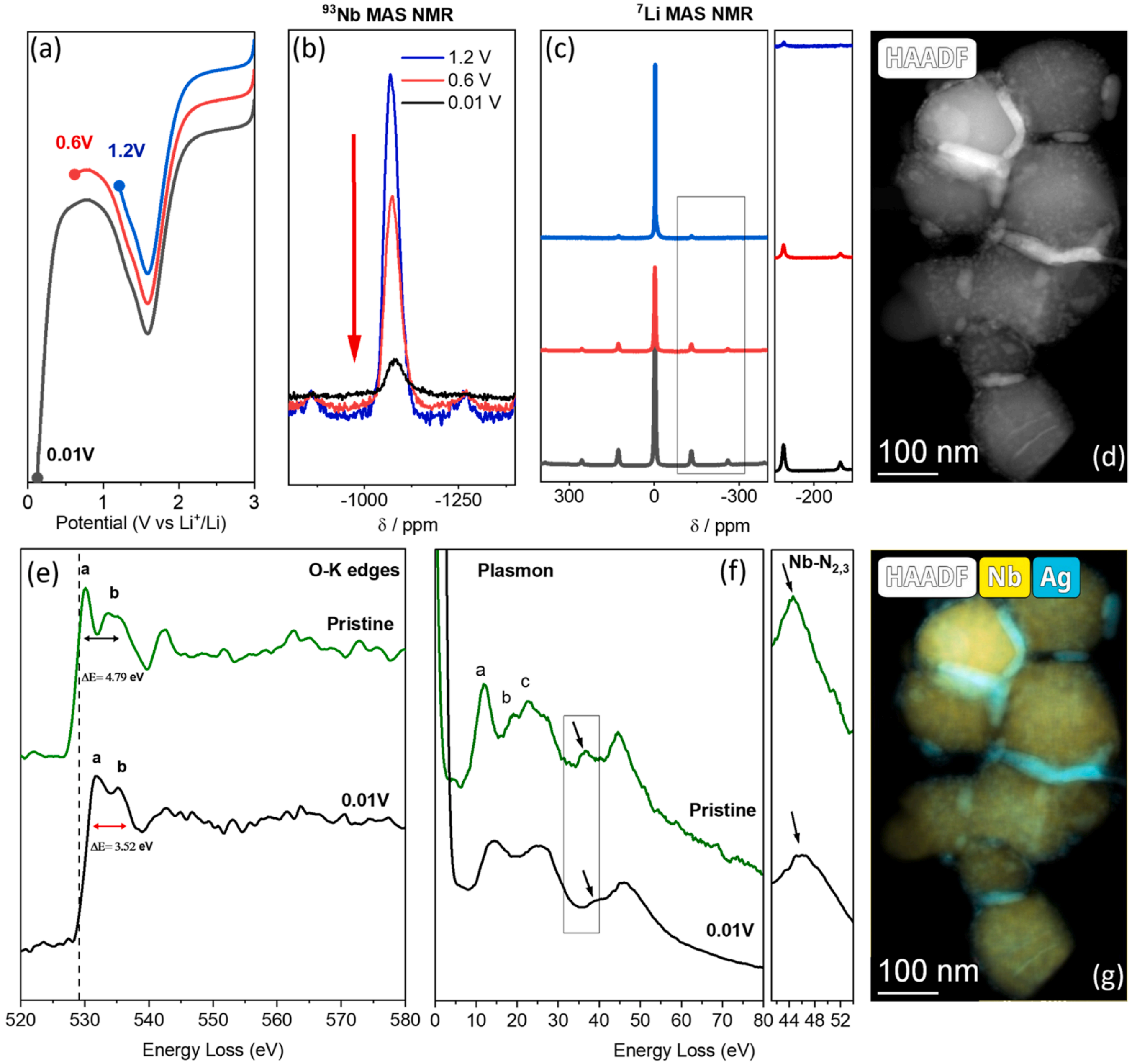

Fig. 6. (a) cutoff potential for each of the associated ex-situ NMR mesurement. (b) ^{93}Niobium NMR at 1.2 V (blue), 0.6 V (red) and 0.01 V (black) *vs.* Li^{+}/Li. (c) ^{7}Lithium NMR at 1.2,0.6 and 0.01 V *vs.* Li^{+}/Li with zoom at 200 ppm. (d) and (g) HAADF-EDS mapping of AgNbO$_3$ electrode at 0.01 V *vs.* Li^{+}/Li showing silver exsolution and contact between particles, as well as nanoclusters on its surface with homogeneous Niobium distribution in the particles. (e) EELS after background subtraction Fourier transformation showing the O-K edges of Pristine and Electrode at 0.01 V *vs.* Li^{+}/Li. (f) plasmon region and Nb-N$_{2,3}$ edges.

potential region. In the lithium-silver binary diagram, 2.72 lithium per silver atom corresponds to the γ_3 phase with redox peaks at 0.28/0.27 V *vs.* Li^{+}/Li associated to Li-Ag alloying [34,44]. An indirect approach is adopted to confirm these results, where Ag-nanoparticles electrode were cycled *vs.* metallic Li keeping the same experimental conditions. The findings reveal a Li/Ag ratio of 2.61 in the alloying process, indicating that the system falls between the γ_3 and γ_2 phases (Fig. S9 & S10) in agreement with Ag-Li alloying obtained in AgNbO$_3$. Finally, HAADF-EDS imaging of AgNbO$_3$-based electrodes at 0.01 V *vs.* Li^{+}/Li were carried out. As shown in Fig. 6d and g, the occurrence of silver extrusion in the cycled electrode compared to the pristine one (Fig. S11 and S12), takes place without affecting Niobium concentration in the material (Fig. 6g). Silver can be seen to percolate particles and grain boundaries but also cluster as nanoparticles at the surface (Fig. 6d and g), which could potentially play a substantial role in increasing the power capability of AgNbO$_3$-based electrodes by improving the electronic conductivity between the grains and further contributes to improved reversibility of electrochemical Ag-Li alloying reaction.

Moreover, According to [34,43,44] and [45,46], the theoretical capacity of AgNbO$_3$ (including a full reduction of Ag^{+} to Ag^{0} and Nb^{5+} to Nb^{3+}, and the formation of Li$_{2.72}$Ag alloy) should reach 604 mAh.g^{-1}. The maximum capacity obtained upon the first reduction is 450 mAh. g^{-1}, thus suggesting only a partial reduction of Nb^{5+} to Nb^{3+}, and some Ag^{0} particles not involved in alloying reaction with lithium. It can be noted that the maximum capacity for 12 wt% Ag$_2$Nb$_4$O$_{11}$ impurity leads to a contribution to the overall capacity of max. 24 mAh/g, *i.e.* 5 % of the AgNbO$_3$ maximum capacity.

Considering the results discussed above, it appears that the AgNbO$_3$-

based electrodes undergo a transition from pristine state (Fig. 7a, stage 1) to Ag-exsolution from A-site of the lattice (Stage 2), and finally to a crystalline-to-amorphous transition and concomitant Li-Ag alloying reaction (stage 3). Fig. 7b and c indicate what occurs to the $AgNbO_3$ electrode from a structural and electrochemical point of view. Undoubtfully, the silver exsolution process accounts for a major part to the reversibility of further reversible reactions.

3.3. *Electrochemical performance characterization*

To understand the impact of the structural changes discussed above, the electrochemical performances of the $AgNbO_3$-based electrodes were investigated at various cutoff potentials. Fig. 8a shows the specific capacity of $AgNbO_3$-based electrode before and after activation with galvanostatic cycling at 1.2, 0.6, and 0.3 V *vs.* Li^+/Li, respectively. As shown, $AgNbO_3$-based electrodes achieve activation which allows a significant and permanent increase of their capacity. *e.g.*, from 14 mAh.g^{-1} at 0.3 V before activation to 55 mAh.g^{-1} at 0.3 V after activation. This activation behavior is seen to improve capacity continuously as the potential decreases up to 0.01 V *vs.* Li^+/Li, in agreement with previous discussions regarding vacancies for lithium intercalation once silver has been exsoluted from the structure. To better understand the effect of activation on the power performance and diffusion kinetics of $AgNbO_3$, time-rate dependency was studied, where different current densities were applied at different cutoff potentials (Fig. 8b). From this study, it is obvious that the activation process is significantly enhancing the energy density of the $AgNbO_3$-based electrodes. Furthermore, discharge cycles can be carried out in less than 2 min while maintaining a capacity of 72 mAh.g^{-1}.

The lithium diffusion coefficient calculated for the activated $AgNbO_3$ electrode from GITT measurements (Fig. S13) is in the order $\sim 10^{-11}$–10^{-12} cm^2 s^{-1}, which is a value comparable to the reported high-rate intercalation type anode materials [47,48]. Another important parameter to consider when studying high-rate anode materials is their stability under severe current load conditions. Fig. 8c depicts rate performance of $AgNbO_3$-based electrodes at 0.01 V and 1.2 V *vs.* Li^+/Li. As shown, the activated $AgNbO_3$-based electrodes display remarkable efficiency and fair rate performance, with capacities reaching 226 mAh.g^{-1}, 200 mAh.g^{-1}, 155 mAh.g^{-1}, 110 mAh.g^{-1} and 72 mAh.g^{-1} at 0.1 A.g^{-1}, 0.2 A.g^{-1}, 0.5 A.g^{-1}, 1 A.g^{-1}, and 2 A.g^{-1}, respectively. Moreover, when the current density is reduced again to 0.1 A.g^{-1}, the initial capacity is fully recovered, demonstrating the high reversibility and stability of the system to various current densities.

Finally, cycling stability of the $AgNbO_3$-based electrodes has been investigated carrying out charge-discharge cycles at 1A.g^{-1}. As shown in Fig. 8d, $AgNbO_3$-based electrodes display very high cycling efficiency (higher than 99,9 %) as they go through activation, and they retain all their initial capacity after 2500 cycles. The good performance of the electrode is also maintained when is used in a proof-of-concept lab scale LIB cell (see figure S14). These results indicate that the investigated electrodes are a promising model electrode for high-power applications and pave the way for novel *exsoluted* and stable ABO_3-type electrodes for high-power lithium storage.

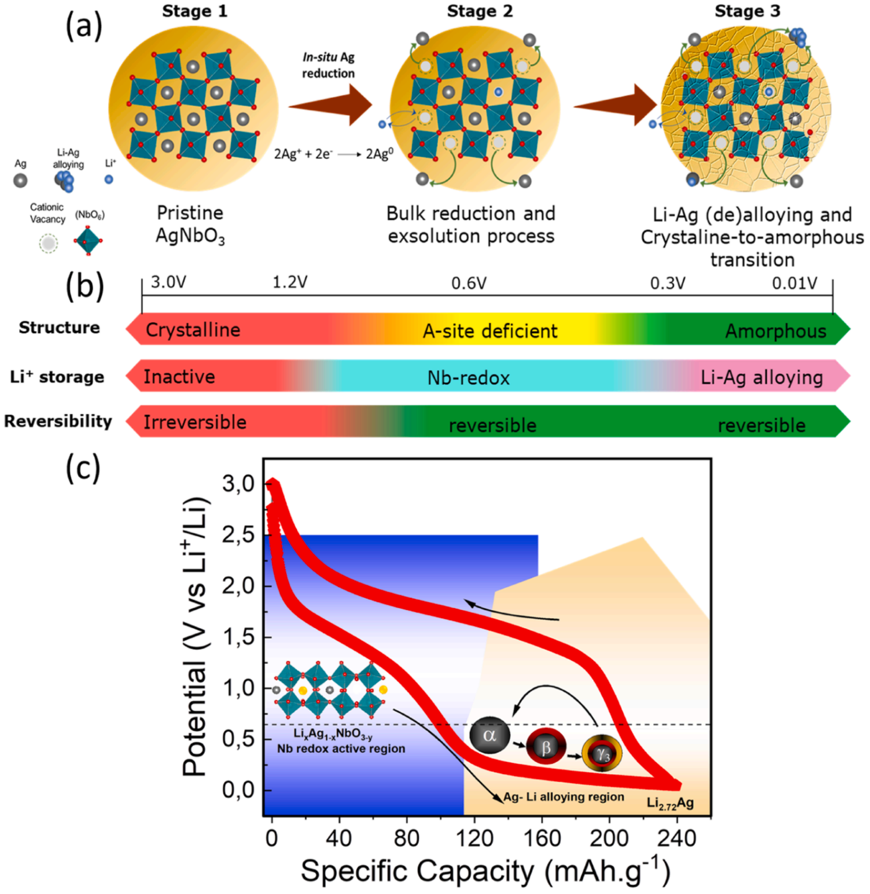

Fig. 7. (a) Schematic representation of whole in-situ material transformation due to surface and bulk Ag reduction, exsolution of Ag nanoparticles, crystalline-to-amorphous transformation, and nanoscale Ag-Li alloying process. (b) Overall summary of material transition and Li^+ storage mechanisms involved in $AgNbO_3$ material. (c) $AgNbO_3$ specific capacity and its associated schematic redox activity and phase changes according to Li-Ag binary phase diagram at room temperature. As the potential decreases, Li-Ag alloying undergoes several phases transitions until γ_3 phase.

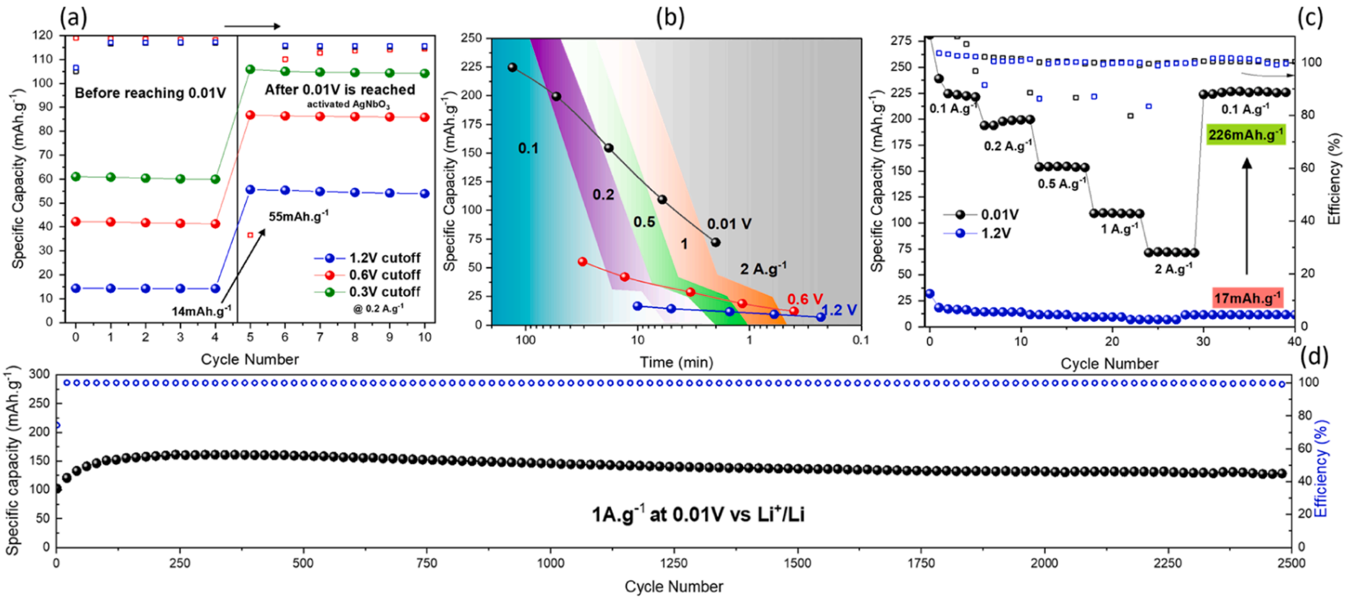

Fig. 8. (a) specific capacity of AgNbO$_3$ electrode before activation (left) and after activation (right) at 0.2 A.g^{-1}. (b) Specific capacity *versus* discharge time for AgNbO$_3$ electrode at 1.2, 0.6, and 0.3 V *vs.* Li$^+$/Li. (c) rate test of AgNbO$_3$ at 0.01 V (black) and 1.2 V (blue) *vs.* Li$^+$/Li. The capacity has been multiplied by 13 for the same electrode at the same current density. (d) Stability test at 1 A.g^{-1} charge/discharge for 2500 cycles. These plots have been recorded after the initial cycles reported in Fig. 3.

4. Conclusion

This work reported the preparation and investigation of perovskite type AgNbO$_3$ as a model material for negative electrode in LIBs. During 1st lithiation, a unique activation process is observed due to Ag-exsolution from A-site of structure causing A/B non-stoichiometry, which results in a compensation of Ag$^+$ by Li$^+$ cation intercalation to a certain extent. Structural transition between crystalline to amorphous oxide is observed below 0.3 V *vs.* Li$^+$/Li. Lithium insertion is accompanied by Nb^{5+} reduction down to an average value of Nb$^{+3.66}$. Moreover, we have demonstrated the reversible Li-Ag nano (de)alloying charge storage mechanisms in this perovskite material at the end of the reduction process. Overall, AgNbO$_3$ delivered a specific capacity of 226 mAh.g^{-1} in extended potential window (0.01 – 3.0 V), which is thirteen-fold compared to the capacity of material in its electrochemically stable potential window (1.2 – 3.V) and 4 folds capacity in comparison to the Nb-electrochemically active (0.6–3 V) region. Furthermore, the outstanding capabilities of such electrode in high-power conditions with a capacity retention of 72 mAh.g^{-1} at 2A.g^{-1} and a very good cycling stability and efficiency at 1A.g^{-1} after 2500 cycles were demonstrated. This work opens the way for exploring the fascinating properties of exsolved ABO$_3$ type perovskites and provides a foundation for their utilization as design material for high power Lithium-ion intercalating perovskite anodes.

CRediT authorship contribution statement

Abbas Khan: Writing – original draft, Investigation, Formal analysis. **Metin Orbay:** Writing – original draft, Investigation, Formal analysis. **Nicolas Dupré:** Investigation. **Eric Gautron:** Investigation. **Etienne Le Calvez:** Investigation. **Olivier Crosnier:** Writing – review & editing, Supervision. **Andrea Balducci:** Writing – review & editing, Supervision, Funding acquisition, Conceptualization. **Thierry Brousse:** Writing – review & editing, Supervision, Funding acquisition, Conceptualization.

Declaration of competing interest

I declare that there are not conflict of interest related to the present manuscript.

Acknowledgments

The authors wish to thank the Université de Nantes and Friedrich-Schiller University Jena for their financial support. Abbas Khan and Metin Orbay, as a part of the DESTINY PhD programme (Doctorate programme on Emerging battery Storage Technologies INspiring Young scientists) acknowledge funding from the European Union's Horizon 2020 research and innovation programme under the Marie Skłodowska-Curie Actions Cofund Grant Agreement No: 945357. Measurements which were performed on IMN's equipment(s) platform, PLASSMAT, Nantes, France. Funded by the French Contrat Plan Etat-Région and the European Regional Development Fund of Pays de la Loire, the CIMEN Electron Microscopy Center in Nantes, France, is greatly acknowledged. The authors are deeply thankful to Dr. Eric Quarez (from Institut des Matériaux de Nantes Jean Rouxel, IMN) for performing Rietveld refinements presented in this research paper.

Supplementary materials

Supplementary material associated with this article can be found, in the online version, at doi:10.1016/j.ensm.2024.103431.

References

[1] M. Armand, J.-M. Tarascon, Building better batteries, Nature 451 (2008) 652–657, https://doi.org/10.1038/451652a.

[2] B. Babu, P. Simon, A. Balducci, Fast charging materials for high power applications, Adv. Energy Mater. 10 (2020) 2001128, https://doi.org/10.1002/aenm.202001128.

[3] M. Schroeder, S. Menne, J. Ségalini, D. Saurel, M. Casas-Cabanas, S. Passerini, M. Winter, A. Balducci, Considerations about the influence of the structural and electrochemical properties of carbonaceous materials on the behavior of lithium-ion capacitors, J. Power Sources 266 (2014) 250–258, https://doi.org/10.1016/j.jpowsour.2014.05.024.

[4] T.-F. Yi, S.-Y. Yang, Y. Xie, Recent advances of Li4Ti5O12 as a promising next generation anode material for high power lithium-ion batteries, J. Mater. Chem. A 3 (2015) 5750–5777, https://doi.org/10.1039/C4TA06882C.

[5] T. Wang, T. Ge, S. Shi, M. Wu, G. Yang, Synthesis of wolframite FeNbO4 nanorods as a novel anode material for improved lithium storage capability, J. Alloys Compd. 740 (2018) 7–15, https://doi.org/10.1016/j.jallcom.2017.12.369.

[6] T. Takashima, T. Tojo, R. Inada, Y. Sakurai, Characterization of mixed titanium–niobium oxide Ti2Nb10O29 annealed in vacuum as anode material for lithium-ion battery, J. Power Sources 276 (2015) 113–119, https://doi.org/10.1016/j.jpowsour.2014.11.109.

[7] J. Come, V. Augustyn, J.W. Kim, P. Rozier, P.-L. Taberna, P. Gogotsi, J.W. Long, B. Dunn, P. Simon, Electrochemical kinetics of nanostructured Nb2O5 electrodes, J. Electrochem. Soc. 161 (2014) A718, https://doi.org/10.1149/2.040405jes.

[8] K.J. Griffith, Y. Harada, S. Egusa, R.M. Ribas, R.S. Monteiro, R.B. Von Dreele, A. K. Cheetham, R.J. Cava, C.P. Grey, J.B. Goodenough, Titanium niobium oxide: from discovery to application in fast-charging lithium-ion batteries, Chem. Mater. 33 (2021) 4–18, https://doi.org/10.1021/acs.chemmater.0c02955.

[9] G.A. Samara, The relaxational properties of compositionally disordered ABO3 perovskites, J. Phys.: Condens. Matter 15 (2003) R367, https://doi.org/10.1088/0953-8984/15/9/202.

[10] N. Ramadass, ABO3-type oxides—Their structure and properties—A bird's eye view, Materials Science and Engineering 36 (1978) 231–239, https://doi.org/10.1016/0025-5416(78)90076-9.

[11] L. Zhang, X. Zhang, G. Tian, Q. Zhang, M. Knapp, H. Ehrenberg, G. Chen, Z. Shen, G. Yang, L. Gu, F. Du, Lithium lanthanum titanate perovskite as an anode for lithium ion batteries, Nat. Commun. 11 (2020) 3490, https://doi.org/10.1038/s41467-020-17233-1.

[12] A. Chaupatnaik, P. Barpanda, Perovskite lead-based oxide anodes for rechargeable batteries, Electrochem. Commun. 127 (2021) 107038, https://doi.org/10.1016/j.elecom.2021.107038.

[13] E.Le Calvez, J.C. Espinosa-Angeles, G.J. Whang, N. Dupré, B.S. Dunn, O. Crosnier, T. Brousse, Investigating the perovskite Ag1-3xLaxNbO3 as a high-rate negative electrode for li-ion batteries, Front. Chem. 10 (2022) 873783.

[14] J.W. Kim, V. Augustyn, B. Dunn, The effect of crystallinity on the rapid pseudocapacitive response of Nb2O5, Adv. Energy Mater. 2 (2012) 141–148, https://doi.org/10.1002/aenm.201100494.

[15] L. Yang, X. Xiong, G. Liang, X. Li, C. Wang, W. You, X. Zhao, X. Liu, R. Che, Atomic short-range order in a cation-deficient perovskite anode for fast-charging and long-life lithium-ion batteries, Adv. Mater. 34 (2022) 2200914, https://doi.org/10.1002/adma.202200914.

[16] Y. Zhou, E. Le Calvez, S.W. Baek, M. Frajnkovič, C. Douard, E. Gautron, O. Crosnier, T. Brousse, L. Pilon, Effect of particle size on thermodynamics and lithium ion transport in electrodes made of Ti2Nb2O9 microparticles or nanoparticles, Energy Storage Materials 52 (2022) 371–385, https://doi.org/10.1016/j.ensm.2022.08.010.

[17] V. Aravindan, J. Sundaramurthy, A. Jain, P.S. Kumar, W.C. Ling, S. Ramakrishna, M.P. Srinivasan, S. Madhavi, Unveiling TiNb2O7 as an insertion anode for lithium ion capacitors with high energy and power density, ChemSusChem 7 (2014) 1858–1863, https://doi.org/10.1002/cssc.201400157.

[18] E.L. Calvez, N. Dupré, É. Gautron, C. Douard, O. Crosnier, T. Brousse, Effect of particle microstructure and the role of proton on the lithium insertion properties of HTiNbO5 electrode material, Electrochim. Acta 455 (2023) 142432, https://doi.org/10.1016/j.electacta.2023.142432.

[19] X. Li, Z. Lin, N. Jin, L. Sun, X. Yang, Y. Liu, High-capacity anode materials for lithium-ion batteries: perovskite strontium vanadate with crystalline-amorphous dual-phase structure, Mater. Today Chem. 30 (2023) 101542, https://doi.org/10.1016/j.mtchem.2023.101542.

[20] X. Li, Z. Lin, N. Jin, L. Sun, X. Yang, Y. Liu, Electrochemically induced crystalline-to-amorphous transition of dinuclear polyoxovanadate for high-rate lithium-ion batteries, Adv. Funct. Mater. 33 (2023) 2214667, https://doi.org/10.1002/adfm.202214667.

[21] D. Neagu, V. Kyriakou, I.-L. Roiban, M. Aouine, C. Tang, A. Caravaca, K. Kousi, I. Schreur-Piet, I.S. Metcalfe, P. Vernoux, M.C.M. van de Sanden, M.N. Tsampas, In Situ observation of nanoparticle exsolution from perovskite oxides: from atomic scale mechanistic insight to nanostructure tailoring, ACS Nano 13 (2019) 12996–13005. https://doi.org/10.1021/acsnano.9b05652.

[22] K. Kousi, C. Tang, I.S. Metcalfe, D. Neagu, Emergence and future of exsolved materials, Small 17 (2021) 2006479, https://doi.org/10.1002/smll.202006479.

[23] H. Jeong, Y.H. Kim, B.-R. Won, H. Jeon, C. Park, J. Myung, Emerging exsolution materials for diverse energy applications: design, mechanism, and future prospects, Chem. Mater. 35 (2023) 3745–3764, https://doi.org/10.1021/acs.chemmater.3c00004.

[24] J.H. Kim, J.K. Kim, J. Liu, A. Curcio, J.-S. Jang, I.-D. Kim, F. Ciucci, W. Jung, Nanoparticle ex-solution for supported catalysts: materials design, mechanism and future perspectives, ACS Nano 15 (2021) 81–110, https://doi.org/10.1021/acsnano.0c07105.

[25] S. Wang, D. Li, C. Yang, G. Sun, J. Zhang, Y. Xia, C. Xie, G. Yang, M. Zhou, W. Liu, A novel method for the synthesize of nanostructured MgFe2O4 photocatalysts, J. Sol-Gel Sci. Technol. 84 (2017) 169–179, https://doi.org/10.1007/s10971-017-4471-3.

[26] J.B. Leriche, S. Hamelet, J. Shu, M. Morcrette, C. Masquelier, G. Ouvrard, M. Zerrouki, P. Soudan, S. Belin, E. Elkaïm, F. Baudelet, An electrochemical cell for operando study of lithium batteries using synchrotron radiation, J. Electrochem. Soc. 157 (2010) A606, https://doi.org/10.1149/1.3355977.

[27] C. Leibing, A. Balducci, Glyoxylic-acetal-based electrolytes in combination with soft and hard carbon electrodes for lithium-ion batteries: an evaluation of room and high temperature performance, J. Electrochem. Soc. 168 (2021) 090533, https://doi.org/10.1149/1945-7111/ac23a2.

[28] P. Sciau, A. Kania, B. Dkhil, E. Suard, A. Ratuszna, Structural investigation of AgNbO3 phases using x-ray and neutron diffraction, J. Phys.: Condens. Matter 16 (2004) 2795, https://doi.org/10.1088/0953-8984/16/16/004.

[29] Y. Tian, P. Song, G. Viola, J. Shi, J. Li, L. Jin, Q. Hu, Y. Xu, W. Ge, Z. Yan, D. Zhang, N.V. Tarakina, I. Abrahams, X. Wei, H. Yan, Silver niobate perovskites: structure, properties and multifunctional applications, J. Mater. Chem. A 10 (2022) 14747–14787, https://doi.org/10.1039/D2TA00905F.

[30] S.F. Wang, H.B. Lv, X.S. Zhou, Y.Q. Fu, X.T. Zu, Magnetic nanocomposites through polyacrylamide gel route, Nanoscience and Nanotechnology Letters 6 (2014) 758–771, https://doi.org/10.1166/nnl.2014.1796.

[31] Y. Yang, J. Zhao, Wadsley–roth crystallographic shear structure niobium-based oxides: promising anode materials for high-safety lithium-ion batteries, Adv. Sci. 8 (2021) 2004855, https://doi.org/10.1002/advs.202004855.

[32] M. Morcrette, P. Rozier, L. Dupont, E. Mugnier, L. Sannier, J. Galy, J.-M. Tarascon, A reversible copper extrusion–insertion electrode for rechargeable Li batteries, Nature Mater 2 (2003) 755–761, https://doi.org/10.1038/nmat1002.

[33] P. Rozier, M. Morcrette, O. Szajwaj, V. Bodenez, M. Dolle, C. Surcin, L. Dupont, J. M. Tarascon, Li-driven copper Extrusion/*Re*-injection in various cu-based oxides and sulfides, Isr. J. Chem. 48 (2008) 235–249, https://doi.org/10.1560/IJC.48.3-4.249.

[34] J.S. Corsi, A.K. Ng, Y. Huang, E. Detsi, Impact of the gibbs–thomson effect on lithium solubility in silver used as an alloy lithium-ion battery anode, ACS Appl. Energy Mater. 5 (2022) 4547–4555, https://doi.org/10.1021/acsaem.1c04127.

[35] S. Jin, Y. Ye, Y. Niu, Y. Xu, H. Jin, J. Wang, Z. Sun, A. Cao, X. Wu, Y. Luo, H. Ji, L.-J. Wan, Solid–solution-based metal alloy phase for highly reversible lithium metal anode, J. Am. Chem. Soc. 142 (2020) 8818–8826, https://doi.org/10.1021/jacs.0c01811.

[36] X. Li, G. Yang, S. Zhang, Z. Wang, L. Chen, Improved lithium deposition on silver plated carbon fiber paper, Nano Energy 66 (2019) 104144, https://doi.org/10.1016/j.nanoen.2019.104144.

[37] C. Yang, S. Yu, C. Lin, F. Lv, S. Wu, Y. Yang, W. Wang, Z.-Z. Zhu, J. Li, N. Wang, S. Guo, Cr0.5Nb24.5O62 nanowires with high electronic conductivity for high-rate and long-life lithium-ion storage, ACS Nano 11 (2017) 4217–4224. https://doi.org/10.1021/acsnano.7b01163.

[38] M. Yang, S. Li, J. Huang, Three-dimensional cross-linked Nb2O5 polymorphs derived from cellulose substances: insights into the mechanisms of lithium storage, ACS Appl. Mater. Interfaces 13 (2021) 39501–39512, https://doi.org/10.1021/acsami.1c11720.

[39] F.M.F. de Groot, M. Grioni, J.C. Fuggle, J. Ghijsen, G.A. Sawatzky, H. Petersen, Oxygen 1s x-ray-absorption edges of transition-metal oxides, Phys. Rev. B 40 (1989) 5715–5723, https://doi.org/10.1103/PhysRevB.40.5715.

[40] D. Bach, R. Schneider, D. Gerthsen, J. Verbeeck, W. Sigle, EELS of niobium and stoichiometric niobium-oxide phases—part i: plasmon and near-edges fine structure, Microsc. Microanal. 15 (2009) 505–523, https://doi.org/10.1017/S143192760999105X.

[41] R. Tao, R. Todorovic, J. Liu, R.J. Meyer, A. Arnold, W. Walkosz, P. Zapol, A. Romanenko, L.D. Cooley, R.F. Klie, Electron energy-loss spectroscopy study of metallic Nb and Nb oxides, J. Appl. Phys. 110 (2011) 124313, https://doi.org/10.1063/1.3665193.

[42] D. Bach, R. Schneider, D. Gerthsen, EELS of niobium and stoichiometric niobium-oxide phases—part ii: quantification, Microscopy and Microanalysis 15 (2009) 524–538, https://doi.org/10.1017/S1431927609991061.

[43] C.-M. Park, H. Jung, H.-J. Sohn, Electrochemical behaviors and reaction mechanism of nanosilver with lithium, Electrochem. Solid-State Lett. 12 (2009) A171, https://doi.org/10.1149/1.3152570.

[44] H. Okamoto, Supplemental literature review of binary phase diagrams: ag-Li, Ag-Sn, Be-Pu, C-Mn, C-Si, Ca-Li, Cd-Pu, Cr-Ti, Cr-V, Cu-Li, La-*Sc*, and Li-*Sc*, J. Phase Equilib. Diffus. 38 (2017) 70–81. https://doi.org/10.1007/s11669-016-0504-9.

[45] T. Brousse, D. Defives, L. Pasquereau, S.M. Lee, U. Herterich, D.M. Schleich, Metal oxide anodes for Li-ion batteries, Ionics (Kiel) 3 (1997) 332–337, https://doi.org/10.1007/BF02375707.

[46] G. Taillades, J. Sarradin, Silver: high performance anode for thin film lithium ion batteries, J. Power Sources 125 (2004) 199–205, https://doi.org/10.1016/j.jpowsour.2003.07.004.

[47] K.J. Griffith, K.M. Wiaderek, G. Cibin, L.E. Marbella, C.P. Grey, Niobium tungsten oxides for high-rate lithium-ion energy storage, Nature 559 (2018) 556–563, https://doi.org/10.1038/s41586-018-0347-0.

[48] X. Li, Z. Lin, N. Jin, X. Yang, Y. Du, L. Lei, P. Rozier, P. Simon, Y. Liu, Perovskite-Type SrVO3 as high-performance anode materials for lithium-ion batteries, Adv. Mater. 34 (2022) 2107262, https://doi.org/10.1002/adma.202107262.

COLLEGE DOCTORAL PAYS DE LA LOIRE
ED MATIERE, MOLECULES MATERIAUX ET GEOSCIENCES

Nantes Université

Titre : Synthèse d’oxydes et de carbures comme matériaux actifs pour des systèmes de stockage d’énergie de haute puissance

Mots clés: Pérovskites, Synthèse des phases MAX, Modifications structurales, Haute puissance, batteries Li-ion

Résumé: La conception de matériaux sur mesure utilisant des approches innovantes permettant des processus de charge/décharge plus rapides pourrait être la clé pour l'avancement de la mobilité électrique. Cette thèse examine des matériaux novateurs pour les électrodes négatives de batteries Li-ion, en se concentrant sur les oxydes multicationiques à base de niobium et les carbures de métaux de transition à base de titane. Les travaux de recherche explorent la synthèse, la structure et les propriétés électrochimiques de ces matériaux, avec une attention particulière aux modifications structurales et aux mécanismes de stockage des charges. Les principaux résultats incluent l'étude de l'activation électrochimique *in-situ* des matériaux et du comportement unique de stockage du Li^+ dans les matériaux Pérovskite $AgNbO_3$, ainsi que dans les matériaux adaptés $Ag_{1-3x}Lax\square_{2x}NbO_3$ (avec $0 \leq x \leq 0{,}40$; $\square$ étant une lacune en site A) et $Ag_{1-x}\square_xNbO_{3-\delta}$ ($0 < x < 0{,}55$). De plus, cette étude examine l'effet des lacunes du site A sur la structure et sur les propriétés d'insertion du Li^+ dans les structures $K_{1-3x}La_x\square_{2x}NbO_3$ (avec $0 \leq x \leq 0{,}15$; $\square$ étant une lacune sur le site A). En outre, des informations sur la voie de synthèse polyacrylamide pour les phases MAX à base de Ti et Al sont fournies. Ce travail présente des approches pour ajuster les matériaux de manière à l’échelle atomique, sans sacrifier la phase initiale, suggérant l'utilisation potentielle de pérovskites de type ABO_3 peu étudiées comme électrodes négatives. De plus, il offre des perspectives mécanistiques sur la synthèse chimique en solution des phases MAX pour leur utilisation comme électrodes de batterie lithium-ion.

Title : Tailored oxides and carbides as active materials for high power energy storage devices

Keywords: Perovskites, MAX phase synthesis, Structural modifications, High power, Li-ion battery

Abstract: Design of tailored materials using innovative approaches that allow faster charging/discharging processes could be the key for advancement of electric mobility. This thesis investigates novel materials for Li-ion battery negative electrodes, focusing on niobium-based multicationic oxides and titanium-based transition metal carbides. This research work explores the synthesis, structure, and electrochemical properties of these materials, with particular emphasis on atomic-scale structural modifications and Li^+ storage mechanisms. Key findings include the investigation of *in-situ* electrochemical activation and unique Li^+ storage behavior in $AgNbO_3$ model perovskite, $Ag_{1-3x}La_x\square_{2x}NbO_3$ (with $0 \leq x \leq 0.40$; $\square$ is an A-site vacancy), and $Ag_{1-x}\square_xNbO_{3-\delta}$ ($0 < x < 0.55$) tailored materials. Additionally, the study examines the effect of A-site deficiency on the structure and Li^+ insertion properties of $K_{1-3x}La_x\square_{2x}NbO_3$ (with $0 \leq x \leq 0.15$; $\square$ is an A-site vacancy). Furthermore, insights into the polyacrylamide synthesis route for Ti and Al-based MAX phases are provided. These work present approaches to atomically tailor the materials without sacrificing the pristine phase, suggesting the potential use of less common ABO_3-type perovskites as negative electrodes. Additionally, it offers mechanistic insights into the wet chemical synthesis of MAX phases for their use as battery electrodes.